Characterization of Vegetal RNP Transport Granules in *Xenopus laevis* Oocytes.

By

Samantha Page Jeschonek

B.A., New College of Florida, 2010

Thesis

Submitted in partial fulfillment of the requirements for the degree of Doctor of Philosophy in the Division of Biology of Medicine at Brown University

PROVIDENCE, RHODE ISLAND

May 2019

This dissertation by Samantha Page Jeschonek is accepted in its present form by the Department of Molecular Biology, Cell Biology and Biochemistry as satisfying the dissertation requirement for the degree of Doctor of Philosophy.

Date: _____

_____
Dr. Kimberly Mowry, Advisor

Recommended to the Graduate Council

Date: _____

_____
Dr. Robbert Creton, Reader

Date: _____

_____
Dr. Alison DeLong, Reader

Date: _____

_____
Dr. Gary Wessel, Reader

Date: _____

_____
Dr. Michael Blower, Reader

Approved by the Graduate Council

Date: _____

_____
Dr. Andrew Campbell,
Dean of the Graduate School

Curriculum Vitae

SAMANTHA PAGE JESCHONEK

DOB: 12-05-1986

ADDRESS Brown University
Department of Molecular Biology, Cell Biology, and Biochemistry (MCB) Box G-L269
60 Olive St
Providence, RI 02912
Work: 401-863-2439 Cell: 561-358-5973
samantha_jeschonek@brown.edu

EDUCATION

2010–2018: **Ph.D. in Molecular Biology, Cell Biology, and Biochemistry**
Brown University, Providence, RI

2010-2014: **M.A. in Molecular Biology, Cell Biology, and Biochemistry**
Brown University, Providence, RI

2005-2010: **B.A. in Biology/Chemistry**
New College of Florida, the Honors College of the State University System, Sarasota, FL

RESEARCH EXPERIENCE

2011-2018: **Graduate Research Assistant / Ph.D. Candidate**. Brown University, Providence, RI.
Ph.D. study of RNA localization and RNP-complexes in *Xenopus laevis* oocytes. Advisor: Dr. Kimberly Mowry

2009: **Summer Scholar.** Wake Forest Institute of Regenerative Medicine, Winston-Salem, NC.
Undergraduate research focused on reprogramming human amniotic-fluid derived fetal stromal cells into induced pluripotent stem cells and validating the expression of pluripotency factors. Advisor: Dr. Patricia Wilson

2007-2008: **Undergraduate Research Assistant.** University of Arizona Cancer Center, Tucson, AZ.
Undergraduate research focused on function and signaling patterns of *Drosophila* integrins. Advisors: Dr. Danny Brower and Dr. Tom Bunch.

CONFERENCES AND PRESENTATIONS

2015: **RNA Society Twentieth Annual Meeting.** Madison, WI

Poster Title: Prrp: An RNA Binding Protein that Anchors mRNA to the Actin Cytoskeleton.

2014: **Brown University MCB Annual Retreat, Abstract-Selected Speaker.** Bristol, RI.
Talk title: Drawing a Blueprint for Cell Polarity: Novel Components of an mRNA Anchoring Complex in Xenopus laevis oocytes

2013: **Northeast Regional Meeting of the Society for Developmental Biology.** Woods Hole, MA
Poster title: Drawing a Blueprint for Cell Polarity: Novel Components of an mRNA Anchoring Complex in Xenopus laevis oocytes

2013-2014: **Molecular Biology, Cell Biology, and Biochemistry Data Club Presentation.** Providence, RI

2011-2016: **Annual Molecular Biology, Cell Biology, and Biochemistry Retreat.** Bristol, RI

2007, 2008: **UBRP (Undergraduate Biology Research Program Conference).** Tucson, AZ

MANUSCRIPTS

Jeschonek SP, Mowry KL. 2018. "Whole-Mount Immunofluorescence for Visualizing Endogenous Protein and Injected RNA in *Xenopus* Oocytes." Cold Spring Harb Protoc. 2018.

Ciocanel MV, Sandstede B, **Jeschonek SP**, Mowry KL. "Modeling microtubule-based transport and anchoring of mRNA." *Under Review*.

Jeschonek SP*, Neil CR*, Cabral SE, Powrie EP, Wood TR, Mowry KL. "Large heterotypic ribonucleoprotein granules drive RNA transport in Xenopus oocytes." In preparation
(*Co-first author)

GRANTS AND AWARDS RECEIVED

2012-2014: **Training in Molecular and Cell Biology and Biochemistry**, Grant#T32 GM007601

2011: **Honorable Mention**, National Science Foundation Graduate Research Fellowship Program

TEACHING EXPERIENCE

2015: Brown University, Summer@Brown Program. **Professor.** Course: Techniques in Molecular Biology and Biochemistry.

2014: Brown University, Summer@Brown Program. **Graduate Teaching Assistant.** Course: Techniques in Molecular Biology and Biochemistry.

2012: Brown University. **Graduate Teaching Assistant.** Course: Molecular Genetics

2006-2010: New College of Florida. **Undergraduate Teaching Assistant.** Courses: General Chemistry I and II, Biochemistry I, Cellular Biology Lecture and Laboratory

2007: Sarasota, FL. **Private tutor.** Course: General Biology

OUTREACH

2011-2013: **Advancing Rhode Island Science Education (ARISE) Program.** Providence, RI.
A professional development program for Rhode Island high school science teachers and students. Duties included helping teachers prepare laboratory modules for students, and helping students design their own science fair projects.

2012: **Nature of Discovery Symposium, Graduate Student Panelist and Poster Judge.** Providence, RI.
Hosted by the ARISE Program, this symposium allowed high school students and teachers to present their research.

2011: **Women in Science and Engineering (WiSE), Athena Science Challenge Judge.** Providence, RI.
A team-based, quiz bowl style math and science tournament which encouraged high school females to pursue careers in scientific research, medicine, and technology.

Acknowledgements

I am touched by the outpouring of mentorship, support, friendship, and love I've received over the past few years. I feel unworthy of how wonderful the friends are that I've made during my time in graduate school, even sticking around during my most hectic and antisocial stretches. Graduate school can be trying and beyond stressful, and I know that I would not have made it through without the support, laughs, fun, and love that I received. Thank you all so much.

Before the more personal acknowledgements, I want to sincerely thank Kim for all her mentorship. I was in a bit of a rut after my final rotation, and due to funding issues, was not sure if I would find a lab, even if I did additional rotations. With the support of Tricia, Kim took me on. I had limited laboratory experience when I joined, and some of the first major experiments I did, Kim donned a lab coat and personally taught me. Kim, you are one of the most meticulous and organized scientists I have ever met, and I have tried to shape my own laboratory behaviors after your example. Thank you for your patience, support, and confidence even through my own anxieties.

I arrived in Rhode Island not knowing a single person, and very quickly through an awkward Grad School social met one of my best friends. Olivia, you were a much better roommate than I ever was, and in doing so helped me learn to adult. We tackled learning to cook in the crockpot together as we secretly enjoyed each other's taste in television. I'll never admit how many episodes of *The Bachelor* I watched with you, but I enjoyed them all. I admire and respect you so much as both a person and a scientist, and I really learned so much from you (including that

not all candles are meant to be functional). The parties we threw at our somewhat-sketchy East Side apartment bring back some of the best memories. I look forward to moving to New York and reuniting as "neighbors".

To the 315 Thayer Boys, you were responsible for the most ridiculous fun I had my first year of graduate school. Thanks for always convincing me to make memories. Tak especially – we met during interview weekend, and I instantly decided I was going to be your friend. Lucky for me, you decided to hang around me too. While all the BME kids were having fun, we were stressing at the library or SFH about the papers to read for Core. Thanks for always bringing me Red Bulls in the morning.

To my BME/MPP/etc friends who I got to know more during "Gen2+"– thanks for taking me on as one of your own, even though the MCB representation was definitely in a minority. Ve, Beth, Cristina, Molly, Kara, Kali, Jess, Hetal, Raza, Mike, Manisha (and all you're +1's…am I forgetting anyone?): Thank you for providing shoulders to vent, but more importantly for teaching me how to have fun. For encouraging (bad) dancing, and the necessity of not living in isolation. Now that this whole grad school ordeal draws to a close, I look forward to hanging out more with people and visiting those who have left the area.

To Family Night, especially Bobby – thanks for being a guiding light through the thesis craziness. If I'm ever trapped in a room with 4 people, I hope that you're one of them.

To my college friends, special shout-out to Carmela, thanks for not forgetting about me way up here in the cold north. I loved all our Florida meetups,

and hope to one day get y'all up here! Carmela, I love you. Thank you thank you for calling every month to check in, because you know how bad I am about phones.

To all my friends that came and visited me in Rhode Island – thanks for being understanding of my strange schedule and being willing to hang out on Thayer or chill out while I finished lab work for the day. It was always a treat when I saw you.

And now to my little corner of Sidney Frank:

Jacob, you're a wonderful friend (believe it or not), and I really enjoyed our morning coffee talks. Thanks for being patient with me as I learned Dungeons and Dragons and created ridiculous characters.

Erin, you were my first mentor (from my rotation to when I started in the lab), and I learned quite a bit from you – including that even *I* can cook. You are a wonderful teacher, very patient and thorough, and always willing to brainstorm experiments. Thank you so much for your patience my first few years as I got my lab-legs. It was a joy to the join the lab with a fellow nerd and certainly made the days go by quickly.

Chris, we've been partners in crime since the beginning. From twin-speak to shared frustrations, you made even the longest lab days fun. We had a bit of a hectic grad school experience, but it was such a relief knowing there was someone to go through the same thing that I was. We never hung out much outside of lab, but there were definitely weeks where I interacted with you more than any other person. Your friendship has meant so much to me over the years, and now that it's in writing you really *can't* deny that we are friends.

Sarah and Liam – the “new kids”: Thank goodness you came along—I think Chris, Erin, and I would have run out of things to say if we didn’t get some fresh faces. You both really complete the lab dynamic and it has been so much fun getting to know the both of you. I wish you all the best success moving forward and hope that the all-mighty *Xenopus* looks down on you kindly.

To my family: Thank you for encouraging my education and providing unconditional love and support even through the 25th grade. Mom, I hope I have made you proud.

John – You are my soulmate. You started dating me while I had my quals and stuck around even through this thesis madness. I would not be where I am today without you. You are my anchor, my support, and my best friend. Every time I felt like giving up, you were by my side, helping keep my head above water. You have made me a better person. I love you.

Everyone: Sincerely, Thank you.

Table of Contents

Chapter 1: Introduction

Abstract

Subcellular mRNA localization is a conserved mechanism across eukaryotes, which is found in both somatic and germ cells. RNA localization in combination with local translation provides a means to generate polarized protein synthesis. In *Xenopus laevis* oocytes, *vg1* mRNA, which encodes a TGFβ growth factor family member, is localized to the vegetal cortex of developing oocytes. Vegetal RNA localization ensures that only the vegetal most blastomeres inherit *vg1* mRNA, resulting in proper germ layer patterning. *Vg1* mRNA is actively transported as a ribonucleoprotein (RNP) complex, but only a handful of *vg1* RNP components are as yet known. Understanding the composition of transport RNPs is critical to reveal not only their molecular nature, assembly, and biochemical properties, but also may provide links to cytoplasmic RNPs in other systems. To that end, we have developed a multi-step approach to biochemically isolate endogenous vegetal transport granules. Proteomic analysis of the transport granules revealed both protein constituents found in other known cytoplasmic RNP granules—including stress granules, processing bodies, neuronal granules and germ granules—as well as a set of unique proteins. Preliminary transcriptome analysis further indicates that vegetal transport granules contain heterotypic populations of RNAs, also consistent with some cytoplasmic granule types. Together our results suggest that vegetal transport RNPs represent a new class of cytoplasmic RNP granules.

"Omne vivum ex ovo" - William Harvey, 1659

Every living thing from the egg

The *ovum* theory of life (Harvey 1737; Walton 1990) suggested that within every egg, within every female, were all the necessary components for life. A miniature version of the final form cradled in a single egg, waiting only to hatch. While incorrect, this theory elevated the *egg,* bringing its importance to the spotlight.

If not *omne vivum ex ovo*, then certainly *absque vita ex ovo* – without the egg, no life. All life starts as a single cell. And while fertilization, fusion of the egg and sperm, is widely regarded as the developmental spark, the importance of the oocyte remains paramount. Within the oocyte, even prior to fertilization, a blueprint is prepared to direct development. That single egg, often a banal sphere by gross morphology, at the molecular level has become a polarized and carefully organized unit. Proper asymmetry in the mature oocyte is critical for developmental success in many, but not all, organisms.

How does the oocyte, preloaded with maternal factors, rearrange to create the blueprint for development? An important answer is subcellular localization of mRNA and polarized protein expression.

Cytoplasmic RNA Localization

Subcellular RNA localization is a conserved strategy across eukaryotes (and some prokaryotes) for creating polarized protein expression (Blower 2013; Buskila et al. 2014) . Such asymmetry is critical for a range of functions in both somatic

and germ cells. Since a single mRNA molecule can be repeatedly translated to create thousands of protein copies, it is energetically favorable to move mRNA transcripts to a location rather than translate many protein copies and subsequently transport them to their destination. In addition to reduced energy costs, the danger of ectopic protein expression or interaction with incorrect protein partners is limited. Widely studied in fields of cell motility, neuronal plasticity, and stress response, RNA localization is perhaps best-characterized as a regulator of early development (Medioni et al. 2012; Houston 2013).

Maternal deposition of RNA in the oocyte is common among various metazoa. In many cases, maternal mRNAs are ubiquitously expressed throughout the cytoplasm. To establish polarity, however, some maternal mRNAs can become spatially restricted through RNA localization. Three main modes of subcellular mRNA localization are known: (1) Selective Degradation and Protection (2) Diffusion and Entrapment, and (3) Active Transport by Molecular Motors. Below, I will review the general modes of RNA of localization with a focus on development.

Selective Degradation and Protection

While recent literature is dominated by transport-based mechanisms of localization (either active transport or diffusion), I will first discuss the mechanism of selective degradation and protection. In this mechanism, RNA is selectively degraded outside of a particular region. Rather than *moving* RNA to a destination, RNA is *removed* from anywhere but that destination.

Some of the best characterized examples of this form of localization come from the *Drosophila* oocyte. One such example is localization of *hsp83*

mRNA. Initially expressed ubiquitously, *hsp83* mRNA becomes restricted to the posterior pole. Outside of the posterior pole, *hsp83* mRNA degradation is initiated through deadeynlation by the CCR4/POP2/NOT complex, recruited by the protein Smaug, which associates with multiple stem loop elements throughout the *hsp83* mRNA open reading frame. It has been hypothesized that association of spatially restricted *oskar* mRNA with the 3′UTR of *hsp83* mRNA at the posterior pole blocks Smaug binding. As a result, *hsp83* mRNA at the posterior fails to be destabilized (Semotok et al. 2005, 2008; Chen et al. 2014).

Nanos, a germ layer determinant in *Drosophila*, also is partially localized by selective degradation. Although *nanos* mRNA is distributed throughout the cytoplasm prior to fertilization, shortly after egg activation, over 90% of the transcript is degraded, with a small population remaining at the posterior pole (Bashirullah et al. 2001). Although one potential mechanism could be that *nanos* mRNA is only redistributed to the posterior pole, northern blot analysis has shown that *nanos* mRNA is degraded (Bashirullah et al. 1999, 2001). Like *hsp83* mRNA, at the posterior pole, a pool of Oskar binds to the 3′UTR of *nanos* mRNA, blocking the Smaug degradation machinery (Zaessinger et al. 2006).

Diffusion and Entrapment

A second mechanism of RNA localization is diffusion and entrapment. Here, as in selective protection, RNA begins with a broad distribution and becomes enriched to a local region. Unlike selective protection, however, RNA is not degraded in the surrounding area, but rather, continues to accumulate from the widely distributed pool. In the *Drosophila* oocyte, for instance, *nanos* mRNA is

maternally loaded from the anteriorly-positioned nurse cells but becomes enriched to the posterior pole during late oogenesis (Gavis and Lehmann 1992). Cytoplasmic streaming of the *Drosophila* ooplasm, enhanced by polarized microtubules, propels *nanos* towards the posterior, where it is trapped by an enriched cortical actin cytoskeleton (Forrest and Gavis 2003). *Nanos* mRNA will continue to accumulate at the posterior. Not to be confused with mechanisms that actively require cytoskeletal elements, *nanos* mRNA enrichment is not dependent on the microtubules. Indeed, oocytes treated with microtubule disrupting drugs still properly localize *nanos* mRNA, although the rate may be reduced (Forrest and Gavis 2003). *Nanos* mRNA also provides an example of how a single transcript can utilize multiple modes of RNA localization. During oogenesis, active transport localizes a portion of *nanos* mRNA to the posterior pole, whereas after fertilization the bulk of *nanos* mRNA in the cytoplasm is selectively degraded.

A *nanos* homologue, *xcat2* mRNA also utilizes a diffusion entrapment mode of localization in early *Xenopus* oocytes (Kloc and Etkin 1995; Chang et al. 2004). *Xcat2* mRNA becomes concentrated in a mitochondria-rich, perinuclear region in the vegetal cytoplasm, known as the Balbiani body (Forristall et al. 1995). During oogenesis, the Balbiani body detaches from the nucleus, moving vegetally, in a microtubule-independent manner, until it breaks down at the vegetal cortex (Houston and King 2000). Enrichment in the mitochondrial cloud occurs without cytoplasmic degradation of *xcat2* mRNA (Chang et al. 2004), further supporting a diffusion-entrapment mechanism. Ultimately, *xcat2* mRNA becomes vegetally enriched and trapped in a disc-like region at the vegetal pole, thought to be maintained by cytoskeletal and ER elements (Chang et al. 2004; Kloc et al. 1996).

Active Transport

The most widely utilized form of RNA localization is motor-mediated active transport along cytoskeletal elements. Somatic cells as well as germ cells localize RNA by active transport (Gagnon and Mowry 2011). One of the first examples of a localized mRNA was actin, which was shown to accumulate in the leading edge of chicken fibroblasts (Lawrence and Singer 1986). In combination with the localization of the RNAs of the Arp2/3 actin-nucleating complex, which are transported via myosin along actin to the lamellipodia of the cell, the cell is able to respond to external stimuli triggering translation of actin and Arp2/3 RNAs, assembly of the Arp2/3 complex, and local actin growth, resulting in directed cell movement (Lawrence and Singer 1986; Mingle et al. 2005; Sundell and Singer 1991).

In neurons, transport along axons is critical for mRNA enrichment at the synapse, where proteins can be rapidly translated and turned over in response to stimuli. Neuronal dendrites are rich in RNAs for neurotransmitters, cytoskeletal proteins, and signaling molecules (Kiebler and Bassell 2006). One of the first identified localized neuronal RNAs was *mbp,* which encodes for myelin basic protein. Fluorescent labeling studies found that *mpb* was actively transported along microtubules in granules, mediated by the motor protein, Kinesin-I (Ainger et al. 1993; Carson et al. 1997). Likewise, the kinase-encoding, *camkIIα* is also localized to dendrites, mediated by a localization signal in its 3′UTR, and dependent on kinesin motor transport (Mori et al. 2000).

In germ cells, active transport mechanisms are well-studied in both *Drosophila* and *Xenopus.* In *Drosophila*, key axis determents like *oskar, gurken*,

and *bicoid* mRNAs are all produced in the nurse cells, accumulated in the oocyte, and become actively localized along microtubules to a specific destination (Weil 2014). While posteriorly localized *oskar* utilizes kinesin for transport, the anterodorsal and anterior localized RNAs, *gurken* and *bicoid*, respectively, utilize dynein (Kugler and Lasko 2009). Organisms are not limited to a single mode of RNA transport. As highlighted in *Drosophila*, in addition to the active transport for *oskar*, *gurken*, and *bicoid*, noted here, *nanos* mRNA is localized both by selective degradation and diffusion and entrapment.

Xenopus oocytes too utilize both diffusion-entrapment and active transport mechanisms (Kloc and Etkin 1995). The earliest localizing RNAs, such as *xlsirts, xpat* mRNA, and the aforementioned *xcat2* mRNA are vegetally localized via the mitochondrial cloud and a diffusion-entrapment mechanism (Chang et al. 2004). After Balbiani breakdown at the vegetal cortex, additional RNAs being to localize. Such "late-localizing" RNAs are transported actively along microtubules (Messitt et al. 2008; Gagnon 2011). The best characterized example in *Xenopus*, and a focus of this thesis, is the TGFβ-growth family member, *vg1* (Weeks and Melton 1987). Tight vegetal localization of *vg1* mRNA in a microtubule dependent manner is critical for proper germ layer formation, as Vg1 protein inherited by the vegetal blastomeres will specify endoderm and induce mesoderm (Thomsen and Melton 1993; Joseph and Melton 1998; Birsoy et al. 2006).

Vg1 mRNA Localization in *Xenopus laevis* Oocytes

Xenopus oogenesis proceeds through six stages, designated stages I – VI, with distinct growth and morphological changes at each milestone (Dumont 1972).

Maternally loaded *vg1* mRNA is uniformly distributed throughout the cytoplasm in stage I oocytes. During mid-oogenesis (stages II and III), *vg1* mRNA becomes restricted to the vegetal hemisphere (Figure 1.1A). Until the end of oogenesis, which lasts months, *vg1* mRNA is tightly restricted and anchored to the vegetal cortex (Melton 1987; Yisraeli et al. 1990). A substantial amount of work has been accomplished to understand the factors required for *vg1* mRNA localization. A common feature of RNA localization is the interaction of *cis*-acting RNA elements and *trans*-acting protein factors (King et al. 2005; Blower 2013). In fact, vegetal RNA localization is conferred by a 340-nucleotide element within the *vg1* 3′UTR, termed the vegetal localization element, or VLE (Mowry and Melton 1992). The VLE is sufficient for vegetal localization, and multiple RNA-binding proteins have been shown to bind the VLE in a sequence specific manner (Mowry and Melton 1992; Mowry 1996); this list includes Vera/Vg1RBP (Deshler et al. 1998; Havin et al. 1998), PTB/hnRNPI (Cote et al. 1999), and hnRNPAB/40LoVe (Czaplinski et al. 2005), which will hereafter be referred to as Vera, PTB, and hnRNPAB. Other RNA binding proteins, including, Elavl-1 and Elavl-2 (Otero et al. 2001) bind to other sites within the *vg1* 3'UTR, and some *in vitro* evidence has suggested binding of proteins like DAZAP1/Prrp to the VLE (Zhao et al. 2001). Still other proteins, like the double stranded RNA binding protein, Staufen (Yoon and Mowry 2004), likely bind in a structure-specific manner.

The initial stages of *vg1* mRNA localization begin in the nucleus with the formation of a core RNA-protein (RNP) complex consisting of *vg1* mRNA, Vera and PTB (Cote et al. 1999; Kress et al. 2004). Once in the cytoplasm, remodeling of the RNP complex occurs (Lewis et al. 2008) initiating recruitment of additional

RNA binding proteins (RBPs), including Prrp (Kress et al. 2004) and Staufen (Yoon and Mowry 2004). Crucially for transport, the motor proteins dynein and kinesin are also associated with the cytoplasmic *vg1* RNP complex (Yoon and Mowry 2004; Messitt et al. 2008; Gagnon et al. 2013). The association of both minus-end and plus-end directed motors, respectively, was initially surprising. The vegetal cytoplasm has long been known to be enriched with microtubules (Becker and Gard 2006). Due to the known polarization of the microtubule cytoskeleton (Pfeiffer and Gard 1999), with perinuclear plus-ends and cortical enrichment of minus ends, the presence of the minus-end-directed dynein was a logical finding. However, it was not until the discovery of a subpopulation of microtubules with plus-ends oriented towards the vegetal pole (Messitt et al. 2008), that a role for plus-end-directed kinesin was also plausible. *Vg1* mRNA undergoes at least two stages of motor transport (Figure 1.1B). Unidirectional, dynein-mediated transport initially brings the *vg1* RNP complexes to the lower vegetal cytoplasm. Here, kinesin-directed transport predominates. FRAP and *in vivo* inhibition experiments have shown that bidirectional transport occurs in the lower vegetal cytoplasm, where both populations of microtubules are present (Gagnon et al. 2013). The rationale for this mechanism is not yet known, but it is hypothesized it may provide the cell with a fine-tuned control over RNA localization, allowing adjustment of the targeting site, and ensuring that RNAs cannot escape the vegetal cytoplasm (Gagnon et al. 2013).

The final stage of *vg1* mRNA transport, anchoring (Yisraeli et al. 1990), is not yet fully characterized. It is known that the process is dependent on an enriched actin and cytokeratin network at the cortex (Klymkowsky et al. 1991;

Alarcón and Elinson 2001; Klymkowsky 1995; Pondel and King 1988; Forristall et al. 1995; Elinson et al. 1993). Early localizing pathway RNAs, like *xlsirts*, are also required for proper anchoring (Kloc and Etkin 1994). It has been suggested that additional RBPs, like the *vg1* RNA-binding protein, Prrp, act to further anchor the RNA at the cortex (Zhao et al. 2001), but such a complex has not been identified. In addition, it is not yet known whether cortical anchoring is a necessary step in the transport pathway.

Cytoplasmic Granules

Cytoplasmic granules (Figure 1.2) are a conserved feature in a variety of cells, though they are quite diverse in function (Buchan 2014). Some, like germ granules, are required for long term storage of developmentally-relevant mRNAs (Voronina et al. 2011). Others, like stress-granules provide shorter term storage for a broader range of mRNAs but only transiently during times of cellular stress (Protter and Parker 2016). Processing bodies are involved in downstream mRNA degradation (Luo et al. 2018). Neuronal granules, exclusively found in neurons, place a greater focus on long-range mRNA transport in axons and dendrites (Kiebler and Bassell 2006). Despite the functional diversity, the broad role of "RNA storage", lends itself to some common features. For instance, all these granules are comprised of RNA and protein. While this common feature of cytoplasmic granules may be apparent, increasing prominence in the literature and fierce debates about biophysical characteristics makes defining core features somewhat challenging.

For clarity, here, I define cytoplasmic granules as membraneless collections of RNA-binding proteins and RNA, in the size range of microns, and discrete from their surroundings (Buchan 2014; Alberti 2017). Though cytoplasmic granules are often comprised of multiple RNP-complexes, an RNP-complex alone cannot be defined as a granule until it is shown to have distinct properties from its cytoplasmic environment. As alluded to above, stress granules, processing bodies, germ granules, and neuronal transport granules are among the most well characterized of cytoplasmic granules.

Stress Granules

Aptly named, stress granules are transiently formed under conditions of cellular stress including heat shock, amino acid starvation, hypoxia, and chemical perturbation. In response, mRNA is sequestered, inhibiting translation and allowing the cell to recover from temporary stressors, or is degraded if the stress is irreversible (Protter and Parker 2016). Phosphorylation of Eif2α, regulated by stress-induced kinases, leads to polysome disassembly as translation initiation is stalled and actively translating ribosomes "run off" their associated mRNA (Kedersha et al. 1999). Stalled preinitiation complexes, minimally containing mRNA and the 40S small ribosomal subunit, are bound by the nucleocytoplasmic RNA-binding protein, Tia-1 (Kedersha et al. 1999, 2002). In addition to an RNA binding domain, Tia-1 also contains a prion-like domain, which could be responsible for aggregation of Tia-1 containing mRNP complexes, leading to stress granule nucleation (Gilks et al. 2004). The local concentration of mRNA and protein increases as mRNP oligomerization continues, leading to additional

recruitment of factors through protein-protein, RNA-protein (Wheeler et al. 2016), and RNA-RNA interactions (Van Treeck et al. 2018).

Of the four types of cytoplasmic granules featured, stress granules are the only class to have identified all known *vg1* RNA binding proteins within their proteome: Staufen, Vera, PTB, Elavl-1, Elavl-2, and hnRNPAB (Jain et al. 2016). In addition, motor proteins like dynein, have also been identified as components of stress granules (Jain et al. 2016). Thus, this overlap makes stress granules an attractive starting point for comparison with *Xenopus* vegetal transport granules.

Recent proteomic analysis of isolated yeast and mammalian stress granules has revealed a dense protein population with distinct regions within the stress granule (Jain et al. 2016; Wheeler et al. 2017). A stable, inner core, comprised of mRNA and high concentrations of RNA binding proteins, was found to be surrounded by a more dynamic outer shell which can interact with additional nascent stress granules to form larger assemblies (Jain et al. 2016). In mammals, smaller stress granules can fuse together to form larger structures (Ohshima et al. 2015). This process is mediated by microtubules, either through active transport with dynein (Tsai et al. 2009) or other motor proteins (Nadezhdina et al. 2010).

Although the stress granule proteome is fairly large, it shows quite a degree of redundancy. In fact, more than 50% of the stress granule core proteome are RNA binding proteins (Wheeler et al. 2016; Jain et al. 2016). Overall, the stress granule proteome consists of proteins with ATPase activity, scaffolding proteins, heat shock proteins, RNA binding proteins, proteins with prion-like domains, and those proteins with modification activity (Jain et al. 2016; Markmiller et al. 2018),

and as noted above, and pertinent to this thesis, seven of the identified stress granule components are known *vg1* RNA binding proteins.

While classes of enriched proteins have been identified in stress granules, the RNA population has been much less studied. Recent work combining single-molecule FISH (smFISH) and RNA-seq on isolated stress granule cores (Khong et al. 2018) has indicated that the stress granule transcriptome is largely heterogenous and diverse, even between stress granules in the same cell. Indeed, it has been shown that nearly all transcripts have the capacity to enter a stress granule (Khong et al. 2017). While no RNA is overly abundant in stress granules, there are a few features that increase the likelihood of stress granule inclusion. First, the majority (approximately 80%) of RNAs contained in stress granules are messenger RNA. Second, those RNAs that have poor translation efficiency and are not actively associated with ribosomes are more likely to be included into stress granules. Third, reduced mitochondrial and ER membrane association increases the likelihood of inclusion. Finally, a longer coding region and/or 3′UTR increases the ability of an RNA to enter a stress granule (Khong et al. 2017), perhaps because of the increased chance of RNA-RNA interactions (Van Treeck et al. 2018).

Processing Bodies (P-Bodies)

Processing bodies (p-bodies) are stable cytoplasmic hubs that act as storage sites for translationally silenced mRNAs. This is a stark contrast to stress granules, which represent a transient response to a cellular threat. While mRNAs stored temporarily in stress granules may be released to the actively translating pool once a stressor has passed, p-body mRNAs are more often destined for decay (Luo et al.

2018). Indeed, p-bodies have been shown to dock with stress granules and exchange components, perhaps capturing those mRNAs for which there is no recovery (Kedersha et al. 2005). Although p-bodies are present even in the absence of stress, forming whenever a critical level of translationally stalled mRNA in the cell is reached, they too can be induced by cellular stress (Sheth and Parker 2003). However, because p-body assembly is not regulated by stress-induced kinase Eif2α phosphorylation, the same stressors do not induce both stress granule and p-body assembly (Shah et al. 2013).

There is an overlap of components between stress granules and p-bodies, but their differences truly highlight the differing functions of the two (Figure 1.2). While stress granules contain translation initiation factors and small ribosomal subunits, due to the nucleation at a stalled preinitiation complex (Kedersha et al. 1999), p-bodies are devoid of these components (Teixeira et al. 2005). Instead, they are rich in non-translating mRNA that is associated with decapping factors (Tharun and Parker 2001). Consistent with this finding is that mRNAs with long poly(A) tails tend to be excluded from p-bodies (Aizer et al. 2014), whereas, oligo(dT) labeling has indicated that mRNA in stress granules is poly-adenylated (Jain et al. 2016).

The inclusion of RNA stabilizing proteins, such as Pabp, in stress granules but not p-bodies and the high concentration of mRNA degradation pathway proteins exclusively found in p-bodies (Kedersha et al. 2005; Jain et al. 2016; Hubstenberger et al. 2017), suggests clear functional differences between these cytoplasmic granules, specifically, that mRNA included in p-bodies, but not stress granules, is fated for decay. However, recent work has suggested that the resident

degradation machinery may be inhibited inside the p-body (Horvathova et al. 2017). To date, the particular role p-bodies play in mRNA degradation is unclear: they are not exclusively necessary for RNA decay (Horvathova et al. 2017; Eulalio et al. 2007), nor are all RNAs fated for p-bodies destined for degradation (Brengues et al. 2005). Escape routes from the p-body can include reassociation with polysomes (Brengues et al. 2005; Cougot et al. 2013) and interaction with other types of cytoplasmic granules (Serman et al. 2007; Wilczynska et al. 2005).

Perhaps further complicating what, on first inspection, might be two distinct classes of granules, is the overlap of many common elements. Like stress granules, p-bodies are rich in RNA binding proteins, including several *vg1* RNA binding proteins: Stau2, Vera, hnRNPAB, and Elavl-1 and Elavl-2 (Hubstenberger et al. 2017). Supporting the notion that p-bodies are not the ultimate sites of decay are the inclusion of mRNA stability factors, such as Pcbp2, HuR, and Ybox1, as in stress granules (Jain et al. 2016; Hubstenberger et al. 2017). Likewise, stress granules contain some components of the decay machinery that is present in p-bodies, including Smaug and the exoribonuclease Xrn1 (Jain et al. 2016; Hubstenberger et al. 2017; Stoecklin and Kedersha 2013; Decker and Parker 2012).

In addition to dynamic associations with other cytoplasmic granules, processing bodies can also be highly mobile. Aside from their intrabody motility, as demonstrated by FRAP (Kedersha et al. 2005; Aizer et al. 2014), some p-body populations have been shown to traverse long distances. For example, in HeLa cells p-bodies move while associated with microtubule networks, as microtubule depolymerization blocks p-body movement (Sweet et al. 2007; Aizer et al. 2008), and in *Arabidopsis*, p-bodies travel on actin networks, mediated by myosin motors

(Steffens et al. 2014). Interestingly, other p-bodies have limited movement, hampered by surrounding actin bundles (Aizer et al. 2008). These characteristics are rather reminiscent of the *vg1* RNP–containing a motile long-range transport phase, partially mediated by dynein, and a stable anchored phase at the actin rich vegetal cortex.

Germ Granules

Germ granules are a unique class of cytoplasmic RNP granules exclusively found in germ cells, containing only those mRNAs required for embryonic development. These granules have different names in different organisms such as germinal granules in *Xenopus* (Heasman et al. 1984), polar granules in *Drosophila* (Mahowald 1962), and perhaps the most extensively studied, P-granules in *C. elegans* (Strome and Wood 1982). Ultrastructural analyses have revealed a membraneless, fibrillar and electron dense structure (Kloc et al. 2002, 2004; Thomson et al. 2008; Sheth et al. 2010). Germ granules share many compositional similarities with both stress granule and p-bodies (Figure 1.2). Rich in RNA binding proteins, translational repressors, and mRNA stability regulators, germ granules also contain unique elements like piRNA, siRNA and miRNA regulators, germ layer determinants, and the hallmark germ granule marker, Vasa (Gruidl et al. 1996; Voronina et al. 2011; DeHaan et al. 2017; Vourekas et al. 2016; Zheng et al. 2016).

Germ granules can be thought of as the storehouse for maternally loaded and translationally silent mRNAs (Cuykendall and Houston 2010; Gao and Arkov 2013; Rangan et al. 2009). They are quite stable as they must persist through

oogenesis and early development. Though stable, they are dynamically remodeled as development proceeds (Voronina et al. 2011).

P-granules, the *C. elegans*' germinal granule, for example, have a dynamic localization pattern through development. Initially, they are dispersed as small RNP aggregates throughout the cytoplasm before coalescing and fusing after segregation into germline blastomeres (Updike and Strome 2010). As development continues, the P-granules move perinuclearly, continuing to grow, and eventually attaching to the nuclear periphery (Pitt et al. 2000). Ultimately, at maturation, P-granules will detach from the nucleus. P-granules have also been found to transiently fuse with other cytoplasmic granules, such as p-bodies, and exchange contents (Gallo et al. 2008). As a result, not all P-granules within a given cell are identical.

In *Xenopus*, the germinal granules are first contained in the perinuclear mitochondrial cloud, or Balbiani body, at the earliest stages of oogenesis (Wilk et al. 2005). In stage I oocytes, the Balbiani body moves vegetally and disassembles at the vegetal pole releasing the germinal granules, which settle as a disc at the vegetal cortex (Kloc and Etkin 1995; Wilk et al. 2005).

Neuronal Transport Granules

In neurons, mRNAs are packaged into transport-competent RNPs that mediate RNA localization. These RNPs are known as neuronal transport granules (Figure 1.2). Neuronal transport granules are an attractive link between the motility of *vg1* RNPs and the mRNA sequestering nature of germ granules, stress granules, and p-bodies. In fact, one of the first identified components of actively

transported neuronal granules was the *vg1* RNA binding protein, Staufen (Köhrmann et al. 1999). Although most RNA in a neuron is in the cell body, a specialized subset of mRNAs is actively transported in neuronal granules along microtubules to synapses. As with *vg1* RNPs, such directional transport is mediated by the motors kinesin (Kanai et al. 2004) and dynein (Xu et al. 2013). At the postsynaptic spines localization may be further refined with the action of myosin along the rich dendritic actin cytoskeleton (Mitsumori et al. 2017). Interestingly, localization may be dictated by the specific components of the individual granules (Mitsumori et al. 2017), highlighting the diversity of these granules even within the same cell. For instance, studies in hippocampal neurons have shown that granules along the dendrite have different protein compositions. Stau1-containing granules tend be located exclusively in dendritic shafts, whereas granules containing Purα were also found in dendritic spines (Mitsumori et al. 2017).

Neuronal granules, similar to the aforementioned granule types, are rich in RNA binding proteins and proteins with roles in translational control, as well as ribosomal subunits (Knowles et al. 1996; Kanai et al. 2004; Fritzsche et al. 2013). After transport to the synapse, the mRNAs, which are primarily polyadenylated as in stress granules (Knowles et al. 1996), can be translated to produce spatially restricted protein expression. Such polarized protein expression is important in axon guidance (Wong et al. 2017), neural plasticity (Puthanveettil 2013), and rapid response to stimuli (Tiruchinapalli et al. 2003). Studies with the mRNA, *camkIIα* in rat neurons have shown that mRNAs in neuronal granules are translationally stalled at initiation (Krichevsky and Kosik 2001). Indeed local stimulation leads to

the release of mRNAs and ribosomal subunits from granules, allowing them to enter polysomes (Krichevsky and Kosik 2001). Neuronal granules also do not exist in isolation from other cytoplasmic granules. P-bodies have been found in dendrites along with neuronal granules in *Drosophila*, rat, and mammalian neurons (Barbee et al. 2006; Cougot et al. 2008) and interactions between these granules is thought to help control translation (Zeitelhofer et al. 2008). Similarly, stress granules have also been found in conjunction with neuronal granules in dendrites, where mRNAs from neuronal granules may redistribute upon cellular stress (Thomas et al. 2005)

As with other cytoplasmic granules, mRNA contained within neuronal transport granules is translationally silenced. In fact, the granules may be important to stabilize transcripts. For instance, in neurons downregulated for Stau2, granules show transcriptional degradation of those mRNAs usually contained in Stau2 particles (Heraud-Farlow et al. 2013). Cargo diversity of neuronal RNPs is another feature – different neuronal granules within the same cell may have different mRNA populations. Neuronal transport granules isolated from rat neurons, for instance, showed different enrichment levels of mRNAs depending on which RNA-binding protein was used to isolate the granule (Fritzsche et al. 2013; Heraud-Farlow et al. 2013).

A Word on Liquid-Liquid Phase Separation and its Relation to Cytoplasmic Granules

In 2009, the Hyman laboratory published a landmark paper in *Science* on the biophysical properties of *C. elegans* P-granules (Brangwynne et al. 2009).

They found that P-granules exhibited liquid-like properties: they were able to fuse and split from one another, "wet" a surface (like raindrops on a window), deform under shearing stress, had similar viscosities and surface tensions to liquids, and had extremely dynamic internal rearrangements, as demonstrated by FRAP experiments (Brangwynne et al. 2009). Brangwynne et al. further proposed that these liquid-like properties were not unique to P-granules but may be represented among many RNPs as a way to self-assemble and form dynamic phase-separated structures (Brangwynne et al. 2009).

Whereas Brangywnne spearheaded the idea of liquid-like like properties of cytoplasmic RNPs, the evidence for phase separation among RNPs in general had been suggested earlier. Indeed, nuclear RNPs, like Cajal bodies had been shown to display the classically-liquid fusion-and-dissolution properties (Platani et al. 2000). Pertinent to our work, many of these initial studies used *Xenopus* oocytes (Brangwynne et al. 2011; Nizami and Gall 2012). Nor was a "liquid-like" state the only phase-separated type difference between RNPs and the surroundings. The nuclear pore complex was found to be rich in phenylalanine and glycine repeats, creating a molecular sieve in the form a hydrogel. Unlike liquid-like droplets, these hydrogels were extremely stable, showing very little recovery in FRAP experiments (Frey et al. 2006). Phase separation between RNPs and surroundings could come in multiple varieties – from liquid-like to more gel or solid-like.

In 2012 the McKnight laboratory published two exciting back-to-back papers in *Cell* (Han et al. 2012; Kato et al. 2012). In, what I imagine to be a Bob Ross style, "happy accident" science moment, the group noted that concentrated GST-tagged Fus, an RNA binding protein, formed a gel-like state at low

temperatures. Upon further investigation, they found that this phenomenon was exclusively observed in the presence of the N-terminus. Truncation at the C-terminal RNA binding domains did not affect gel formation. Instead, this altered phase state was linked to an N-terminal low complexity domain (LCD). LCDs are amino acid sequences lacking defined structure (Cumberworth et al. 2013). They are often rich in glutamine, glycine and asparagine repeats and have little sequence diversity. Also called intrinsically disordered regions (IDRs), they are prominent in proteins associated with neurodegenerative diseases, often mutated in a way to cause the disease phenotype, such as the glutamine expansion in Huntington's disease (Kaganovich 2017).

The hydrogel formed by the LCD of Fus also was able to selectively retain the LCD of other RNA binding proteins. Transmission electron microscopy revealed the hydrogels were actually comprised of amyloid-like fibers (Kato et al. 2012). The LCD of these proteins effectively form a phase-separated scaffold, but inclusion was somewhat dependent on post-translational modification state, providing a possible mechanism of formation. The McKnight laboratory went on to show that these hydrogels retained mRNAs commonly found in neuronal granules (Han et al. 2012; Kato et al. 2012).

Together, this work has solidified (no pun intended), the idea of phase-separation in RNPs and provided a new opportunity to study mechanisms and properties of cytoplasmic bodies. Nearly every cytoplasmic RNP (including germ granules, processing bodies, stress granules, and neuronal granules) has been found to have some sort of phase separated property (Kaganovich 2017). Germ granules, such as *C. elegans* P-granules, continue to have much research focused

on their distinct liquid properties. Other membraneless cytoplasmic bodies found in germ cells, like Balbiani bodies, were revealed to have more amyloid or hydrogel like structure (Kloc et al. 2004; Voronina et al. 2011; Boke et al. 2016). More liquid-like properties were seen in stress granules and processing bodies where even fusion between the two was possible (Protter and Parker 2016; Luo et al. 2018). Neuronal granules were found to have dynamic viscosities, becoming more or less liquid-like depending on location (De Graeve et al. 2018).

A Granular View of the Cytoplasm

More than two decades after their respective discoveries, stress granules, germ granules, processing bodies, and neuronal transport granules have been extensively studied. Despite the already vast literature on these granules, new traits and concepts are still being identified. For instance, the involvement of phase separation and liquid-liquid like characteristics of these granules has only sparked interest in the past few years. By contrast, relatively little published literature is available on transport granules in germ cells. As such, defining the characteristics of a germ-cell transport granule is critical for further investigation.

Here, I define a germ-cell transport granule by the following features: (1) Contains mRNA and RNA binding proteins, (2) Is associated with motor proteins and a cytoskeletal network, (3) Is actively transported to a particular region within the germ cell, (4) Is membraneless and distinct from its surroundings, potentially rich in proteins containing low-complexity domains, (5) Is distinct from germinal granules, lacking germinal-granule specific markers like the protein Vasa and the mRNA, *velo*.

The vegetal transport granules in *Xenopus laevis* oocytes are a unique system for study, encompassing distinct features from other granule types. Like neuronal transport granules, vegetal transport granules must traverse long distances within the cell (owing to the large size of the *Xenopus* oocyte). As with germ granules, the vegetal transport granules are exclusively located in a germ cell and are required for long-term storage. As this thesis will show, the diversity of proteins and RNAs associated with the vegetal transport RNP extend beyond those required for developmental regulation. In fact, many of the protein components are like those of stress granules and processing bodies. And like all granule types mentioned, there is an abundance of RNA binding proteins and LCD-containing proteins, though the biophysical properties of the vegetal RNP transport granules may be unique.

Vegetal transport granules are a potentially "hybrid" granule and study of this new granule type may give insight into core functionality of shared granule-proteins. As this thesis will demonstrate, vegetal transport granules can be successfully isolated from oocytes, allowing for biochemical investigation while maintaining *in vivo* composition. The work described in this thesis provides a unique platform to study these endogenous granules, *ex vivo*–something which investigators have struggled with in other systems. With the increasing evidence that LCD-containing proteins play a pivotal role in neurogenerative disease, could studying the LCD-rich vegetal transport granules of the model vertebrate *Xenopus laevis* inform us about human disease? What are these vegetal transport granules? What can their component overlap but functional divergence tell us about the core components of other systems? How can studying these vegetal transport granules

fill the gap in knowledge about relationships among a variety cytoplasmic RNP granules? The goal of this thesis is to explore these questions by isolating and characterizing the constituents of vegetal transport granules.

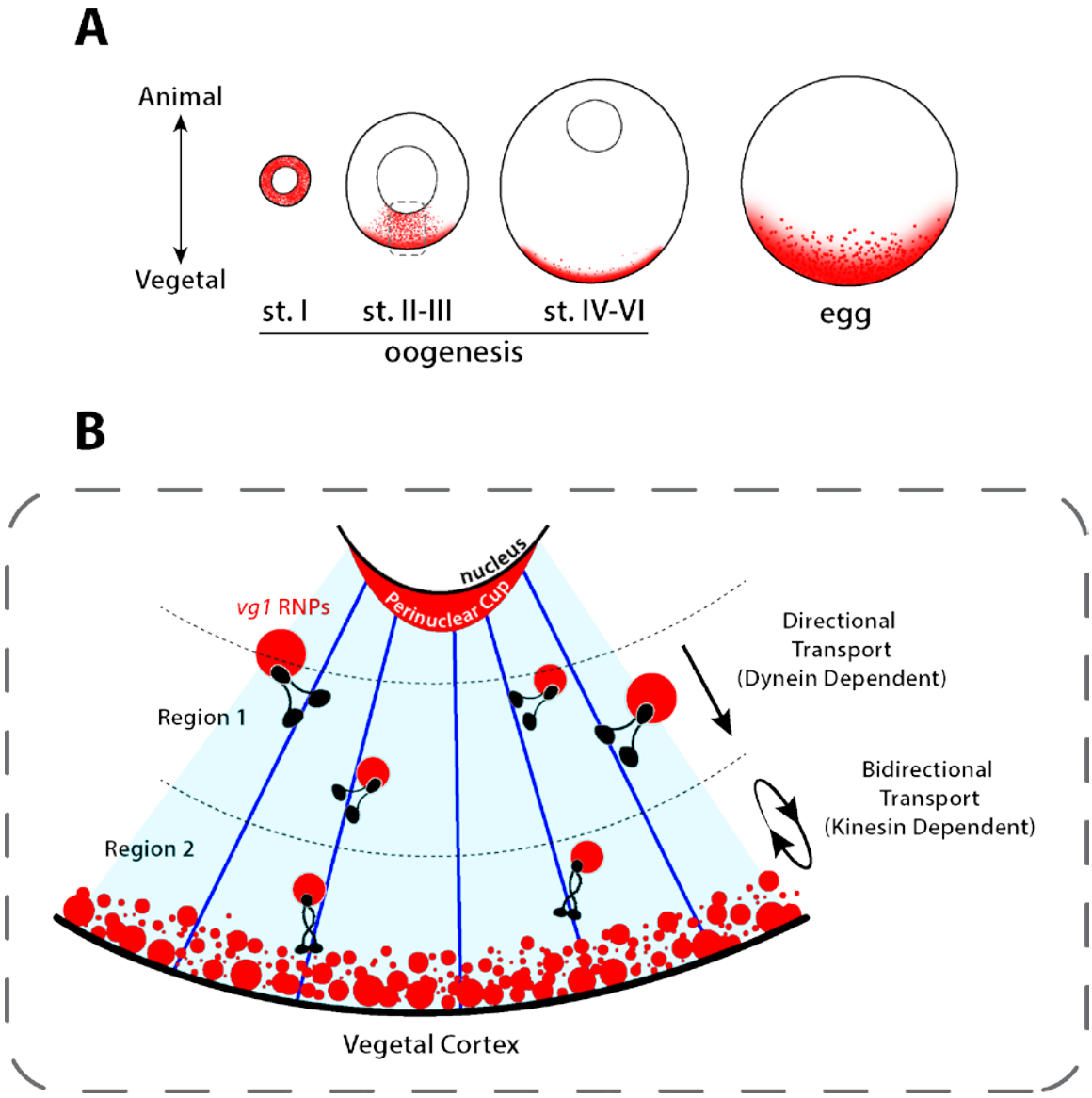

Figure 1.1. ***Vegetal mRNA transport in* Xenopus *oocytes*.** **(A)** The distribution of *vg1* mRNA (red stipples) is shown during early (st. I), middle (st. II-III) and late (st. IV-VI) stages of oogenesis. In the egg (right) and early embryo (not shown), Vg1 protein is restricted to the vegetal hemisphere and vegetal blastomeres, respectively. **(B)** View of the vegetal cytoplasm of a stage II-III oocyte (gray box from A). *Vg1* RNPs (red) are transported by motor proteins (black) along polarized microtubules (blue lines) towards the vegetal cortex. The vegetal

cytoplasm is schematically divided into two regions: In Region 1, vegetally-directed transport is driven by dynein and in Region 2, bidirectional transport depends on kinesin motors.

	Stress Granules	Processing Bodies (P-Bodies)	Neuronal Transport Granules	Germ Granules
Overall Function	Temporary RNA storage & protection	RNA storage, RNA decay targeting	Transport of mRNA to synapses and dendrites	Storage of developmentally important factors
RNA Translational Status	Stalled at preinitiation complex	Stalled	Translationally silenced	Translationally silenced
Formation	Stress induced	By high levels of translational silencing, can be stress induced	Independent of stress	Early oogenesis
Overall Stability	Transient	Mostly stable, some transient	Stable	Long-term, persists through oogenesis
Molecular Stability	Stable core, dynamic outer shell	Dynamic	Dynamic	Dynamic remodeling during development
Hallmark Proteins and Reported Protein Classes	ATPase modulated proteins ribosomal subunits RNA stabilizing proteins RNA binding proteins	Decapping enzymes mRNA degradation pathway proteins RISC machinery RNA binding proteins	Molecular motors Ribosomal components RNA binding proteins	Vasa Translational repressors mRNA stability proteins small RNA pathway components RNA binding proteins
RNA Properties	mRNA with long poly(A) tails	Short poly(A) tails	mRNA, poly(A) tails	Developmentally regulated mRNA
Phase Properties	Liquid-like	Liquid-like	Less characterized; some liquid-like properties	Liquid-like
Motility	Fusion with other granules Microtubule and motor mediated	Very motile Fusion with other granules Microtubule and motor mediated Actin controlled	Long range transport across axons Shorter range transport in dendrites Microtubule and motor mediated	Dynamic localization during oogenesis or development Can be motor independent
Interaction with Other Granules	Yes	Yes	Yes	Yes
Cell Type	Any, with stress	Any	Neurons	Germ Cells

Figure 1.2. ***Comparison of cytoplasmic granules.*** Four classes of cytoplasmic granules are compared: Stress granules, Processing bodies (p-bodies), Neuronal transport granules, and Germ granules. See text for references.

References

Ainger K, Avossa D, Morgan F, Hill SJ, Barry C, Barbarese E, Carson JH. 1993. Transport and localization of exogenous myelin basic protein mRNA microinjected into oligodendrocytes. *J Cell Biol* **123**: 431–41.

Aizer A, Brody Y, Ler LW, Sonenberg N, Singer RH, Shav-Tal Y. 2008. The dynamics of mammalian P body transport, assembly, and disassembly in vivo. *Mol Biol Cell* **19**: 4154–66.

Aizer A, Kalo A, Kafri P, Shraga A, Ben-Yishay R, Jacob A, Kinor N, Shav-Tal Y. 2014. Quantifying mRNA targeting to P-bodies in living human cells reveals their dual role in mRNA decay and storage. *J Cell Sci* **127**: 4443–4456.

Alarcón VB, Elinson RP. 2001. RNA anchoring in the vegetal cortex of the *Xenopus* oocyte. *J Cell Sci* **114**: 1731–41.

Alberti S. 2017. Phase separation in biology. *Curr Biol* **27**: R1097–R1102.

Barbee SA, Estes PS, Cziko A-MM, Hillebrand J, Luedeman RA, Coller JM, Johnson N, Howlett IC, Geng C, Ueda R, et al. 2006. Staufen- and FMRP-containing neuronal RNPs are structurally and functionally related to somatic P bodies. *Neuron* **52**: 997–1009.

Bashirullah a, Cooperstock RL, Lipshitz HD. 2001. Spatial and temporal control of RNA stability. *Proc Natl Acad Sci USA* **98**: 7025–8.

Bashirullah a, Halsell SR, Cooperstock RL, Kloc M, Karaiskakis a, Fisher WW, Fu W, Hamilton JK, Etkin LD, Lipshitz HD. 1999. Joint action of two RNA degradation pathways controls the timing of maternal transcript elimination at the midblastula transition in *Drosophila melanogaster*. *EMBO J* **18**: 2610–20.

Becker BE, Gard DL. 2006. Visualization of the cytoskeleton in *Xenopus* oocytes and eggs by confocal immunofluorescence microscopy. *Methods Mol Biol* **322**: 69–86.

Birsoy B, Kofron M, Schaible K, Wylie C, Heasman J. 2006. Vg1 is an essential signaling molecule in *Xenopus* development. *Development* **133**: 15–20.

Blower MD. 2013. Molecular insights into intracellular RNA localization. *Int Rev Cell Mol Biol* **302**: 1–39.

Boke E, Ruer M, Wühr M, Coughlin M, Lemaitre R, Gygi SP, Alberti S, Drechsel D, Hyman AA, Mitchison TJ. 2016. Amyloid-like self-assembly of a cellular compartment. *Cell* **166**: 637–650.

Brangwynne CP, Eckmann CR, Courson DS, Rybarska A, Hoege C, Gharakhani J, Julicher F, Hyman AA, Jülicher F, Hyman AA. 2009. Germline P granules are liquid droplets that localize by controlled dissolution/condensation. *Science* **324**: 1729–32.

Brangwynne CP, Mitchison TJ, Hyman A a. 2011. Active liquid-like behavior of nucleoli determines their size and shape in *Xenopus laevis* oocytes. *Proc Natl Acad Sci USA* **108**: 4334–9.

Brengues M, Teixeira D, Parker R. 2005. Movement of eukaryotic mRNAs between polysomes and cytoplasmic processing bodies. *Science* **310**: 486–489.

Buchan JR. 2014. mRNP granules. *RNA Biol* **11**: 1019–30.

Buskila AA, Kannaiah S, Amster-Choder O. 2014. RNA localization in bacteria. *RNA Biol* **11**: 1051–1060.

Carson JH, Worboys K, Ainger K, Barbarese E. 1997. Translocation of myelin basic protein mRNA in oligodendrocytes requires microtubules and kinesin. *Cell*

Motil Cytoskel **38**: 318–28.

Chang P, Torres J, Lewis RA, Mowry KL, Houliston E, King ML. 2004. Localization of RNAs to the mitochondrial cloud in *Xenopus* oocytes through entrapment and association with endoplasmic reticulum. *Mol Biol Cell* **15**: 4669–81.

Chen L, Dumelie JG, Li X, Cheng MH, Yang Z, Laver JD, Siddiqui NU, Westwood JT, Morris Q, Lipshitz HD, et al. 2014. Global regulation of mRNA translation and stability in the early *Drosophila* embryo by the Smaug RNA-binding protein. *Genome Biol* **15**: R4.

Cote CA, Gautreau D, Denegre JM, Kress TL, Terry NA, Mowry KL. 1999. A *Xenopus* protein related to hnRNP I has a role in cytoplasmic RNA localization. *Mol Cell* **4**: 431–7.

Cougot N, Bhattacharyya SN, Tapia-Arancibia L, Bordonné R, Filipowicz W, Bertrand E, Rage F. 2008. Dendrites of mammalian neurons contain specialized P-body-like structures that respond to neuronal activation. *J Neurosci* **28**: 13793–804.

Cougot N, Molza A-EE, Giudice E, Cavalier A, Thomas D, Gillet R. 2013. Structural organization of the polysomes adjacent to mammalian processing bodies (P-bodies). *RNA Biol* **10**: 314–320.

Cumberworth A, Lamour G, Babu MM, Gsponer J. 2013. Promiscuity as a functional trait: intrinsically disordered regions as central players of interactomes. *Biochem J* **454**: 361–9.

Cuykendall TN, Houston DW. 2010. Identification of germ plasm-associated transcripts by microarray analysis of *Xenopus* vegetal cortex RNA. *Dev Dynam* **239**: 1838–48.

Czaplinski K, Köcher T, Schelder M, Segref A, Wilm M, Mattaj IW. 2005. Identification of 40LoVe, a *Xenopus* hnRNP D family protein involved in localizing a TGF-beta-related mRNA during oogenesis. *Dev Cell* **8**: 505–15.

De Graeve F, Besse F, Graeve F De, Bessé F. 2018. Neuronal RNP granules: from physiological to pathological assemblies. *Biol Chem* **0**: 623–635.

Decker CJ, Parker R. 2012. P-bodies and stress granules: possible roles in the control of translation and mRNA degradation. *Cold Spring Harb Perspect Biol* **4**: a012286.

DeHaan H, McCambridge A, Armstrong B, Cruse C, Solanki D, Trinidad JC, Arkov AL, Gao M. 2017. An in vivo proteomic analysis of the Me31B interactome in *Drosophila* germ granules. *FEBS Lett* **591**: 3536–3547.

Deshler JO, Highett MI, Abramson T, Schnapp BJ. 1998. A highly conserved RNA-binding protein for cytoplasmic mRNA localization in vertebrates. *Curr Biol* **8**: 489–96.

Dumont JN. 1972. Oogenesis in *Xenopus laevis* (Daudin). I. Stages of oocyte development in laboratory maintained animals. *J Morph* **136**: 153–179.

Elinson RP, King M Lou, Forristall C. 1993. Isolated vegetal cortex from *Xenopus* oocytes selectively retains localized mRNAs. *Dev Biol* **160**: 554–562.

Eulalio A, Behm-Ansmant I, Schweizer D, Izaurralde E. 2007. P-body formation is a consequence, not the cause, of RNA-mediated gene silencing. *Mol Cell Biol* **27**: 3970–81.

Forrest KM, Gavis ER. 2003. Live imaging of endogenous RNA reveals a diffusion and entrapment mechanism for nanos mRNA localization in *Drosophila*. *Curr Biol* **13**: 1159–68.

Forristall C, Pondel M, Chen L, King M Lou. 1995. Patterns of localization and cytoskeletal association of two vegetally localized, vg1 and xcat-2. **208**: 201–208.

Frey S, Richter RP, Görlich D. 2006. FG-rich repeats of nuclear pore proteins form a three-dimensional meshwork with hydrogel-like properties. *Science* **314**: 815–817.

Fritzsche R, Karra D, Bennett KL, Ang FY, Heraud-Farlow JE, Tolino M, Doyle M, Bauer KE, Thomas S, Planyavsky M, et al. 2013. Interactome of two diverse RNA granules links mRNA localization to translational repression in neurons. *Cell Rep* **5**: 1749–1762.

Gagnon J a, Mowry KL. 2011. Molecular motors: directing traffic during RNA localization. *Crit Rev Biochem Mol Biol* **46**: 229–39.

Gagnon JA. 2011. Insights into Directional Motor-Driven RNA Localization from the *Xenopus* Oocyte. 232.

Gagnon JA, Kreiling J a, Powrie EA, Wood TR, Mowry KL. 2013. Directional transport is mediated by a Dynein-dependent step in an RNA localization pathway. *PLoS Biol* **11**: e1001551.

Gallo CM, Munro E, Rasoloson D, Merritt C, Seydoux G. 2008. Processing bodies and germ granules are distinct RNA granules that interact in *C. elegans* embryos. *Dev Biol* **323**: 76–87.

Gao M, Arkov AL. 2013. Next generation organelles: structure and role of germ granules in the germline. *Mol Reprod Dev* **80**: 610–23.

Gavis ER, Lehmann R. 1992. Localization of *nanos* RNA controls embryonic polarity. *Cell* **71**: 301–13.

Gilks N, Kedersha N, Ayodele M, Shen L, Stoecklin G, Dember LM, Anderson P. 2004. Stress granule assembly is mediated by prion-like aggregation of TIA-1. *Mol Biol Cell* **15**: 5383–98.

Gruidl ME, Smith PA, Kuznicki KA, McCrone JS, Kirchner J, Roussell DL, Strome S, Bennett KL. 1996. Multiple potential germ-line helicases are components of the germ-line-specific P granules of *Caenorhabditis elegans*. *Proc Natl Acad Sci U S A* **93**: 13837–42.

Han TWW, Kato M, Xie S, Wu LCC, Mirzaei H, Pei J, Chen M, Xie Y, Allen J, Xiao G, et al. 2012. Cell-free formation of RNA granules: Bound RNAs identify features and components of cellular assemblies. *Cell* **149**: 768–779.

Harvey W. 1737. *Exercitationes de generatione animalium*. apud Johannem van Kerckhem, 1737.

Havin L, Git A, Elisha Z, Oberman F, Yaniv K, Schwartz SP, Standart N, Yisraeli JK. 1998. RNA-binding protein conserved in both microtubule- and microfilament-based RNA localization. *Genes Dev* **12**: 1593–1598.

Heasman J, Quarmby J, Wylie CC. 1984. The mitochondrial cloud of *Xenopus* oocytes: The source of germinal granule material. *Dev Biol* **105**: 458–469.

Heraud-Farlow JE, Sharangdhar T, Li X, Pfeifer P, Tauber S, Orozco D, Hörmann A, Thomas S, Bakosova A, Farlow AR, et al. 2013. Staufen2 regulates neuronal target RNAs. *Cell Rep* **5**: 1511–1518.

Horvathova I, Voigt F, Kotrys A V., Zhan Y, Artus-Revel CG, Eglinger J, Stadler MB, Giorgetti L, Chao JA. 2017. The dynamics of mRNA turnover revealed by single-molecule imaging in single Cells. *Mol Cell* **68**: 615–625.

Houston DW. 2013. Regulation of cell polarity and RNA localization in vertebrate

oocytes. *Int Rev Cell Mol Biol* **306**: 127–85.

Houston DW, King M Lou. 2000. Germ plasm and molecular determinants of germ cell fate. *Curr Top Dev Biol* **50**: 155-181.

Hubstenberger A, Courel M, Bénard M, Souquere S, Ernoult-Lange M, Chouaib R, Yi Z, Morlot J-BB, Munier A, Fradet M, et al. 2017. P-body purification reveals the condensation of repressed mRNA regulons. *Mol Cell* **68**: 144–157.e5.

Jain S, Wheeler JR, Walters RW, Agrawal A, Barsic A, Parker R. 2016. ATPase-modulated stress granules contain a diverse proteome and substructure. *Cell* **164**: 487–498.

Joseph EM, Melton D a. 1998. Mutant Vg1 ligands disrupt endoderm and mesoderm formation in *Xenopus* embryos. *Development* **125**: 2677–85.

Kaganovich D. 2017. There Is an Inclusion for That: Material Properties of Protein Granules Provide a Platform for Building Diverse Cellular Functions. *Trends Biochem Sci* **42**: 765–776.

Kanai Y, Dohmae N, Hirokawa N. 2004. Kinesin transports RNA: isolation and characterization of an RNA-transporting granule. *Neuron* **43**: 513–25.

Kato M, Han TW, Xie S, Shi K, Du X, Wu LC, Mirzaei H, Goldsmith EJ, Longgood J, Pei J, et al. 2012. Cell-free formation of RNA granules: Low complexity sequence domains form dynamic fibers within hydrogels. *Cell* **149**: 753–767.

Kedersha N, Chen S, Gilks N, Li W, Miller IJ, Stahl J, Anderson P. 2002. Evidence that ternary complex (eIF2-GTP-tRNA(i)(Met))-deficient preinitiation complexes are core constituents of mammalian stress granules. *Mol Biol Cell* **13**: 195–210.

Kedersha N, Stoecklin G, Ayodele M, Yacono P, Lykke-Andersen J, Fritzler MJ,

Scheuner D, Kaufman RJ, Golan DE, Anderson P. 2005. Stress granules and processing bodies are dynamically linked sites of mRNP remodeling. *J Cell Biol* **169**: 871–84.

Kedersha NL, Gupta M, Li W, Miller I, Anderson P. 1999. RNA-binding proteins TIA-1 and TIAR link the phosphorylation of eIF-2 alpha to the assembly of mammalian stress granules. *J Cell Biol* **147**: 1431–42.

Khong A, Jain S, Matheny T, Wheeler JR, Parker R. 2018. Isolation of mammalian stress granule cores for RNA-Seq analysis. *Methods* **137**: 49–54.

Khong A, Matheny T, Jain S, Mitchell SF, Wheeler JR, Parker R. 2017. The stress granule transcriptome reveals principles of mRNA accumulation in stress granules. *Mol Cell* **68**: 808–820.e5.

Kiebler MA, Bassell GJ. 2006. Neuronal RNA granules: movers and makers. *Neuron* **51**: 685–90.

King M Lou, Messitt TJ, Mowry KL. 2005. Putting RNAs in the right place at the right time: RNA localization in the frog oocyte. *Biol Cell* **97**: 19–33.

Kloc M, Bilinski S, Etkin LD. 2004. The balbiani body and germ cell determinants: 150 years later. *Curr Top Dev Biol* **59**: 1–36.

Kloc M, Dougherty MT, Bilinski S, Chan AP, Brey E, King M Lou, Patrick CW, Etkin LD. 2002. Three-dimensional ultrastructural analysis of RNA distribution within germinal granules of *Xenopus*. *Dev Biol* **241**: 79–93.

Kloc M, Etkin LD. 1994. Delocalization of Vg1 mRNA from the vegetal cortex in *Xenopus* oocytes after destruction of Xlsirt RNA. *Science* **265**: 1101–1103.

Kloc M, Etkin LD. 1995. Two distinct pathways for the localization of RNAs at the vegetal cortex in *Xenopus* oocytes. *Development* **121**: 287–97.

Kloc M, Larabell C, Etkin LD. 1996. Elaboration of the messenger transport organizer pathway for localization of RNA to the vegetal cortex of *Xenopus* oocytes. *Dev Biol* **180**: 119–30.

Klymkowsky MW. 1995. Intermediate filament organization, reorganization, and function in the clawed frog *Xenopus*. *Curr Top Dev Biol* **31**: 455–86.

Klymkowsky MW, Maynell LA, Nislow C. 1991. Cytokeratin phosphorylation, cytokeratin filament severing and the solubilization of the maternal mRNA Vg1. *J Cell Biol* **114**: 787–797.

Knowles RB, Sabry JH, Martone ME, Deerinck TJ, Ellisman MH, Bassell GJ, Kosik KS. 1996. Translocation of RNA granules in living neurons. *J Neurosci* **16**: 7812–20.

Köhrmann M, Luo M, Kaether C, DesGroseillers L, Dotti CG, Kiebler MA. 1999. Microtubule-dependent recruitment of staufen-green fluorescent protein into large RNA-containing granules and subsequent dendritic transport in living hippocampal neurons ed. J. Lippincott-Schwartz. *Mol Biol Cell* **10**: 2945–2953.

Kress TL, Yoon YJ, Mowry KL. 2004. Nuclear RNP complex assembly initiates cytoplasmic RNA localization. *J Cell Biol* **165**: 203–211.

Krichevsky AM, Kosik KS. 2001. Neuronal RNA Granules: A link between RNA localization and stimulation-dependent translation. *Neuron* **32**: 683–696.

Kugler J-M, Lasko P. 2009. Localization, anchoring and translational control of *oskar*, *gurken*, *bicoid* and *nanos* mRNA during *Drosophila* oogenesis. *Fly (Austin)* **3**: 15–28.

Lawrence JB, Singer RH. 1986. Intracellular localization of messenger RNAs for

cytoskeletal proteins. *Cell* **45**: 407–15.

Lewis RA, Gagnon JA, Mowry KL. 2008. PTB/hnRNP I is required for RNP remodeling during RNA localization in *Xenopus* oocytes. *Mol Cell Biol* **28**: 678–686.

Luo Y, Na Z, Slavoff SA. 2018. P-Bodies: Composition, properties, and functions. *Biochemistry* **57**: acs.biochem.7b01162.

Mahowald AP. 1962. Fine structure of pole cells and polar granules in *Drosophila melanogaster*. *J Exp Zool* **151**: 201–215.

Markmiller S, Soltanieh S, Server KL, Mak R, Jin W, Fang MY, Luo E, Krach F, Yang D, Sen A, et al. 2018. Context-dependent and disease-specific diversity in protein interactions within stress granules. *Cell* **172**: 590–604.e13.

Medioni C, Mowry K, Besse F. 2012. Principles and roles of mRNA localization in animal development. *Development* **139**: 3263–76.

Melton DA. 1987. Translocation of a localized maternal mRNA to the vegetal pole of *Xenopus* oocytes. *Nature* **328**: 80–2.

Messitt TJ, Gagnon JA, Kreiling JA, Pratt CA, Yoon YJ, Mowry KL. 2008. Multiple kinesin motors coordinate cytoplasmic RNA transport on a subpopulation of microtubules in *Xenopus* oocytes. *Dev Cell* **15**: 426–436.

Mingle LA, Okuhama NN, Shi J, Singer RH, Condeelis J, Liu G. 2005. Localization of all seven messenger RNAs for the actin-polymerization nucleator Arp2/3 complex in the protrusions of fibroblasts. *J Cell Sci* **118**: 2425–33.

Mitsumori K, Takei Y, Hirokawa N. 2017. Components of RNA granules affect their localization and dynamics in neuronal dendrites. *Mol Biol Cell* **28**: 1412–1417.

Mori Y, Imaizumi K, Katayama T, Yoneda T, Tohyama M. 2000. Two cis-acting

elements in the 3' untranslated region of alpha-CaMKII regulate its dendritic targeting. *Nat Neurosci* **3**: 1079–84.

Mowry KL. 1996. Complex formation between stage-specific oocyte factors and a *Xenopus* mRNA localization element. *Proc Natl Acad Sci USA* **93**: 14608–13.

Mowry KL, Melton DA. 1992. Vegetal messenger RNA localization directed by a 340-nt RNA sequence element in *Xenopus* oocytes. *Science* **255**: 991–4.

Nadezhdina ES, Lomakin AJ, Shpilman AA, Chudinova EM, Ivanov PA. 2010. Microtubules govern stress granule mobility and dynamics. *Biochim Biophys Acta - Mol Cell Res* **1803**: 361–371.

Nizami ZF, Gall JG. 2012. Pearls are novel Cajal body-like structures in the *Xenopus* germinal vesicle that are dependent on RNA pol III transcription. *Chromosom Res* **20**: 953–969.

Ohshima D, Arimoto-Matsuzaki K, Tomida T, Takekawa M, Ichikawa K. 2015. Spatio-temporal dynamics and mechanisms of stress granule assembly. ed. F. Mac Gabhann. *PLoS Comput Biol* **11**: e1004326.

Otero LJ, Devaux A, Standart N. 2001. A 250-nucleotide UA-rich element in the 3' untranslated region of *Xenopus laevis* Vg1 mRNA represses translation both in vivo and in vitro. *RNA* **7**: 1753–67.

Pfeiffer DC, Gard DL. 1999. Microtubules in *Xenopus* oocytes are oriented with their minus-ends towards the cortex. *Cell Motil Cytoskeleton* **44**: 34–43.

Pitt JN, Schisa JA, Priess JR. 2000. P granules in the germ cells of *Caenorhabditis elegans* adults are associated with clusters of nuclear pores and contain RNA. *Dev Biol* **219**: 315–33.

Platani M, Goldberg I, Swedlow JR, Lamond AI. 2000. *In vivo* analysis of Cajal

body movement, separation, and joining in live human cells. *J Cell Biol* **151**: 1561–74.

Pondel MD, King ML. 1988. Localized maternal mRNA related to transforming growth factor beta mRNA is concentrated in a cytokeratin-enriched fraction from *Xenopus* oocytes. *Proc Natl Acad Sci USA* **85**: 7612–6.

Protter DSW, Parker R. 2016. Principles and properties of stress granules. *Trends Cell Biol* **26**: 668–79.

Puthanveettil S V. 2013. RNA transport and long-term memory storage. *RNA Biol* **10**: 1765–70.

Rangan P, DeGennaro M, Jaime-Bustamante K, Coux R-X, Martinho RG, Lehmann R. 2009. Temporal and spatial control of germ-plasm RNAs. *Curr Biol* **19**: 72–7.

Semotok JL, Cooperstock RL, Pinder BD, Vari HK, Lipshitz HD, Smibert CA. 2005. Smaug recruits the CCR4/POP2/NOT deadenylase complex to trigger maternal transcript localization in the early *Drosophila* embryo. *Curr Biol* **15**: 284–94.

Semotok JL, Luo H, Cooperstock RL, Karaiskakis A, Vari HK, Smibert CA, Lipshitz HD. 2008. *Drosophila* maternal Hsp83 mRNA destabilization is directed by multiple SMAUG recognition elements in the open reading frame. *Mol Cell Biol* **28**: 6757–6772.

Serman A, Le Roy F, Aigueperse C, Kress M, Dautry F, Weil D. 2007. GW body disassembly triggered by siRNAs independently of their silencing activity. *Nucleic Acids Res* **35**: 4715–4727.

Shah KH, Zhang B, Ramachandran V, Herman PK. 2013. Processing body and

stress granule assembly occur by independent and differentially regulated pathways in Saccharomyces cerevisiae. *Genetics* **193**: 109–23.

Sheth U, Parker R. 2003. Decapping and decay of messenger RNA occur in cytoplasmic processing bodies. *Science* **300**: 805–808.

Sheth U, Pitt J, Dennis S, Priess JR. 2010. Perinuclear P granules are the principal sites of mRNA export in adult *C. elegans* germ cells. *Development* **137**: 1305–14.

Steffens A, Jaegle B, Tresch A, Hulskamp M, Jakoby M. 2014. Processing-body movement in *Arabidopsis* depends on an interaction between myosins and decapping protein1. *Plant Physiol* **164**: 1879–1892.

Stoecklin G, Kedersha N. 2013. Relationship of GW/P-bodies with stress granules. pp. 197–211.

Strome S, Wood WB. 1982. Immunofluorescence visualization of germ-line-specific cytoplasmic granules in embryos, larvae, and adults of *Caenorhabditis elegans*. *Proc Natl Acad Sci U S A* **79**: 1558–62.

Sundell CL, Singer RH. 1991. Requirement of microfilaments in sorting of actin messenger RNA. *Science* **253**: 1275–7.

Sweet TJ, Boyer B, Hu W, Baker KE, Coller J. 2007. Microtubule disruption stimulates P-body formation. *RNA* **13**: 493–502.

Teixeira D, Sheth U, Valencia-Sanchez MA, Brengues M, Parker R. 2005. Processing bodies require RNA for assembly and contain nontranslating mRNAs. *RNA* **11**: 371–82.

Tharun S, Parker R. 2001. Targeting an mRNA for decapping: Displacement of translation factors and association of the lsm1p–7p complex on deadenylated

yeast mRNAs. *Mol Cell* **8**: 1075–1083.

Thomas MG, Tosar LJM, Loschi M, Pasquini JM, Correale J, Kindler S, Boccaccio GL. 2005. Staufen recruitment into stress granules does not affect early mRNA transport in oligodendrocytes. *Mol Biol Cell* **16**: 405–420.

Thomsen GH, Melton DA. 1993. Processed Vg1 protein is an axial mesoderm inducer in *Xenopus*. *Cell* **74**: 433–441.

Thomson T, Liu N, Arkov A, Lehmann R, Lasko P. 2008. Isolation of new polar granule components in *Drosophila* reveals P body and ER associated proteins. *Mech Dev* **125**: 865–73.

Tiruchinapalli DM, Oleynikov Y, Kelic S, Shenoy SM, Hartley A, Stanton PK, Singer RH, Bassell GJ. 2003. Activity-dependent trafficking and dynamic localization of zipcode binding protein 1 and beta-actin mRNA in dendrites and spines of hippocampal neurons. *J Neurosci* **23**: 3251–61.

Tsai N-P, Tsui Y-C, Wei L-N. 2009. Dynein motor contributes to stress granule dynamics in primary neurons. *Neuroscience* **159**: 647–656.

Updike D, Strome S. 2010. P granule assembly and function in *Caenorhabditis elegans* germ cells. *J Androl* **31**: 53–60.

Van Treeck B, Protter DSW, Matheny T, Khong A, Link CD, Parker R. 2018. RNA self-assembly contributes to stress granule formation and defining the stress granule transcriptome. *Proc Natl Acad Sci U S A* **115**: 2734–2739.

Voronina E, Seydoux G, Sassone-Corsi P, Nagamori I. 2011. RNA granules in germ cells. *Cold Spring Harb Perspect Biol* **3**: a002774.

Vourekas A, Alexiou P, Vrettos N, Maragkakis M, Mourelatos Z. 2016. Sequence-dependent but not sequence-specific piRNA adhesion traps mRNAs to the

germ plasm. *Nature* **531**: 390–394.

Walton M. 1990. The works of William Harvey. *JAMA* **263**: 3090–3091.

Weeks DL, Melton DA. 1987. A maternal mRNA localized to the vegetal hemisphere in *Xenopus* eggs codes for a growth factor related to TGF-β. *Cell* **51**: 861–867.

Weil TT. 2014. mRNA localization in the *Drosophila* germline. *RNA Biol* **11**: 1010–8.

Wheeler JR, Jain S, Khong A, Parker R, Kong A, Parker R. 2017. Isolation of yeast and mammalian stress granule cores. *Methods* **126**: 12–17.

Wheeler JR, Matheny T, Jain S, Abrisch R, Parker R. 2016. Distinct stages in stress granule assembly and disassembly. *Elife* **5**: 1–25.

Wilczynska A, Aigueperse C, Kress M, Dautry F, Weil D. 2005. The translational regulator CPEB1 provides a link between dcp1 bodies and stress granules. *J Cell Sci* **118**: 981–92.

Wilk K, Bilinski S, Dougherty MT, Kloc M. 2005. Delivery of germinal granules and localized RNAs via the messenger transport organizer pathway to the vegetal cortex of *Xenopus* oocytes occurs through directional expansion of the mitochondrial cloud. *Int J Dev Biol* **49**: 17–21.

Wong HH, Lin JQ, Ströhl F, Roque CG, Cioni J-M, Cagnetta R, Turner-Bridger B, Laine RF, Harris WA, Kaminski CF, et al. 2017. RNA docking and local translation regulate site-specific axon remodeling *in vivo*. *Neuron* **95**: 852–868.e8.

Xu X, Brechbiel JL, Gavis ER. 2013. Dynein-dependent transport of *nanos* RNA in *Drosophila* sensory neurons requires Rumpelstiltskin and the germ plasm

organizer Oskar. *J Neurosci* **33**: 14791–800.

Yisraeli JK, Sokol S, Melton DA. 1990. A two-step model for the localization of maternal mRNA in *Xenopus* oocytes: involvement of microtubules and microfilaments in the translocation and anchoring of Vg1 mRNA. *Development* **108**: 289–98.

Yoon YJ, Mowry KL. 2004. *Xenopus* Staufen is a component of a ribonucleoprotein complex containing Vg1 RNA and kinesin. *Development* **131**: 3035–45.

Zaessinger S, Busseau I, Simonelig M. 2006. Oskar allows *nanos* mRNA translation in *Drosophila* embryos by preventing its deadenylation by Smaug/CCR4. *Development* **133**: 4573–83.

Zeitelhofer M, Karra D, Macchi P, Tolino M, Thomas S, Schwarz M, Kiebler M, Dahm R. 2008. Dynamic interaction between P-bodies and transport ribonucleoprotein particles in dendrites of mature hippocampal neurons. *J Neurosci* **28**: 7555–7562.

Zhao WM, Jiang C, Kroll TT, Huber PW. 2001. A proline-rich protein binds to the localization element of *Xenopus* Vg1 mRNA and to ligands involved in actin polymerization. *EMBO J* **20**: 2315–25.

Zheng J, Gao M, Huynh N, Tindell SJ, Vo HD, McDonald WH, Arkov AL. 2016. *In vivo* mapping of a dynamic ribonucleoprotein granule interactome in early *Drosophila* embryos. *FEBS Open Bio* **6**: 1248–1256.

Chapter 2: Proteomic Analysis of Vegetal RNP Transport Granules

I organized and prepared all figures in Chapter 2. My specific experimental contributions to these Figures include: Figure 2.2, panels (A-D) and panels (K-L). Figure 2.3, panels (A-D), including all sample preparation and data analysis. Figure 2.4, Pabpc1 of panel (A). Figure 2.5, panels (A-D), including all sample preparation and data analysis. Figure 2.6, panels (A-C), including all sample preparation and data analysis.

Abstract

Cytoplasmic mRNA localization is an important biological strategy for establishing cell and developmental polarity in a variety of organisms and cell types. In diverse examples including oocytes, fibroblasts and neurons, mRNA localization results in spatially restricted gene expression through local protein synthesis. In *Xenopus* oocytes, *vg1* mRNA is transported to the vegetal hemisphere of the developing oocyte and local translation of this member of the TGFβ growth factor family is critical for proper embryonic patterning. Vegetal transport of *vg1* mRNA relies on both kinesin and dynein microtubule motor proteins, and assembly of vegetal RNP transport cargos represents a critical step in this, and other, RNA localization pathways. However, the molecular nature of these transport RNPs is as yet unknown. To address this important question, we have developed a procedure for biochemical isolation of vegetal transport RNPs. Proteomic analysis of the *Xenopus* vegetal transport RNPs revealed both a high number of protein constituents of known cytoplasmic granules—including stress granules, p-bodies, germ granules, and neuronal granules—as well proteins unique to vegetal RNP transport granules. Our results suggest that vegetal transport RNPs represent a new class of cytoplasmic RNP granules: germ cell transport granules.

Introduction

Subcellular mRNA localization is a conserved mechanism among eukaryotes to control gene expression and establish cellular asymmetry. Coupled with local translational control, mRNA localization provides a highly efficient means to regulate protein expression, both spatially and temporally (Chin and Lécuyer 2017). Diverse cell types from germ cells to fibroblasts to neurons all utilize mRNA localization (Blower 2013). In fibroblasts, local translation of β-actin at the leading edge of lamellipodia is important for cellular motility (Eliscovich et al. 2013). In neurons, localized collections of mRNAs at the synapse allow rapid protein expression in response to environmental cues (Van Driesche and Martin 2018). Germ cells require tight local and spatial control of germ layer determinants (Medioni et al. 2012), and in fact *Drosophila* embryos have been shown to localize the mRNA transcripts 70% of more than 3,300 expressed genes (Lécuyer et al. 2007).

Despite the diversity of functions mediated by mRNA localization, only a handful of conserved mechanisms have been identified (Chin and Lécuyer 2017). One method for accomplishing subcellular localization of mRNA is co-packaging mRNA with proteins into structures known as ribonucleoprotein (RNP) particles. However, it is not known whether such RNPs are assembled into higher order structures, such as RNP granules, during RNA transport.

RNP granules are membraneless, distinct from their surroundings, comprised of multiple RNPs, and can take many different forms (Nielsen et al. 2016). Unlike single RNPs which can technically be comprised of a single RNA and

protein, RNP granules are more complex structures, often containing multiple RNAs and proteins (Rajgor and Shanahan 2014). Stress granules, for instance, are sites of mRNA storage and protection during periods of cellular stress (Protter and Parker 2016). Here, mRNA is translationally stalled until the stressor has passed, preventing disadvantageous protein expression. Depending on the degree of stress, RNA may be ultimately released into the translating population, destined for degradation, or transferred to other cytoplasmic granules. For example, processing bodies (p-bodies), have been shown to exchange contents with stress granules (Protter and Parker 2016). P-bodies are a more stable feature of cells and, unlike stress granules, contain an abundance of decapping enzymes, suggesting a greater role in degradation rather than temporary protection (Luo et al. 2018). Germ granules provide a longer-term storage role for mRNAs, often rich in RNAs that are important for proper embryonic development (Schisa 2012). Whereas stress and processing bodies are generally found throughout the cytoplasm, germ granules are often asymmetrically distributed. In this manner, they establish a blueprint for polarized protein expression that can be initiated once fertilization occurs and embryogenesis begins (Voronina et al. 2011). Like germ granules, neuronal granules also play important roles in spatial control of protein expression. Though most RNAs in a neuron are in the cell body, a subset of mRNAs are actively transported along microtubules in the axon or in dendrites (Van Driesche and Martin 2018). There, in response to a local stimulus, RNAs can be released from their transport-competent granules and resume translation, creating the necessary protein population to respond (De Graeve et al. 2018).

Much work to characterize these various granules has focused on *in vivo* perturbation or *in vitro* proxies created by overexpressing a single protein or RNA component (Protter and Parker 2016; Luo et al. 2018). Both approaches have complementary technical limitations. While *in vitro* reconstitution studies provide insight to the potential mechanisms of RNP formation and control, they lack the full biologically-relevant complex. *In vivo* studies provide a more accurate representation of RNP function, but due to inherent biological variability within the cell, they lack precise control over perturbations, limiting the degree of mechanistic insight.

One approach to overcome such limitations is to isolate granules from cells for *ex vivo* analysis. However, the dynamic nature of p-bodies and stress granules, for instance, has made isolating these structures extremely challenging. Recent studies have had success isolating stable subcomponents of stress granules and p-bodies (Jain et al. 2016; Hubstenberger et al. 2017). These high-throughput studies have provided new insight, but are just beginning to the scratch the surface, and additional studies on other types of cytoplasmic granules are needed.

Xenopus laevis oocytes are an important model system in which to study RNA localization (Kloc et al. 2001). One of the first identified maternally localizing vertebrate mRNAs, *vg1* (also known as *gdf1* and *dvr1*), was initially identified in *Xenopus* oocytes, where it is tightly localized to the vegetal hemisphere (Rebagliati et al. 1985; Weeks and Melton 1987). However, this TGFβ family member is also present in a range of vertebrates, including zebrafish, chickens, mice, and humans, where it is implicated in establishing left-right asymmetry and proper germ layer

formation (Montague and Schier 2017). Perhaps most well-studied in *Xenopus laevis* oocytes, *vg1* has been shown critical for proper endoderm and mesoderm formation (Birsoy et al. 2006). Highlighting the importance of proper localization of *vg1* mRNA, ectopic expression of *vg1* in the animal hemisphere of *Xenopus* eggs causes mesoderm expansion and non-viable embryos (Thomsen and Melton 1993; Joseph and Melton 1998).

Initially ubiquitously expressed throughout the cytoplasm in early oogenesis, *vg1* mRNA becomes spatially restricted to the vegetal hemisphere, in a distinct wedge shape, during mid oogenesis. By the end of oogenesis, *vg1* is tightly localized to the vegetal cortex, where ultimately, it will be inherited by vegetal blastomeres (Melton 1987). Localization is mediated by a 340-nt vegetal localization element (VLE) within the *vg1* 3′UTR (Mowry and Melton 1992). The VLE contains multiple sequence motifs, critical for RNA localization (Deshler et al. 1997; Gautreau et al. 1997), some of which have been shown to be binding sites for specific RNA-binding proteins (RBPs) (Kwon et al. 2002; Lewis et al. 2004). In the nucleus, *vg1* mRNA first interacts via the VLE with a set of core RBPs, including PTB/hnRNPI and Vera/Vg1RBP/Igf2bp3 (Kress et al. 2004). Once exported to the cytoplasm, the interaction between PTB, Vera, and the *vg1* VLE is remodeled (Lewis et al. 2008), enabling recruitment of additional RBPs including hnRNPAB/40LoVe and the double-stranded RBP, Stau/Staufen (Yoon and Mowry 2004; Czaplinski and Mattaj 2006). Transport of these RNPs to the vegetal cortex is achieved through active transport along microtubules, mediated by the motor proteins Kinesin and Dynein (Messitt et al. 2008; Gagnon et al. 2013).

Although much work has been done to investigate the mechanisms directing *vg1* mRNA transport, our understanding of the RNP transport cargos remains incomplete. The *vg1* RBPs, hnRNPAB, Stau, Vera, and PTB are found in other cytoplasmic RNPs and in fact, all four have recently been identified in purified stress granules (Kanai et al. 2004; Jain et al. 2016; Hubstenberger et al. 2017). This notable overlap in core RBPs raises the question whether *vg1* RNPs might be cytoplasmic granules.

To address this question, we developed a novel multi-step biochemical approach for isolating intact vegetal transport RNPs from *Xenopus laevis* oocytes, which allows us, for the first time, to reveal the proteome of these structures. We report that *vg1* RNPs are rich in proteins conserved in stress granules, p-bodies, neuronal transport granules, and germinal granules. Most notably, over 75% of identified protein components contain putative intrinsically disordered domains, suggesting similar biochemical properties, in addition to protein constituents. Our results suggest that vegetal transport RNPs represent a new class of cytoplasmic RNP granules.

Results

Multiple copies of vg1 *mRNA are packaged into large RNP complexes*

Studies of vegetal RNA transport in *Xenopus* oocytes have long relied on microinjection of fluorescently-labeled RNA to probe the localization pathway. In particular, a vegetal localization element (VLE) from the 3′UTR of *vg1* mRNA is faithfully localized to the vegetal cortex (Gautreau et al. 1997). During the process of vegetal localization, microinjected VLE RNA is enriched in the vegetal cytoplasm (Figure 2.1A), and accumulates at the vegetal cortex over time in culture (Lewis et al. 2008). However, investigation of endogenous mRNAs during vegetal transport had not been possible, until recently (Neil and Mowry, 2018). Using fluorescence *in situ* hybridization (FISH) on cryosectioned stage II oocytes (Figure 2.1B), we find that endogenous *vg1* mRNA is enriched in the vegetal cytoplasm in apparently large RNA clusters, which are evident for both endogenous *vg1* mRNA and VLE RNA (Figure 2.1A, B). At higher magnification, individual foci of *vg1* mRNAs can be visualized in surprisingly large clusters (Figure 2.1C). Due to the sensitivity of the Stellaris RNA FISH method used here (Neil and Mowry, 2018), these foci represent near single molecule resolution. On average, each large cluster, comprised of multiple *vg1* foci, is between 5-10 μm in the vegetal cytoplasm and appears to merge into much larger structures (>10 μm) at the vegetal cortex (Figure 2.1B). Our results suggest that multiple copies of *vg1* mRNA are packaged together during vegetal transport and we hypothesized that these large *vg1* mRNA clusters may represent vegetal RNP transport granules.

Vg*1 mRNA is transported in large RNPs*

In order to determine the characteristics of the *vg1* mRNA clusters, we next examined the localization of three known *vg1* mRNA binding proteins, hnRNPAB/40LoVe (Czaplinski et al. 2005), Staufen (Deshler et al. 1998; Yoon and Mowry 2004), and Vera/Vg1RBP (Havin et al. 1998) by combined FISH-immunofluorescence (FISH-IF). Each of the RNA-binding proteins, hnRNPAB (Figure 2.1D, E), Staufen (Figure 2.1F, G), and Vera (Figure 2.1H, I), show strong colocalization with *vg1* mRNA. These results suggest that the *vg1* mRNA is localized to the vegetal cortex of the *Xenopus* oocyte in a large RNP.

We have previously shown that vegetal RNA transport relies on microtubules and requires dynein and kinesin motor proteins (Messitt et al. 2008; Gagnon et al. 2013). To determine whether the large *vg1* RNPs are associated with motor proteins and the microtubule cytoskeleton, we performed FISH-IF for *vg1* mRNA and tubulin (Figure 2.1J, K), cytoplasmic dynein (Figure 2.1L), and kinesin-1 (Figure 2.1M). The *vg1* RNPs appear to be enclosed in microtubule baskets (Figure 1K), which are decorated by both dynein and kinesin motors (Fig 2.1L, M), suggesting that the large *vg1* complexes are transport RNPs.

Purification of vegetal transport RNPs

To fully characterize the vegetal transport RNPs, we developed a multi-step biochemical approach to isolate the transport RNPs from oocytes. As depicted in Figure 2.2A, our approach is as follows: (1) Manual sorting and crosslinking of whole stage II oocytes to reduce the possibility of reassociation of proteins and

RNAs after oocyte lysis (Mili and Steitz 2004). (2) Generation of yolk-cleared oocyte lysate. (3) Enrichment of large RNP complexes by size-exclusion chromatography. (4) Enrichment of specific vegetal RNP transport complexes via immunoprecipitation with known vegetal RNA transport markers.

After size exclusion chromatography (Figure 2.2A), we used the well-characterized *vg1* RNA binding protein, Stau1 (Yoon and Mowry 2004), to identify fractions that contain *vg1* RNP transport complexes by western blot analysis (Figure 2.2B). We found that the bulk of Stau1 protein was present in the void volume, while monomeric tubulin appeared in later fractions. To determine the location of endogenous *vg1* mRNA in the column fractions, we performed qRT-PCR using absolute quantitation on each fraction (Figure 2.2C). In this manner, we were able to reproducibly capture the fractions most enriched with *vg1* mRNA, which were pooled and termed the "*vg1*-RNP pool" (VP; Figure 2.2A).

Co-purification (Figure 2.2B,C) and co-localization by immunofluorescence (Figure 2.1) of known *vg1* mRNA and *vg1* RNA binding proteins, suggests that *vg1* mRNA is transported in a large RNP complex. To further test this, we treated oocyte lysates with RNase A prior to size exclusion chromatography. After RNase treatment, the *vg1* RNA-binding protein Stau1 (Figure 2.2D) no longer chromatographs as a large complex and is instead included in the column fractions containing dimeric or monomeric tubulin. Similarly, other known *vg1* RNA binding proteins, such as Vera and hnRNPAB, shift from large complexes after RNase treatment, also eluting in later fractions representing smaller complexes. These results demonstrate that *vg1* mRNA is contained in a large RNP that

contains *vg1* mRNA and RNA-binding proteins, including Stau1, Vera, and hnRNPAB.

We next addressed whether RNP incorporation is necessary for vegetal transport. While VLE RNA (Gautreau et al. 1997) is faithfully localized to the vegetal hemisphere after microinjection (Figures 2.1A, 2.2F), recapitulating endogenous *vg1* mRNA localization (Figures 2.1B, 2.2E, 2.2H), a mutated version of the VLE (VLE-mt), which lacks binding sites for both Vera and PTB (Lewis et al. 2004), does not localize (Figure 2.2I). Notably, the injected VLE RNA colocalizes in the large RNPs with endogenous *vg1* mRNA (Figure 2.2G). Mutant VLE RNA (VLE-mt), however, is not incorporated into the *vg1* RNPs, and instead is diffusely localized throughout the cytoplasm (Figure 2.2J), suggesting that incorporation into these large RNPs is required for vegetal localization.

The vegetal transport RNP proteome

In order to specifically isolate the large *vg1*-RNP complexes for further analysis, we performed four parallel immunoprecipitations from the VP (Figure 2.2A) using Vera, Stau1, hnRNPAB antibodies, with IgG as a negative control. Immunoblot analysis confirmed that each of the three known *vg1* RNA binding proteins (Stau1, Vera, and hnRNPAB) co-immunoprecipitated with each of the others, but not with IgG (Figure 2.2K).

Next, we confirmed by RIP-qRTPCR that *vg1* mRNA was significantly enriched in the RNA binding protein-IPs (RBP-IPs) compared to IgG (Figure 2.2L). Here, we faced an interesting technical challenge. Since the RNA

population of these *vg1*-RNP complexes has not been identified, we did not have a reliable transcript to use as a comparative normalization control for qPCR relative enrichment calculations. While recent work has identified putative housekeeping genes in *Xenopus laevis* (Mughal et al. 2018), this study did not focus on oocytes in early oogenesis, where RNA populations likely differ. Furthermore, studies that have suggested normalization by geometric averaging of multiple housekeeping genes (Vandesompele et al. 2002), may fail to account for the more complicated case of RNA-IPs. Unlike standard qRT-PCR where the background RNA pool is maintained between samples and the expression of RNAs varies only based on experimental condition, the isolated pool of RNAs in an IP will vary for each antibody. In addition to biological variability between samples, each antibody may also possess a different IP efficiency. We therefore modified a normalization strategy (Johnston et al. 2012) utilizing an economical exogenous spike-in control, poly-adenylated *luciferase* RNA. Equal amounts of *luciferase* RNA were applied to samples just prior to RNA extraction and thoroughly mixed. Our spike-in *luciferase* served both as a true negative control and as an extraction efficiency control. To further heighten the stringency of our qRT-PCR evaluations, we calculated the efficiency of each primer per experiment (Ramakers et al. 2003) in combination with the Pffafl method of relative enrichment (Pfaffl 2001). By this approach we confirmed that *vg1* mRNA was significantly enriched in our RBP-IPs, by nearly $\log_2(7)$ fold (Figure 2.2L).

Next, we performed mass spectrometry, in biological quadruplicates, on each eluate from the four immunoprecipitations. We consider a candidate protein

to be a vegetal RNP transport granule component if it had identified peptides in at least three of the four replicates, and if these peptides counts were at least two-fold enriched over those in IgG in each replicate. Comparing all three RBP-IPs (Stau1, hnRNPAB, and Vera), we identified a common set of 70 proteins (Figure 2.3A).

We also compared the overlapping lists for, hnRNPAB/Stau1 (Figure 2.3B), and Vera/Stau1 (Figure 2.3C), and hnRNPAB/Vera (Figure 2.3D). Of the two-way comparisons, we were most intrigued by the common components between hnRNPAB and Stau1 (Figure 2.3B). Both Stau1 and Vera are widely studied RNA binding proteins, that in addition to interacting with *vg1*, have multiple other functions (Yisraeli 2005; Heraud-Farlow and Kiebler 2014). Likewise, by immunofluorescence they are distributed throughout the oocyte, with an enrichment in the *vg1* RNPs (Figure 2.1F-I). Due to the extended distribution of both of these RNA-binding proteins, the Vera-Staufen overlap may include components that are not exclusively part of the *vg1*-RNPs. The distribution of hnRNPAB, however, is almost exclusively localized to the *vg1*-RNPs (Figure 2.1D-E) and is a much stronger candidate for a specific *vg1*-RNP granule marker.

We then considered both the intersection of Vera-hnRNPAB and Stau-hnRNPAB and we reasoned that Stau-hnRNPAB is a stronger marker of *bona-fide* *vg1*-RNPs for three reasons. First, unlike both Stau1 and hnRNPAB antibodies, the Vera antibody was not affinity purified. Second, previous results have suggested that of a core set of six *vg1* RNA binding proteins, Stau specifically is a driver of vegetal RNA localization (Snedden et al. 2013). Finally, a closer examination of the mass spec results revealed that in the Vera-IP, hnRNPAB was

not above our stringent requirements for enrichment which may have been due to the Vera antibody quality.

Therefore, we conclude that our core set of *vg1*-RNP components is comprised by the 86 proteins identified in the hnRNPAB/Stau1 dataset (Figure 2.3B). The second tier of components are those identified in hnRNPAB/Vera dataset (Figure 2.3D), and the third tier are those identified in Vera/Staufen dataset (Figure 2.3C).

Among the identified proteins in the hnRNPAB/Stau1 dataset are known *vg1* RNA binding proteins, Stau1 and Stau2, hnRNPAB, PTBP1 and PTBP3, Elavl1 and Elavl2, and Vera. In addition, we note the presence of both dynein (Dynll1 and Dynll2) and Kinesin (Kif3b). Both kinesin and dynein have previously been identified as the motors responsible for *vg1* active transport along microtubules (Messitt et al. 2008; Gagnon et al. 2013). We thus felt confident in our isolation of vegetal transport granules. While this list of 86 proteins in the hnRNPAB/Stau1 dataset may not be exhaustive, we validated more than 30% of our granule hits by FISH/IF and about 10% of the hits by gel filtration chromatography +/- RNase treatment (Figure 2.4, and data not shown). As shown in Figure 2.4A, hnRNPAB, Vera, and two newly identified vegetal transport granule components, G3bp2 and Pabpc1 shift to smaller protein fractions when treated with RNase. We therefore conclude that inclusion into large vegetal transport granules is RNA dependent.

The interaction between RNA and protein is further supported by the localization of *vg1* and granule protein components by FISH/IF (Figure 2.4B-D). Here, oocytes were probed for *vg1* mRNA (red), Tubulin (blue), and candidate

granule components (green). In all cases, we find that *vg1*, Tubulin, and granule protein components all localize within the same large *vg1*-RNP clusters, but do not necessarily exhibit perfect colocalization within these granules. We consistently found four localization phenotypes or classes.

Class I proteins are strongly enriched in the granule interior, and termed "Granule Enriched". This category includes Cpeb1, Elavl2, and PTB (Figure 2.4B), as well as hnRNPAB, Vera, and Stau (Figure 2.1D-I). Interestingly, 5 of these 6 proteins, Cpeb1 excluded, have been shown to directly bind *vg1* mRNA. Although Cpeb1 has not been shown to bind *vg1* directly, it was enriched in all three RBP-IPs (Vera, Stau, and hnRNPAB). Localization of this type might represent core granule components or those that can directly bind *vg1* mRNA.

The second class of localization (Figure 2.4C) exhibits a more diffuse granule staining and are termed "Microtubule Network Enriched". These proteins are enriched in the microtubule network surrounding the granules, but show more diffuse localization compared to Class I. Although granule enrichment is not as strong as Class I, it is still enriched relative to the cytoplasm. The level of enrichment is consistent with proteins found in *C. elegans* P-granules, where concentration is only about two-fold greater than the surrounding area (Wei et al. 2017). These proteins, including Cct6a, Cnot1, Ddx1, and Tia1, might represent a more dynamic subset of granule components.

The last two classes are the least abundant among the proteins identified. Class III includes Ybx2 (Figure 2.4D) and those proteins whose localization resembles that of fibrillar-like structures, termed "Fibrillar-Like" (Figure 2.6D-E).

There is a greater density of protein within the granule, even compared to Class I, and the protein seems to localize in structures with fibril-like extensions. These structures are similar to staining done with the cross-beta strand dye, Thioflavin S (Figure0, which has been used as marker for amyloid like structures (Guntern et al. 1992). Class IV represents those proteins, like Dynein and Kinesin (Figure 2.1L-M), which coat the microtubule tracks, termed "Microtubule Associated". Proteins in this category may be involved in active granule transport t.

The vegetal transport RNP is a new type of cytoplasmic granule

To further characterize the components of the vegetal transport RNP (Figure 2.5A), we performed gene ontology (GO) analysis (Figure 2.5B). Four of the five top GO-categories related to nucleic acid binding, with the top category, unsurprisingly, being RNA binding (Figure 2.5B). We also found a significant enrichment of ATP binding, primarily contributed by the number of DDX helicases identified in the vegetal transport RNP (Figure 2.5B), which may act as granule remodeling enzymes utilizing their ability to unwind RNA and alter RNA-protein interactions (Gilman et al. 2017).

Proteomic analysis of the vegetal transport RNP further revealed a set of proteins that are known components of other cytoplasmic granules, including stress granules, processing bodies, neuronal granules, and germ granules (S, P, N, G respectively in Figure 2.5A). Specifically, approximately two-thirds of the identified components are present in at least one other granule type (colored squares, Figure 2.5CD), with the last third representing novel identified components.

Based on the prevalence of low-complexity domain and intrinsically disordered regions in the proteomes of other cytoplasmic granules (Uversky 2017), we also examined the prevalence of such domains in the vegetal transport RNP components. Using, SLIDER (Peng et al. 2014), a predictive tool for intrinsically disordered domains, we found that nearly 75% of our components contained an putative intrinsically disordered domain, and 60% of our novel identified components fall into this category (Figure 2.6A). This is a significant enrichment compared to that of the *Xenopus* proteome. Prion-like domains represent a more specific category of intrinsically disorder regions, and also indicate overrepresentation in our vegetal transport protein. Our vegetal transport granules are enriched 6-fold in prion-like domains compared to the entire *Xenopus* proteome, as determined with the predictor PLAAC (Lancaster et al. 2014)(Figure 2.6B).

Low complexity and prion-like domains are, by definition, rich in particular amino acids. Intrinsically disordered domains are overrepresented with arginine and glycine, and prion-like domains are rich in glutamine and asparagine (Kaganovich 2017). We therefore investigated overrepresented motifs in our vegetal transport granules, using the online-suite, MEME (Bailey and Elkan 1994). We found an enrichment of phenylalanine-glycine repeats (Figure 2.6C). These motifs are classically found in nuclear pore proteins where they have shown the ability to form hydrogels and act as molecular sieves (Frey et al. 2006).

Due to the over-enrichment of prion-like domains in the vegetal transport RNP proteome, we next tested whether the vegetal transport RNPs contained

amyloid like structures. We stained oocyte sections with Thioflavin S, a dye that selectively fluoresces in the presence of cross-beta strands, characteristic of amyloid structures (Guntern et al. 1992). The Thioflavin S staining (Figure 2.6D-E) reveals that the vegetal transport RNPs exhibit amyloid like properties, and that the vegetal mRNA is interspersed between the amyloid-like fibrils. Taken together, our results indicate that vegetal RNP transport complexes represent a new class of cytoplasmic RNP granule that shares some components with other cytoplasmic RNP granules, but also exhibits unique characteristics.

Discussion

Here, we have shown that *vg1* mRNA is localized to the vegetal cortex of developing oocytes in large RNP complexes. We purified the vegetal RNP transport complexes using a multi-step biochemical isolation procedure and carried out proteomic analysis. We identified 86 protein constituents of the vegetal transport RNP granule. Of those, approximately 29% of components are novel to the vegetal transport granule (Figure 2.5C). The remaining 71% (Figure 2.5D) have been identified as components of other cytoplasmic granules, including stress granules, processing bodies, neuronal granules, and germ granules (Kanai et al. 2004; Elvira et al. 2006; Fritzsche et al. 2013; Jain et al. 2016; Hubstenberger et al. 2017; Markmiller et al. 2018). A prominent feature among many of the proteins shared with other cytoplasmic granules is the presence of prion and/or low-complexity domains (Figure 2.6A,B). Notably, however, the protein components of the *vg1* transport RNP are also enriched in phenylalanine-glycine repeats, which may form hydrogel-like assemblages (Figure 2.6C). Indeed, Thioflavin S staining (Figure 2.6D-E) reveals an amyloid-rich structure enclosing the *vg1* mRNAs. Taken together, our results reveal the *vg1* transport RNP to be a new type of cytoplasmic granule.

In light of previous work on *vg1* RNPs and known roles of components in other cytoplasmic granules, our current proteomic study provides new insights into the functional aspects of vegetal transport granules. First, *vg1* mRNA has been found to be translationally quiescent throughout transport and until late oogenesis (Tannahill and Melton 1989). Notably, approximately 18% of the identified *vg1*

transport granule proteins play roles in translational regulation, with approximately half of those (9%) involved in negative regulation. Some proteins, such as and Ybox1 have demonstrated roles in suppressing translation initiation (Nekrasov et al. 2003). Because some ribosomal subunits, such as rps28p9 are detected by mass spectrometry, RNA translation may be stalled at a preinitiation-complex formation stage as has been shown in stress granules (Kedersha et al. 2002). It is possible that the vegetal transport granule is also responsible for transporting factors required for initiating translation after successful transport, such as the aminoacyl tRNA synthetases Iars, Kars, Aimp1. Given that translation of *vg1* mRNA initiated well after vegetal transport at the end of oogenesis, an RNP granule that transports both silenced RNA and necessary translational factors, may be critical for establishing a seamless transition into translation.

Second, due to the length of oogenesis, up to many months (Dumont 1972), long-term storage of *vg1* mRNA is required. Thus, factors promoting mRNA stability, such as Elavl1 and Elval2 (Colegrove-Otero *et al.*, 2005), may play roles in protecting transported mRNA from degradation. Surprisingly, however, several factors relating to mRNA poly(A) tail shortening and decapping, including Pabpc1, Cnot1, and Lsm1, are also present in the *vg1* RNP transport granule. One possibility for this is that destabilizing proteins are inactive (similar to some decapping enzymes in p-bodies (Luo et al. 2018)), either because of spatial separation or through inhibition by other proteins within the *vg1* RNP transport granules. One speculative possibility is that as oogenesis concludes, the granule

components may rearrange (perhaps mediated by DDX helicases), first promoting RNA translation and subsequently RNA decay.

Previous work from our laboratory has shown that remodeling of *vg1* mRNA and RNA binding-proteins is necessary for localization (Lewis et al. 2008). Such remodeling may also be necessary for inhibiting interaction of mRNA destabilizing proteins and RNA. The ATP-dependent, DEAD-box RNA-helicase (DDX/DHX) family of proteins (Gilman et al. 2017) could be responsible for such rearrangement(s) during and/or after *vg1* mRNA transport. We identified four DDX/DHX proteins in the *vg1* RNP transport granule (Ddx1, Ddx3x, Ddx5, and Dhx9). All four of these DEAD-box proteins have also been identified in stress granules (Jain et al. 2016; Markmiller et al. 2018), where they may also be necessary for remodeling steps. Further, it also possible that the low complexity domains, identified in nearly 75% of Vg1 granule proteins, mediate rearrangement within the granule.

One-third of the identified *vg1* RNP granule proteome components have not been identified in the other known classes of cytoplasmic granules. These proteins may give us insight into the unique nature and function of *vg1* RNP transport granules. Some proteins identified are oocyte-specific, such as Zar1 and Zar2, and act as translational repressors (Charlesworth et al. 2012; Yamamoto et al. 2013). Others, such as Kif3b (encoding a kinesin II subunit) and Dynll1/2 (encoding cytoplasmic dynein subunits), highlight the known roles for motor proteins in vegetal RNA transport (Messitt et al. 2008; Gagnon et al. 2013). Once at the vegetal cortex, *vg1* mRNA is stably anchored as oogenesis continues. Mechanistically,

little is known about anchoring, though cytokeratins have been shown to be necessary for RNA anchoring (Klymkowsky et al. 1991). Indeed, the cytokeratin protein, Krt12, is found in the *vg1* RNP transport granule proteome. It is also noteworthy that Krt12 has prominent prion domain, which could play a role in structure of the granule during transport or in anchoring at the cortex, or both.

Taken together, the *vg1* RNP transport granule represents a unique cytoplasmic granule displaying features from several other cytoplasmic granules. Like neuronal granules, *vg1* RNP granules travel long distances to reach their destination, and thus require multiple motors. Throughout transport the RNA is translationally quiescent, perhaps stalled in an assembling preinitiation complex, as in stress granules. As with germ granules, long-term RNA storage is required, thereby necessitating mRNA stabilization factors. However, several mRNA decay factors are also present in *vg1* RNP granules, but they are perhaps inhibited, as they may be in processing bodies. Finally, the incorporation of both mRNA stabilizing and mRNA decay factors in a translationally-repressed granule suggest that rearrangement, potentially mediated by ATP-dependent helicases, may be critical. In addition, *vg1* RNP transport granules contain both chaperones important for protein scaffolding, and enzymes critical for protein folding, such as Cct6a and Hspa8 (Jain et al. 2016). By containing components required for both long-term RNA stability and storage and accelerated translation, the *vg1* RNP transport granule may act as an efficient “one-stop-shop”, able to both spatially and temporally remodel RNP granules in order to activate functionally diverse proteins based on cues triggered at oocyte maturation and fertilization. With the

vg1 RNP transport granule proteome now revealed, future studies focused on analyzing functional, spatial, and temporal regulation of proteins within the granule are now possible.

Methods

Oocyte isolation and culture

Oocytes were harvested and isolated from J-strain *Xenopus laevis* females (NXR) as described in (Newman et al. 2018), with the following exceptions. Oocytes were enzymatically defolliculated by manual rocking in collagenase solution (3 mg/ml Collagenase I, 0.1 M KPO_3) for 8 minutes, followed by 3-5 washes in MBSH [880 mM NaCl, 100 mM HEPES (pH 7.6), 10 mM KCl, 24 mM $NaHCO_3$, 8.2 mM $MgSO_4$, 3.3 mM $Ca(NO_3)_2$, 4.1 mM $CaCl_2$]. Stage II and III oocytes were manually sorted using sequential passing through nylon meshes of 1000-micron, 475-micron, and 300-micron pores. To ensure collection of appropriate stages, sorted oocytes were visually inspected under a dissecting microscope, and any stage I or stage IV and older oocytes were removed. Oocytes were cultured in 15-mm glass dishes overnight (16-18 hours) at 18°C in XOCM (Jeschonek and Mowry, 2018).

Fluorescence in situ hybridization and immunofluorescence

Oocytes were treated for 1 hour at 22°C with FTG fixative (80 mM K PIPES, pH6.8, 1 mM $MgCl_2$, 5 mM EGTA, 0.2% Triton X-100, 3.7% formaldehyde, 0.25% glutaraldehyde, 0.5 μm paclitaxel), followed by post-fixation in 100% methanol overnight at 22°C as in (Becker and Gard 2006). After re-hydration in TBS (10 mM Tris, pH 7.4, 155 mM NaCl), oocytes were incubated overnight at 4°C in 100 mM $NaBH_4$ in TBS (Becker and Gard 2006). After washing 2× in TBSN (0.1% NP-40 in TBS), followed by 2 washes in TBSNB (0.2% ultrapure BSA in TBSN) oocytes were equilibrated stepwise in TBSNB-30S (30% sucrose in TBSNB) and after

equilibration in an embedding mold for 30 minutes at 22°C, TBSNB-30S was replaced with O.C.T. compound (Fisher 23-730). Cryosectioning and fluorescence in situ hybridization (FISH) was performed as in (Neil and Mowry 2018), with the *vg1* Quasar 570 probe set (LGC Biosearch Technologies) applied at 500 nM. Subsequently, slides were washed twice in TBSNB and incubated for 3 hours at 22°C in TBS-plus (5% v/v normal goat serum, 2 mg/ml ultrapure BSA in TBSN) and incubated overnight at 4°C with primary antibodies at 20 μg/ml in TBS-plus. Primary antibodies [Stau1 (Abcam ab73478), hnRNPAB (Abcam ab19974), Vera (Gagnon *et al*., 2013), dynein intermediate chain (Abcam ab23905), Kif5B/kinesin (Abcam ab28060), α-tubulin (Abcam ab4074), Cct6A (Novus NBP2-33583), Cnot1 (Novus NBP2-31892), Cpeb (Proteintech 13274-1-AP), Ddx1 (Abcam ab151962), Elav2 (Novus NBP2-30812), PTB (Kress et al. 2004), RpS6 (Abcam ab137826), Tia1 (Novus NBP1-33452), and Ybx2 (ThermoFisher PA5-30614)] were directly labeled with Alexa-405, Alexa-546, or Alexa-647 using Zenon labeling kits (ThermoFisher). After four 10-minute washes in TBSNB at 22°C, slides were mounted with ProLong Gold Antifade.

Oocyte lysate preparation

Approximately 2500 oocytes were washed 3× with PBS. On the last wash, all PBS was removed and replaced with 1 ml freshly prepared crosslinking solution (0.1% ultrapure formaldehyde in PBS) and rocked for 10 minutes at 22°C. The reaction was quenched by replacing the crosslinking solution with 1 ml of quenching buffer (25 mM Tris pH 7.4, 0.25 M Glycine), and rocking for 5 minutes at 22°C. Oocytes were then washed 3× in 1 ml of freshly prepared column running

buffer [CRB; 0.05% NP-40, 1 mM DTT, 10 mM Hepes 7.4, 100 mM KOAc, 3 mM MgOAc, 5 mM EGTA, 100 mM sucrose, 2 nU/ml Ribolock RNase Inhibitor, 1× HALT Protease Inhibitors (ThermoFisher), prepared fresh in DEPC-treated water]. Oocytes were resuspended in 120 µl CRB, syringe homogenized by 10 strokes with a 26 gauge needle, and immediately placed on ice. The lysate was clarified by centrifugation at 10,000×*g* for 10 minutes at 4°C, twice, removing the supernatant to a new tube each time. Protein concentration was determined by measuring absorbance at 280 nm (A_{280}), and the lysate was adjusted to a protein concentration of 50 mg/ml using CRB buffer.

For RNase treatment of oocyte lysates, Ribolock RNase Inhibitor was omitted from all buffers. After crosslinking, lysis and clarification, RNase A (Sigma-Aldrich) was added to a final concentration of 0.1 µg/µl of added and incubated for 10 minutes at 37°C.

Size Exclusion Chromatography

Sephacryl S400 HR resin (GE Healthcare) was washed once in DEPC-treated water and then twice in CRB– buffer (CRB minus protease and RNAse inhibitors) buffer. S400 resin was resuspended 1:1 with CRB– buffer and degassed for 15 minutes at 22°C. To each chromatography (0.7 × 15 cm) column, 10 ml of S400 slurry was added (to generate a 5 ml bed volume). Columns were washed 3× with degassed CRB– buffer and stored at 4°C. The day of experiment, columns were washed an additional 3× with degassed CRB buffer at 4°C.

Two chromatography columns were used per biological replicate, run in tandem with two fraction collectors. Each column was loaded with 150 µl of

prepared crosslinked oocyte lysate. The fraction collectors were set to collect fractions every 6 drops (about 100 µl). Sixty fractions were collected. To predict the location of the *vg1* RNA peak, A_{280} was measured and plotted versus fraction number. The first fraction exhibiting an A_{280} reading >0.100 was designated as "Fraction 1". The four fractions prior to the A_{280} peak were collected, and 90 µl of each individual fraction combined into the vegetal RNP pool (VP). In addition, 5 µl from each the VP fractions, and one fraction prior and three subsequent fractions, were collected for qRTPCR quality control (see below).

Immunoprecipitation

We took great care to optimize the immunoprecipitation procedure below. To avoid antibody leakage, which could be a problem for downstream Mass Spectrometry, while maintaining maximum binding activity, we covalently crosslinked antibodies to Dynabead M270 Epoxy Magnetic Beads (Invitrogen, #14311D). To reduce nonspecific interactions with plasticware, only low-retention Eppendorf tubes and low-retention pipette tips were used.

The following antibodies were used for IP: Stau1 (Abcam, ab73478), hnRNPAB (Abcam, ab19974), Vera (Gagnon *et al.*, 2013), and normal rabbit IgG (EMD, NI01). To reduce the amount of glycerol in the IgG antibody, as recommended by manufacturer protocol (Invitrogen), we used a buffer exchange column (Amicon 10K, #UFC501096), effectively replacing the buffer with PBS. The Vera antibody, which was prepared in-house, was not affinity purified. To remove any unknown contaminants or stabilizing proteins from the Vera antibody, we used a resin-based antibody cleanup kit (Pierce #44600). Coupling of

Dynabeads with antibody was followed as per manufacture's protocol. We note that a single IP reaction consisted of 3 mg of Dynabeads and approximately 8 µg of antibody. To reduce nonspecific interactions, antibody-coupled Dynabeads were blocked in 0.1% BSA for 5 minutes at 22°C, followed by 1-hour incubation in torula RNA blocking solution (0.05% CHAPS, 160 µg torula yeast RNA, PBS). After blocking, beads were washed three-times in CRB.

The VP from each of the two columns per replicate were combined (approximately 800 µl). The resulting VP was then split equally among eight IP reactions: Vera (×2), Stau (×2), hnRNPAB (×2), and IgG (×2). 5% of the VP was saved as input. IPs were incubated for 6 hours at 4°C with rocking.

Beads were washed 4× in the appropriate chilled wash buffer. Wash buffers were optimized per downstream experiment. For protein co-immunoprecipitation reactions, we used a buffer optimized for best results among all three RNA binding proteins (PW buffer; 50 mM Tris pH 7.4, 0.1% NP40, 0.05 mM MgCl2, 2 nU/ml Ribolock RNase Inhibitor, and 1x Protease Inhibitors. For RNA-IP experiments, buffers were optimized for best results in *vg1* mRNA immunoprecipitation among all three RNA binding proteins (RW buffer; 25 mM Tris pH 7.4, 0.5% NP40, 0.5 mM DTT, 150 mM KCl, 5 mM EDTA, 2 nU/ml Ribolock RNase Inhibitor, 1× HALT Protease Inhibitors). On the final wash in RW or PW, beads were moved to a new low-retention tube to reduce nonspecific and background binding. To further reduce background, beads were washed once more in DEPC-treated water.

To reduce the amount of immunoglobin eluted that could interfere with downstream applications, particularly mass spectrometry, we adopted a soft elution protocol (Antrobus and Borner 2011). Briefly, 100 µl of soft elution buffer

(50 mM Tris pH 8.0, 0.2% SDS, 0.1% Tween-20) was incubated with beads for 7 minutes at 25C with shaking (1200 rpm). This elution step was performed twice, and the eluents pooled. Finally, the pooled eluents from each pair of IPs (i.e.: Vera-Vera, Stau-Stau, hnRNPAB-hnRNPAB, IgG-IgG) were also pooled. To reverse the formaldehyde crosslink, eluents were incubated at 70°C for 1 hour and allowed to gradually cool to room temperature. Mass spectrometry is incompatible with many detergents. Tween-20 was removed from the eluents using HiPPR detergent removal resin columns (ThermoFisher, #88305), and eluted into PBS.

Immunoblotting

For co-IP analysis, 10 µl of IP eluent or VP input was mixed with Laemmli sample buffer containing 5% β-mercaptoethanol. Samples were boiled for 5 minutes at 100°C and allowed to gradually cool to room temperature. Samples were run on 8% Tris-Glycine gels (Novex) and the gel then transferred to nitrocellulose membrane at 120V for 1 hour. Membranes were blocked overnight at 4°C in a 3% nonfat milk solution. Membranes were incubated in primary antibody overnight at 4°C with either Staufen 1:1000, (Yoon and Mowry 2004), Vera, 1:2000 (Gagnon et al. 2013), G3bp2, 1:1000 (Novus, NBP1-82977), hnRNPAB 1:1000 (Abcam, ab199724), Epabp/Pabpc1, 1:1000 (Antibodies-Online, ABIN108538), or Tubulin 1:500 (Abcam ab4074), washed 3× in blocking solution, then incubated for two hours at room temperature with secondary antibody, Goat anti-Rabbit IgG (abcam ab97200) or Goat Ani-Mouse IgG (Abcam ab97265) at 1:10,000). Membranes were developed using the Pico ECL Developing solution

(Thermo, #34580). Analysis of column fractions was performed as described above, with the exception that Criterion AnykD gels (BioRad) were used.

RNA-Extraction

To isolate RNA from column fractions, 5 µl of each fraction was diluted to 50 µl with DEPC-treated water, and reversed crosslinked, as above. To control for extraction efficiency, 2.5 pg of *luciferase* RNA (Promega #L4561) was added to each sample and mixed. After addition of 150 µl of TriZol (Invitrogen), RNA was extracted using the Direct-Zol RNA MicroPrep kit (Genesee #11-300MB) with on-column DNAse I digestion, as per manufacturer's protocol. RNA was eluted in 15 µl of nuclease and RNase free water.

To isolate RNA immunoprecipitated with RNA binding proteins, 2.5 pg of *luciferase* RNA was added to samples after addition of TriZol (see above). 100 µl of chloroform was added to samples, mixed, and incubated at 22°C for 3 minutes. To separate RNA, samples were centrifuged at 12000×*g* for 15 minutes at 4°C. The upper aqueous phase, containing RNA, was saved. Isopropanol and ammonium acetate were used to precipitate RNA overnight at -20°C. Pelleted RNA was resuspended in 12 µl of nuclease free water. cDNA was prepared from 10 µl of RNA using the iScript cDNA synthesis kit (BioRad, #1708891) as per manufacturer's protocols.

Preparation of RNA standards for Absolute Quantitative qRTPCR

To determine the numbers of copies of *vg1* mRNA in each fraction, we created RNA standards for absolute quantitation. Absolute quantitation for fraction analysis allowed us to reduce sample bias by not having to choose a

"reference" fraction. The first fraction collected for qRTPCR (normalized fraction 1) often had variable low levels of *vg1* mRNA (data not shown) making comparisons difficult. Although a quicker process, it is inappropriate to use DNA based standards for absolute quantitation by qRTPCR, as the efficiency of the reverse transcription reaction must be taken into account (Bustin 2002). Using the iScript cDNA synthesis kit, cDNA for oocytes stages I-VI was prepared. Endogenous *vg1* was isolated from cDNA using Phusion High-Fidelity DNA Polymerase (NEB, #M0530) per manufacturer protocol. Primers for *vg1* mRNA were designed with a T7 promoter to bypass cloning and proceed directly to *in vitro* transcription (Cazenave and Uhlenbeck 1994).

Forward *vg1* primer:

5′-GAAATTAATACGACTCACTATAGGGGGAGACTAGCTTGTCAGTATGG-3′.

Reverse *vg1* primer:

5′-ACGCCTCTGTGCAGTGAATA-3′.

DNA was purified using the column-based PCR Wizard Cleanup (Promega). The *in vitro* transcription reaction was performed with the T7 Megascript kit, using the PCR product as template. RNA was extracted by phenol/chloroform followed by ethanol precipitation. RNA concentration was determined using the Qubit RNA BR assay (Invitrogen). Both *vg1* and *luciferase* RNAs were initially diluted to 1×10^9 copies/µl in nuclease and RNase-free water. RNA was serially diluted 10-fold (1×10^8 to 1×10^3 copies/µl) in nuclease free water containing 50 ng/µl of yeast torula RNA.

Quantitative RT-PCR

For analysis of *vg1* mRNA distribution across fractions, 1-step q-RTPCR was performed using Luna One-Step qPCR (NEB), as per manufacturer protocol, using 10 µl reactions. For RNA-IPs, two step qRTPCR was performed using SybrGreen Powerup MasterMix (ABI), as per manufacturer protocols. In both cases, reactions were performed in technical triplicate. Primers were designed using NCBI primer blast to ensure there would be no off-target amplicons. Primers against *vg1* mRNA were also designed to span an exon-exon junction to avoid amplification of any residual DNA. Melting curves were examined for each reaction to ensure specificity. For quantitation of *vg1* mRNA, RNA standards were run on each plate, in triplicate, and used to produce a standard curve.

Forward *vg1* primer: 5′- GGTATCTCCTCCTCCTGTCCCT-3′.

Reverse *vg1 primer:* 5′- TTGGGTGGATGTCATCGGAGT-3′.

Forward *luciferase* primer: 5′- GGATACCGGGAAAACGCTGG-3′.

Reverse *luciferase primer:* 5′- ATCAAGGCGTTGGTCGCTTC-3′.

Absolute copy numbers of *vg1* and *luciferase* were determined by standard curve. To normalize *vg1* expression and account for any differences in extraction efficiency, *vg1* copy number was divided by *luciferase* copy number per fraction. Both absolute *vg1* copy number and *vg1/luciferase* normalized ratios were plotted as a function of fraction number. For stringency, we proceeded only with those experiments where the *vg1* peak fell within 1 fraction of each other for both the *vg1* copy number analysis and the normalized *vg1/luciferase* ratio.

For RNA-IP analysis, LinRegPCR (Ramakers et al. 2003) was used to calculate primer efficiency for both *vg1* and *luciferase* primers. The geometric mean was determined for primers across experiments. Relative fold enrichment was calculated using the Pfaffl (Pfaffl 2001) method (an assumption-free version of the commonly misused ΔΔCt calculation), and the geometric mean efficiency of *vg1* and *luciferase* primers as determined by LinRegPCR. Log2 fold enrichment of *vg1* in RBP-IPs was calculated relative to IgG and normalized to *luciferase.* A Mann-Whitney U test was performed for statistically significance (De Neve et al. 2013).

Mass Spectrometry

Mass spectrometry was performed at the COBRE Proteomics Core Facility affiliated with Brown University on a Q-Exactive Plus LC-MS/MS mass spectrometer. Sample preparation for LC-MS/MS analysis was performed as follows. Cell pellets were subjected in lysis buffer (8 M urea, 1 mM sodium orthovanadate, 20 mM HEPES, 2.5 mM sodium pyrophosphate, 1 mM β-glycerophosphate, pH 8.0, 20 min, 4°C), sonicated and cleared by centrifugation (14 000 × g, 15 min, 4°C). Protein concentration was measured (Pierce BCA Protein Assay, Thermo Fisher Scientific, IL, USA) and a total of 100 μg of protein per sample was subjected for trypsin digestion. Tryptic peptides were desalted using C18 Sep-Pak plus cartridges (Waters, Milford, MA) and were lyophilized for 48 hours to dryness. The dried eluted peptides were reconstituted in buffer A (0.1 M acetic acid) at a concentration of 1 μg/μl and 5 μl was injected for each analysis.

The LC-MS/MS was performed on a fully automated proteomic technology platform (Yu and Salomon 2010, 2009) that includes an Agilent 1200 Series Quaternary HPLC system (Agilent Technologies, Santa Clara, CA) connected to a Q Exactive Plus mass spectrometer (Thermo Fisher Scientific, Waltham, MA). The LC-MS/MS set up was used as described earlier (Ahsan et al. 2017). Briefly, the peptides were separated through a linear reversed-phase 90 min gradient from 0% to 40% buffer B (0.1 M acetic acid in acetonitrile) at a flow rate of 3 µl /min through a 3 µm 20 cm C18 column. The electrospray voltage of 2.0 kV was applied in a split flow configuration, and spectra were collected using a top-9 data-dependent method. Survey full scan MS spectra (m/z 400-1800) were acquired at a resolution of 70,000 with an AGC target value of 3×106 ions or a maximum ion injection time of 200 ms. The peptide fragmentation was performed via higher-energy collision dissociation with the energy set at 28 NCE. The MS/MS spectra were acquired at a resolution of 17,500, with a targeted value of 2×104 ions or a maximum integration time of 200 ms. The ion selection abundance threshold was set at 8.0×102 with charge state exclusion of unassigned and z =1, or 6-8 ions and dynamic exclusion time of 30 seconds.

Peptide spectrum matching of MS/MS spectra of each file was searched against a species-specific database for *Xenopus laevis* (UniProt; downloaded 2/1/2015) using MASCOT v. 2.4 (Matrix Science, Ltd, London, UK). A concatenated database containing “target” and “decoy” sequences was employed to estimate the false discovery rate (FDR) [4]. Msconvert from ProteoWizard (v. 3.0.5047), using default parameters and with the MS2Deisotope filter on, was employed to create peak lists for Mascot. The Mascot database search was

performed with the following parameters: trypsin enzyme cleavage specificity, 2 possible missed cleavages, 10 ppm mass tolerance for precursor ions, 20 mmu mass tolerance for fragment ions. Search parameters permitted variable modification of methionine oxidation (+15.9949 Da) and static modification of carbamidomethylation (+57.0215 Da) on cysteine. The resulting peptide spectrum matches (PSMs) were reduced to sets of unique PSMs by eliminating lower scoring duplicates. To provide high confidence, the Mascot results were filtered for Mowse Score (>20). Peptide assignments from the database search were filtered down to a 1% FDR by a logistic spectral score as previously described (Elias and Gygi 2007; Yu et al. 2009).

Peptide counts were generated by the core facility as described above. Downstream analysis was performed in-house using R. For Vera, Stau, and hnRNPAB, only those proteins with peptides in at least 3 replicates were considered. Enrichment over IgG was determined if the sum of peptides across all four biological replicates was as least two-fold greater than the sum of the peptides in all four IgG experiments. For unannotated protein hits (i.e.: LOC, MGC, Xelaev, Xetrov delimitators), peptides were BLAST against the *Xenopus laevis* JGI 9.1v1.8.3.2 annotation database, available from xenbase.org. Area proportional venn diagrams were produced using the VennDiagram package for R.

Gene Ontology

GO analysis was determined using DAVID (Huang et al. 2009b, 2009a), using *Xenopus tropicalis* as background, and using the Xenbase ID as identifiers.

Three genes could not be identified by DAVID, and these were manually annotated using Xenbase. P-values represent the likelihood of an ontology category being overrepresented in the vegetal transport granule proteome compared to the entire *Xenopus tropicalis* proteome. P-values are calculated using a modified Fisher Exact test, which is more conservative estimate of significance compared to the Fisher's Exact Test.

Intrinsically Disordered and Prion-Like Domain Analysis

Identification of putative intrinsically disordered domains were determined using SLIDER (Peng et al. 2014), which predicts long disordered segments (>30 consecutive disordered residues), against the hnRNPAB/Stau1 dataset or the *Xenopus laevis* J-strain 9.2 genome available at xenbase.org. Only those proteins with a SLIDER score greater than 0.55 were considered likely to have an IDR. Prion-like domains were calculated using PLAAC (Lancaster et al. 2014) with default settings. Only those proteins with a COREscore greater than zero were considered to have a prion-like domain. Statistics were performed in R using the Fisher's exact test.

Motif Enrichment Analysis

Motif analysis was performed with MEME in Classic Mode, allowing for one or more occurrences per sequence (Bailey and Elkan 1994).

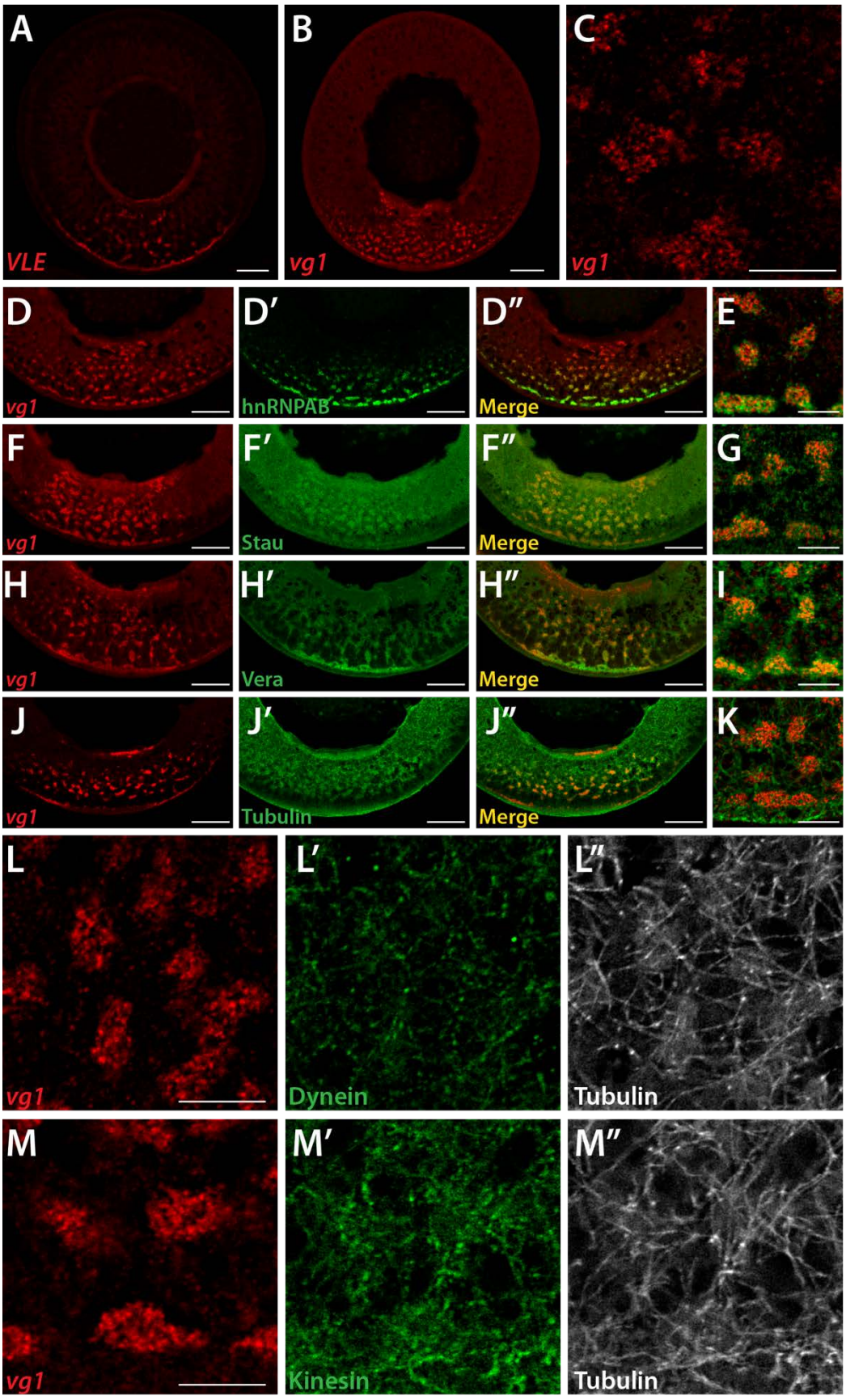
A
VLE
B
vg1
C
vg1
D
vg1
D′
hnRNPAB
D″
Merge
E
F
vg1
F′
Stau
F″
Merge
G
H
vg1
H′
Vera
H″
Merge
I
J
vg1
J′
Tubulin
J″
Merge
K
L
vg1
L′
Dynein
L″
Tubulin
M
vg1
M′
Kinesin
M″
Tubulin

Figure 2.1. vg1 *mRNA is transported in large mRNPs*. **(A)** A cryosection of a stage II oocyte injected with fluorescently-labeled VLE RNA is shown, with the vegetal cortex at the bottom. **(B)** A cryosection of a stage II oocyte probed by FISH for *vg1* mRNA is shown, with the vegetal cortex at the bottom. **(C)** Higher magnification view of *vg1* RNP complexes in the vegetal cytoplasm of a stage II oocyte. **(D)** FISH/IF is shown for *vg1* mRNA (D), hnRNPAB (D′) and colocalization of *vg1* and hnRNPAB. (D′′). **(E)** Higher magnification view is shown of *vg1* mRNA and hnRNPAB colocalization. **(F)** FISH/IF is shown for *vg1* mRNA (F), Stau1 (F′) and colocalization of *vg1* mRNA and Stau1 (F′′). **(G)** Higher magnification view is shown of *vg1* mRNA and Stau1 colocalization. **(H)** FISH/IF is shown for *vg1* mRNA (H), Vera (H′) and colocalization of *vg1* mRNA and Vera (H′). **(I)** Higher magnification view is shown of *vg1* and Vera colocalization. **(J)** FISH/IF is shown for *vg1* mRNA (J), α-tubulin (J′) and colocalization of *vg1* mRNA and α-tubulin. (J′′). **(L)** FISH/IF is shown for *vg1* mRNA (L), dynein intermediate chain (L′) and colocalization of *vg1* mRNA and dynein (H′). **(M)** FISH/IF is shown for *vg1* mRNA (M), conventional kinesin (M′) and colocalization of *vg1* mRNA and kinesin (M′). For (A), (B), (D-D”), (F-F”), (H-H”), scale bars = 50 μm. For (C), (E), (G), (I), (K), (L), (M), scale bars = 10 μm.

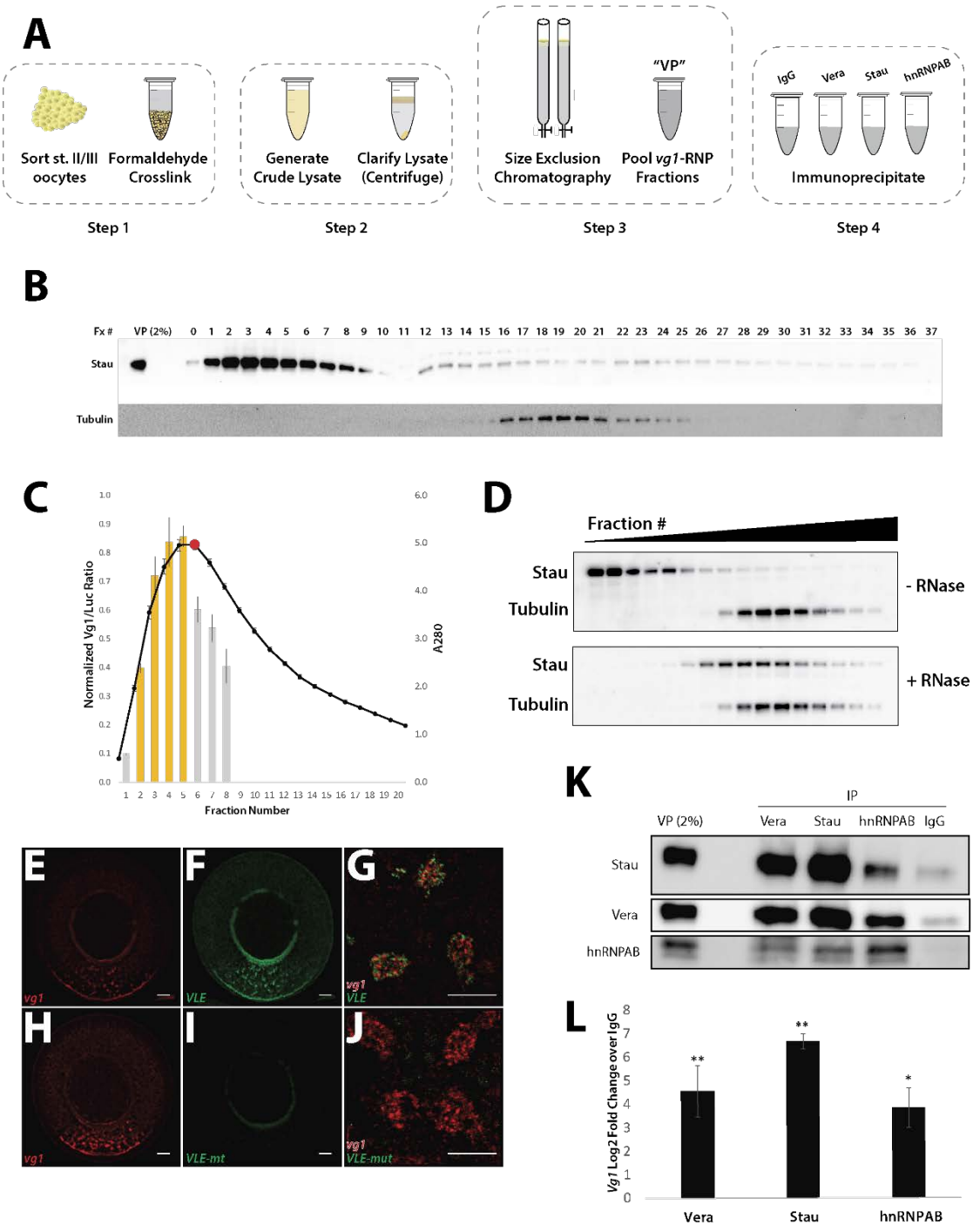

Figure 2.2. ***Isolation of* vg1 *transport mRNPs*.** **(A)** Schematic of the *vg1* RNP isolation procedure. Stage II/III oocytes are crosslinked, lysed, clarified by centrifugation, and fractionated by Sephacryl S-400 size-exclusion chromatography. Fractions containing *vg1* mRNA are pooled into the vegetal RNP

pool (VP). The VP is split equally among four immunoprecipitations using anti-Vera, anti-Stau, and anti-hnRNPAB antibodies and IgG as a negative control. **(B)** Immunoblot analysis of S-400 column fractions probed with anti-Stau1 or anti-αtubulin antibodies. The input (VP) is at the left and the normalized fraction numbers are indicated at the top. Stau1 chromatographs primarily in the void volume (fractions 2-9) and tubulin is present in later fractions (17-27). **(C)** S-400 column fractions (1-8) were probed for *vg1* mRNA by qRTPCR (bars) and total protein concentration was analyzed by A_{280} (black line). For qRTPCR, values were normalized to a luciferase (Luc) control RNA. Yellow bars indicate fractions selected for pooling into the VP, gray bars are additional fractions probed, but not pooled. Red dot indicates peak A_{280}. Error bars represent standard error of the mean (n=11 columns). **(D)** Oocyte lysate was treated with RNase A prior to size exclusion chromatography, followed by immunoblot analysis with anti-Stau1 and anti-tubulin. S-400 column fractions from untreated (-RNase) lysate are shown at the top and column fractions using RNAse-treated lysate is shown at the bottom. **(E)** A cryosection of a stage II oocyte probed by FISH for *vg1* mRNA (red) is shown, with the vegetal cortex at the bottom. **(F)** A cryosection of a stage II oocyte injected with fluorescently-labeled VLE RNA (green) is shown, with the vegetal cortex at the bottom. **(G)** High magnification view of the vegetal cytoplasm of a stage II oocyte injected with VLE RNA (green). Endogenous *vg1* mRNA is detected by FISH (red). **(H)** A cryosection of a stage II oocyte probed by FISH for *vg1* mRNA (red) is shown, with the vegetal cortex at the bottom. **(I)** A cryosection of a stage II oocyte injected with fluorescently-labeled mutant VLE RNA (VLE-mt, green) is shown, with the vegetal cortex at the bottom. **(J)** High magnification

view of the vegetal cytoplasm of a stage II oocyte injected with mutant VLE RNA (VLE-mt, green). Endogenous *vg1* mRNA is detected by FISH (red). For (E-F) and (H-I) scale bars = 50 μm. For (G) and (J) scale bars = 10 μm. **(J)** The VP (left, 2% of input) was immunoprecipitated (IP) using anti-Vera, anti-Stau1, anti-hnRNPAB, and IgG. After SDS-PAGE, co-immunoprecipitation of Stau, Vera and hnRNPAB were confirmed by immunoblotting with anti-Stau1 (top), anti-Vera (middle), and anti-hnRNPAB (bottom). **(K)** The VP was immunoprecipitated using anti-Vera, anti-Stau1, anti-hnRNPAB, and IgG. Following isolation of bound RNAs, *vg1* RNA was detected by qRT-PCR, with normalization to a *luciferase* control. Shown is log2 fold enrichment for Vera (left), Stau (middle), and hnRNPAB (right) over IgG. $n=5$ and error bars represent standard error of mean. ** indicates $p < 0.01$, * indicates $p < 0.05$.

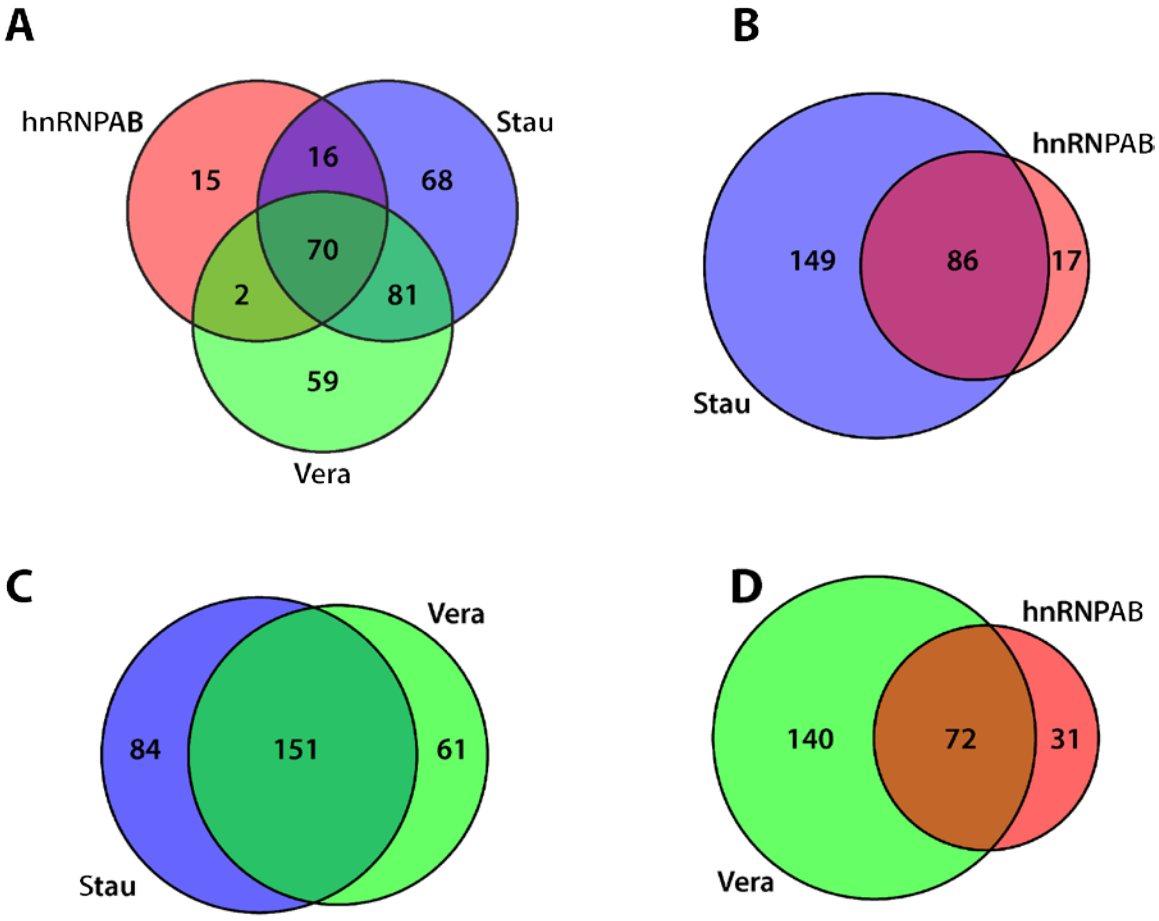

Figure 2.3. ***Mass spectrometry analysis of* vg1 *transport mRNPs***. Mass spectrometry was performed on parallel immunoprecipitations (IPs) of *vg1* RBPs, hnRNPAB, Stau1 and Vera. **(A)** Venn diagram of proteins enriched in hnRNPAB, Stau1 and Vera IPs over IgG control. **(B)** Venn diagram of proteins enriched in hnRNPAB and Stau1 Ps over IgG control. **(C)** Venn diagram of proteins enriched in hnRNPAB and Vera IPs over IgG control. **(D)** Venn diagram of proteins enriched in Stau1 and Vera IPs over IgG control.

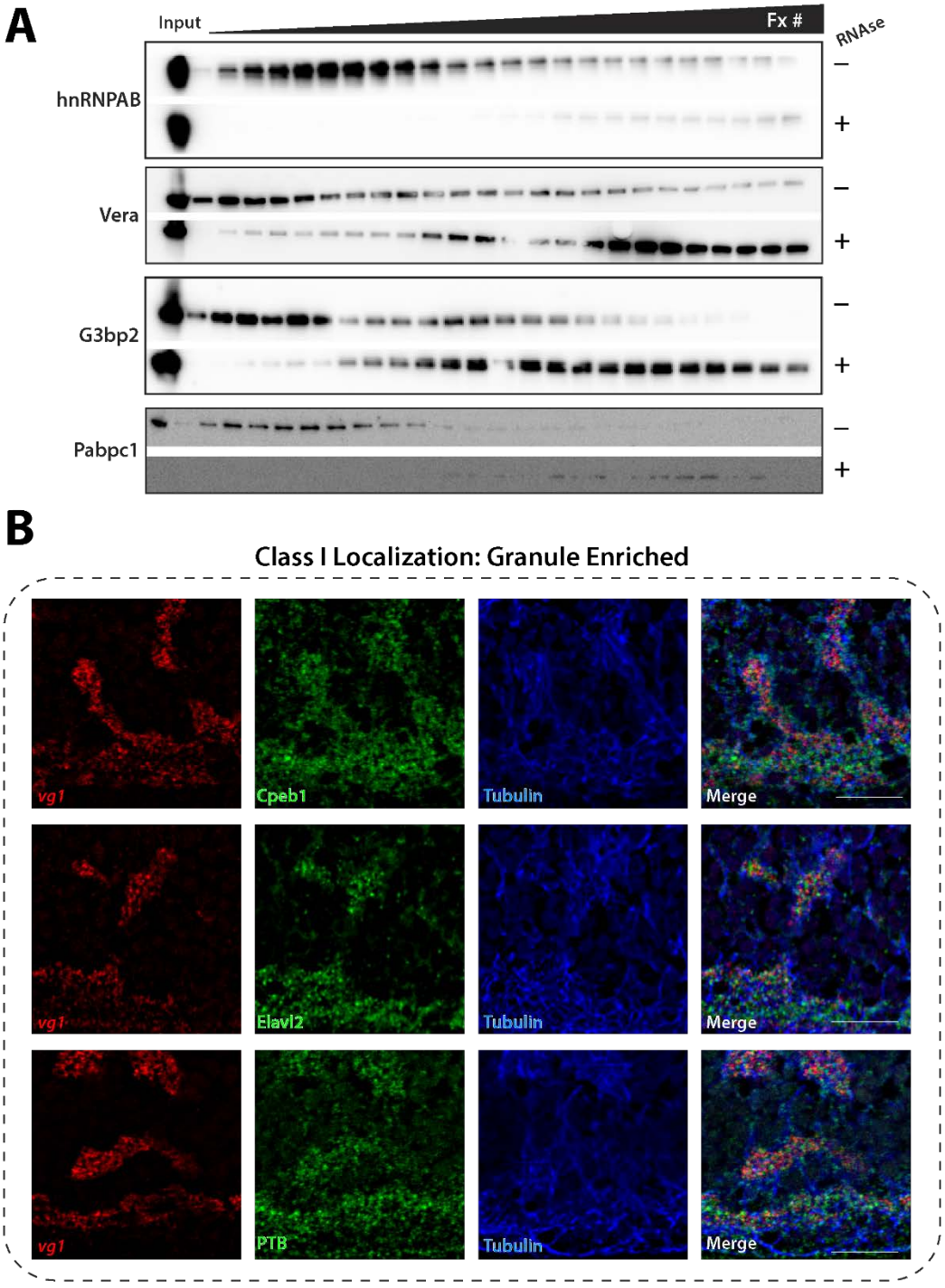
A
Input
Fx #
RNAse
hnRNPAB
Vera
G3bp2
Pabpc1
–
+
B
Class I Localization: Granule Enriched
vg1
Cpeb1
Tubulin
Merge
vg1
Elavl2
Tubulin
Merge
vg1
PTB
Tubulin
Merge

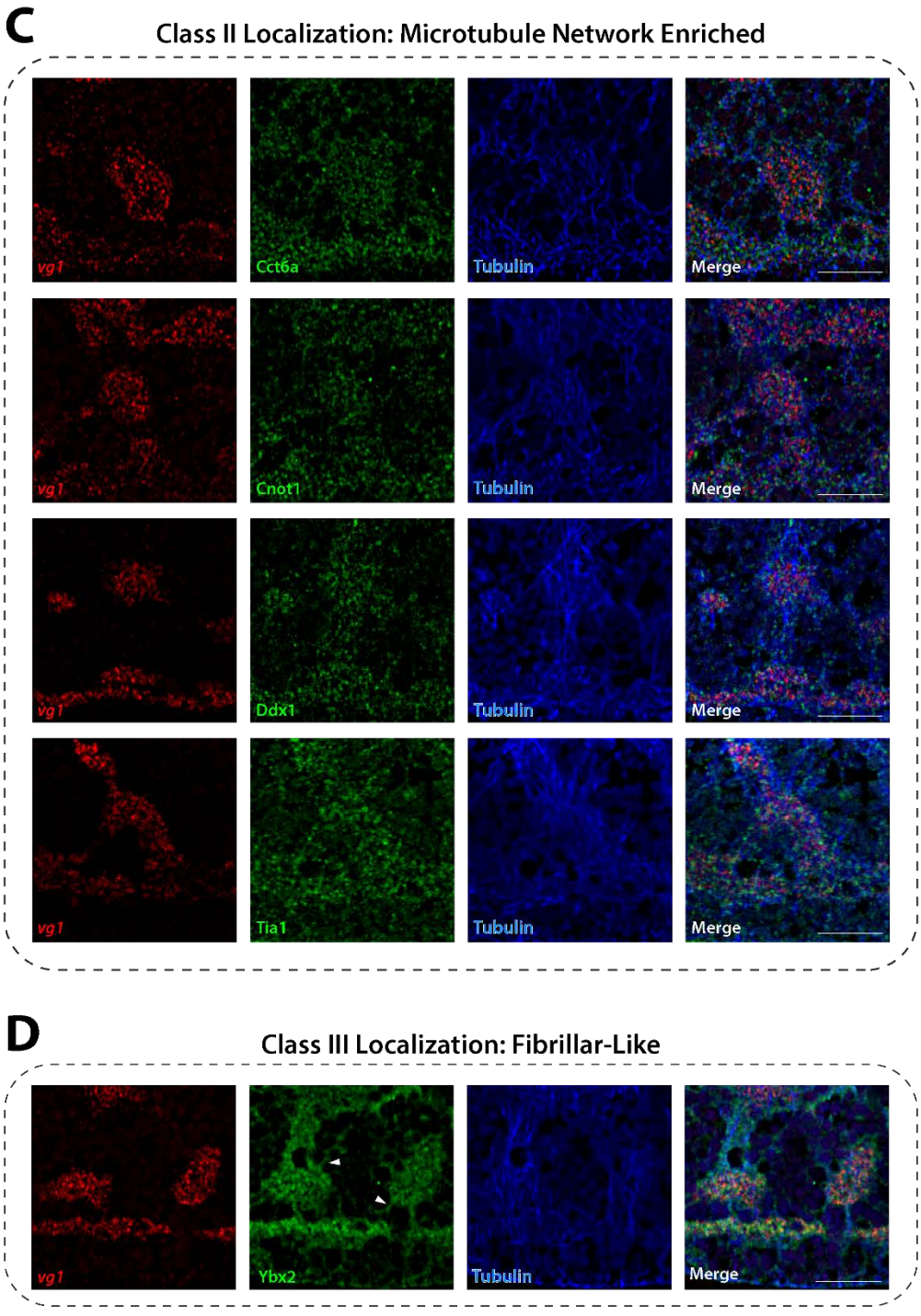

Figure 2.4. ***Validation and classification of*** **vg1** ***RNP transport granule constituents***. **(A)** Oocyte lysates were treated with RNase A prior to size

exclusion chromatography, followed by immunoblot analysis with anti-hnRNPAB, anti-Vera, anti-G3bp2, and anti-Pabpc1. S-400 column fractions from untreated (-) lysate are shown at the top and column fractions using RNAse-treated lysate (+) are shown at the bottom for each protein. The input (VP) is shown at the left. **(B)** Class I constituents are enriched in *vg1* RNP transport granules. Left (red) panels show *vg1* mRNA FISH from cryosectioned oocytes. Middle left panels (green) show IF for Cpeb1 (top), Elavl2 (middle), and PTB (bottom). Middle right panels (blue) show IF for α-tubulin, and right panels show the merge. **(C)** Class II constituents are colocalized with microtubules associated with *vg1* RNP transport granules. Left (red) panels show *vg1* mRNA FISH from cryosectioned oocytes. Middle left panels (green) show IF for Cct6a (top), Cnot1 (upper middle), Ddx1 (lower middle), and Tia1 (bottom). Middle right panels (blue) show IF for α-tubulin, and right panels show the merge. **(D)** Class III exhibits amyloid-like distribution. Left (red) panel shows *vg1* mRNA FISH from cryosectioned oocytes, middle left panel (green) shows IF for Ybx2, middle right panel (blue) shows IF for α-tubulin, and the right panel shows a merge. For (B—D) scale bars = 10 μm.

A

Gene	S	P	N	G	Gene	S	P	N	G	Gene	S	P	N	G
actg1					**hist1h2bj**					**ppia**				
aimp1					hnrnpab†‡#					prkra				
c14orf166‡					hnrnpd‡					ptbp1†‡#				
cct6a‡					hnrnpk					ptbp3†‡				
cltc					hnrnpm					rbpms2				
cnot1‡					hspa8					**rps28p9**				
copa					**iars**					rtcb				
cpeb1‡					ilf2					ruvbl1‡				
cpsf2					ilf3‡					slbp				
ddx1‡					**kars**					stau1†‡				
ddx3x‡					**kif3b**‡					stau2†‡				
ddx5					**krt12**					stip1				
dhx9‡					**larp6**					**stk33**				
dynll1‡					lsm1					strap				
dynll2‡					lsm14a‡					tia1‡				
eef1a2					lsm14b‡					**tsn**				
eif3a					**lsm2**‡					tuba3c				
eif3e					nop56					tubb‡				
eif4enif1					nop58					**txndc17**				
eif4g3l					nudt16‡					upf1				
elavl1‡#					**pabpc1**†‡					usp10				
elavl2†‡#					**pabpc1l**					usp5				
fam98a‡					**pabpn1l**					vera†‡#				
fam98b					**padi2**					**vtga2**				
fmr1					parp1					ybx1‡				
ftcd					**patl2**					**ybx2**‡				
g3bp1					**pcm1**					ythdf1				
g3bp2†					piwil3					**zar1**				
grsf1										**zar2**				

B

Molecular Function - Gene Ontology	Count	Percentage	P-value
RNA binding	27	31.4	6.46E-19
nucleotide binding	18	20.9	3.96E-11
ATP binding	15	17.4	7.78E-02
nucleic acid binding	10	11.6	4.53E-02
mRNA binding	6	7.0	5.59E-05
mRNA 3'-UTR binding	4	4.7	1.59E-03
ATP-dependent RNA helicase activity	4	4.7	1.14E-02
double-stranded RNA binding	4	4.7	3.93E-04
helicase activity	3	3.5	2.60E-02
poly(A) binding	3	3.5	1.09E-03
poly(U) RNA binding	2	2.3	2.58E-02
mRNA 5'-UTR binding	2	2.3	4.23E-02

C

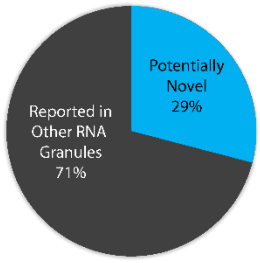

D

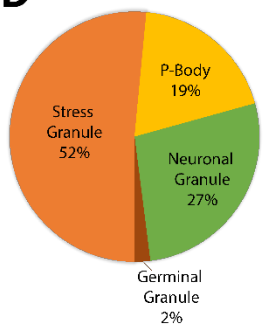

Figure 2.5. ***Comparison of* vg1 *RNP transport granules with constituents of other cytoplasmic RNP granules.*** **(A)** Protein constituents of *vg1* transport RNPs share constituents with stress granules (S, orange), p-bodies (P, yellow), neuronal granules (N, green), and germ granules (G, red). Proteins found in *vg1* transport RNPs but not reported in other granules, are bolded. Proteins that have been validated by immunoblotting are indicated by †. Proteins that have been validated by IF are indicated by ‡. Those proteins previously shown to directly bind *vg1* RNA are indicated by #. **(B)** Gene ontology (GO) analysis of the proteins enriched in *vg1* transport RNPs, determined by DAVID Functional Annotation. The Count column indicates the number of proteins identified in (A) with a given molecular function gene ontology category. The Percentage column

indicates the percent of proteins in (A) containing a given gene ontology category. The P-value column represents the significance as a measure of overrepresentation of each of these categories compared to the *Xenopus tropicalis* proteome, using a modified Fisher's Exact Test. **(C)** Overlap (gray) of *vg1* transport RNPs constituents with other cytoplasmic granules; unique proteins are indicated by blue. **(D)** Overlap of *vg1* transport RNPs constituents with stress granules (orange), p-bodies (yellow), neuronal granules (green), and germ granules (red).

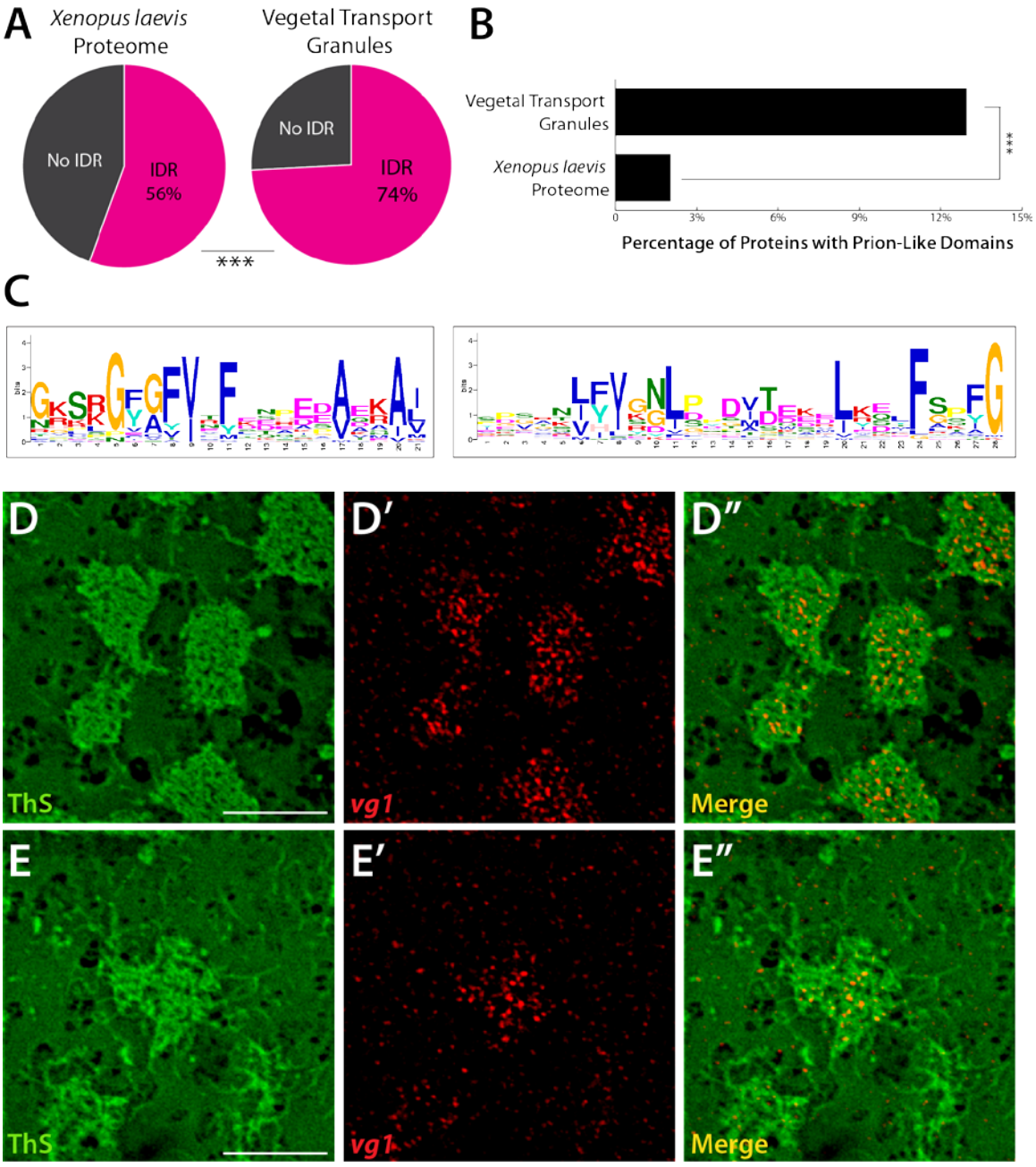

Figure 2.6. ***Vg1 RNP transport granules display amyloid-like characteristics.*** **(A)** Comparison by SLIDER analysis for long stretches of intrinsically disordered regions (IDR) for the *X. laevis* proteome *vs.* the vegetal RNP transport granule proteome. *** indicates $p < 0.001$ **(B)** Comparison of the percentage of prion-like domains in the vegetal RNP transport granule proteome

compared to the entire *Xenopus* proteome, as determined with the predictor PLAAC. *** indicates $p < 0.001$ **(C)** MEME motif analysis of vegetal RNP transport granule proteome reveals enrichment of FG motifs. **(D-E)** Thioflavin S staining (green, left) was combined with *vg1* mRNA FISH (red, middle) reveals (right, merge) interspersion of *vg1* mRNA with amyloid-like fibrils. Scale bars = 10 μm.

References

Ahsan N, Belmont J, Chen Z, Clifton JG, Salomon AR. 2017. Highly reproducible improved label-free quantitative analysis of cellular phosphoproteome by optimization of LC-MS/MS gradient and analytical column construction. *J Proteomics* **165**: 69–74.

Antrobus R, Borner GH. 2011. Improved elution conditions for native co-immunoprecipitation. *PLoS One* **6**: 2–7.

Bailey TL, Elkan C. 1994. Fitting a mixture model by expectation maximization to discover motifs in biopolymers. *Proceedings Int Conf Intell Syst Mol Biol* **2**: 28–36.

Becker BE, Gard DL. 2006. Visualization of the cytoskeleton in *Xenopus* oocytes and eggs by confocal immunofluorescence microscopy. *Methods Mol Biol* **322**: 69–86.

Birsoy B, Kofron M, Schaible K, Wylie C, Heasman J. 2006. Vg1 is an essential signaling molecule in *Xenopus* development. *Development* **133**: 15–20.

Blower MD. 2013. Molecular insights into intracellular RNA localization. *Int Rev Cell Mol Biol* **302**: 1–39.

Bustin SA. 2002. Quantification of mRNA using real-time reverse transcription PCR (RT-PCR): trends and problems. *J Mol Endocrinol* **29**: 23–39.

Cazenave C, Uhlenbeck OC. 1994. RNA template-directed RNA synthesis by T7 RNA polymerase. *Proc Natl Acad Sci* **91**: 6972–6976.

Charlesworth A, Yamamoto TM, Cook JM, Silva KD, Kotter C V., Carter GS, Holt JW, Lavender HF, MacNicol AM, Ying Wang Y, et al. 2012. *Xenopus laevis* zygote arrest 2 (*zar2*) encodes a zinc finger RNA-binding protein that binds to the translational control sequence in the maternal Wee1 mRNA and regulates translation. *Dev Biol* **369**: 177–190.

Chin A, Lécuyer E. 2017. RNA localization: Making its way to the center stage. *Biochim Biophys Acta - Gen Subj* **1861**: 2956–2970.

Czaplinski K, Köcher T, Schelder M, Segref A, Wilm M, Mattaj IW. 2005. Identification of 40LoVe, a *Xenopus* hnRNP D family protein involved in localizing a TGF-beta-related mRNA during oogenesis. *Dev Cell* **8**: 505–15.

Czaplinski K, Mattaj IW. 2006. 40LoVe interacts with Vg1RBP/Vera and hnRNP I in binding the Vg1-localization element. *RNA* **12**: 213–22.

De Graeve F, Besse F, Graeve F De, Bessé F. 2018. Neuronal RNP granules: from physiological to pathological assemblies. *Biol Chem* **0**: 623–635.

De Neve J, Thas O, Ottoy JP, Clement L. 2013. An extension of the Wilcoxon-Mann-Whitney test for analyzing RT-qPCR data. *Stat Appl Genet Mol Biol* **12**: 333–346.

Deshler JO, Highett MI, Abramson T, Schnapp BJ. 1998. A highly conserved RNA-binding protein for cytoplasmic mRNA localization in vertebrates. *Curr Biol* **8**: 489–96.

Deshler JO, Highett MI, Schnapp BJ. 1997. Localization of *Xenopus Vg1* mRNA by

Vera protein and the endoplasmic reticulum. *Science (80-)* **276**: 1128–1131.

Dumont JN. 1972. Oogenesis in *Xenopus laevis* (Daudin). I. Stages of oocyte development in laboratory maintained animals. *J Morph* **136**: 153–179.

Elias JE, Gygi SP. 2007. Target-decoy search strategy for increased confidence in large-scale protein identifications by mass spectrometry. *Nat Methods* **4**: 207–214.

Eliscovich C, Buxbaum AR, Katz ZB, Singer RH. 2013. mRNA on the move: the road to its biological destiny. *J Biol Chem* **288**: 20361–20368.

Elvira G, Wasiak S, Blandford V, Tong XK, Serrano A, Fan X, del Rayo Sánchez-Carbente M, Servant F, Bell AW, Boismenu D, et al. 2006. Characterization of an RNA granule from developing brain. *Mol Cell Proteomics* **5**: 635–651.

Frey S, Richter RP, Görlich D. 2006. FG-rich repeats of nuclear pore proteins form a three-dimensional meshwork with hydrogel-like properties. *Science* **314**: 815–817.

Fritzsche R, Karra D, Bennett KL, Ang FY, Heraud-Farlow JE, Tolino M, Doyle M, Bauer KE, Thomas S, Planyavsky M, et al. 2013. Interactome of two diverse RNA granules links mRNA localization to translational repression in neurons. *Cell Rep* **5**: 1749–1762.

Gagnon JA, Kreiling JA, Powrie EA, Wood TR, Mowry KL. 2013. Directional transport is mediated by a Dynein-dependent step in an RNA localization pathway. *PLoS Biol* **11**: e1001551.

Gautreau D, Cote C a, Mowry KL. 1997. Two copies of a subelement from the Vg1 RNA localization sequence are sufficient to direct vegetal localization in *Xenopus* oocytes. *Development* **124**: 5013–20.

Gilman B, Tijerina P, Russell R. 2017. Distinct RNA-unwinding mechanisms of DEAD-box and DEAH-box RNA helicase proteins in remodeling structured RNAs and RNPs. *Biochem Soc Trans* **45**: 1313–1321.

Guntern R, Bouras C, Hof PR, Vallet PG. 1992. An improved thioflavine S method for staining neurofibrillary tangles and senile plaques in Alzheimer's disease. *Experientia* **48**: 8–10.

Havin L, Git A, Elisha Z, Oberman F, Yaniv K, Schwartz SP, Standart N, Yisraeli JK. 1998. RNA-binding protein conserved in both microtubule- and microfilament-based RNA localization. *Genes Dev* **12**: 1593–1598.

Heraud-Farlow JE, Kiebler MA. 2014. The multifunctional Staufen proteins: Conserved roles from neurogenesis to synaptic plasticity. *Trends Neurosci* **37**: 470–479.

Huang DW, Sherman BT, Lempicki RA. 2009a. Bioinformatics enrichment tools: paths toward the comprehensive functional analysis of large gene lists. *Nucleic Acids Res* **37**: 1–13.

Huang DW, Sherman BT, Lempicki RA. 2009b. Systematic and integrative analysis of large gene lists using DAVID bioinformatics resources. *Nat Protoc* **4**: 44–57.

Hubstenberger A, Courel M, Bénard M, Souquere S, Ernoult-Lange M, Chouaib R, Yi Z, Morlot J-BB, Munier A, Fradet M, et al. 2017. P-body purification reveals the condensation of repressed mRNA regulons. *Mol Cell* **68**: 144–157.e5.

Jain S, Wheeler JR, Walters RW, Agrawal A, Barsic A, Parker R. 2016. ATPase-modulated stress granules contain a diverse proteome and substructure. *Cell* **164**: 487–498.

Johnston S, Gallaher Z, Czaja K. 2012. Exogenous reference gene normalization for real-time reverse transcription-polymerase chain reaction analysis under dynamic endogenous transcription. *Neural Regen Res* **7**: 1064–72.

Joseph EM, Melton DA. 1998. Mutant Vg1 ligands disrupt endoderm and mesoderm formation in *Xenopus* embryos. *Development* **125**: 2677–85.

Kaganovich D. 2017. There is an inclusion for that: Material properties of protein granules provide a platform for building diverse cellular functions. *Trends Biochem Sci* **42**: 765–776.

Kanai Y, Dohmae N, Hirokawa N. 2004. Kinesin transports RNA: Isolation and characterization of an RNA-transporting granule. *Neuron* **43**: 513–25.

Kedersha N, Chen S, Gilks N, Li W, Miller IJ, Stahl J, Anderson P. 2002. Evidence that ternary complex (eIF2-GTP-tRNA(i)(Met))-deficient preinitiation complexes are core constituents of mammalian stress granules. *Mol Biol Cell* **13**: 195–210.

Kloc M, Bilinski S, Chan AP, Allen LH, Zearfoss NR, Etkin LD. 2001. RNA

localization and germ cell determination in *Xenopus*. *Int Rev Cytol* **203**: 63–91.

Klymkowsky MW, Maynell LA, Nislow C. 1991. Cytokeratin phosphorylation, cytokeratin filament severing and the solubilization of the maternal mRNA *Vg1*. *J Cell Biol* **114**: 787–797.

Kress TL, Yoon YJ, Mowry KL. 2004. Nuclear RNP complex assembly initiates cytoplasmic RNA localization. *J Cell Biol* **165**: 203–211.

Kwon S, Abramson T, Munro TP, John CM, Köhrmann M, Schnapp BJ. 2002. UUCAC- and Vera-dependent localization of *VegT* RNA in *Xenopus* oocytes. *Curr Biol* **12**: 558–564.

Lancaster AK, Nutter-Upham A, Lindquist S, King OD. 2014. PLAAC: A web and command-line application to identify proteins with prion-like amino acid composition. *Bioinformatics* **30**: 2501–2502.

Lécuyer E, Yoshida H, Parthasarathy N, Alm C, Babak T, Cerovina T, Hughes TR, Tomancak P, Krause HM. 2007. Global analysis of mRNA localization reveals a prominent role in organizing cellular architecture and function. *Cell* **131**: 174–87.

Lewis RA, Kress TL, Cote CA, Gautreau D, Rokop ME, Mowry KL. 2004. Conserved and clustered RNA recognition sequences are a critical feature of signals directing RNA localization in *Xenopus* oocytes. *Mech Dev* **121**: 101–9.

Lewis RA, Gagnon JA, Mowry KL. 2008. PTB/hnRNP I is required for RNP

remodeling during RNA localization in *Xenopus* oocytes. *Mol Cell Biol* **28**: 678–686.

Luo Y, Na Z, Slavoff SA. 2018. P-bodies: Composition, properties, and functions. *Biochemistry* **57**: 2424-2431.

Markmiller S, Soltanieh S, Server KL, Mak R, Jin W, Fang MY, Luo EC, Krach F, Yang D, Sen A, et al. 2018. Context-dependent and disease-specific diversity in protein interactions within stress granules. *Cell* **172**: 590–604.e13.

Medioni C, Mowry K, Besse F. 2012. Principles and roles of mRNA localization in animal development. *Development* **139**: 3263–76.

Melton DA. 1987. Translocation of a localized maternal mRNA to the vegetal pole of *Xenopus* oocytes. *Nature* **328**: 80–2.

Messitt TJ, Gagnon JA, Kreiling JA, Pratt CA, Yoon YJ, Mowry KL. 2008. Multiple kinesin motors coordinate cytoplasmic RNA transport on a subpopulation of microtubules in *Xenopus* oocytes. *Dev Cell* **15**: 426–436.

Mili S, Steitz JA. 2004. Evidence for reassociation of RNA-binding proteins after cell lysis: implications for the interpretation of immunoprecipitation analyses. *RNA* **10**: 1692–4.

Montague TG, Schier AF. 2017. Vg1-Nodal heterodimers are the endogenous inducers of mesendoderm. *Elife* **6**.

Mowry KL, Melton DA. 1992. Vegetal messenger RNA localization directed by a 340-nt RNA sequence element in *Xenopus* oocytes. *Science* **255**: 991–4.

Mughal BB, Leemans M, Spirhanzlova P, Demeneix B, Fini J-B. 2018. Reference gene identification and validation for quantitative real-time PCR studies in developing *Xenopus laevis*. *Sci Rep* **8**: 496.

Neil CR, Mowry K. 2018. Fluorescence *in situ* hybridization of cryosectioned *Xenopus* oocytes. *Cold Spring Harb Protoc* **2018**: pdb.prot097030.

Nekrasov MP, Ivshina MP, Chernov KG, Kovrigina EA, Evdokimova VM, Thomas AM, Hershey JB, Ovchinnikov LP. 2003. The mRNA-binding protein YB-1 (p50) prevents association of the eukaryotic initiation factor eIF4G with mRNA and inhibits protein synthesis at the initiation stage. *J Biol Chem* **278**: 13936–43.

Newman K, Aguero T, King ML. 2018. Isolation of *Xenopus* oocytes. *Cold Spring Harb Protoc* **2018**: pdb.prot095851.

Nielsen FC, Hansen HT, Christiansen J. 2016. RNA assemblages orchestrate complex cellular processes. *BioEssays* **38**: 1–8.

Peng Z, Mizianty MJ, Kurgan L. 2014. Genome-scale prediction of proteins with long intrinsically disordered regions. *Proteins Struct Funct Bioinforma* **82**: 145–158.

Pfaffl MW. 2001. A new mathematical model for relative quantification in real-time RT-PCR. *Nucleic Acids Res* **29**: e45.

Protter DSW, Parker R. 2016. Principles and properties of stress granules. *Trends Cell Biol* **26**: 668–79.

Rajgor D, Shanahan CMM. 2014. RNA granules and cytoskeletal links. *Biochem Soc Trans* **42**: 1206–1210.

Ramakers C, Ruijter JM, Deprez RHL, Moorman AFM. 2003. Assumption-free analysis of quantitative real-time polymerase chain reaction (PCR) data. *Neurosci Lett* **339**: 62–6.

Rebagliati MR, Weeks DL, Harvey RP, Melton DA. 1985. Identification and cloning of localized maternal RNAs from *Xenopus* eggs. *Cell* **42**: 769–777.

Schisa JA. 2012. New insights into the regulation of RNP granule assembly in oocytes. *Int Rev Cell Mol Biol* **295**: 233–89.

Snedden DD, Bertke MM, Vernon D, Huber PW. 2013. RNA localization in *Xenopus* oocytes uses a core group of trans-acting factors irrespective of destination. *RNA* **19**: 889–895.

Tannahill D, Melton D a. 1989. Localized synthesis of the Vg1 protein during early *Xenopus* development. *Development* **106**: 775–85.

Thomsen GH, Melton DA. 1993. Processed Vg1 protein is an axial mesoderm inducer in *Xenopus*. *Cell* **74**: 433–441.

Uversky VN. 2017. Intrinsically disordered proteins in overcrowded milieu: Membrane-less organelles, phase separation, and intrinsic disorder. *Curr Opin Struct Biol* **44**: 18–30.

Van Driesche S, Martin K. 2018. New frontiers in RNA transport and local translation in neurons. *Dev Neurobiol* 1–43.

Vandesompele J, De Preter K, Pattyn F, Poppe B, Van Roy N, De Paepe A, Speleman F. 2002. Accurate normalization of real-time quantitative RT-PCR data by geometric averaging of multiple internal control genes. *Genome Biol* **3**: RESEARCH0034.

Voronina E, Seydoux G, Sassone-Corsi P, Nagamori I. 2011. RNA granules in germ cells. *Cold Spring Harb Perspect Biol* **3**: a002774.

Weeks DL, Melton DA. 1987. A maternal mRNA localized to the vegetal hemisphere in *Xenopus* eggs codes for a growth factor related to TGF-β. *Cell* **51**: 861–867.

Wei MT, Elbaum-Garfinkle S, Holehouse AS, Chen CC-H, Feric M, Arnold CB, Priestley RD, Pappu R V., Brangwynne CP. 2017. Phase behaviour of disordered proteins underlying low density and high permeability of liquid organelles. *Nat Chem* **9**: 1118–1125.

Yamamoto TM, Cook JM, Kotter C V., Khat T, Silva KD, Ferreyros M, Holt JW, Knight JD, Charlesworth A. 2013. Zar1 represses translation in *Xenopus* oocytes and binds to the TCS in maternal mRNAs with different characteristics than Zar2. *Biochim Biophys Acta - Gene Regul Mech* **1829**: 1034–1046.

Yisraeli JK. 2005. VICKZ proteins: a multi-talented family of regulatory RNA-binding proteins. *Biol Cell* **97**: 87–96.

Yoon YJ, Mowry KL. 2004. *Xenopus* Staufen is a component of a ribonucleoprotein complex containing *Vg1* RNA and kinesin. *Development* **131**: 3035–45.

Yu K, Sabelli A, DeKeukelaere L, Park R, Sindi S, Gatsonis CA, Salomon A. 2009. Integrated platform for manual and high-throughput statistical validation of tandem mass spectra. *Proteomics* **9**: 3115–25.

Yu K, Salomon AR. 2010. HTAPP: High-throughput autonomous proteomic pipeline. *Proteomics* **10**: 2113–2122.

Yu K, Salomon AR. 2009. PeptideDepot: flexible relational database for visual analysis of quantitative proteomic data and integration of existing protein information. *Proteomics* **9**: 5350–8.

Chapter 3: Whole-mount Immunofluorescence for Visualizing Endogenous Protein and Injected RNA in *Xenopus* Oocytes

This chapter has been published: Jeschonek, S.P. And Mowry, K.L. (2018) Visualizing Endogenous Protein and Injected RNA in *Xenopus* Oocytes. *Cold Spring Protoc* doi: 10.1101/pdb.prot097022.

Abstract

The *Xenopus laevis* oocyte provides a unique model to study cell polarity. During oogenesis, numerous mRNAs and proteins become asymmetrically distributed in the oocyte cytoplasm and their analysis is important for understanding the establishment of developmental polarity. Microinjection of fluorescently labeled RNA can recapitulate the localization pattern of endogenous mRNA and can be combined with immunofluorescence analysis of proteins of interest. Such analyses can provide insight into the cytoplasmic interactions contributing to polarity and imaging by confocal microscopy allows a high-resolution view of RNA-protein interactions. Here, we present an updated method to image endogenous protein and microinjected RNA in immature *X. laevis* oocytes.

Materials

It is essential that you consult the appropriate Material Safety Data Sheets and your institution's Environmental Health and Safety Office for proper handling of equipment and hazardous materials used in this protocol.

Recipes

Recipes, indicated by <R>*, are detailed are the end of this manuscript.*

Reagents

- Ammonium acetate (7 M, RNase-free)
- Collagenase solution <R>
- Cy5-UTP or Cy3-UTP (GE Healthcare Life Sciences, PA55026/PA53026)
- Ethanol (70%, RNase-free)
- Ethanol (100%, RNase-free)
- Glycogen (20 mg/mL; Thermo Scientific, R0561)
- MBSH Buffer (10x) <R>
- MEMFA <R>
- Methanol (anhydrous, 100%)
- mMessage machine SP6/T7/T3 transcription kit (Ambion)
- Murray's clear <R>
- Nuclease-free H_2O (Thermo Fisher, AM9914G) or H_2O treated with DEPC (Sigma D5758)
- Oocyte culture medium (OCM) <R>
- PBT for *Xenopus* oocytes/PBT-Plus <R>

- Phenol/chloroform/isoamylalcohol (25:24:1, Fisher Scientific, AC327115000)
- Plasmid containing sequence of interest downstream of an RNA polymerase promoter (T7, SP6, or T3)
- Proteinase K buffer for *Xenopus* oocytes <R>
- Primary antibody
- Restriction enzyme appropriate for plasmid linearization
- RNase-ZAP (Ambion, AM9780)
- Secondary antibody, fluorescently-labeled

Equipment

- Aluminum foil
- Barrier pipette tips
- Dissecting microscope
- Fluorodishes (10 mm inside diameter; World Precision Instruments, FD3510-100)
- Heat blocks (37°C and 72°C)
- Ice bucket
- Illustra ProbeQuant G-50 Micro Columns (GE Healthcare, 29-9034-08)
- Inverted confocal microscope (such as Zeiss LSM 510 Meta Confocal Laser Scanning Microscope)
- Microcentrifuges at room temperature and 4°C
- Microcentrifuge tubes (1.5 mL, RNase-free)
- Microcentrifuge tubes (1.5 mL, siliconized or low-retention)

- Microinjection setup (such as Harvard Apparatus PLI-100 PicoInjector and Narishige MN-151 Joystick Micromanipulator)
- NanoDrop spectrophotometer
- Pasteur pipettes
- Pulled glass pipette with a fine tip
- Rocking platform
- Surgical instruments for removing oocytes from *Xenopus laevis* females
- Tissue culture plate (24-well)
- Vortex mixer
- *Xenopus laevis* females for oocyte preparation

Methods

This protocol covers co-imaging of injected RNA and protein. Alternatively, RNA or protein can be visualized independently of each other. If imaging only endogenous protein, proceed to "Preparation of oocytes" (Step 16).

Preparation of fluorescently-labeled RNA

1. Linearize plasmid DNA containing the sequence of interest cloned downstream of a T7, SP6, or T3 promoter with an appropriate restriction enzyme.
2. Purify the plasmid DNA by phenol chloroform extraction followed by ethanol precipitation and resuspend in nuclease-free H_2O at 500-1000 ng/μL.
3. Prepare an RNase-free working area by treating all surfaces and gloves with RNase-ZAP.

   For subsequent steps, up to Step 15, use only barrier pipette tips and RNase-free reagents.
4. Modify the Ambion mMessage machine transcription kit by adding the reagents in the table below, in the order shown, to an RNase-free microfuge tube:

Reagent	Volume	Final Concentration	Notes
10× Transcription buffer	2.0 μL	1×	
2× NTP/cap mixture	6.0 μL	3.3×	The amount of NTP/cap mixture is altered from the manufacturer's protocol to facilitate incorporation of fluorescent UTP
Cy3-UTP or Cy5-UTP	1.5 μL	0.375 mM	ChromaTide Alexa-Fluor UTPs (Thermo-Fisher) may

			also be used at a final concentration of 0.3 mM
Linearized DNA	(variable)	1 µg	Less than 1 µg can be used per reaction but will reduce yield
10× enzyme mix	2.0 µL	1×	Reactions using SP6 RNA polymerase require longer incubation times (4 hours) compared with those using T7 or T3 RNA polymerases (2 hours) for similar yields
Nuclease-free H_2O	(variable)	-	
Total	20 µl		Reaction may be scaled up for increased RNA production.

5. Mix reaction by gentle pipetting.
6. Incubate at 37°C for 2-4 hours. Protect tubes from light by covering with foil.
7. Pulse spin in a microcentrifuge. Add 1 µL Turbo DNase (included in mMessage machine kit).
8. Incubate at 37°C for 15 minutes with protection from light.
9. Add 179 µL 200 mM EDTA, pH 8.0, to stop the reaction. Mix gently by pipetting.
10. Add 200 µL phenol/chloroform/isoamylalchohol (1:1 ratio) to the reaction. Vortex for 15 seconds. Centrifuge at room temperature for 10 minutes at maximum speed.
11. Carefully remove the upper aqueous phase containing the RNA, and transfer to an RNAse-free tube. Avoid transferring any of the interphase.
12. To remove unincorporated nucleotides (including free fluorescent UTP) pass the RNA through an Illustra ProbeQuant G-50 Micro Column, following manufacturer's instructions (GE Healthcare).

13. Concentrate the RNA by ethanol precipitation.
    i. Add 500 µL 100% ethanol, (2.5× volume), 20 µL 7 M ammonium acetate (0.1× volume) and 1 µL 20 mg/mL glycogen. Mix well by vortexing, and incubate for 1 hour at -80°C.
    ii. Centrifuge at maximum speed at 4°C for 20 minutes. Remove and discard the supernatant and add 1 mL 70% ethanol (stored at -20°C).
    iii. Centrifuge at maximum speed at 4°C for 5 minutes. Remove and discard the supernatant, wash again with 70% ethanol. Centrifuge at maximum speed at 4°C for 5 minutes.
    iv. Remove and discard the supernatant. Allow the RNA pellet to dry at room temperature for 10 minutes, or until most residual 70% ethanol has evaporated. Do not let the pellet dry completely.
    v. Resuspend RNA in 15 µL nuclease-free H_2O.
14. Determine RNA concentration using a NanoDrop spectrophotometer, according to the manufacturer's instructions. (The RNA should generate a curve with a single peak at 280 nM, and a 260/280 nM ratio of ~2.0.) Calculate RNA molarity, and adjust to a final concentration of 1 µM.
15. Store RNA at -80°C in 2 µL aliquots (for single use only). RNA will be stable for several months at -80°C.

Preparation of oocytes

For a detailed procedure see Protocol: Isolation of Xenopus oocytes (Newman et al. 2018).

16. Surgically remove oocytes from *Xenopus laevis* females. For imaging oocytes beyond stage II, albino frogs must be used.
17. Defolliculate oocytes using collagenase solution.
18. Wash oocytes 3-5 times in 1× MBSH buffer, until the wash buffer is clear.
19. Sort oocytes to obtain stages of interest and place in OCM.
20. Allow oocytes to recover in OCM at 18°C for at least 1 hour. Overnight recovery is preferable.

Microinjection

For a detailed microinjection protocol, see Protocol: Microinjection of Xenopus Oocytes (Aguero et al. 2018). If imaging only endogenous protein, go to "Fixation and immunofluorescence", Step 28.

21. Thaw an aliquot of fluorescently-labeled RNA (from Step 15) on ice. Dilute the RNA to a final concentration of 125-500 nM using nuclease-free H_2O.
22. Denature RNA at 72°C for 5 minutes. Immediately place on ice for 3 minutes.
23. Centrifuge RNA at maximum speed for 10 minutes at 4°C to remove any particulates. Carefully pipette RNA into a fresh microcentrifuge tube and place on ice.
24. Calibrate a beveled micropipette with nuclease-free H_2O to deliver 2 nL per injection.
25. Place oocytes into an injection dish containing 1× MBSH.
26. Load RNA into the calibrated micropipette and inject each oocyte with 2 nL of RNA.

27. Culture oocytes at 18°C for 8-48 hrs in a 24-well dish containing 500 µL OCM containing antibiotics.

Fixation and immunofluorescence

28. Examine cultured oocytes for survival.

    If more than 25% of oocytes have lysed, consider repeating microinjections with new oocytes.

29. Place cultured oocytes in a siliconized microfuge tube.

    If visualizing only fluorescent RNA and not co-imaging protein, proceed to Step 33.

30. Remove OCM and wash oocytes with proteinase K buffer (without enzyme added).
31. Add 500 µl proteinase K solution. Gently rock oocytes for 5 minutes at room temperature.
32. Immediately remove proteinase K solution.
33. To fix oocytes, add 500 µL MEMFA. Incubate for 1 hr., with rocking, in the dark.
34. Remove MEMFA and add 500 µL PBT. Wash oocytes for 15 minutes in the dark with rocking.
35. Wash twice more in PBT, for a total of three washes.

    If only visualizing fluorescent RNA, proceed to Step 41.

36. Add 500 µL PBT-Plus blocking solution. Rock oocytes in the dark for at least 2 hours.

37. Remove PBT-Plus. Incubate oocytes with primary antibody diluted in 500 µL PBT-Plus, overnight at 4°C with rocking. If antibody is limiting, oocytes may be incubated in a 250 µL dilution of primary antibody.
38. Replace primary antibody with 500 µL of PBT and rock in the dark at room temperature for 1.5 – 2 hrs. Repeat wash twice for a total of three washes.
39. Add 500 µL of PBT-Plus containing an appropriate fluorescently-labeled secondary antibody. Incubate overnight at 4°C with rocking.

    Xenopus oocytes exhibit strong autofluorescence at 488 nm, limiting the choice of secondary antibodies. When possible, use secondary antibodies with emission at higher wavelengths.
40. Wash oocytes three times in PBT for 1.5-2 hrs at room temperature to remove secondary antibody. After the final wash, resuspend oocytes in 1 mL PBT.
41. Dehydrate oocytes stepwise into 100% anhydrous methanol:

    Oocytes must be completely dehydrated in anhydrous methanol to be compatible with Murray's clear for imaging.

    i. Remove 100 µL of PBT solution and replace with 100 µL anhydrous methanol. Rock oocytes for 5-10 minutes at room temperature. Repeat twice.
    ii. Remove 200 µL and replace with 200 µL anhydrous methanol. Rock oocytes for 5-10 minutes at room temperature. Repeat twice.
    iii. Remove 300 µL and replace with 300 µL anhydrous methanol. Rock for 5-10 minutes at room temperature. Repeat twice.
    iv. Remove 400 µL and replace with 400 µL anhydrous methanol. Rock for 5-10 minutes at room temperature. Repeat twice.

v. Remove 500 µL and replace with 500 µL anhydrous methanol. Rock for 5-10 minutes at room temperature. Repeat twice.

vi. Remove 750 µL and replace with 750 µL anhydrous methanol. Rock for 5-10 minutes at room temperature. Repeat twice.

vii. Remove all buffer and perform three washes with 1 ml 100% anhydrous methanol. At the end of dehydration, the solution should be clear. If solution is cloudy or Schlieren lines are visible, continue washing with anhydrous methanol.

42. Store oocytes in 100% anhydrous methanol at -20°C until ready for imaging. Oocytes may be stored for 2-3 weeks in methanol.

Confocal Imaging

43. Use a Pasteur pipette to transfer oocytes to a fluorodish. Try to keep oocytes in the center of the dish and transfer as little methanol as possible.
44. Using a pulled glass pipette with a fine tip, remove any methanol transferred to the fluorodish.
45. With a Pasteur pipette, add Murray's clear dropwise to the fluorodish, until oocytes are covered completely.
46. Wait at least 5 minutes for oocytes to optically clear. Larger oocytes (stages III-VI) will take longer to clear than smaller oocytes.
47. Image the oocytes using an inverted confocal microscope (Figure 3.1).

i. Locate individual oocytes using a 488 nm laser and a 10× objective. Oocytes can be easily located due to autofluorescence at 488 nm.

ii. Once located, image oocytes at the desired magnification. It may be necessary to open the pinhole >1 airy unit to detect an RNA fluorescence signal.

iii. To decrease cross-excitation between channels, image with each laser separately (not simultaneously).

Troubleshooting

(1) *Problem (Step 14):* Low RNA yield

Solution: Increase the concentration of linear template in the *in vitro* transcription reaction and/or increase incubation time at 37°C to 6 hours. If necessary, multiple reactions can be pooled together prior to ethanol precipitation.

(2) *Problem (Step 47):* RNA Fluorescence signal is dim

Solution: If using Cy3-UTP, switch to the brighter Cy5-UTP. Increase concentration of RNA injected or standardize injection concentration based on fluorescence intensity (e.g., 5,000 RFU, which can be measured with a NanoDrop 3300 Fluorospectrometer).

(3) *Problem (Step 47):* Antibody does not penetrate oocyte interior

Solution: Increase incubation with proteinase K. A time-series may be necessary to determine optimal digestion time for a particular antibody. Increase incubation period with primary antibody to 48 hours.

Discussion

The *X. laevis* oocyte provides an important model to study cell polarity. Oogenesis in *X. laevis* proceeds through six distinct stages, during which the cytoplasm becomes increasingly polarized (Dumont 1972). Both mRNAs and proteins can be asymmetrically distributed in the oocyte cytoplasm, in many cases acting to specify embryonic polarity (reviewed in Houston 2013). Thus, analysis of protein and mRNA distributions in vertebrate oocytes is important for understanding establishment of developmental polarity. The *X. laevis* oocyte, in particular, offers many technical advantages for studying polarity. A single *X. laevis* ovary provides thousands of oocytes in a mixture of different maturity levels (Dumont 1972). Due to their large size, even the youngest oocytes can be manually microinjected (Yisraeli and Melton 1988; Chang et al. 2004). Microinjection of fluorescently labeled RNA can recapitulate the localization pattern of endogenous mRNAs and can be combined with immunofluorescence analysis of proteins of interest (Yoon and Mowry 2004). Furthermore, imaging by confocal microscopy allows a high-resolution view of RNA-protein interactions. Such analyses can provide insight into the cytoplasmic interactions contributing to polarity. The protocol presented here provides an updated method for imaging endogenous protein and microinjected RNA in immature *X. laevis* oocytes.

Acknowledgements

Development of this method was supported by NIH grant GM071049 to KLM.

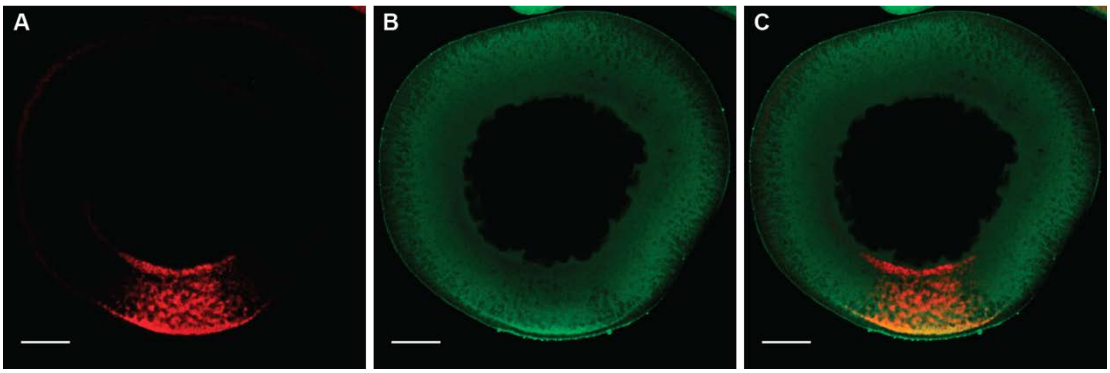

Figure 3.1. ***Co-localization of endogenous Staufen protein and injected VLE RNA.*** Stage II oocytes were injected with 500 nM Cy5-UTP-labeled *VLE* RNA (Mowry and Melton, 1992) and cultured for 18 hr to allow for vegetal localization. Immunofluorescence was performed using an anti-XStau antibody (Yoon and Mowry 2004) at 1:250 dilution and an Alexa-546-secondary antibody (Thermo-Fisher) at 1:500 dilution. Oocytes were imaged on a Zeiss LSM 510 Meta Confocal Laser Scanning Microscope using a 20× objective. Shown is a confocal section with (A) *VLE* RNA in red, (B) Staufen protein in green, and (C) merged red and green channels, showing Staufen protein and *VLE* RNA colocalization. The oocyte is oriented with the vegetal pole at the bottom and the scale bars = 50 μm.

Recipes

Collagenase Solution (3 mg/mL)

0.1 M KPO_3^+ (pH 7.4)

3 mg/mL collagenase I (Sigma C0130)

Prepare fresh. Do not store.

MBSH Buffer (10x)

880 mM NaCl

10 mM KCl

24 mM $NaHCO_3$

8.2 mM $MgSO_4 \cdot 7H_2O$

3.3 mM $Ca(NO_3)_2 \cdot 4H_2O$

4.1 mM $CaCl_2 \cdot 6H_2O$

100 mM HEPES (pH 7.6)

Store as a sterilized 10x stock solution and prepare fresh 1x MBSH prior to use.

Oocyte Culture Media (OCM)

50% Leibovitz's L-15 Medium (Thermo Fisher Scientific, 11415064)

15 mM HEPES, pH 7.6

1 mg/mL insulin

Sterilize though a 0.22 µm filter. OCM without antibiotics can be stored at 4°C for up to two months.

Add the following antibiotics to OCM just prior to culture. Do not store. Do not reuse.

50 U/mL nystatin (Sigma-Aldrich, N1638)

100 U/mL penicillin/streptomycin (Life Technologies, 15070063)

0.1 mg/mL gentamicin (Thermo Fisher Scientific, 15750060)

PBT for Xenopus oocytes/PBT-Plus

137 mM NaCl

2.7 mM KCl

10 mM Na_2HPO_4

1.8 mM KH_2PO_4

0.2% (w/v) BSA (Sigma-Aldrich, A2153)

0.1% (v/v) Triton X-100 in 1×PBS.

Mix and sterilize through 0.22 μm filter. Store at 4°C.

For PBT-Plus, supplement PBT with:

2% (v/v) goat serum

2% (w/v) BSA (for a total of 2.2% BSA).

Mix and sterilize through a 0.22 μm filter. Store at 4°C.

Proteinase K Buffer for Xenopus oocytes

10 mM EDTA, pH 8.0

100 mM Tris-HCl, pH 7.5

For Proteinase K solution:

Add proteinase K to a final concentration of 50 μg/mL. Prepare fresh, do not re-use.

References

Aguero T, Newman, K and King, ML. 2018. Microinjection of *Xenopus* Oocytes. *Cold Spring Harb Protoc* doi:10.1101/pdb.prot096974.

Chang P, Torres J, Lewis RA, Mowry KL, Houliston E, King ML. 2004. Localization of RNAs to the mitochondrial cloud in *Xenopus* oocytes through entrapment and association with endoplasmic reticulum. *Mol Biol Cell* **15**: 4669–4681.

Dumont JN. 1972. Oogenesis in *Xenopus* laevis (Daudin). I. Stages of oocyte development in laboratory maintained animals. *J Morph* **136**: 153–179.

Houston DW. 2013. Regulation of cell polarity and RNA localization in vertebrate oocytes. *Int Rev Cell Mol Biol* **306**: 127–185.

Mowry KL, Melton DA. 1992. Vegetal messenger RNA localization directed by a 340-nt RNA sequence element in *Xenopus* oocytes. *Science* **255:** 991–994.

Newman K, Aguero T, King ML. 2018. Isolation of *Xenopus* Oocytes. *Cold Spring Harb Protoc* doi:10.1101/pdb.prot095851.

Yisraeli JK, Melton DA. 1988. The material mRNA Vg1 is correctly localized following injection into *Xenopus* oocytes. *Nature* **336**: 592–595.

Yoon YJ, Mowry KL. 2004. *Xenopus* Staufen is a component of a ribonucleoprotein complex containing Vg1 RNA and kinesin. *Development* **131**: 3035–3045.

Chapter 4: Discussion

The work presented in this thesis has, for the first time, introduced high-throughput characterization of the *vg1*-containing vegetal transport granules in the *Xenopus laevis* oocyte. While much prior work from the Mowry laboratory has focused on studying the mechanisms of vegetal RNA transport, the molecular nature of the RNP cargos was largely unknown. My thesis work broadens the study of vegetal transport granules, providing insight into the transport process and its potential mechanisms.

In Chapter 2, I introduced a multi-step biochemical process to specifically isolate vegetal transport granules. The isolation method presented here specifically utilizes stage II/III oocytes – a period when the vegetal transport granules are actively being transported and remodeled (Lewis and Mowry 2007). Light formaldehyde crosslinking of whole oocytes allowed us to capture potentially transient interactions and to prevent non-physiological re-associations (Mili and Steitz 2004). Prior studies that have attempted to capture vegetal RNPs have used slightly later stages III/IV (Huber and Zhao 2010; Bauermeister et al. 2015), at which time localization is near complete and relief of translational repression has begun (Tannahill and Melton 1989). In addition, our vegetal transport granule isolation technique is currently the most stringent developed in *Xenopus* oocytes, requiring not only a size-exclusion step to guarantee capture of large macromolecular RNPs, but also interaction with at least *two* previously identified *vg1* RNA binding proteins. Importantly, supporting specific isolation of vegetal transport granules, both of the *vg1* RNA binding proteins used are enriched in the vegetal hemisphere, colocalizing with *vg1*. hnRNPAB is almost exclusively

localized to the large *vg1* complexes (Chapter 2, Figure 2.1D), and Stau while more broadly distributed (Chapter 2, Figure 2.1F), has been shown to specifically bind only RNAs localizing to the vegetal (but not animal) hemisphere (Snedden et al. 2013).

Mass spectrometry performed on these isolated vegetal transport granules provides, for the first time, proteomic characterization of these structures. Most intriguingly, approximately two-thirds of the protein constituents were found to have roles in other cytoplasmic RNP granules, including stress granules, processing bodies, and neuronal granules (Chapter 2, Figure 2.5). We found that the remaining third of the identified proteins are unique to the *Xenopus* vegetal transport granules. We propose that the *Xenopus* vegetal transport granule is a new class of cytoplasmic granule, with hybrid characteristics from both somatic and germ cell granules.

The overlap of somatic granule features combined with the germ cell environment may provide insight into the conserved function of these proteins. Of the 86 proteins we have identified in the vegetal transport granule, several overlapping themes are intriguing. I argue that each identified protein within the transport granule has a role that falls into at least one of four major functional themes. Below, I will examine the proteome of these newly isolated and characterized vegetal transport granules, highlighting potential insights into their function.

Functional Themes of Vegetal Transport Granules

Through gene ontology analysis in combination with manual literature curation I have found that protein elements of the vegetal transport granule have a functional role in at least one of the four overarching categories: (1) Translational Control (2) Translocation and Mobility (3) Environmental Segregation / Potential Phase Separation (4) mRNA Stability and Remodeling. While these themes are not unique to vegetal transport granules, they do emphasize the tight spatial and temporal control in this particular granule.

Act I: Translational Control

Or – At the Right Place, Awaiting the Right Time

Translational Repression: A Unifying Feature

In this thesis, I have discussed five types of cytoplasmic RNP granules: (1) Stress Granules (2) Processing Bodies (3) Neuronal Transport Granules (4) Germinal Granules, and the newly introduced (5) Vegetal Transport Granule. Each granule type is distinct in morphology, constituents, subcellular location, duration, and function (Figure 4.1). At their simplest common denominator: each is cytoplasmically located consisting of RNA and RNA binding proteins, serving as a translationally silenced RNA warehouse.

It is perhaps not surprising, therefore, that more than 20% of the vegetal transport granule proteome includes proteins with a role in translational regulation, as determined by gene ontology analysis (Mi et al. 2017). To

understand the roles these might play specifically in the vegetal transport granules, we must first consider what is known about *vg1* translational repression.

Translational repression of vg1 mRNA during oogenesis

Maternally loaded *vg1* mRNA is expressed throughout oogenesis, first uniformly in stage I, restricted to the vegetal hemisphere in stages II and III, and ultimately tightly localized and anchored at the vegetal cortex at the end of stage III and into stage IV (Melton 1987). During localization in stages I-III, *vg1* remains translationally quiescent. It is not until stage IV that Vg1 protein is first synthesized, albeit in low levels (Tannahill and Melton 1989). Translation continues throughout oogenesis and into embryogenesis, until gastrulation. At gastrulation, *vg1* mRNA is degraded, while Vg1 protein remains relatively constant until neurulation, with protein levels declining through the tailbud stage (Rebagliati et al. 1985; Melton 1987; Birsoy et al. 2006). These results prompt an important question: *What changes that occur between stages III and IV of oogenesis that could trigger translational activation?* One striking alteration is the localization status of *vg1* mRNA (Chapter 1, Figure 1). During stages II and III *vg1* mRNA is actively localized. By stage III, a subpopulation of *vg1* mRNA is anchored at the vegetal cortex, but some RNA remains distributed throughout the vegetal hemisphere in a wedge-like distribution (Kloc and Etkin 1995). By stage IV, however, *vg1* mRNA is fully localized at the vegetal cortex (Melton 1987). During stage IV, *vg1* translation begins, producing low levels of Vg1 protein that increase throughout the remainder of oogenesis. The translated protein remains localized in the vegetal hemisphere, near the vegetal cortex (Tannahill and Melton

1989). Could vegetal transport granule remodeling at the vegetal cortex, post-localization, displace repressors, activating translation?

This remodeling theory makes three assumptions: (1) A translational repressor (or repressors) engages directly or indirectly with *vg1* mRNA to inhibit Vg1 protein synthesis. (2) Release of this repressor is coincident with the onset translational. (3) Remodeling of transport granules can occur at the cortex.

Repressors of vg1 *mRNA translation*

The 3′UTR of *vg1* mRNA contains the vegetal localization element, sufficient for proper vegetal localization (Mowry and Melton 1992). However, just downstream of the VLE is an AU-rich element known as vegetal translational control element or VTE (Otero et al. 2001). Crosslinking experiments have shown that six proteins specifically bind to the VTE in stage I-III oocytes, including Vera/Igf2bp3, Ybox2, Elavl1, Elavl2, p45, and p60 (Otero et al. 2001; Colegrove-Otero et al. 2005). Of the six, Vera/Igf2bp3, Ybox2, Elavl1, Elavl2, and p60 (which may represent PTB/VgRBP60) are all present in vegetal transport granules (Chapter 2, Figure 2.5). Of particular interest is Elavl2, which has an experimentally demonstrated role in *vg1* mRNA translational repression, as antibody interference experiments resulted in ectopic translation of *vg1* mRNA in stage III oocytes (Colegrove-Otero et al. 2005). In addition, Elavl2 fails to crosslink to VTE RNA after stage III of oogenesis (Otero et al. 2001).

Thus, at least one example of a translational repressor meets all requirements of our remodeling hypothesis. (1) Elavl2 directly binds the

translational control element of *vg1,* (2) Antibody interference of Elavl2 results in ectopic translation of Vg1 protein. (3) Loss of Elavl2 binding to the *vg1* translational control element in late stage oocytes suggests changes in intragranular associations and could potentially represent cortical remodeling.

Elavl2 acts in an RNA cap-dependent manner to regulate *vg1* mRNA translation (Otero et al. 2001; Colegrove-Otero et al. 2005). This is curious given that vegetal transport granules contain the decapping enzyme, Nudt16, and two enzymes known to interact with the decapping complex, Lsm1 and Lsm2 (Chapter 2, Figure 5). If either of these two enzymes is active during transport, it could cause premature *vg1* translation by disrupting the interaction with Elavl2. However, Nudt16, Lsm1, and Lsm2, may be inhibited during vegetal localization, perhaps similar to the inhibition of some decapping enzymes in processing-bodies (Eulalio et al. 2007; Horvathova et al. 2017), and become active at the cortex during stage IV. Although speculative, one possibility is that decapping by Nudt16 and the associated Lsm proteins disrupts the cap-dependent interaction of Elavl2 with the VTE (Devaux et al. 2006), displacing the translational repressor, leading to translation of Vg1 protein (Otero et al. 2001).

Another mode of translational regulation is through modulation of poly(A) tail length during oogenesis (Richter 1999). Results presented in Appendix A indicate that the vegetal transport granules are comprised of a heterogenous population of RNAs. Therefore, it is not surprising that poly(A)-dependent translational repressors are among those identified in the vegetal transport granules (Chapter 2, Figure 2.5). The classic translational repressor, CPEB1 may

also be controlled by spatial rearrangement at the cortex. Although CPEB1 has been shown to act as a repressor during oogenesis, it is also known to temporally switch to translational activation with poly(A)-lengthening (Richter 1999; Colegrove-Otero et al. 2005). Could temporally regulated poly(A)-lengthening be mediated by granule remodeling? The polyadenylation factor, CPSF2, which has been found to associate with CPEB1 during activation (Mendez et al. 2000), was also identified in our granules. Continuing with the stage IV remodeling hypothesis, CPSF2 may become active at the cortex in late stages, where it can induce poly(A) lengthening, resulting in translational activation of localized transcripts, potentially mediated by CPEB1.

Remodeling leading to repressor release and activation

As a final example of potential stage IV granule rearrangement, I present the case of Patl2. Pat1, the Patl2 homologue, was first characterized as a translational repressor in yeast (Coller and Parker 2005). In vertebrates, Patl2 has previously been shown to bind several components of the vegetal transport granule, including Ybox2, Lsm14a, EPAB, Lsm1, Zar1, PABPC, and CPEB (Nakamura et al. 2010; Ayache et al. 2015). Similar to its role in yeast, Patl2 has been shown to repress translation in *Xenopus* oocytes (Marnef et al. 2010). Patl2 protein is expressed during early oogenesis, but decreases after stage III, eventually becoming completely degraded in matured eggs (Nakamura et al. 2010). Interestingly, Patl2 maintains translational silencing capacity even in stage VI oocytes (if exogenously expressed), but only if mRNA is directly tethered to Patl2 (Nakamura et al. 2010). Within the vegetal transport granule, Patl2 may be

protected from degradation while it is actively repressing mRNA targets. However, in later stages of oogenesis and development, degradation of Patl2 could lead to translational derepression.

Translational efficiency: Streamlining protein synthesis

In addition to negative and positive regulators of translation in vegetal transport granules, we also found several tRNA modifying enzymes. The least surprising of these was C14orf166/Rtraf, which is a well-conserved protein in stress granules (Jain et al. 2016). As in stress granules, C14orf166 in our system is also found present with Ddx1, Fam98a/b, Rtcb, and ribosomal subunits (Pérez-González et al. 2014). Together, these elements are part of the tRNA splicing ligase unit. In cells containing stress granules, each member of the complex is in both the nucleus and within cytoplasmic stress granules. It has been suggested that the unit might serve as a nucleocytoplasmic shuttle, especially since cytoskeletal elements have been found associated with the complex (Pérez-González et al. 2014; Akter et al. 2017). Since tRNA splicing in *Xenopus* is limited to the nucleus (Großhans et al. 2000), the C14orf166 complex must either initially associate with vegetal transport granules leaving the nucleus, interacting with one of the core components, shuttle independently from the vegetal transport granules before localization, or some combination of both. Because the core components of the tRNA splicing ligase complex are identified both in stress granules and vegetal transport granules, it is possible that function is conserved between the two. Perhaps the role in translational repression hypothesized for the tRNA splicing complex in stress

granules is also conserved in vegetal transport granules (Pérez-González et al. 2014).

We identified three proteins unique to *Xenopus* vegetal transport granules and not found in other cytoplasmic granule types but fitting nicely with the idea of tRNA modulation. Two aminoacyl-tRNA synthetases, Iars (isoleucyl tRNA) and Kars (lysyl tRNA), were enriched in our vegetal transport granules, with other components including Dars (aspartyl tRNA), Eprs (glutamyl-prolyl tRNA) Farsb (phenylalanyl tRNA), Lars (leucyl tRNA), Qars (glutaminyl tRNA), and Rars (arginyl tRNA) identified in our mass spectrometry list, but not quite meeting our stringent threshold for enrichment (data not shown). Together these tRNA synthetases interact via the scaffold, Aimp1 to form a multisynthetase complex, which, has been implicated in increasing efficiency of protein biosynthesis (Kim et al. 2013). For instance, after interaction with the multisynthetase complex, aminoacyl-linked tRNAs might be able to directly interact with Ef1α associated ribosomes, and truly be queued for translational activation (Pang et al. 2014). Indeed, this model may apply in our system, where Eef1a2/Ef1α also associate with vegetal transport granules.

A streamlined system might operate in *Xenopus* oocytes with the C14orf166-Ddx1-Fam98a/b complex shuttling tRNAs to the vegetal transport granule, where they are transported together to the vegetal cortex. Concurrent expression of the multisynthetase unit could allow preparation of activated amino acids (Kim et al. 2013). Thus, for localized mRNAs in *Xenopus*, once translational repression is released in stage IV oocytes, protein synthesis has already been

primed. But why might this organization be present in the vegetal transport granules, but not other cytoplasmic granules? Unlike stress granules and processing bodies the vegetal transport granules is highly regulated both spatially and temporally. Translational activation may occur on a per-transcript timeline, with some proteins like Vg1 translated at stage IV, and others synthesized in later stages. As further support to a "poised-and-ready" model, several molecular chaperones were also identified in our vegetal transport granules. Two of these, Hspa8 and Cct6a, are also present in stress granules (Jain et al. 2016), and may help to efficiently fold proteins. Having translational factors poised for action presents an assembly line scenario, where proteins can be synthesized quickly in response to cellular and developmental cues.

Act II: Motility and Transportation

Or – All Aboard the Cytoskeletal Express!

Previous research from our laboratory has shown that *vg1* mRNA is transported in RNPs along microtubules, mediated by dynein and kinesin motors (Messitt et al. 2008; Gagnon et al. 2013). The presence of Kif3b, Dynll1, and Dynll2 in the vegetal transport granules confirmed our isolation of *bona-fide* transport RNPs.

We also identified the presence of additional cytoskeletal mediators. Unexpected in our results was Cltc/Chc or clathrin heavy chain, which has also been identified in neuronal transport granules (Elvira et al. 2006; Kanai et al.

2004). While conventional roles for Cltc have involved vesicle transport (Robinson 2015), research in *Drosophila* oocytes has suggested Cltc is critical for establishing microtubule polarity (Vazquez-Pianzola et al. 2014). In early stage *Drosophila* oocytes, Cltc is localized to the posterior cortex mediated by Bic-D. When a mutant form of Cltc is expressed, microtubule polarity is disrupted. The plus end of microtubules, normally located at the posterior cortex and marked by both kinesin and EB1, fails to show cortical accumulation. Intriguingly, of the clathrin vesicle related proteins in *Drosophila* oocytes, only Cltc affects the early localization and organization of microtubules (Vazquez-Pianzola et al. 2014).

Might Cltc play a similar role in the *Xenopus* oocyte? While most microtubules are oriented with the minus end directed towards the cortex, a sub-population of microtubules at the cortex are in the opposite orientation (Messitt et al. 2008). The opposing direction of these motors allows bidirectional transport with both dynein and kinesin (Gagnon et al. 2013). Perhaps Cltc helps maintain the organizations of both populations of microtubules in the vegetal hemisphere.

Another surprising protein identified in vegetal transport granules is Copa, a coatomer protein. Traditional roles for coatomer proteins involve association with the endoplasmic reticulum and Golgi (Nickel and Wieland 1998). One possibility is that in stage II oocytes, Copa interacts with remnants of the ER present from breakdown of the Balbiani body (Deshler et al. 1997; Chang et al. 2004), still present in the vegetal hemisphere. However, another, and possibly more attractive option, is that Copa is involved in a later stage of mRNA localization. Indeed, in yeast, coatomer proteins have been found to play a role in

anchoring RNA at the cortex, and copa proteins have greater binding affinity to areas of high curvature (Hermesh and Jansen 2013), perhaps increasing affinity to the vegetal cortex of *Xenopus* oocytes, though it should be noted that membrane curvature between yeast and *Xenopus* oocyte vegetal cortex vary by orders of magnitude.

Act III: Environmental Segregation / Potential for Phase Separation

Or – More than 'Just a Phase': The Case for Phase Separation

One of the recent 'hot-topics' in biology has been the increased research on liquid-liquid like phase separation properties mediated by low-complexity domains. By definition, cytoplasmic RNA granules are membraneless structures, yet distinct from their environment (Kaganovich 2017). The obvious question is how are these membraneless structures maintained?

Research within the past five years has shown that many RNA-binding proteins possess low complexity sequences in addition to their RNA binding domains. High concentrations of RNA binding proteins can lead to aggregation and phase transition into a more liquid-liquid or hydrogel-like state (Kato et al. 2012; Han et al. 2012).

From stress granules to germinal granules, liquid-like properties of these cytoplasmic bodies have been explored. Low complexity domains establishing phase separation engenders some unique dynamic properties to these bodies. First, they form distinct liquid-like structures detectable by DIC-microscopy.

Second, granules are able to interact with one another: fusing and splitting. Finally, FRAP studies have shown extremely mobile fractions within the granule (Shin and Brangwynne 2017). In some cases, such as stress granules, a mobile fraction may be present as a dynamic outer core, with a more stationary fraction representing the stable inner core (Jain et al. 2016)

In our system, we found that approximately 75% of vegetal transport granule components potentially contain a long (greater than 30 amino acids) intrinsically disordered region or low complexity domains (Chapter 2, Figure 2.6). This value is on par with that of mammalian stress granules where ~80% of features have the propensity to phase separate (Jain et al. 2016). However, recent (unpublished) work from our laboratory has begun to study the dynamic properties of the vegetal transport granules. Using FRAP in live oocytes we have shown that vegetal transport granules are more gel- or solid-like (E. Powrie, unpublished data). Unlike stress granules, p-bodies, and germ granules, FRAP on a localized RNA in the vegetal transport granules is extremely stable, while FRAP on some constituent proteins, such as mCherry-Stau and mCherry-Vera, shows high motility (E. Powrie, unpublished data).

It is possible, that RNAs in vegetal transport granules are locked in a stable core, perhaps associating tightly with hnRNPAB (which contains an LCD), during active transport. The RNA maintains a very stable structure even at the cortex where it is anchored. Perhaps a more dynamic outer shell, associated with RNA-binding proteins such as Stau or Vera, allows remodeling of additional protein

factors at the cortex, allowing for different interactions, and potentially altering the translational status of localized RNAs.

Act IV: RNA Remodeling and Stability

Or – Trading Spaces: A Remodeling Hypothesis

In the preceding sections, I've provided rationale for the inclusion of mRNA destabilizing elements within the mRNA transport granule. I've discussed proteins such as the decapping enzymes as influencing translational regulation. An alternative is that these elements have roles in mRNA decay. We also know that RNA anchoring is dependent on RNAs at the cortex. For instance, disruption of *xlsirts* or *vegT* causes release of *vg1* from the cortex (Kloc and Etkin 1994). Proteins like UPF1, for instance, might nonspecifically degrade RNA localized at the cortex, including those localized earlier such as *xlsirts* (Kloc et al. 1993; Heasman et al. 2001; Kloc et al. 2005). It is possible that remodeling could activate UPF1 or other mRNA destabilizing elements, which could release anchored RNA from the cortex, and initiate subsequent (or concurrent) translation.

But what mechanism could mediate remodeling? The vegetal transport granule is rich in ATP-dependent DEAD-box RNA helicases, including Ddx1, Ddx5, Dhx9, and Ddx3x. By unwinding duplexed RNA, the DDX enzymes could either directly disrupt interaction with bound proteins, or indirectly by temporarily relieving secondary structure (Linder and Jankowsky 2011; Kim and Myong 2016). The vegetal hemisphere is rich in mitochondria from the breakdown of the Balbiani

body in stage I oocytes. Though the activity of these mitochondria in stage II/III oocytes has not been investigated it is possible that they could provide a high concentration of ATP necessary for DDX-activation

Alternatively, the vegetal transport granules also contain enzymes that may affect post translational modifications: including the kinase, Skt33 and its receptor protein Strap, Padi2, Ppia, Parp1, or the dsRNA-activated kinase and translational repressor, Prkra. Post translational modification may provide be responsible for the switch between translation repression in stage III and activation in stage IV. This model has some precedence. Phosphorylation of Vera during oocyte maturation leads to its release from the vegetal cortex, coincident with that of *vg1* mRNA. The phosphorylation does not affect binding between Vera and *vg1,* perhaps explaining why both elements are released. Stau1, alternatively, also undergoes phosphorylation at maturation, but does not redistribute from the cortex (Git et al. 2009). Thus, it is possible that a subpopulation of RNA and protein can be cortically released after post translational modification.

A New Type of Granule

Vegetal transport granules represent a new type of cytoplasmic granule that shares features with other known granules, specifically stress granules, processing bodies, neuronal granules, and germ granules. Nearly 75% of the vegetal transport granule constituents are found in at least one other type of cytoplasmic granule (Chapter 2, Figure 2.5). A unique subset of proteins is also present. Some of these, like the translational repressors Zar1 and Zar2 are oocyte specific (Yamamoto et al.

2013; Charlesworth et al. 2012). However, the vegetal transport granule does not represent a germ granule. First, the hallmark germ granule proteins are absent, including Vasa/DDX4, Tudor domain proteins, and an abundance of WD-rich repeat proteins (Voronina et al. 2011). Second, known *Xenopus* germ granule RNAs, including *xcat2/nanos,* and *xlsirts*, are also absent. Finally, *Xenopus* germ granules are deposited at the cortex in stage I oocytes, where they accumulate in a central disc at the vegetal cortex. Conversely, high-resolution confocal images (C. Neil, unpublished data) show a de-enrichment of *vg1* mRNA and other vegetal transport granule components at this central disc region in *Xenopus* oocytes.

One Size Does Not Fit All

Functionally, however, the vegetal transport granule may be most similar to germ granules, though they share fewer common protein components (Figure 4.1). As with germ granules, vegetal transport granule RNAs involved in germ layer patterning must be stored long-term in the germ cell. Unlike most germ granules, however, vegetal transport granules are transported over relatively long distances. In *Xenopus* oocytes, which are up to 450 μm in diameter during stages II-III, vegetal transport granules must be transported from the nucleus to the vegetal cortex. This is reminiscent of the long-range distances traveled by neuronal granules. We therefore propose the vegetal transport granule as a novel type of cytoplasmic RNP granule with unique properties.

Xenopus vegetal transport granules are surprisingly large, between 5-10 μm during transit, and merging into much larger structures at the cortex (Chapter 2,

Figure 2.1). Other cytoplasmic granules range in size to about one-tenth of our vegetal transport granules. The large size of vegetal transport granules could be due to the overall large size of the *Xenopus* oocyte compared to *C. elegans*, human cell lines, and yeast cells in which other cytoplasmic granules are most commonly studied. One interesting observation from *C. elegans* P-granules is that the amount of mRNA within a granule increase substantially if oogenesis is arrested (Schisa et al. 2001). Perhaps the huge size of granules in *Xenopus* is merely a function of their overall oocyte size.

What's next for vegetal transport granules?

One of the complications studying cytoplasmic granules in other systems is the difficulty in successfully isolating large quantities of intact granules. Since thousands of oocytes can be harvested from a single *Xenopus* female, large scale isolation of vegetal transport granules is highly feasible. Although proteomic and transcriptomic characterization required immunoprecipitations for the final isolation, we have found that the granule fraction pool from size exclusion chromatography, can serve as an abundant source of *ex vivo* granules (C. Neil, S. Cabral, S. Jeschonek, unpublished data). Although the granule pool contains an impure collection of vegetal transport granules, specific vegetal transport granules can be identified when oocytes are micro-injected with fluorescently labeled VLE RNA.

Recent work in our laboratory has shown that these vegetal transport granules are experimentally malleable under a range of buffer conditions, and

recent work from other laboratories has suggested that isolated subsets of transport RNPs retain *in vivo* characteristics, such as the ability to interact with microtubules and transit via associated motors (McClintock et al. 2018). Studies of RNP granules using *in vitro* proxies, consisting of only a single purified protein, tend to dominate the literature. To study biophysical characteristics of cytoplasmic granules, oversimplified *in vitro* granules are often subjected to different conditions aimed to test molecular interactions. Varying salt concentration and observing "phase separation" reactions, can give an indication of ionic interactions, whereas chemicals like 1,6-hexanediol disrupt hydrophobic interactions. Though this type of *in vitro* work has been important in beginning to understand granule-intra-dynamics, it is difficult to conclude biological relevance for such oversimplified models. Studies of isolated vegetal transport granules provide an advantage in that they represent an intact granule, rather than an *in vitro* simplification. Such studies are critical, as biophysical properties, such as phase separation, have been implicated in several neurodegenerative diseases. Diseases related to RNA expansion, such as Huntington's, have been shown to phase separate into hydrogels. Likewise, many RNA binding proteins have been shown to aggregate and form polymers at high concentrations, resembling fibrils like those of Alzheimer's amyloid plaques. Perhaps, this newly defined cytoplasmic granule will one day serve as models to test such neurodegenerative diseases.

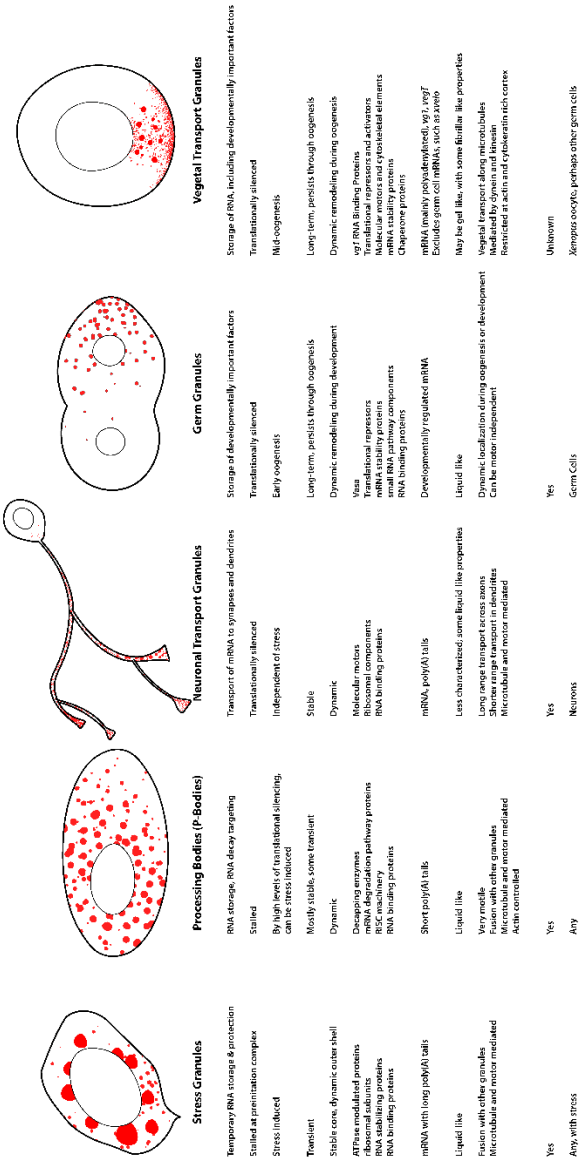

	Stress Granules	Processing Bodies (P-Bodies)	Neuronal Transport Granules	Germ Granules	Vegetal Transport Granules
Overall Function	Temporary RNA storage & protection	RNA storage, RNA decay targeting	Transport of mRNA to synapses and dendrites	Storage of developmentally important factors	Storage of RNA, including developmentally important factors
RNA Translational Status	Stalled at preinitiation complex	Stalled	Translationally silenced	Translationally silenced	Translationally silenced
Formation	Stress induced	By high levels of translational silencing, can be stress induced	Independent of stress	Early oogenesis	Mid-oogenesis
Overall Stability	Transient	Mostly stable, some transient	Stable	Long-term, persists through oogenesis	Long-term, persists through oogenesis
Molecular Stability	Stable core, dynamic outer shell	Dynamic	Dynamic	Dynamic remodeling during development	Dynamic remodeling during oogenesis
Hallmark Proteins and Reported Protein Classes	ATPase modulated proteins ribosomal subunits RNA stabilizing proteins RNA binding proteins	Decapping enzymes mRNA degradation pathway proteins RISC machinery RNA binding proteins	Molecular motors Ribosomal components RNA binding proteins	Vasa Translational repressors mRNA stability proteins small RNA pathway components RNA binding proteins	vg1 RNA Binding Proteins Translational repressors and activators Molecular motors and cytoskeletal elements mRNA stability proteins Chaperone proteins
RNA Properties	mRNA with long polyA tails	Short polyA tails	mRNA, polyA tails	Developmentally regulated mRNA	mRNA (mainly polyadenylated), vg1, vegT Excludes germ cell mRNAs, such as xvelo
Phase Properties	Liquid like	Liquid like	Less characterized; some liquid like properties	Liquid like	May be gel like, with some fibrillar like properties
Motility	Fusion with other granules Microtubule and motor mediated	Very motile Fusion with other granules Microtubule and motor mediated Actin controlled	Long range transport across axons Shortes range transport in dendrites Microtubule and motor mediated	Dynamic localization during oogenesis or development Can be motor independent	Vegetal transport along microtubules Mediated by dynein and kinesin Restricted at actin and cytokeratin rich cortex
Interaction with Other Granules	Yes	Yes	Yes	Yes	Unknown
Cell Type	Any, with stress	Any	Neurons	Germ Cells	*Xenopus* oocyte, perhaps other germ cells

Figure 4.1. ***Comparison of cytoplasmic granules.*** Five classes of cytoplasmic granules are compared: Stress granules, Processing bodies (p-bodies), Neuronal transport granules, Germ granules, and Vegetal Transport Granules.

References

Akter KA, Mansour MA, Hyodo T, Senga T. 2017. FAM98A associates with DDX1-C14orf166-FAM98B in a novel complex involved in colorectal cancer progression. *Int J Biochem Cell Biol* **84**: 1–13.

Ayache J, Bénard M, Ernoult-Lange M, Minshall N, Standart N, Kress M, Weil D. 2015. P-body assembly requires DDX6 repression complexes rather than decay or Ataxin2/2L complexes. *Mol Biol Cell* **26**: 1–30.

Bauermeister D, Claussen M, Pieler T. 2015. A novel role for Celf1 in vegetal RNA localization during *Xenopus* oogenesis. *Dev Biol* **405**: 214–224.

Birsoy B, Kofron M, Schaible K, Wylie C, Heasman J. 2006. Vg1 is an essential signaling molecule in *Xenopus* development. *Development* **133**: 15–20.

Chang P, Torres J, Lewis RA, Mowry KL, Houliston E, King M Lou, Marie P. 2004. Localization of RNAs to the mitochondrial cloud in *Xenopus* oocytes through entrapment and association with endoplasmic reticulum. *Mol Biol Cell* **15**: 4669–81.

Charlesworth A, Yamamoto TM, Cook JM, Silva KD, Kotter C V., Carter GS, Holt JW, Lavender HF, MacNicol AM, Ying Wang Y, et al. 2012. *Xenopus laevis* zygote arrest 2 (*zar2*) encodes a zinc finger RNA-binding protein that binds to the translational control sequence in the maternal *Wee1* mRNA and regulates translation. *Dev Biol* **369**: 177–190.

Colegrove-Otero LJ, Devaux A, Standart N. 2005. The *Xenopus* ELAV protein ElrB

represses *Vg1* mRNA translation during oogenesis. *Mol Cell Biol* **25**: 9028–39.

Coller J, Parker R. 2005. General translational repression by activators of mRNA decapping. *Cell* **122**: 875–86.

Deshler JO, Highett MI, Schnapp BJ. 1997. Localization of *Xenopus Vg1* mRNA by Vera protein and the endoplasmic reticulum. *Science* **276**: 1128–1131.

Devaux A, Colegrove-Otero LJ, Standart N. 2006. *Xenopus* ElrB, but not ElrA, binds RNA as an oligomer: Possible role of the linker. *FEBS Lett* **580**: 4947–4952.

Elvira G, Wasiak S, Blandford V, Tong XK, Serrano A, Fan X, del Rayo Sánchez-Carbente M, Servant F, Bell AW, Boismenu D, et al. 2006. Characterization of an RNA granule from developing brain. *Mol Cell Proteomics* **5**: 635–651.

Eulalio A, Behm-Ansmant I, Schweizer D, Izaurralde E. 2007. P-body formation is a consequence, not the cause, of RNA-mediated gene silencing. *Mol Cell Biol* **27**: 3970–81.

Gagnon JA, Kreiling JA, Powrie EA, Wood TR, Mowry KL. 2013. Directional transport is mediated by a Dynein-dependent step in an RNA localization pathway. *PLoS Biol* **11**: e1001551.

Git A, Allison R, Perdiguero E, Nebreda AR, Houliston E, Standart N. 2009. Vg1RBP phosphorylation by Erk2 MAP kinase correlates with the cortical release of *Vg1* mRNA during meiotic maturation of *Xenopus* oocytes. *RNA* **15**:

1121–33.

Großhans H, Simos G, Hurt E. 2000. Review: Transport of tRNA out of the nucleus - Direct channeling to the ribosome? *J Struct Biol* **129**: 288–294.

Han TW, Kato M, Xie S, Wu LC, Mirzaei H, Pei J, Chen M, Xie Y, Allen J, Xiao G, et al. 2012. Cell-free formation of RNA granules: Bound RNAs identify features and components of cellular assemblies. *Cell* **149**: 768–779.

Heasman J, Wessely O, Langland R, Craig EJ, Kessler DS. 2001. Vegetal localization of maternal mRNAs is disrupted by VegT depletion. *Dev Biol* **240**: 377–86.

Hermesh O, Jansen RP. 2013. Take the (RN)A-train: Localization of mRNA to the endoplasmic reticulum. *Biochim Biophys Acta - Mol Cell Res* **1833**: 2519–2525.

Horvathova I, Voigt F, Kotrys A V., Zhan Y, Artus-Revel CG, Eglinger J, Stadler MB, Giorgetti L, Chao JA. 2017. The dynamics of mRNA turnover revealed by single-molecule imaging in single cells. *Mol Cell* **68**: 615–625.e9.

Huber PW, Zhao WM. 2010. Detection of protein-RNA complexes in *Xenopus* oocytes. *Methods* **51**: 82–86.

Jain S, Wheeler JR, Walters RW, Agrawal A, Barsic A, Parker R. 2016. ATPase-modulated stress granules contain a diverse proteome and substructure. *Cell* **164**: 487–498.

Kaganovich D. 2017. There is an inclusion for that: Material properties of protein

granules provide a platform for building diverse cellular functions. *Trends Biochem Sci* **42**: 765–776.

Kanai Y, Dohmae N, Hirokawa N. 2004. Kinesin transports RNA: isolation and characterization of an RNA-transporting granule. *Neuron* **43**: 513–25.

Kato M, Han TW, Xie S, Shi K, Du X, Wu LC, Mirzaei H, Goldsmith EJ, Longgood J, Pei J, et al. 2012. Cell-free formation of RNA granules: Low complexity sequence domains form dynamic fibers within hydrogels. *Cell* **149**: 753–767.

Kim K, Park S-J, Na S, Kim JS, Choi H, Kim YK, Paek E, Lee C. 2013. Reinvestigation of aminoacyl-tRNA synthetase core complex by affinity purification-mass spectrometry reveals TARSL2 as a potential member of the complex. *PLoS One* **8**: e81734.

Kim Y, Myong S. 2016. RNA remodeling activity of DEAD box proteins tuned by protein concentration, RNA length, and ATP. *Mol Cell* **63**: 865–876.

Kloc M, Etkin LD. 1994. Delocalization of *Vg1* mRNA from the vegetal cortex in *Xenopus* oocytes after destruction of *Xlsirt* RNA. *Science* **265**: 1101–1103.

Kloc M, Etkin LD. 1995. Two distinct pathways for the localization of RNAs at the vegetal cortex in *Xenopus* oocytes. *Development* **121**: 287–97.

Kloc M, Spohr G, Etkin LD. 1993. Translocation of repetitive RNA sequences with the germ plasm in *Xenopus* oocytes. *Science* **262**: 1712–4.

Kloc M, Wilk K, Vargas D, Shirato Y, Bilinski S, Etkin LD. 2005. Potential structural role of non-coding and coding RNAs in the organization of the

cytoskeleton at the vegetal cortex of *Xenopus* oocytes. *Development* **132**: 3445–57.

Lewis RA, Mowry KL. 2007. Ribonucleoprotein remodeling during RNA localization. *Differentiation* **75**: 507–18.

Linder P, Jankowsky E. 2011. From unwinding to clamping - the DEAD box RNA helicase family. *Nat Rev Mol Cell Bio* **12**: 505–16.

Marnef A, Maldonado M, Bugaut A, Balasubramanian S, Kress M, Weil D, Standart N. 2010. Distinct functions of maternal and somatic Pat1 protein paralogs. *RNA* **16**: 2094–107.

McClintock MA, Dix CI, Johnson CM, McLaughlin SH, Maizels RJ, Hoang HT, Bullock SL. 2018. RNA-directed activation of cytoplasmic dynein-1 in reconstituted transport RNPs. *Elife* **7**.

Melton DA. 1987. Translocation of a localized maternal mRNA to the vegetal pole of *Xenopus* oocytes. *Nature* **328**: 80–2.

Mendez R, Murthy KG, Ryan K, Manley JL, Richter JD. 2000. Phosphorylation of CPEB by Eg2 mediates the recruitment of CPSF into an active cytoplasmic polyadenylation complex. *Mol Cell* **6**: 1253–9.

Messitt TJ, Gagnon JA, Kreiling JA, Pratt CA, Yoon YJ, Mowry KL. 2008. Multiple kinesin motors coordinate cytoplasmic RNA transport on a subpopulation of microtubules in *Xenopus* oocytes. *Dev Cell* **15**: 426–436.

Mi H, Huang X, Muruganujan A, Tang H, Mills C, Kang D, Thomas PD. 2017.

PANTHER version 11: expanded annotation data from Gene Ontology and Reactome pathways, and data analysis tool enhancements. *Nucleic Acids Res* **45**: D183–D189.

Mili S, Steitz JA. 2004. Evidence for reassociation of RNA-binding proteins after cell lysis: implications for the interpretation of immunoprecipitation analyses. *RNA* **10**: 1692–4.

Mowry KL, Melton DA. 1992. Vegetal messenger RNA localization directed by a 340-nt RNA sequence element in *Xenopus* oocytes. *Science* **255**: 991–4.

Nakamura Y, Tanaka KJ, Miyauchi M, Huang L, Tsujimoto M, Matsumoto K. 2010. Translational repression by the oocyte-specific protein P100 in *Xenopus*. *Dev Biol* **344**: 272–283.

Nickel W, Wieland FT. 1998. Biosynthetic protein transport through the early secretory pathway. *Histochem Cell Biol* **109**: 477–86.

Otero LJ, Devaux A, Standart N. 2001. A 250-nucleotide UA-rich element in the 3' untranslated region of *Xenopus laevis Vg1* mRNA represses translation both *in vivo* and *in vitro*. *RNA* **7**: 1753–67.

Pang YLJ, Poruri K, Martinis SA. 2014. tRNA synthetase: tRNA aminoacylation and beyond. *Wiley Interdiscip Rev RNA* **5**: 461–480.

Pérez-González A, Pazo A, Navajas R, Ciordia S, Rodriguez-Frandsen A, Nieto A. 2014. hCLE/C14orf166 associates with DDX1-HSPC117-FAM98B in a novel transcription-dependent shuttling RNA-transporting complex. *PLoS One* **9**:

e90957.

Rebagliati MR, Weeks DL, Harvey RP, Melton DA. 1985. Identification and cloning of localized maternal RNAs from *Xenopus* eggs. *Cell* **42**: 769–777.

Richter JD. 1999. Cytoplasmic polyadenylation in development and beyond. *Microbiol Mol Biol Rev* **63**: 446–56.

Robinson MS. 2015. Forty years of clathrin-coated vesicles. *Traffic* **16**: 1210–1238.

Schisa JA, Pitt JN, Priess JR. 2001. Analysis of RNA associated with P granules in germ cells of *C. elegans* adults. *Development* **128**: 1287–98.

Shin Y, Brangwynne CP. 2017. Liquid phase condensation in cell physiology and disease. *Science* **357**: eaaf4382.

Snedden DD, Bertke MM, Vernon D, Huber PW. 2013. RNA localization in *Xenopus* oocytes uses a core group of trans-acting factors irrespective of destination. *RNA* **19**: 889–895.

Tannahill D, Melton D a. 1989. Localized synthesis of the Vg1 protein during early *Xenopus* development. *Development* **106**: 775–85.

Vazquez-Pianzola P, Adam J, Haldemann D, Hain D, Urlaub H, Suter B. 2014. Clathrin heavy chain plays multiple roles in polarizing the *Drosophila* oocyte downstream of Bic-D. *Development* **141**: 1915–26.

Voronina E, Seydoux G, Sassone-Corsi P, Nagamori I. 2011. RNA granules in germ cells. *Cold Spring Harb Perspect Biol* **3**: a002774.

Yamamoto TM, Cook JM, Kotter C V., Khat T, Silva KD, Ferreyros M, Holt JW, Knight JD, Charlesworth A. 2013. Zar1 represses translation in *Xenopus* oocytes and binds to the TCS in maternal mRNAs with different characteristics than Zar2. *Biochim Biophys Acta - Gene Regul Mech* **1829**: 1034–1046.

Appendix A: The Vegetal Transport Granule Transcriptome

In Chapter 2, we determined the proteome of *vg1*-containing, vegetal transport granules. To date, however, the only known RNA component of these vegetal transport granules is *vg1*. We sought to determine if vegetal transport granules also contained a heterotypic population of mRNA. *VegT*, like *vg1*, is a germ layer determinant in *Xenopus* oocytes, and is known to vegetally localize in stage II oocytes (Zhang et al. 1998; Kwon et al. 2002). To determine if *vegT* is cotransported with *vg1* in vegetal transport granules we first performed FISH (Figure A.1.A-B). We find that *vg1* and *vegT* colocalize in large RNPs. To test whether the vegetal transport granules indiscriminately incorporate mRNA, we performed FISH with the non-localizing RNA, *gapdh* (Fig A.1.C-D). We find that *gapdh* is uniformly expressed throughout the cytoplasm. At higher magnification, we note that *gapdh* lacks specific accumulation in the vegetal transport granules. Although *gapdh* is not specifically excluded from the granules, it is equally distributed throughout the oocyte. We conclude that vegetal transport granules are selectively comprised of at least two mRNAs.

Given that our vegetal transport granules exhibited some RNA selectivity, enriching for the two-germ line determinants, *vg1* and *vegT*, but not *gapdh*, we decided to more thoroughly investigate the RNA population. To that end, we preformed ribodepletion, paired-end, RNA-seq, on isolated vegetal transport granules (Chapter 2).

Most ribodepletion kits are based on sequence specific capture of rRNA. Although no commercial kit yet officially supports *Xenopus laevis*, we opted for ribodepletion rather than poly(A) enrichment of samples. We were concerned that

the variable poly(A) tail length during oogenesis might bias results (Richter 1999). However, we do note that there are novel techniques, such as mRNA cap-capture (Blower et al. 2013), that provide an alternative. To determine the most effective commercial ribodepletion kit, we tested in tandem three available products: Illumina RiboZero, NEBNext Ribodepletion, and Lexogen RiboCop rRNA Depletion Kit. We probed Total RNA (non-treated) RNA as a control, and normalized samples with *luciferase* (as described in Chapter 2). We found, consistent with previous literature (Peshkin et al. 2015; Session et al. 2016), that Illumina RiboZero was the most effective at removing 28S, 18S, and 5S rRNA while leaving non ribosomal RNA, i.e.: *vg1* mRNA was unaffected (Figure A.2).

In terms of probing RNA and protein interactions, RNA-Immunoprecipitation followed by RNA-seq (RIP-seq) is a rarely used method. Most published techniques focus on mapping the direct binding sites between RNA and protein, requiring crosslinking of RNA and protein, followed by RNase digestion. Since we were more interested the general population of RNAs, we opted to use RIP-seq. RIP-seq is a challenging protocol, partially because it is not widely utilized, and there is not yet a "gold-standard" for an analysis pipeline. We analyzed our read data by several different methods in order to choose the most appropriate method for our data. We used statistically significant enrichment of *vg1* over a negative control and exclusion of the nonlocalizing *gapdh*, as a marker for success. Further, as in Chapter 2, we preformed three RNA-binding protein IPs (Vera, Stau1, hnRNPAB). Thus, our requirements had to be fulfilled in at least two of the IPs.

Evaluation began at the mapping stage (Figure A.3). We mapped our pre-processed reads to both the *Xenopus laevis* 9.2 transcriptome and the 9.2 genome. We found that the best downstream analysis software, by our standards, required genome alignment. We tested 6 mappers including HISAT2 (Kim et al. 2015), Bowtie2 (Langmead and Salzberg 2012), BBMAP (Bushnell 2014), BWA (Li and Durbin 2009), and STAR (Dobin et al. 2013). In all cases, STAR and BWA identified the highest percentage of aligned reads, in agreement with previous benchmarking literature (Kwon 2015) though we note that the default STAR parameters required adjusting to account for a larger vertebrate genome. We removed PCR duplicates using Piccard tools (Broad Institute) and multimapping reads with a custom python script provided by Taejoon Kwon (Kwon 2015), but found this step did not provide a significant improvement. Using the STAR mapped reads, we trailed two different methods of quantification. To test raw count programs, we tested RSEM (Li and Dewey 2011), eXpress (Roberts et al. 2011), and HTseq (Anders et al. 2015). We found HTseq outperformed the others. We also tried two ultra-fast pseudoaligners (which did not require mapping), including Salmon (Patro et al. 2015) and the related Kallisto. Finally, we used several peak-calling programs, generally designed for ChIP-seq experiments. Of the peak callers, Homer (Heinz et al. 2010) performed the best. RIPseeker (Li et al. 2013) and ASpeak (Kucukural et al. 2013), although more specifically designed for RIP-seq analysis provided little user support and had too high a computational resource requirement. For differential expression analysis, we ultimately used counts generated by HTseq.

The final step of RIP-seq analysis is differential expression. We tried several programs, all which differ based on assumptions and normalization techniques. For the pseudoaligners, Salmon (Patro et al. 2015) and Kallisto (Bray et al. 2016), we followed with the Sleuth (Bray et al. 2016) differential expression package. For HISAT2, we used the StringTie package (Pertea et al. 2016). For all other variations of the pipeline, we used either DESeq2 (Love et al. 2016) or edgeR (Robinson et al. 2010). We found that edgeR provided the most consistent results as compared to our experimental data (*vg1* mRNA enrichment by qRT-PCR and FISH, see Chapter 2). One complication with RIP-seq is the different library sizes between negative controls and experimental samples. To this end, we compared two different controls: an IgG-IP and an input control. The two behaved similarly, and we used IgG as our negative control.

To maintain consistency with the methods for proteomic analysis (Chapter 2), we compared the following IPs: Stau1, hnRNPAB, and IgG (Fig A.4). Each IP was performed in biological quadruplicate. Post-processing library sizes between Stau1 and hnRNPAB were consistent and between 8-10 million reads. As expected, the library sizes for IgG were significantly lower (Fig A.4A). Multidimensional analysis (Fig A.4B) indicates minimal batch effect. IPs of the same type are more closely correlated than IPs from the same biological replicate. Mean difference analysis (Fig A.4C) indicates that composition bias between samples was removed, with only a small subset of genes showing differential expression between samples.

To determine RNAs included in our vegetal transport granules, we considered only those transcripts enriched in both Stau1 (Figure A.4A) and

hnRNPAB RIP-IPs (Figure A.4B), at least 1.5-fold over IgG and with a significance of $p < 0.05$ (Figure A.4C). We found 256 transcripts significantly enriched in our vegetal transport granules, including *vg1* mRNA, (Fig A.4C) and 446 transcripts significantly de-enriched, including *gapdh* mRNA. However, as *vegT* mRNA did not meet our requirements for inclusion, we note that this list is not exhaustive. Over enrichment analysis of GO terms (Fig A.5), compared to the *Xenopus tropicalis* transcriptome, indicated the greatest enrichment in RNAs involved in post-transcriptional silencing, supported by the inclusion of *ago1, ago3,* and *ago4*, in our vegetal transport granules. We also found several regulatory RNAs in our transcriptome list, with protein tyrosine kinases most overrepresented (Figure A.5). The full list of enriched is shown in Figure A.6.

We next decide to examine motif enrichment, using the MEME online-suite (in particular DREME) on our enriched transcripts (Figure A.7)(Bailey 2011). We find that fives motifs are overrepresented. We find that 211/256 transcripts contained a poly(A) motif, suggesting that our vegetal transcript granules consist primarily of mRNA, given that sequences were not trimmed of poly(A) tails prior to analysis. We were intrigued to find enrichment of a CAGCAG motif. CAG expansions are found in a number of neurodegenerative diseases, including Huntington's disease, spinocerebellar ataxias, and mental retardation (Nalavade et al. 2013).

The preliminary RIP-seq data here introduces the transcriptome of vegetal transport granules, confirming that they are heterotypic collections of both RNA and protein.

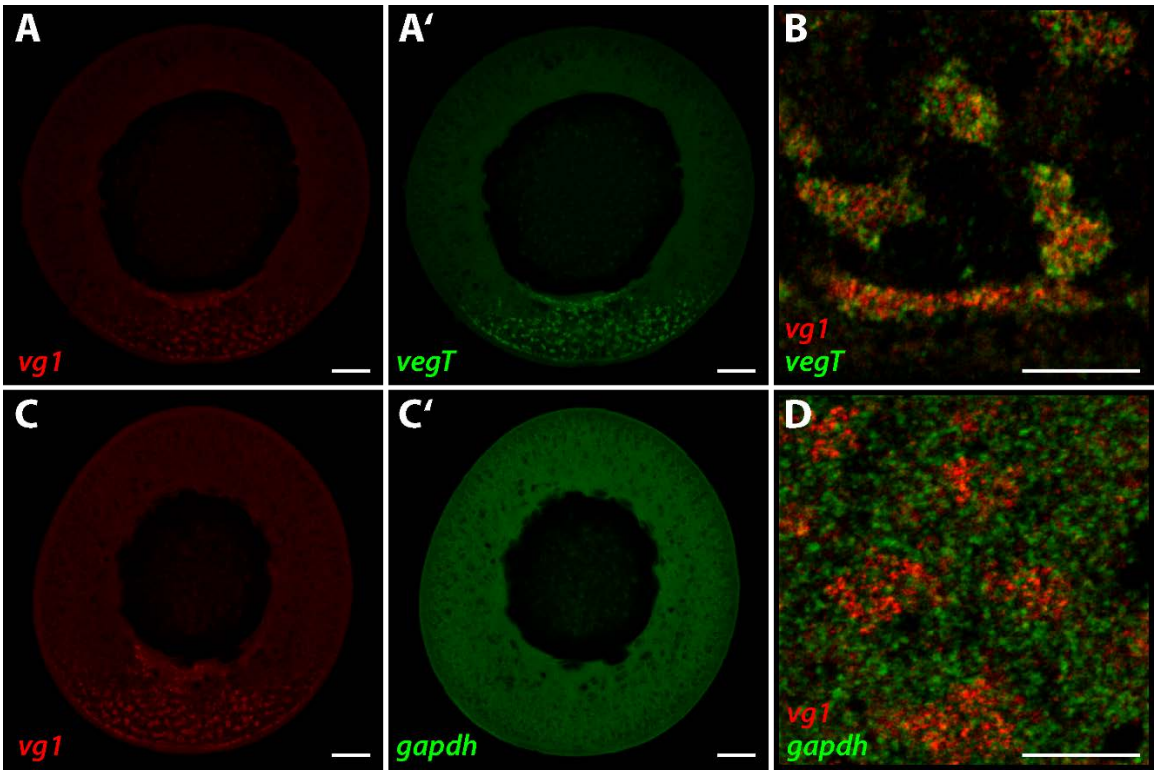

Figure A.1. ***Vegetal transport granules contain heterotypic populations of mRNA.*** (A) A cryosection of stage II oocyte probed by FISH for *vg1* (red) and *vegT* (green). (B) Higher magnification view of vegetal transport granules. (C) A cryosection of stage II oocytes probed by FISH for *vg1* (red) and *gapdh* (green). (D) Higher magnification view of vegetal transport granules. Scale bars in (A) and (C) = 50 μm. Scale bars in (B) and (D) = 10 μm.

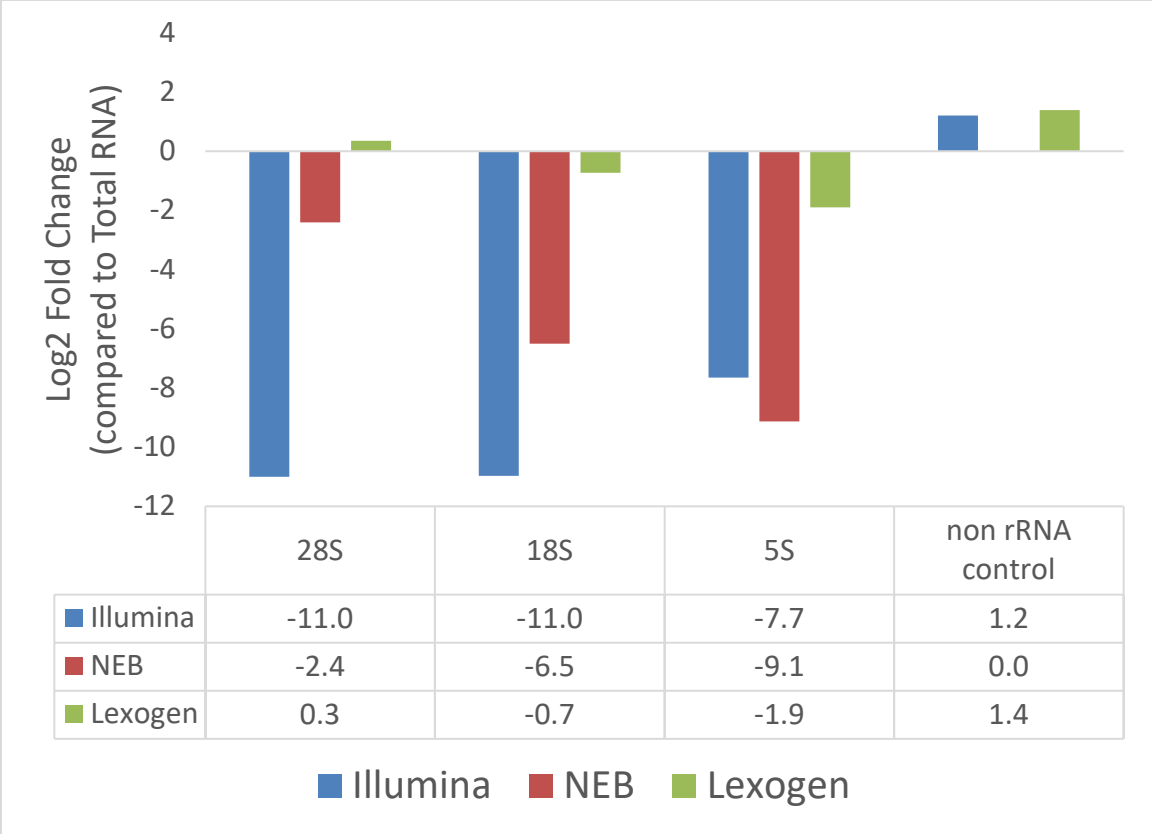

Figure A.2. ***Illumina RiboZero most effectively depletes rRNA from Xenopus laevis oocytes.*** qRT-PCR results of commercial kit comparison of rRNA depletion methods. Three rRNAs were probed: *28S*, *18S*, and *5S*. *Vg1* served a control. Log2 fold enrichment is expressed relative to total RNA and normalized to *luciferase*.

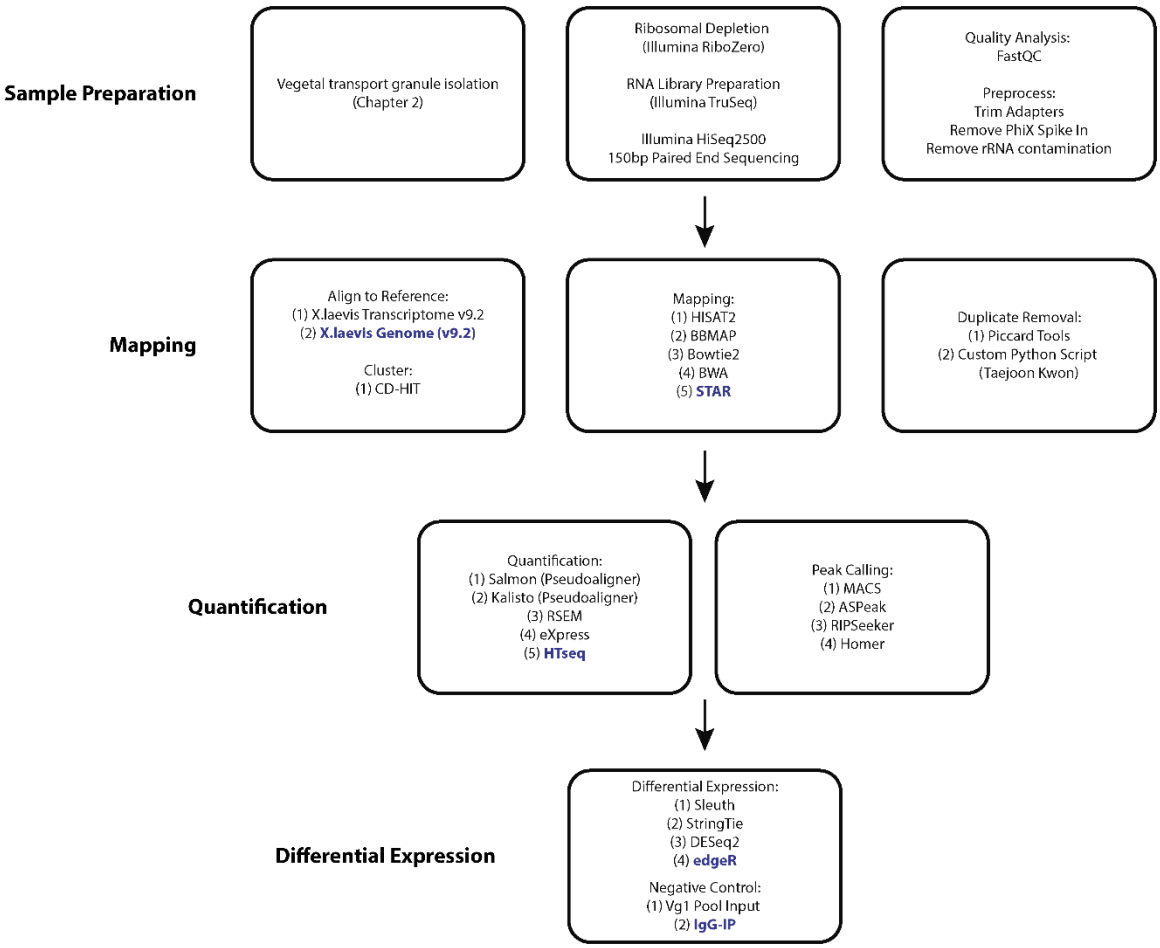

Figure A.3. ***Schematic of RIP-seq Analysis Pipeline.*** As described in the text, different programs for Mapping, Quantification, and Differential Expression, of aligned RIP-seq data were tested. Purple text indicates the final analysis choice.

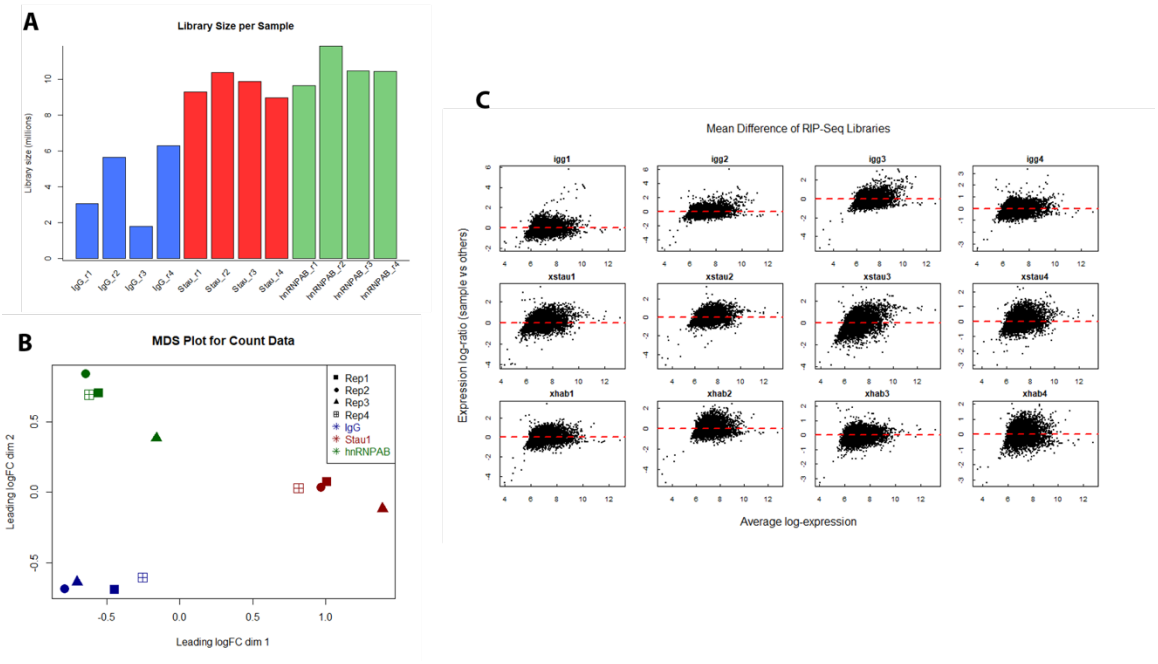

Figure A.4. ***RIP Seq Library Details.*** **(A)** Library size in millions of reads for each replicate of each RIP-seq library. Blue = IgG, red = Stau1; green = hnRNPAB. **(B)** Multidimensional scaling plot for count data. Different shapes represent different replicates. Different colors represent different RIP-seq libraries. Blue = IgG, red = Stau1, green = hnRNPAB. **(C)** Mean Difference of RIP-seq libraries. Count data is compared per sample against all other samples. Dotted red line indicates log2(0), or no difference in expression. Top row = IgG replicates. Center row = Stau1 replicates. Bottom row = hnRNPAB replicates.

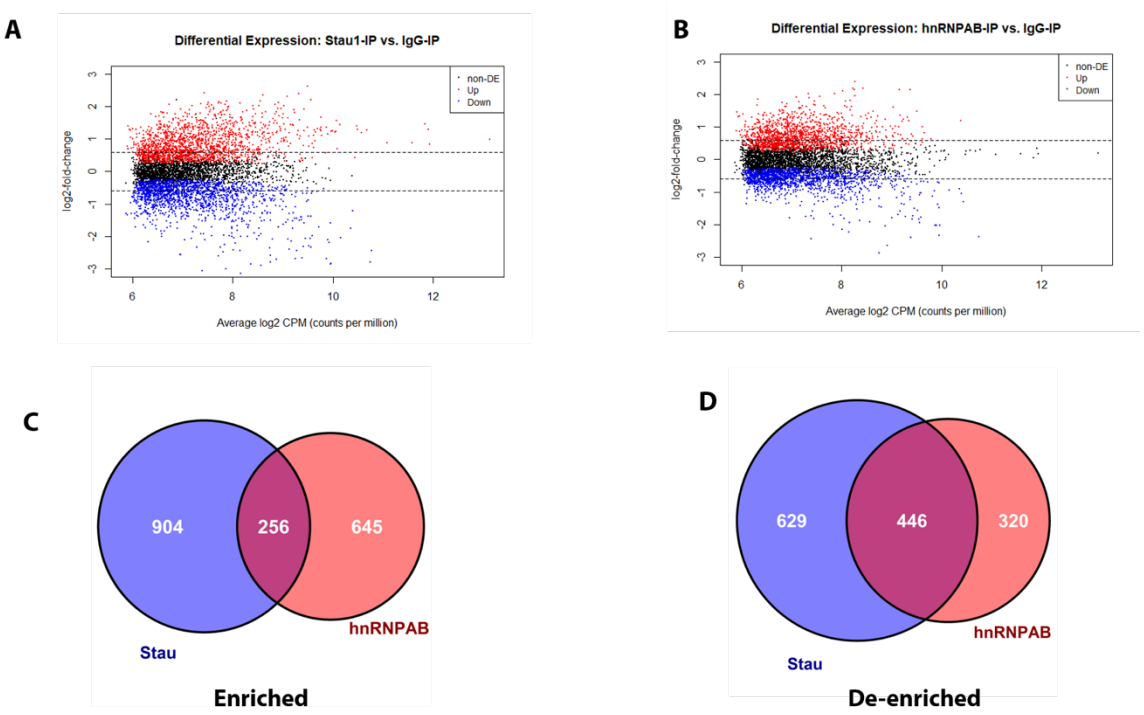

Figure A.5. ***The vegetal transport granule is enriched in over 250 transcripts.*** **(A, B)** Differentially expressed transcripts in Stau1 **(A)** and hnRNPAB **(B)** RIPs. Red dots are significantly enriched, p<0.05 and blue dots are significantly de-enriched p<0.05. Dotted lines indicate a 1.5-fold change compared to IgG. **(C)** Overlap of statistically enriched **(C)** or de-enriched **(D)** genes compared to IgG. Constituents of the vegetal transport granule are based on inclusion in both Stau and hnRNPAB. The vegetal transport granule consists of 256 transcripts at least 1.5 -enriched over IgG at p<0.05 significance. **(D)** Over 400 transcripts are found significantly de-enriched at least 1.5-fold, p<0.05 compared to IgG.

acvr1b
adam10
adarb1
adpgk
adrbk2
agbl5
ago1
ago3
ago4
ahr1a
akt2
aldh5a1
alt2
ankrd12
ankrd13c
ankrd52
arc2
arf1
arf6
arg-a
arid3b
arl6ip6
armc9
arrdc1
atf1
atf2
atf7
atxn1l
bach1
baiap2
bak1
bax
bmpr1a
btbd7
bub3
c1galt1
cbx2
cckar
ccnt1
cd151
cenpn
chic2
chpt1
chst7
cnep1r1
cnot6l
cpeb3

cpeb4
crtc3
csnk1d
ctcf
dcun1d3
ddx39b
depdc1b
dnajb1
dpf2
dr1
dusp11
dusp4
dyrk1a
dyrk3
eomes
epb41l4b
ergic1
esyt2
ets1
fam122b
fam126b
fam20b
fam219b
fam46b
fam83f
fam89a
fam98b
fbxo45
fnip1
foxn2
foxo3
fzd1
gabpb2
gdf1
glce
gls
gna11
gna13
gnal
goalpha
gpatch2
gpc4
grk6-like
gucd1
hbegf
hgsnat
hipk1

homez
hook2
hsd17b7
igfbp5
ikzf4
ing4
inpp4a
insr
ipmk
irf2bp2
jmy
jund
kazn
kbtbd7
kiaa1328
klf15
klhl15
klhl8
limk2
lin28b
lix1l
cnnm2
lrch3
lrp8
lsr
lxr2
man1a1
mast3
mau2
mbp
mctp2
meaf6
mfsd13a
MGC115708
MGC81399
MGC84433
mief1
mier3
mtm1
mtss1
mxd1
mxd3
nadk
nampt
napepld
ncoa7
prc1

prkci
psap
nfia
nox1
nt5c1a
nucb1
nxf1
orphan2
osbpl8
pan3
papss1
pard6b
pcsk5
pcsk7
pdpk1
pex14
pid1
pim3
pip4k2c
pla2g6
plpp6
plscr1
ppm1h
ptpn21
qki
rab4b
rac1
rad21
rap2c
rbm15
rbpj
rnf128
rp2
samd13
scyl2
sdf4
sepn1
sertad2
sgms1
sgpp1
slc25a30
slc25a37
slc35f2
slc4a7
slc4a8
aslc9a8
smap1

snrk
snx3
sorbs1
sorl1
spryd3
stam
stk17a
stxbp2
suox
synrg
tbc1d17
tbcel
tcf19
tead1
tecpr1
tfeb
tmem189
tnfs11
tnfsf11
tns3
tob2
trim36
tsc22d2
ttl
tulp3
ubtd1
unc119b
vsig10
wdr5
xarp-like
Xelaev18012 317m
Xelaev18029 654m
Xetrov9002 0135m
yap1
zbtb33
zbtb34
zbtb45
zbtb5
zcchc14
zdhhc21
zdhhc9
zfx
znf362
znf395
znf852

Figure A.6. ***RNA transcripts enriched in RNP transport granules.*** More than 200 transcripts enriched in RNP transport granules; 236 transcripts are listed, the remaining 20 transcripts were manually curated as duplicates and removed from this final list.

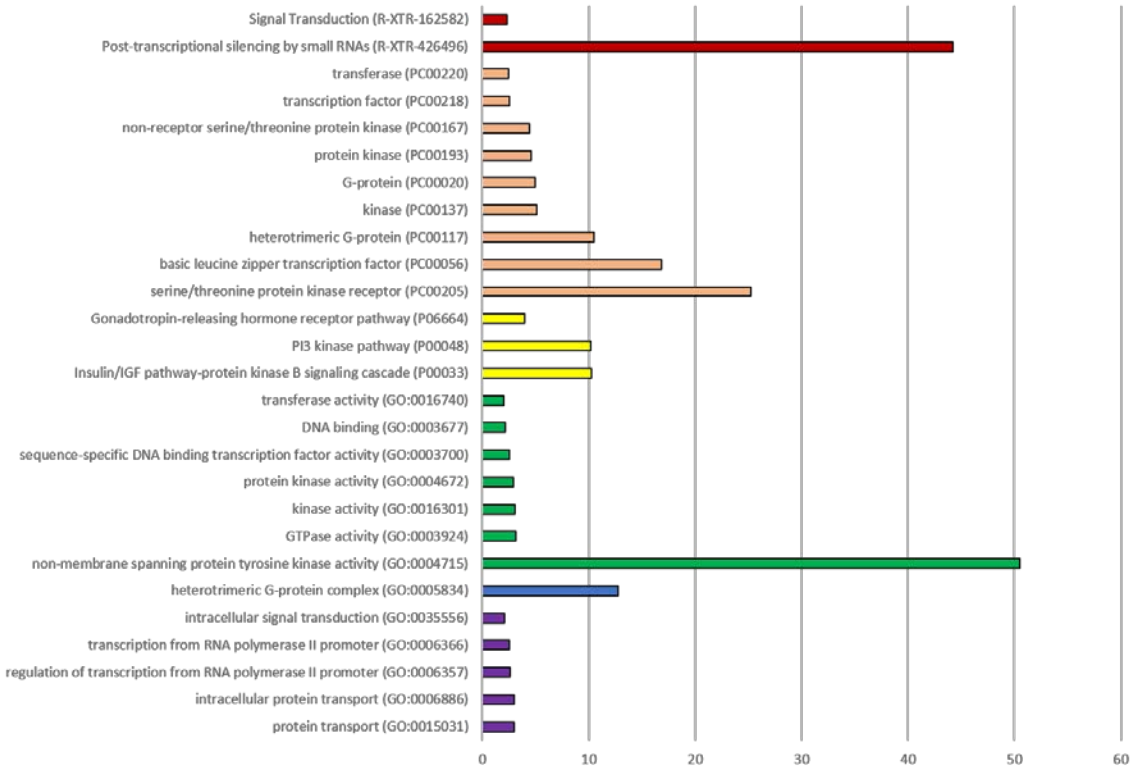

Figure A.7. ***Gene ontology over-enrichment analysis if vegetal transport granule transcripts.*** Gene ontology over enrichment was determined using PANTHER (Thomas et al. 2003; Mi et al. 2017). Fold change compared to the enrichment in the *Xenopus tropicalis* transcriptome is shown. Red bars = PANTHER Reactome category. Orange bars = PANTHER Protein type category. Yellow bars = Pathway category. Green = Molecular Function category. Blue = Cellular Compartment category. Purple = Biological process category. All bars are $p < 0.05$.

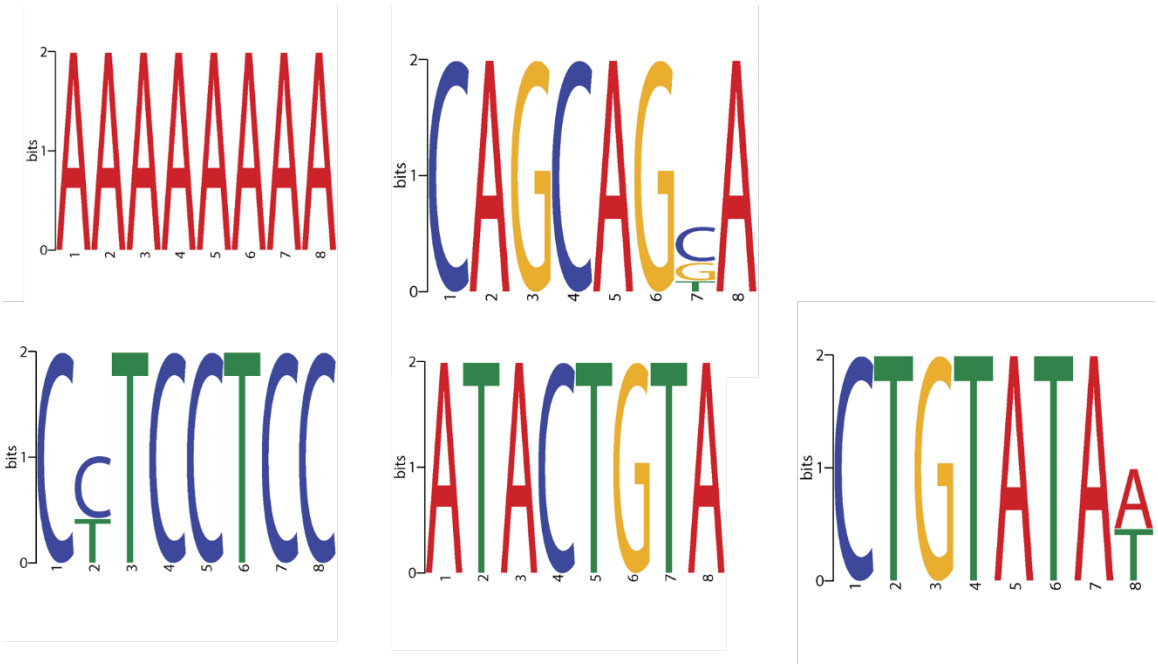

Figure A.8. ***Enriched motifs of vegetal transport granule transcripts.*** DREME (Bailey 2011) was used to determine enriched motifs, and identified five enriched motifs.

References

Anders S, Pyl PT, Huber W. 2015. HTSeq-A Python framework to work with high-throughput sequencing data. *Bioinformatics*.

Bailey TL. 2011. DREME: motif discovery in transcription factor ChIP-seq data. *Bioinformatics* **27**: 1653–1659.

Blower MD, Jambhekar A, Schwarz DS, Toombs JA. 2013. Combining different mRNA capture methods to analyze the transcriptome: Analysis of the *Xenopus laevis* transcriptome. *PLoS One* **8**: 1–15.

Bray NL, Pimentel H, Melsted P, Pachter L. 2016. Near-optimal probabilistic RNA-seq quantification. *Nat Biotechnol* **34**: 525–527.

Bushnell B. 2014. *BBMap short read aligner*. https://jgi.doe.gov/data-and-tools/bbtools/

Dobin A, Davis CA, Schlesinger F, Drenkow J, Zaleski C, Jha S, Batut P, Chaisson M, Gingeras TR. 2013. STAR: Ultrafast universal RNA-seq aligner. *Bioinformatics* **29**: 15–21.

Heinz S, Benner C, Spann N, Bertolino E, Lin YC, Laslo P, Cheng JX, Murre C, Singh H, Glass CK. 2010. Simple combinations of lineage-determining transcription factors prime *cis*-regulatory elements required for macrophage and B cell identities. *Mol Cell*.

Kim D, Langmead B, Salzberg SL. 2015. HISAT: a fast spliced aligner with low

memory requirements. *Nat Methods* **12**: 357–360.

Kucukural A, Özadam H, Singh G, Moore MJ, Cenik C. 2013. ASPeak: An abundance sensitive peak detection algorithm for RIP-Seq. *Bioinformatics* **29**: 2485–2486.

Kwon S, Abramson T, Munro TP, John CM, Köhrmann M, Schnapp BJ. 2002. UUCAC- and Vera-dependent localization of VegT RNA in *Xenopus* oocytes. *Curr Biol* **12**: 558–564.

Kwon T. 2015. Benchmarking transcriptome quantification methods for duplicated genes in *Xenopus laevis*. *Cytogenet Genome Res* **145**: 253–264.

Langmead B, Salzberg SL. 2012. Fast gapped-read alignment with Bowtie 2. *Nat Methods* **9**: 357–359.

Li B, Dewey CN. 2011. RSEM: accurate transcript quantification from RNA-Seq data with or without a reference genome. *BMC Bioinformatics* **12**: 323.

Li H, Durbin R. 2009. Fast and accurate short read alignment with Burrows-Wheeler transform. *Bioinformatics* **25**: 1754–60.

Li Y, Zhao DY, Greenblatt JF, Zhang Z. 2013. RIPSeeker: A statistical package for identifying protein-associated transcripts from RIP-seq experiments. *Nucleic Acids Res* **41**: 1–18.

Love MI, Anders S, Huber W. 2016. Differential analysis of count data – the DESeq2 package. *Vignettes* 1–62.

Mi H, Huang X, Muruganujan A, Tang H, Mills C, Kang D, Thomas PD. 2017. PANTHER version 11: expanded annotation data from Gene Ontology and Reactome pathways, and data analysis tool enhancements. *Nucleic Acids Res* **45**: D183–D189.

Nalavade R, Griesche N, Ryan DP, Hildebrand S, Krauss S. 2013. Mechanisms of RNA-induced toxicity in CAG repeat disorders. *Cell Death Dis* **4**: e752.

Patro R, Duggal G, Kingsford C. 2015. Salmon: Accurate, versatile and ultrafast quantification from RNA-seq data using lightweight-alignment. *bioRxiv* 021592.

Pertea M, Kim D, Pertea GM, Leek JT, Salzberg SL. 2016. Transcript-level expression analysis of RNA-seq experiments with HISAT, StringTie and Ballgown. *Nat Protoc.*

Peshkin L, Wühr M, Pearl E, Haas W, Freeman RM, Gerhart JC, Klein AM, Horb M, Gygi SP, Kirschner MW, et al. 2015. On the relationship of protein and mRNA dynamics in vertebrate embryonic development. *Dev Cell* **35**: 383–394.

Richter JD. 1999. Cytoplasmic polyadenylation in development and beyond. *Microbiol Mol Biol Rev* **63**: 446–56.

Roberts A, Trapnell C, Donaghey J, Rinn JL, Pachter L. 2011. Improving RNA-Seq expression estimates by correcting for fragment bias. *Genome Biol.*

Robinson MD, McCarthy DJ, Smyth GK. 2010. edgeR: a Bioconductor package for

differential expression analysis of digital gene expression data. *Bioinformatics* **26**: 139-40.

Session AM, Uno Y, Kwon T, Chapman JA, Toyoda A, Takahashi S, Fukui A, Hikosaka A, Suzuki A, Kondo M, et al. 2016. Genome evolution in the allotetraploid frog *Xenopus laevis*. *Nature* **538**: 336–343.

Thomas PD, Campbell MJ, Kejariwal A, Mi H, Karlak B, Daverman R, Diemer K, Muruganujan A, Narechania A. 2003. PANTHER: A library of protein families and subfamilies indexed by function. *Genome Res*.

Zhang J, Houston DW, King ML, Payne C, Wylie C, Heasman J. 1998. The role of maternal VegT in establishing the primary germ layers in *Xenopus* embryos. *Cell* **94**: 515–24.

Appendix B: The Case of Prrp: Approaches to Study RNA Anchoring in *Xenopus* Oocytes.

One of the final stages of RNA localization is anchoring of RNA at its destination. In the case of vegetal transport granules in *Xenopus laevis* oocytes, *vg1* becomes anchored to the vegetal cortex until the end of oogenesis (Weeks and Melton 1987; Tannahill and Melton 1989). Previous work from our laboratory has shown by FRAP, that cortical RNA is immobile whereas RNA in transport granules is highly mobile (Powrie et al. 2016). The FRAP data suggests that cortical anchoring represents a stable subpopulation, rather than a continuous cycle of delivery and release. Although studies disrupting cortical actin, cytokeratin (Klymkowsky et al. 1991; Kloc et al. 2007) , and predeposited RNAs (Kloc and Etkin 1994; Heasman et al. 2001) have suggested their importance in RNA anchoring, no specific RNA anchoring complex has been identified.

Prrp/DAZAP1 was identified *in vitro* as a binding partner of the vegetal localization element of *vg1* mRNA (Zhao et al. 2001). In addition to containing two N-terminal RNA Binding domains, the C-terminal contains a proline-rich domain (Figure B.1A). This region has previously been shown to interact with the actin remodeling protein, Profilin (Zhao et al. 2001). We considered Prrp to be a good candidate as an anchoring component given its ability to both bind *vg1* mRNA and interact with the cortical cytoskeleton (Figure B.1B). In addition, immunofluorescence in whole-mount oocytes indicated that endogenous Prrp localized to the vegetal cortex in stage II oocytes (Figure B.1C), concurrent with *vg1* mRNA localization.

To investigate Prrp function, we first generated FLAG-tagged versions of Prrp (Figure B.2). We note that the full-length construct, PrrpFL-FLAG, retains

ability to localize to the vegetal cortex during stage II oogenesis (Figure B.2B). We also generated two truncation forms of Prrp. The PrrpΔPro-FLAG contains only the N-terminal RNA binding domains (Figure B.2C). The PrrpΔRRM-FLAG contains only the proline rich domain (Figure B.2D)

We next sought to investigate the nature of Prrp-*VLE* binding. Using a UV crosslinking immunoprecipitation approach, we found that Prrp bound the *VLE* in a sequence specific manner (Figure B.3). We also found that the PrrpΔPro mutant retained the ability to bind the *VLE* in a sequence dependent manner, but that the PrrpΔRRM mutant was unable to bind the *VLE*.

One of the challenges of working with *Xenopus laevis* oocytes is that knockdown of maternally loaded protein is extremely difficult. Due to technical challenges we are unable to use classic RNAi, and morpholinos do not remove the already translated maternally loaded protein. Although TALEN technology has been successfully used in *Xenopus laevis* (Nakajima and Yaoita 2015), the time frame to generate a mature female from whom ovaries need to be harvested, is not practical. Antibody interference provides another technique to limit endogenous protein activity in *Xenopus* oocytes and has been an approach successful in the past (Gagnon et al. 2013). However, this requires an abundant stock of antibody—which we did not have for Prrp.

However, given that the PrrpΔPro mutant could bind the VLE of *vg1* mRNA but lacked the proline-rich domain that was predicted to interact with the cortex, we reasoned that PrrpΔPro could be used as a dominant negative mutant. This approach has its own set of caveats. The primary issue is that the dominant

negative mutant is expressed over a wild-type background. A such, it is possible that the mutant phenotype could be masked.

We fluorescently labeled *vg1* VLE RNA, *in vitro*, and injected it into stage II oocytes. To allow proper localization we cultured the oocytes for 24 hours (Figure B.4A). We then injected RNA encoding the FLAG formed of Prrp, either full length (Figure B.4B) or PrrpΔPro. We cultured the oocytes for and additional 48 hours to allow Prrp protein to fully express. As predicted in PrrpΔPro, a subset of VLE anchored normally at the cortex, perhaps due to the presence of wild-type protein, however, a bulk of the RNA appeared to remain diffuse throughout the cytoplasm. (Figure B.4C).

Studying non-fully penetrant defects in anchoring requires a quantitative approach. To this end, I developed two plugins for ImageJ to classify the distribution of VLE in oocyte. The first program probes the idea that a defect in anchoring could result in a spreading of RNA the cortex. That is, the RNA may localize beyond its normal bounds. The program created measures angle, α – or the distribution of RNA across the cortex (Figure B.5A). The program works by measuring the average fluorescence along a line that moves 360 degrees across the image of a spherical oocyte (Figure B.5B). We found, distribution of *vg1* RNA expanded in the PrrpΔPro mutant. On average, RNA spread about 103 degrees from the central vegetal cortex in PrrpFL-FLAG constructs. However, in mutants, the spread increased to 144 degrees (Figure B.5C).

The second plugin automatically calculates the relative amount of fluorescently labeled RNA in each of the four oocyte quadrants (Figure B.6A), by

manually dividing (Figure B.6B) the oocyte based on a set of user-inputs. Perfect localization would show 100% localization, whereas no specific localization would show 25% localized RNA in any cortex. We found that vegetal localization was disrupted with the PrrpΔPro mutant, suggesting that approximately a quarter is mislocalized to other cortices (Figure B.6C).

Although studies on Prrp were initially promising, we found the experiments were very difficult to replicate. The phenotype was not fully penetrant and was often masked by correct RNA localization masked by the presence of endogenous protein. From the Prrp project, however, we developed two user-friendly ImageJ plugins for accessing RNA distribution in oocytes. In fact, the plugin shown in Figure B.5, was later further modified and developed to measure the fluorescence in concentric rings around the oocyte, as used in Appendix D. We can also conclude that anchoring is very difficult process to study in *Xenopus* oocytes, particularly because it is difficult to separate phenotypes due to localization defects and those due to anchoring defects. I personally advise if anchoring studies continue in the laboratory that they be extremely focused on biochemical assays rather than immunofluorescence.

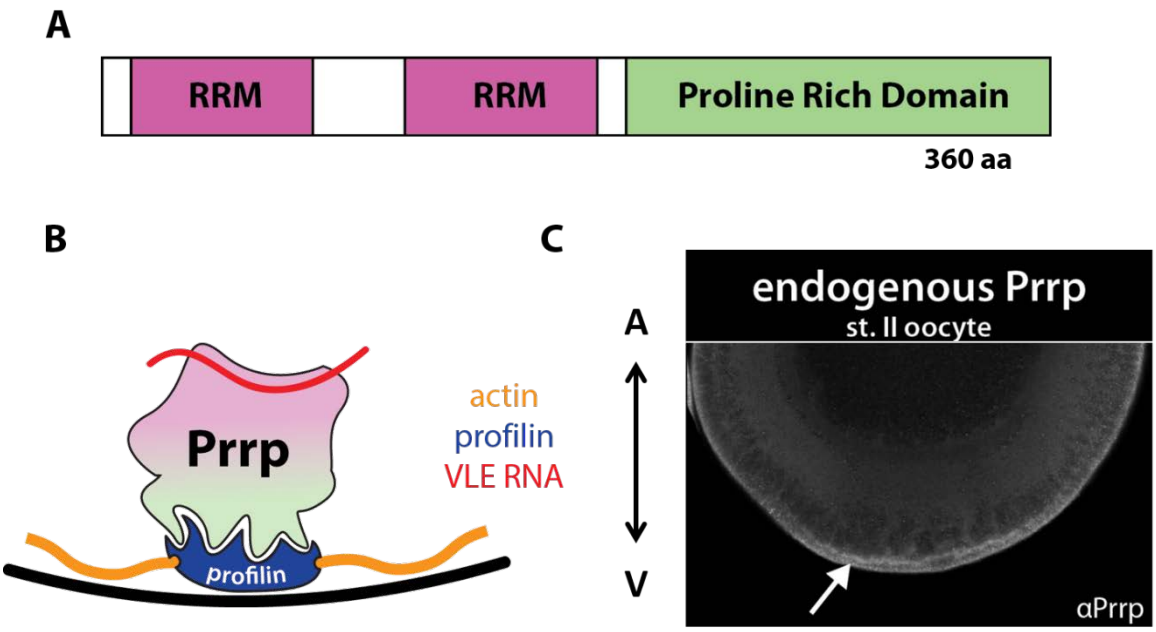

Figure B.1. Prrp is an RNA binding protein that is a candidate RNA anchoring component. (A) Schematic of Prrp sequence. The N terminal contains two RRMs (purple), and the C-terminus contains a proline rich domain (green). **(B)** Graphical representation of how Prrp might interact with *VLE* RNA (red) to interact via profilin (blue) with cortical actin cytoskeleton (gold). **(C)** Whole mount immunofluorescence of a stage II oocyte stained for Prrp. White arrow indicates cortical position of Prrp.

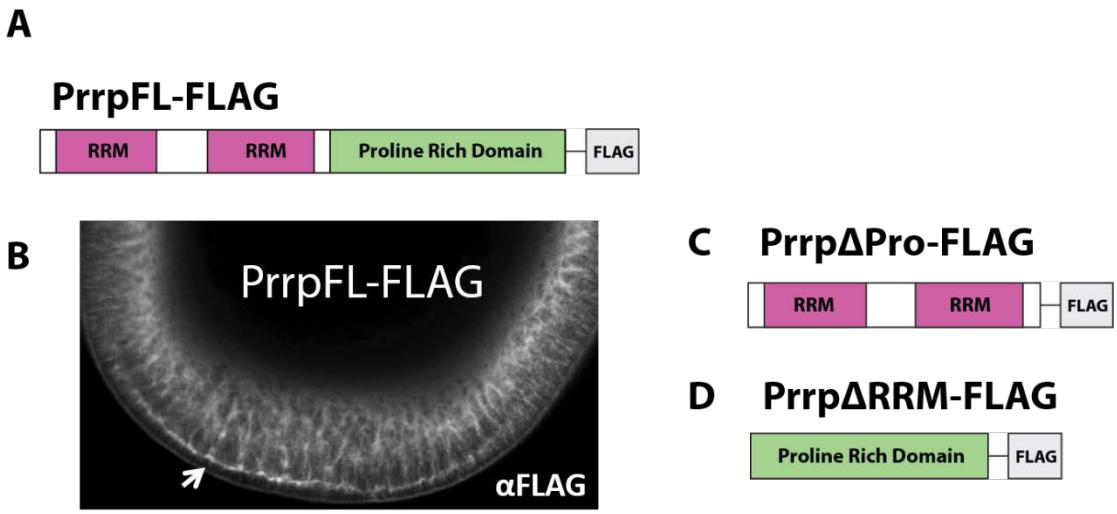

Figure B.2. FLAG constructs provide an opportunity to study Prrp *in vivo*. (A) Schematic of FLAG-tagged full length Prrp (PrrpFL-FLAG). **(B)** PrrpFL-FLAG localizes to the cortex in stage II oocytes consistent with endogenous Prrp staining (Figure A.1). **(C)** Schematic of PrrpΔPro-FLAG construct, lacking the proline rich domain. **(D)** Schematic of PrrpΔRRM-FLAG construct, lacking both RRM domains.

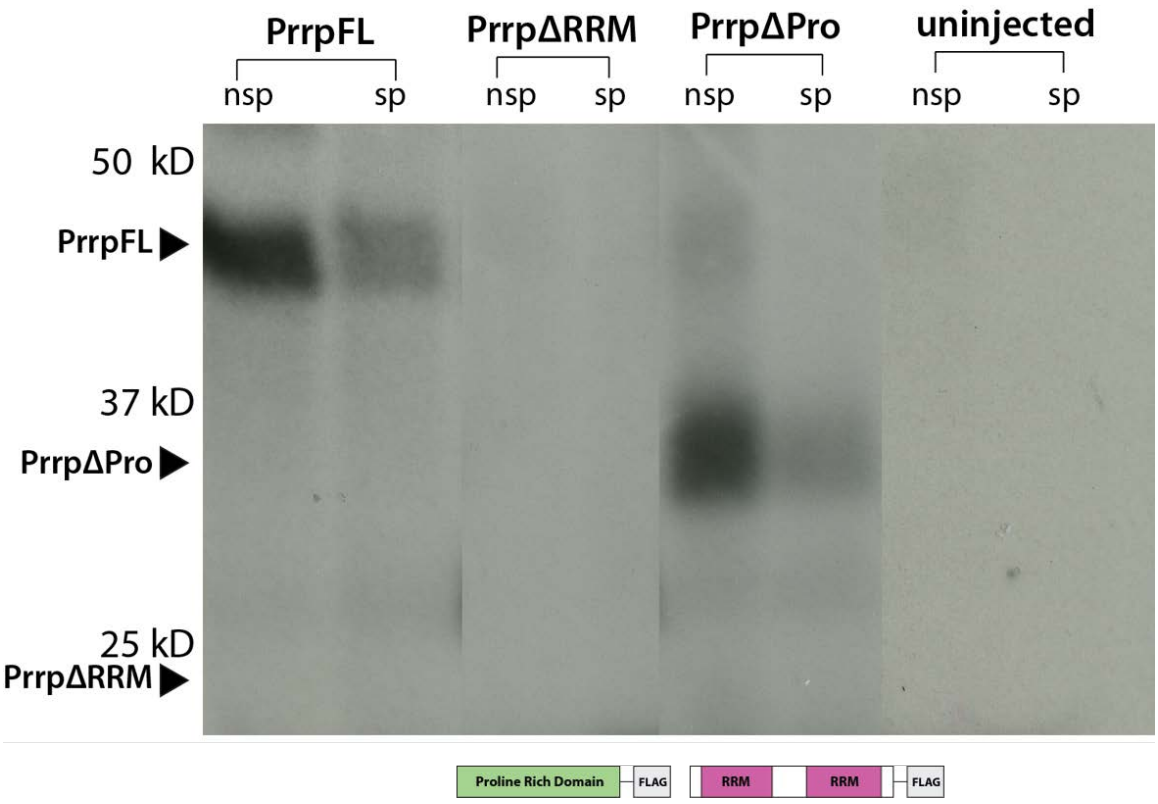

Figure B.3. Prrp binds VLE RNA in a sequence-dependent manner. Autoradiogram results of a UV crosslink immunoprecipitation assay to determine binding capabilities of the Prrp-FLAG constructs. Briefly, oocyte lysate (expressing exogenous PrrpFLAG) was incubated with ^{32}P-labeled *VLE* RNA prior to introducing unlabeled specific (sp) or nonspecific (nsp) RNA competitors. Lysate was cross linked by UV, immunoprecipitated with FLAG antibody, and RNAse treated. PrrpFL and PrrpΔPro bind the *VLE* RNA sequence-specifically. PrrpΔRRM is unable to bind *VLE* RNA, as is oocytes not injected with PrrpFL.

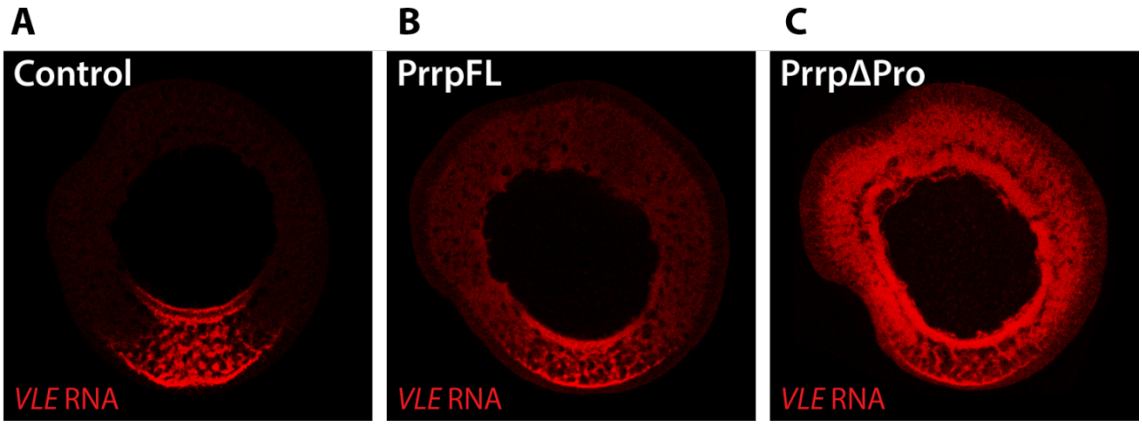

Figure B.4. PrrpΔPro prevents complete cortical RNA anchoring. Whole mount images of fluorescent VLE RNA (red) localization in stage II oocytes expressing **(A)** no exogenous protein **(B)** co-expressing PrrpFL-FLAG or **(C)** PrrpΔPro-FLAG.

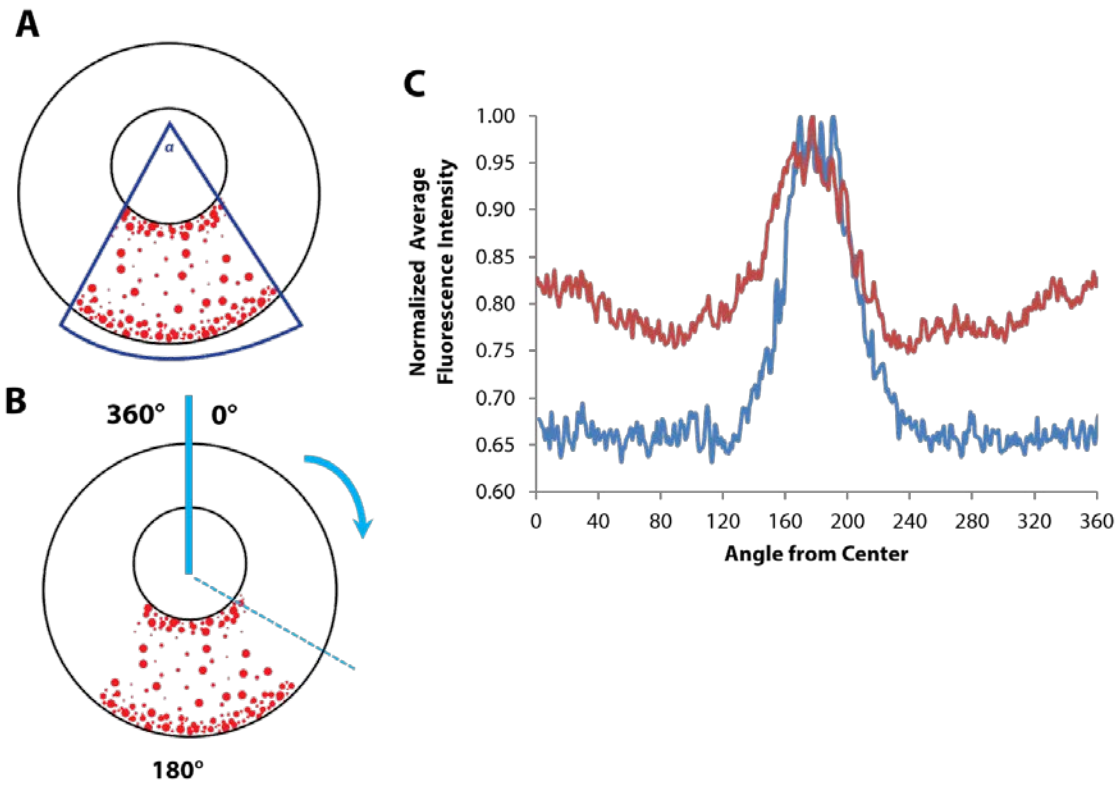

Figure B.5. PrrpΔPro disrupts cortical distribution of *VLE RNA*. (A) Cortical RNA distribution is measured as a function of the angle from the center of the oocyte alpha. **(B)** Schematic of ImageJ plugin to measure RNA distribution. **(C)** Distribution of *VLE* RNA, represented as normalized average fluorescence intensity as a function of alpha. Blue line = PrrpFL-FLAG injected oocytes (*n*=8). Red line = PrrpΔPro-FLAG injected oocytes (*n*=10). Vegetal cortex is located at 180 degrees. For *VLE* in PrrpFL-FLAG injected oocytes, alpha = 103 degrees. In PrrpΔPro-FLAG injected oocytes, alpha increase to 144 degrees.

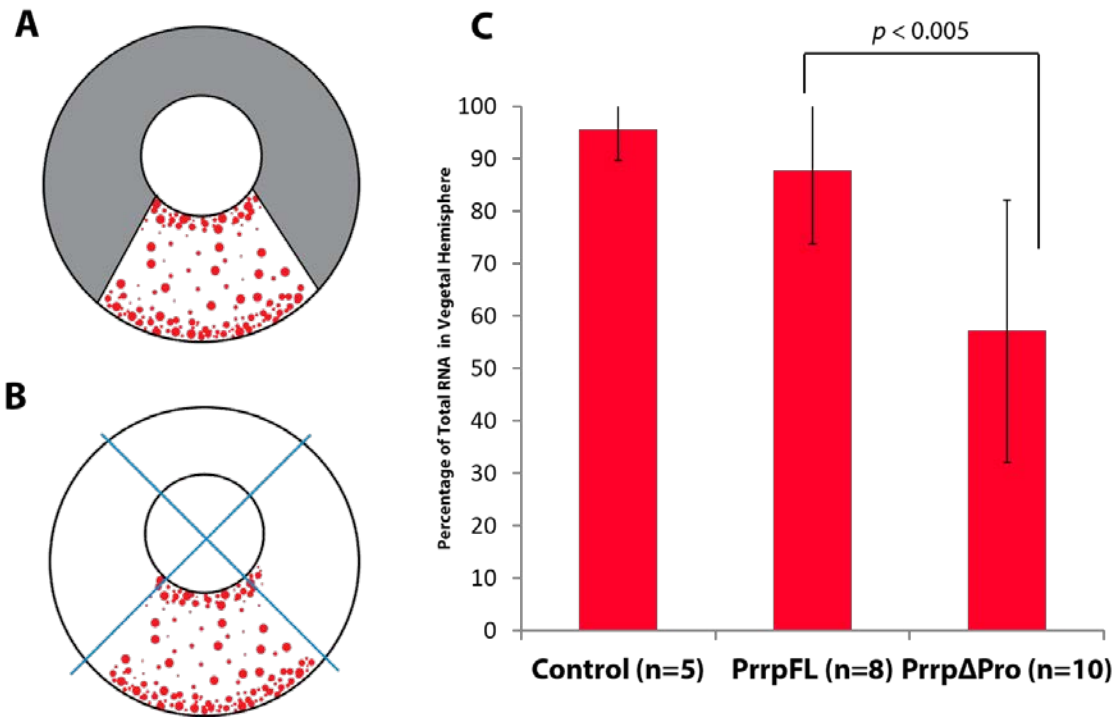

Figure B.6. PrrpΔPro reduces vegetal localization of *VLE* RNA. (A) Schematic representing the endogenous region of *VLE* localization in the vegetal hemisphere (white background with red dots representing *VLE* RNA). **(B)** Schematic representing ImageJ plugin for calculating quadrant expression of RNA. The center of the oocyte is determined as the center of the nucleus. **(C)** Percent of total RNA in the vegetal hemisphere localized to the vegetal cortex in oocytes injected with *VLE* RNA alone (Control, *n*=5), PrrpFL-FLAG (*n*=8), or PrrpΔPro-FLAG (*n*=10). Vegetal localization in control is nearly 100%. Oocytes injected with a wildtype form of Prrp retain approximately 90% vegetal localization, but those injected with PrrpΔPro reduce vegetal localization to approximately 60%. Error bars represent standard deviation. P < 0.005 where indicated.

References

Gagnon JA, Kreiling JA, Powrie EA, Wood TR, Mowry KL. 2013. Directional transport is mediated by a Dynein-dependent step in an RNA localization pathway. *PLoS Biol* **11**: e1001551.

Heasman J, Wessely O, Langland R, Craig EJ, Kessler DS. 2001. Vegetal localization of maternal mRNAs is disrupted by VegT depletion. *Dev Biol* **240**: 377–86.

Kloc M, Bilinski S, Dougherty MT. 2007. Organization of cytokeratin cytoskeleton and germ plasm in the vegetal cortex of *Xenopus laevis* oocytes depends on coding and non-coding RNAs: Three-dimensional and ultrastructural analysis. *Exp Cell Res* **313**: 1639–1651.

Kloc M, Etkin LD. 1994. Delocalization of *Vg1* mRNA from the vegetal cortex in *Xenopus* oocytes after destruction of *Xlsirt* RNA. *Science* **265**: 1101–1103.

Klymkowsky MW, Maynell LA, Nislow C. 1991. Cytokeratin phosphorylation, cytokeratin filament severing and the solubilization of the maternal mRNA *Vg1*. *J Cell Biol* **114**: 787–797.

Nakajima K, Yaoita Y. 2015. Highly efficient gene knockout by injection of TALEN mRNAs into oocytes and host transfer in *Xenopus laevis*. *Biol Open* **4**: 180–5.

Powrie EA, Ciocanel V, Kreiling JA, Gagnon JA, Sandstede B, Mowry KL. 2016. Using *in vivo* imaging to measure RNA mobility in *Xenopus laevis* oocytes.

Methods **98**: 60–65.

Tannahill D, Melton DA. 1989. Localized synthesis of the Vg1 protein during early *Xenopus* development. *Development* **106**: 775–85.

Weeks DL, Melton DA. 1987. A maternal mRNA localized to the vegetal hemisphere in *Xenopus* eggs codes for a growth factor related to TGF-β. *Cell* **51**: 861–867.

Zhao WM, Jiang C, Kroll TT, Huber PW. 2001. A proline-rich protein binds to the localization element of *Xenopus Vg1* mRNA and to ligands involved in actin polymerization. *EMBO J* **20**: 2315–25.

Appendix C: Developing a Strategy to Quantify *Ex Vivo* Vegetal Transport Granules

One of the downstream applications of the vegetal transport RNP granule isolation strategy is *ex vivo* analysis of *in vivo*-assembled granules. As alluded to in the Discussion (Chapter 4), we can isolate intact vegetal transport granules and test their biophysical and biochemical properties in response to treatment with various buffers. Only a few microliters of sample contain thousands of vegetal transport granules. We have recently optimized conditions to image the *ex vivo* granules by confocal microscopy (C. Neil and S. Kaptur, unpublished data). However, to generate high confidence, unbiased data, a data quantitation method was necessary. To solve this problem, I have developed a custom user-friendly FIJI/ImageJ (Schindelin et al. 2012; Rueden et al. 2017) plugin for analyzing large amounts of *ex vivo* granule data. The script takes advantage of a few externally developed plugins, namely the Analyze Particles (Schindelin et al. 2012; Rueden et al. 2017) and Binary Feature Extractor (Brocher) plugins.

Since the *ex vivo* granule analysis, as noted in the Discussion (Chapter 5) uses an abbreviated isolation procedure (bypassing the immunoprecipitation steps), we need to selectively mark the granules prior to isolation. This is accomplished by injecting oocytes with two fluorescently labeled RNAs, using different fluorophores: wildtype VLE RNA and mutant VLE RNA. Only those structures which are positive for the wildtype *VLE* and negative for the mutant *VLE* represent vegetal transport granules.

The experimental setup for *ex vivo* granule analysis requires four confocal images per single analysis:

(1) Wildtype Image. Lysate, (the VP – see Chapter 2) from oocytes injected with wildtype and mutant VLE RNA. Only the wildtype laser is captured.

(2) Mutant Image. Same as (1) but only the mutant VLE RNA is captured.

(3) Background image, namely to control for autofluorescence (background)

(4) Phase Contrast image (DIC).

In essence, the plugin identifies a vegetal transport granule if there is signal in the wildtype image, but not the background or mutant image. The plugin also counts any vegetal transport granules that are phase separated, as indicated by phase contrast microscopy (DIC).

As the *ex vivo* granules are 1-2 microns (Figure C.1), and difficult to distinguish by eye, we wanted to ensure that we accurately captured true vegetal transport granules and not artifacts. I included other parameters with this program to ensure we are accurately capturing granules.

(1) Minimum Threshold. Only the highest fluorescence intensity particles are included for granule consideration.

(2) Minimum Granule Size. To avoid capturing artifacts, including noise introduced on the microscope camera, I set a minimum size

(3) Minimum granule shape (circularity). Preliminary studies have shown that the *ex vivo* granules are roughly circular. Elongated shapes, like rods, usually represent artifacts, but are bright enough to pass the minimum threshold and size parameters.

(4) Maximum granule size. Large artifacts, including shadows in the DIC channel can pass the first three parameter settings. This setting helps limit the number of large artifacts.

(5) Minimum percent overlap. The *ex vivo* granules are constantly moving inside the imaging chamber. As a result, particles do not 100% overlap between fluorescence and DIC images. To account for this, a minimum, but not perfect, overlap is required.

(6) Exclude particles on the perimeter. To avoid potentially capturing half granules, any granules that are not fully captured within the image are excluded.

The output file gives details about the average granule size, average granule shape, and average phase separated granules. Initial testing has shown that our program can distinguish changes in granule size, number, or phase separation due to chemical treatment.

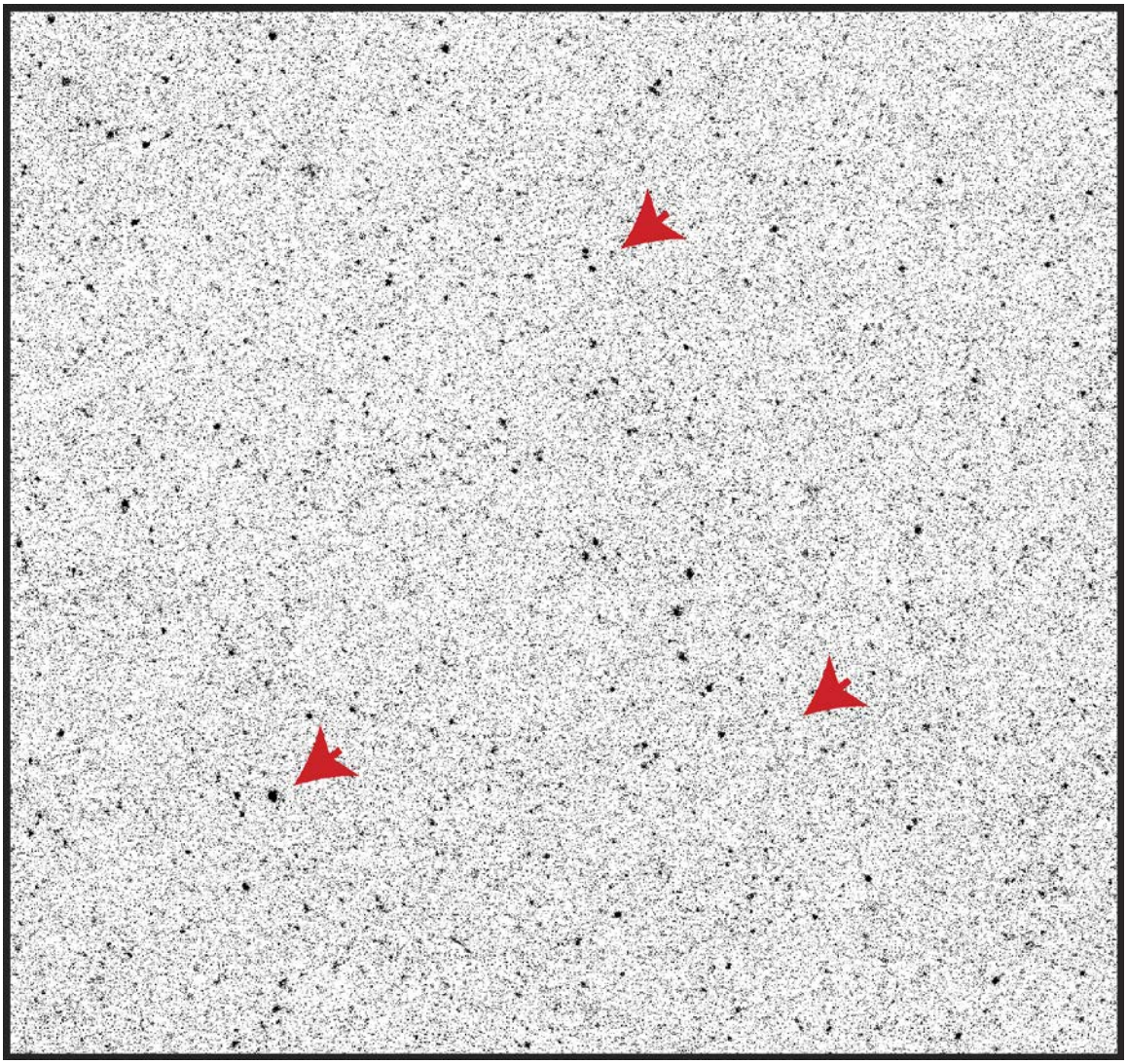

Figure C.1. Ex vivo *image analysis of vegetal transport granules*. Confocal images of untreated fluorescently labeled (VLE) vegetal transport granules, as isolated by size exclusion chromatography. Red arrows indicate three vegetal transport granules, but do not represent the full granule population.

References

Brocher J. The BioVoxxel Image Processing and Analysis Toolbox. http://eubias.org/eubias2015/wp-content/uploads/2014/11/Biovoxxel.pdf

Rueden CT, Schindelin J, Hiner MC, DeZonia BE, Walter AE, Arena ET, Eliceiri KW. 2017. ImageJ2: ImageJ for the next generation of scientific image data. *BMC Bioinformatics*.

Schindelin J, Arganda-Carreras I, Frise E, Kaynig V, Longair M, Pietzsch T, Preibisch S, Rueden C, Saalfeld S, Schmid B, et al. 2012. Fiji: An open-source platform for biological-image analysis. *Nat Methods*.

Appendix D: Modeling Microtubule-based Transport and Anchoring of mRNA

This chapter is under review for the *SIAM Journal on Applied Dynamical Systems*: Ciocanel, M.V., Sanstede, B., Jeschonek, S.P., Mowry, K.L. (2018) Modeling microtubule-based transport and anchoring of mRNA.

I developed the ImageJ/FIJI plugin for analyzing RNA distribution and analyzed the experimental data with that plugin.

Modeling microtubule-based transport and anchoring of mRNA*

Maria-Veronica Ciocanel†, Björn Sandstede‡, Samantha P Jeschonek§, and Kimberly L Mowry¶

Abstract. Localization of messenger RNA (mRNA) at the vegetal cortex plays an important role in the early development of *Xenopus laevis* oocytes. While it is known that molecular motors are responsible for the transport of mRNA cargo along microtubules to the cortex, the mechanisms of localization remain unclear. We model cargo transport along microtubules using partial differential equations with spatially-dependent rates. A theoretical analysis of reduced versions of our model predicts effective velocity and diffusion rates for the cargo and shows that randomness of microtubule networks enhances effective transport. A more complex model using parameters estimated from fluorescence microscopy data reproduces the spatial and timescales of mRNA localization observed in *Xenopus* oocytes, corroborates experimental hypotheses that anchoring may be necessary to achieve complete localization, and shows that anchoring of mRNA complexes actively transported to the cortex is most effective in achieving robust accumulation at the cortex.

Key words. intracellular transport, microtubules, anchoring, long-time dynamics, reaction-diffusion model

AMS subject classifications. 35B40, 35K57, 92C15, 92C40

1. Introduction.

The cellular cytoskeleton is key in ensuring the dynamic transport and localization of many different RNAs, proteins, and vesicles. Polarized networks of microtubule tracks often provide the basis for directional transport of various intracellular cargoes that regulate essential processes such as cell division, cell motility, and embryogenesis in various organisms. In many of these biological processes, the mechanisms underlying the time and spatial scales of protein and RNA localization are not known, and a better understanding of the impact of the microtubule geometry on transport processes is required.

One example where the cytoskeleton plays a key role in transport is mRNA localization to the vegetal cortex during oogenesis of the frog *Xenopus laevis*. The asymmetric distribution of Vg1 mRNA in the vegetal cytoplasm of the frog oocyte is critical for correct embryonic patterning in this organism, and similar localization processes occur in many others [13, 33]. Molecular motors kinesin and dynein are responsible for the transport of mRNA cargo along polarized microtubules to the vegetal cortex of the *Xenopus* oocyte [14, 34] (see Figure 1). Dynein moves cargo to the minus ends of microtubules and is hypothesized to contribute to directional transport towards the cortex in the upper cytoplasm (Regions 1 and 2 in Figure 1),

*Submitted to the editors 05/07/2018.

Funding: This work was funded by NSF grant number DMS 1408742 (to BS) and R01GM071049 (to KLM). MVC was also supported in part by the Mathematical Biosciences Institute and the NSF under grant number DMS 1440386.

†Mathematical Biosciences Institute, The Ohio State University, Columbus, OH (ciocanel.1@mbi.osu.edu).

‡Division of Applied Mathematics, Brown University, Providence, RI (bjorn_sandstede@brown.edu).

§Department of Molecular Biology, Cell Biology, and Biochemistry, Brown University, Providence, RI (samantha_jeschonek@brown.edu).

¶Department of Molecular Biology, Cell Biology, and Biochemistry, Brown University, Providence, RI (kimberly_mowry@brown.edu).

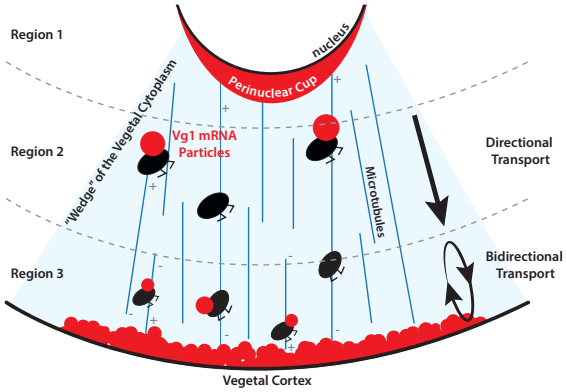

Figure 1. *Schematic of mRNA localization in the vegetal cytoplasm of a Xenopus oocyte. mRNA cargoes (red) are transported by motor proteins (black) along polarized microtubule filaments (blue lines) towards the vegetal cortex. The vegetal cytoplasm is schematically divided into three regions where transport parameters have been found to differ [9].*

while kinesin moves cargo to the plus ends of microtubules and may be involved in bidirectional transport in the lower cytoplasm (Region 3 in Figure 1) [14]. Despite these experimental insights, the mechanisms of localization remain unclear. In particular, experiments suggest that mRNA is anchored at the cortex [1, 38, 49], but it is not known whether this is necessary for mRNA localization. Our goal is therefore to take into account the microtubules in modeling the mRNA localization process in *Xenopus* oocytes and to provide insights into the mechanisms behind the time and spatial scales of localization and anchoring in this developmental process.

In our previous work [9] (see also [38]), we used linear transport models coupled with parameter estimation and analysis to determine diffusion coefficients, motor speeds, and transition rates for dynamic populations of mRNA in *Xenopus* oocytes using FRAP (fluorescence recovery after photobleaching) data [14]. The analysis there allowed us to suggest differences in transport efficiency of mRNA in different regions of the oocyte cytoplasm. These constant transition rate models are useful in modeling dynamics on the short time scale of the FRAP experiments, however they cannot provide insights on the longer time scale of mRNA localization, where the transport directionality depends on the complex microtubule cytoskeleton. Here we build on the models and parameter estimates in [9] and incorporate the spatial microtubule networks through spatially-dependent transition rates. We carry out a large-time analysis of reaction-advection-diffusion transport models on parallel filaments using Fourier expansion and Lyapunov-Schmidt reduction and extend existing effective transport results [7] to general systems with an arbitrary number of dynamical states and under no assumptions on the scales of the parameters or on the filament density. Our findings and predictions for the dynamics of mRNA in *Xenopus* can be summarized as follows:

- An inhomogeneous or random microtubule cytoskeleton leads to more effective spread of diffusing cargo;
- Anchoring may be necessary to achieve complete localization and to reproduce the timescales of mRNA localization observed in *Xenopus* oocytes;

- Anchoring of mRNA actively delivered to the cortex is most effective in achieving robust localization;
- mRNA anchoring may be enhanced by mRNA already anchored at the cortex.

The models we propose do not explicitly account for the polarity (plus/minus ends) of the microtubules or for the specific motor species carrying out the transport in each region. Instead, we assume that this information is embedded in the different kinetic parameters estimated for each region of the *Xenopus* oocyte cytoplasm (see Figure 1) in [9]. The models proposed do however account for the geometry and orientation of the microtubule filaments in the domain, which we henceforth refer to as the microtubule structure.

Previous models for the transport of RNA and proteins along realistic cellular cytoskeleton geometries have been proposed to study cell polarization in the mating budding yeast and neural growth cones [7, 19], as well as mRNA localization in *Drosophila* oocytes [43]. These studies use partial differential equations and stochastic models to represent switching between a diffusion state and a state of active transport along directed microtubule networks. Analytically, the transport properties of the particles in these dynamic models (effective velocity and diffusion) are determined in [7] using the quasi-steady-state reduction method [6, 36, 37], under assumptions of very fast switching rates and very slow diffusion relative to the motor protein velocities. In many systems, however, these assumptions on the parameters of the dynamics are unlikely to be biologically relevant. For instance, our parameter estimation based on FRAP microscopy data in [9] revealed that diffusion coefficients may be larger in magnitude than motor speeds in Vg1 mRNA localization during *Xenopus laevis* oogenesis. Our theoretical results therefore extend the analysis of transport models with parallel filaments to general systems with arbitrary parameters.

In addition to the applicability of this analysis to many biological systems where transport relies on parallel filaments, our derived effective transport predictions contain additional terms in the predicted diffusivity, which can be numerically evaluated to show that non-uniform cytoskeleton networks lead to faster transport and a wider spread of the particles modeled. This observation motivates the use of accurate microtubule structures with biologically-informed orientations as in [43]. The study [43] tested the localization of two types of mRNA at a late stage in *Drosophila* oogenesis using a two-state model of the dynamics and standard values for key dynamic parameters. We focus on a more complex four-state model for mRNA transport and localization in the frog *Xenopus laevis* [9] coupled to a random but radially-biased microtubule network informed from experimental observations in [4, 14, 15, 34]. This model accounts for the bidirectional movement of the particles driven by kinesin and dynein motors, which have been found to both contribute to mRNA localization in this system [9, 14, 34]. In this model, parameters such as diffusion coefficients, motor velocities, and transition rates depend on the location in the cytoplasm [9] and we use estimates of these parameters based on the experimental data in [14].

Our approach allows us to assess transport timelines in mRNA localization and to provide insight into additional mechanisms such as anchoring, which are challenging to study experimentally in *Xenopus* oocytes. In particular, anchoring of mRNA at the target destination in developing oocytes and embryos is not fully understood, with some studies suggesting an actin-dependent mechanism at the cortex [1, 49] and proposing a role for mediating factors and vesicles [1, 20, 26, 49, 50]. In *Drosophila* oocytes, [44] proposes a microtubule-independent

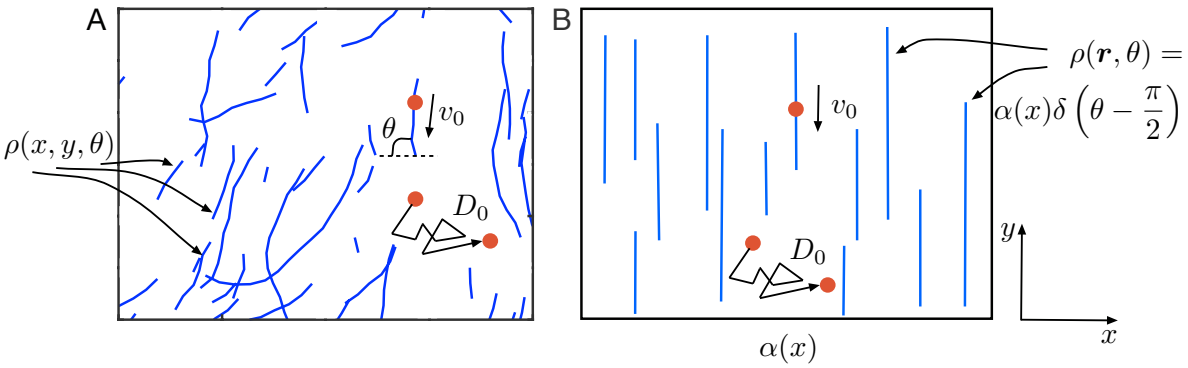

Figure 2. *(A) Illustration of a microtubule structure with density ρ (blue lines). Particles (red dots) can either be transported with velocity v_0 along microtubule filaments, or freely diffuse in the cytoplasm with diffusion coefficient D_0. The density of microtubules at location (x, y) with orientation θ is given by $\rho(x, y, \theta)$. (B) Illustration of a parallel microtubule structure with density $\rho(\boldsymbol{r}, \theta) = \alpha(x)\delta(\theta - \pi/2)$ (blue lines). Here particle transport can occur with velocity v_0 down along microtubule filaments.*

anchoring mechanism of bicoid mRNA at the anterior pole, while [10] suggests that apical anchoring of RNA is microtubule-dependent in blastoderm embryos. Despite the different experimental findings in different organisms or stages of development, the numerical framework we propose provides a way to investigate these questions and suggests that active delivery (likely by molecular motors) is necessary for proper vegetal localization and that anchoring is required for robust accumulation of mRNA at the cortex in *Xenopus* oocytes.

2. Quantifying transport along microtubule networks using PDE models.

2.1. Motivation. Similar to [7, 19], we consider a model of the dynamics of mRNA particles where transport is restricted to given microtubule structures. Particles can switch between a freely diffusing state and a transport state for motor-cargo complexes with velocity $\boldsymbol{V}(\theta)$. The direction of transport θ is determined by the orientation of the cytoskeletal filament bound to the complex at location (x, y) (see Figure 2A). We assume as in [7] that there is a density $\rho(\boldsymbol{r}, \theta)$ of filaments with a given orientation θ at each location $\boldsymbol{r} = (x, y)$. Particle movement is then modeled using the equations

$$\begin{aligned} \frac{\partial p(\boldsymbol{r},\theta,t)}{\partial t} &= -\boldsymbol{V}(\theta)\cdot\nabla p(\boldsymbol{r},\theta,t) - \beta p(\boldsymbol{r},\theta,t) + \alpha\rho(\boldsymbol{r},\theta)p_0(\boldsymbol{r},t)\,, \\ \frac{\partial p_0(\boldsymbol{r},t)}{\partial t} &= D\nabla^2 p_0(\boldsymbol{r},t) + \beta\int_0^\pi p(\boldsymbol{r},\theta,t)d\theta - \alpha\bar{\rho}(\boldsymbol{r})p_0(\boldsymbol{r},t)\,, \end{aligned} \tag{1}$$

where $p_0(\boldsymbol{r}, t)$ denotes the concentration of diffusing particles at position $\boldsymbol{r} = (x, y)$ at time t, and $p(\boldsymbol{r}, \theta, t)$ is the concentration of particles bound to a microtubule at location $\boldsymbol{r}$ and moving with velocity $\boldsymbol{V}(\theta)$ [7]. Here $\bar{\rho}(\boldsymbol{r}) = \int_0^\pi \rho(\boldsymbol{r}, \theta)d\theta$ is the availability of filaments at a certain location averaged over all orientations θ, β corresponds to the transition rate from the transport state to the diffusing state, and α corresponds to the transition rate from diffusion to transport.

Our parameter estimation results in [9] indicate that diffusion and binding rate parameters can vary throughout the cytoplasm and that neither diffusion nor binding dominates the dynamics. This suggests that existing approaches to analyze equations (1), which assume very fast switching rates and slow diffusion compared to typical motor velocities [7], do not hold in the case of mobility of mRNA in *Xenopus* oocytes. In particular, the quasi-steady-state (QSS) approximation in [7] does not apply in this setting, and we therefore proceed with different analytical methods that do not require assumptions on the magnitude of the system parameters. To simplify the analysis, we start by considering the case where filaments are oriented parallel to each other. As in [7], we let the density of filaments vary with spatial dimension x via

$$\rho(\boldsymbol{r},\theta) = \alpha(x)\delta(\theta - \pi/2)$$

where we recall that $\boldsymbol{r} = (x, y)$ (see Figure 2B). The function $\alpha(x)$ corresponds to the concentration of signaling molecules on the membrane in [7].

Letting $\bar{p}(\boldsymbol{r}, t) = \int_0^\pi p(\boldsymbol{r}, \theta, t)d\theta$ and noting that $\bar{\rho} = \int_0^\pi \rho(\boldsymbol{r}, \theta)d\theta = \alpha(x)$, we obtain the equations

$$\begin{aligned} \frac{\partial \bar{p}(\boldsymbol{r},t)}{\partial t} &= v_0 \boldsymbol{e_y} \cdot \nabla \bar{p}(\boldsymbol{r},t) - \beta \bar{p}(\boldsymbol{r},t) + \alpha(x) p_0(\boldsymbol{r},t)\,, \\ \frac{\partial p_0(\boldsymbol{r},t)}{\partial t} &= D\nabla^2 p_0(\boldsymbol{r},t) + \beta \bar{p}(\boldsymbol{r},t) - \alpha(x) p_0(\boldsymbol{r},t) \end{aligned} \tag{2}$$

for the concentrations of particles in the two states that correspond to active transport and diffusion, respectively.

To account for bidirectional movement, more complex models with additional dynamic states would be of interest. For instance, we found in [9] that a model with four dynamical states that account for movement up along filaments, movement down along filaments, diffusion, and pausing (see equations (38) below) may be more accurate for describing the mRNA dynamics in different regions of the cytoplasm. Therefore, the theoretical result in the next section is obtained for general systems of linear advection-reaction-diffusion partial differential equations with spatially-dependent transition rates.

2.2. Main result. To determine the asymptotic behavior of particles restricted to transport on parallel filaments, we calculate their effective velocity and diffusion at large time. We consider the general case of an arbitrary number of particle populations that can move bidirectionally on the microtubule tracks, diffuse or pause when off-track, and switch between these states at given rates; more precisely, we consider the system of advection-reaction-diffusion equations given by

$$\frac{d}{dt}\begin{pmatrix} u_0 \\ u_1 \\ \dots \\ u_n \end{pmatrix} = D\nabla^2 \begin{pmatrix} u_0 \\ u_1 \\ \dots \\ u_n \end{pmatrix} + C\frac{d}{dy}\begin{pmatrix} u_0 \\ u_1 \\ \dots \\ u_n \end{pmatrix} + A(x)\begin{pmatrix} u_0 \\ u_1 \\ \dots \\ u_n \end{pmatrix}, \qquad \nabla = \begin{pmatrix} \partial_x \\ \partial_y \end{pmatrix}, \tag{3}$$

where $(x, y) \in [0, 1] \times \mathbb{R}$, together with the boundary conditions

$$\frac{\partial u_i}{\partial x}(x = 0, y, t) = \frac{\partial u_i}{\partial x}(x = 1, y, t) = 0, \quad i = 1, \dots, n\,. \tag{4}$$

The variables $u_i \in \mathbb{R}$ model concentrations of particles that diffuse and are transported along a cytoskeleton of parallel vertical filaments. The diagonal matrices C and D contain the speeds and diffusion coefficients, respectively, in each state, while the transitions between states are described by the reaction-rate matrix $A(x)$. The x-dependence of the reaction-rate matrix $A(x)$ accounts for the availability of microtubules at a certain location.

Theorem 2.1. *Assume that C and D are diagonal matrices and that the entries of D are non-negative. We also assume that $A(x) \in C^0(\mathbb{R}, \mathbb{R}^{n\times n})$. Finally, we assume that the operator $L_0 := D\partial_x^2 + A(x)$ posed on $[0,1]$ with Neumann boundary conditions has a zero eigenvalue with algebraic and geometric multiplicity one and that all other eigenvalues have negative real part. Let $\boldsymbol{u_0}(x)$ be a nonzero element of the null space of L_0, and $\boldsymbol{\psi_0}(x)$ be a nonzero element of the null space of the adjoint operator $L_0^* := D\partial_x^2 + A^*(x)$. Let $\boldsymbol{u}(\boldsymbol{r},t)$ denote the solution of (3) with initial condition given by a Gaussian initial condition for each u_i, then, as $t \to \infty$, the solution has the asymptotic Gaussian form*

$$\boldsymbol{u}(\boldsymbol{r},t) = \frac{a}{\sqrt{2\pi\sigma_{\text{eff}}t}} e^{\frac{(y+v_{\text{eff}}t)^2}{2\sigma_{\text{eff}}t}} \boldsymbol{u_0}(x)$$

for some $a \in \mathbb{R}$. Furthermore, the effective velocity v_{eff} and the effective diffusion coefficient σ_{eff} of the particles in the direction y of transport are given by

$$v_{\text{eff}} = \frac{\langle \boldsymbol{\psi_0}, C\boldsymbol{u_0}\rangle}{\langle \boldsymbol{\psi_0}, \boldsymbol{u_0}\rangle}\,, \tag{5}$$

$$\sigma_{\text{eff}} = \frac{\langle \boldsymbol{\psi_0}, D\boldsymbol{u_0}\rangle}{\langle \boldsymbol{\psi_0}, \boldsymbol{u_0}\rangle} + \frac{\langle \boldsymbol{\psi_0}, C\boldsymbol{w_1}(x)\rangle}{\langle \boldsymbol{\psi_0}, \boldsymbol{u_0}\rangle}\,, \tag{6}$$

where $\langle f(x), g(x)\rangle = \int_0^1 f(x)g(x)dx$, and $\boldsymbol{w_1}$ is the unique solution of

$$L_0\boldsymbol{w_1}(x) + C\boldsymbol{u_0}(x) - \frac{\langle \boldsymbol{\psi_0}, C\boldsymbol{u_0}\rangle}{\langle \boldsymbol{\psi_0}, \boldsymbol{u_0}\rangle}\boldsymbol{u_0}(x) = 0\,, \qquad \boldsymbol{w_1'}(0) = 0 = \boldsymbol{w_1'}(1)\,. \tag{7}$$

We prove Theorem 2.1 in §2.5.

2.3. Remarks on Theorem 2.1. To motivate the assumptions for Theorem 2.1 and show their broad applicability, we provide the following remarks.

Remark 1. If matrix $A(x)$ models conservation of particles, then $A(x)$ is a quasi-positive irreducible matrix. The Perron-Frobenius theory for quasi-positive matrices then ensures that the zero eigenvalue has algebraic multiplicity 1 and that all other eigenvalues of $A(x)$ have strictly negative real part for each x. The linear operator $L_0 = D\partial_x^2 + A(x)$ can only add diagonal entries to matrix $A(x)$ and is therefore also quasi-positive and irreducible. The real part of all other eigenvalues is thus guaranteed to be zero and the assumption in the theorem is satisfied.

Remark 2. Note that the assumption that the zero eigenvalue has geometric multiplicity 1 is equivalent to $\dim(ker(L(0,0))) = \dim(ker(L^*(0,0))) = 1$. This condition is automatically satisfied in the case of models with one diffusing population. To see this, assume that there are q populations that have diffusion dynamics, and $p = n - q$ populations that do not. We

write:

$$\boldsymbol{v}(x) = \begin{pmatrix} \boldsymbol{v_1}(x) \\ \boldsymbol{v_1}(x) \end{pmatrix},$$

$$D = \begin{pmatrix} 0 & \\ & D_0 \end{pmatrix},$$

$$A(x) = \begin{pmatrix} A_1(x) \\ A_2(x) \end{pmatrix},$$

where A_1 is a p by n and A_2 is a q by n matrix of the reaction rates. Then equation (15) becomes:

$$A_1(x)\boldsymbol{v} = 0\,, \tag{8}$$

$$D_0\partial_x^2 \boldsymbol{v_2} + A_2(x)\boldsymbol{v} = 0\,. \tag{9}$$

Since matrix $A(x)$ reflects conservation of the particles, the sum of each of its columns is 0. If we have $q = 1$ (one diffusing population), it is clear that the sum of the rows in matrix A_1 yields $-A_2$. Thus $A_1(x)\boldsymbol{v} = 0$ implies $A_2(x)\boldsymbol{v} = 0$ and therefore v_2 satisfies the pure diffusion equation with Neumann BC's: $D_0\partial_x^2\boldsymbol{v_2} = 0$. This yields $v_2 = 1$ and the vector $\boldsymbol{v_1}$ can then be found by solving the rank-p system for p unknowns in (8) with given v_2. Therefore, the dimension of the kernel is clearly 1 in this case.

For the case $q > 1$, the conservative nature of the rate matrix A also ensures that $(1, 1, ..., 1)^T \in N(L^*(0,0))$, however there is no guarantee that this is the only solution of $L^*(0,0)\boldsymbol{v} = 0$ (see counter-example in Remark 3). This motivates our assumption that $\dim(ker(L_0^*)) = 1$. We note however that models with two diffusing species and one non-diffusing population can also be shown to satisfy the theorem assumption.

Remark 3. An example of a system that does not satisfy the theorem assumption would consist of two decoupled copies of the 2-state system, each with an advection and a diffusion state. In this case, each individual system has an eigenvalue at 0 (with one corresponding eigenvector each). This means that the eigenvalue zero is no longer algebraically simple.

2.4. Application to the 2-state model. We now discuss the implications of Theorem 2.1 for the 2-state system (2) with one moving and one diffusing particle population. Remark 2 of §2.3 guarantees that the 2-state model satisfies the conditions of Theorem 2.1. The effective velocity and diffusion of the particles under this model are given by the following expressions:

$$v_{\text{eff}} = \frac{\langle\alpha\rangle}{\langle\alpha\rangle + \beta} v_0\,,$$

$$\sigma_{\text{eff}} = \frac{\beta}{\langle\alpha\rangle + \beta} D_0 + \frac{\beta\langle\alpha\rangle}{(\beta + \langle\alpha\rangle)^3} v_0^2 + \frac{\beta}{(\beta + \langle\alpha\rangle)^2} v_0 \langle\alpha(x), w^0(x)\rangle\,, \tag{10}$$

where $\langle\alpha\rangle = \int_0^1 \alpha(x)dx$, and $w^0(x)$ is the unique solution of

$$D_0 w^0_{xx} = \frac{v_0}{\beta + \langle\alpha\rangle}(\langle\alpha\rangle - \alpha(x))\,, \qquad w^0_x(0) = w^0_x(1) = 0\,. \tag{11}$$

Before discussing the implications of these results for transport, we briefly comment on the expressions we obtained above. First, when the filaments are equidistributed in the domain so that $\alpha(x) = \bar{\alpha}$ is a constant function, we have $\langle\alpha\rangle = \bar{\alpha}$, and therefore $w^0(x) = 0$, so that the effective velocity and diffusion constants in this simpler case are given by

$$v^0_{\text{eff}} = \frac{\bar{\alpha}}{\bar{\alpha}+\beta} v_0\,, \qquad \sigma^0_{\text{eff}} = \frac{\beta}{\bar{\alpha}+\beta} D_0 + \frac{\beta\bar{\alpha}}{(\beta+\bar{\alpha})^3} v_0^2\,, \tag{12}$$

see also [9]. Next, we compare our results with those in [7] where the additional assumption $|\alpha| \ll \beta$ was used. In [7], the effective equation describing sum $c(\boldsymbol{r},t) = \bar{p}(\boldsymbol{r},t) + p_0(\boldsymbol{r},t)$ of the particle populations for parallel filaments became:

$$\frac{\partial c}{\partial t} = v_{\text{eff}} \frac{\partial c}{\partial y} + D(x,t)\nabla^2 c(\boldsymbol{r},t) + Q_{yy}(x,t)\frac{\partial^2 c}{\partial y^2}\,,$$

with effective velocity $v_{\text{eff}} = \frac{\alpha}{\beta} v_0$ and effective diffusion $D(x,t) + Q_{yy}(x,t) = (1-\frac{\alpha}{\beta})D_0 + \frac{\alpha}{\beta^2} v_0^2$ in the y-direction. While our results are very similar to these expressions (when using the hypothesis $|\alpha| \ll \beta$ that was used in [7]), it is worth noting that the expressions for the effective velocity and diffusion in [7] maintain the spatial dependence through the concentration of signaling molecules $\alpha(x)$, whereas our large-time results depend only on the space-averaged quantity $\bar{\alpha}$. Note that the last term in our expression (10) for the effective diffusion is not captured by the analysis in [7]. The advantage of our method is that it allows derivation of complete expressions for effective velocity and diffusion under no assumptions on the density of the microtubules, the magnitude of the reaction rates, and the diffusion coefficient.

Next, we discuss the consequences of our results for transport. Comparing the expressions for the effective diffusion for general filament densities $\alpha(x)$ in (10) with those in (12) for constant α, we see that the expression for the effective diffusion in (10) contains the additional term $\frac{\beta}{(\beta+\langle\alpha\rangle)^2} v_0 \langle\alpha(x), w^0(x)\rangle$: it is this term that captures the density-dependence of diffusion. Our next result shows that diffusion is enhanced when the filament density is not constant.

Lemma 2.2. *For the 2-state advection-diffusion system (2) and any relevant parameters, the additional term in the effective diffusion expression is non-negative:*

$$v = \frac{\beta}{(\beta+\langle\alpha\rangle)^2} v_0 \langle\alpha(x), w^0(x)\rangle \geq 0\,.$$

Proof. Noting that $\langle\alpha\rangle = \alpha$ in the case where filaments are assumed to be available throughout the domain,

$$\sigma_{\text{eff}} - \sigma^0_{\text{eff}} = v\,.$$

To determine the sign of term v, we integrate equation (11) against w^0:

$$\int_0^1 D_0 (w^0)_{xx} w^0 dx = \frac{v_0}{\beta+\langle\alpha\rangle} \int_0^1 (\langle\alpha\rangle - \alpha(x)) w^0 dx\,. \tag{13}$$

Denoting $f = \frac{v_0}{\beta+\langle\alpha\rangle}$, we have:

$$\int_0^1 \alpha(x) w^0(x) dx = (1/f)\left(f\langle\alpha\rangle \int_0^1 w^0(x) dx - \int_0^1 D_0 (w^0)_{xx} w^0 dx \right)\,.$$

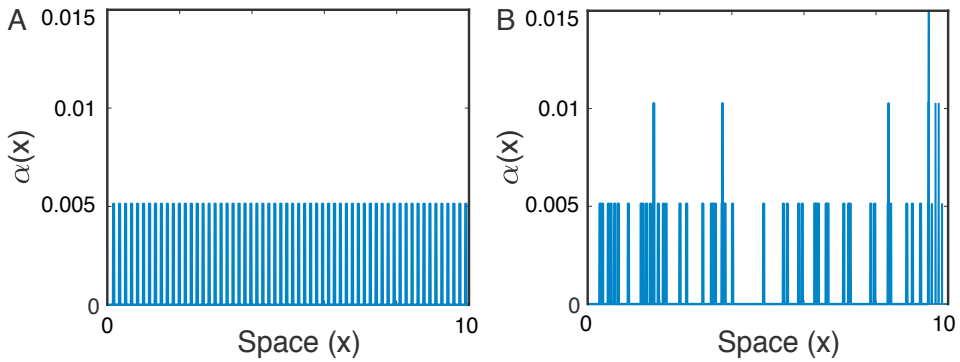

Figure 3. *A. Illustration of $\alpha(x)$ for a uniformly-spaced MT structure. B. Illustration of $\alpha(x)$ for a randomly-spaced MT structure.*

Using that $\langle w^0(x)\rangle = 0$ and integration by parts combined with the Neumann boundary conditions in (11) yields:

$$\int_0^1 \alpha(x) w^0 dx = (1/f) \int_0^1 D_0 (w_x^0)^2 dx \geq 0\,.$$

Therefore

$$v = \frac{\beta}{(\beta + \langle\alpha\rangle)^2} \frac{v_0}{f} \int_0^1 D_0 (w_x^0)^2 dx\rangle \geq 0\,,$$

so the additional term in (36) is non-negative for all biologically-relevant (positive) choices of the transition rates, diffusion coefficient, and velocity parameters. ∎

Thus, Lemma 2.2 suggests that accounting for the microtubule geometry when modeling particle transport consistently increases the effective spread of the particles in the large time limit. In other words, we predict that the microtubule-dependent dynamics in equations (2) have a larger spatial variability (effective diffusion in equation (10)) than dynamics where the transition rates are assumed to be constant. To investigate how different arrangements of filaments may contribute differently to the effective diffusion, we consider functions $\alpha(x)$ that correspond to a uniform arrangement of microtubules (see Figure 3A) as well as a random arrangement of filaments (see Figure 3B).

The contribution to the spread of particles is determined by integrating the second order equation (11):

$$D_0 w_{xx}^0 = \frac{v_0}{\beta + \langle\alpha\rangle}(\langle\alpha\rangle - \alpha(x))\,, \qquad w_x^0(0) = w_x^0(1) = 0\,.$$

using a centered finite difference scheme. We consider this equation on a domain of $20-30$ μm (10 μm visualized in Figure 3A-B) and assume a realistic microtubule diameter of 25 nm.

Figure 4 shows the percentage increase in the effective diffusion of particles for a set of parameters ($\bar{\alpha}$, β, v_0, D) estimated from mRNA FRAP data in *Xenopus laevis* [9]. The choice of $\alpha(x)$ that reflects the uniform arrangement of microtubules in Figure 3A shows an increase of almost 10% (blue line) compared to the case where spatial microtubules are not modeled and $\alpha(x) = \alpha$ (constant). For $\alpha(x)$ corresponding to a random arrangement of microtubules,

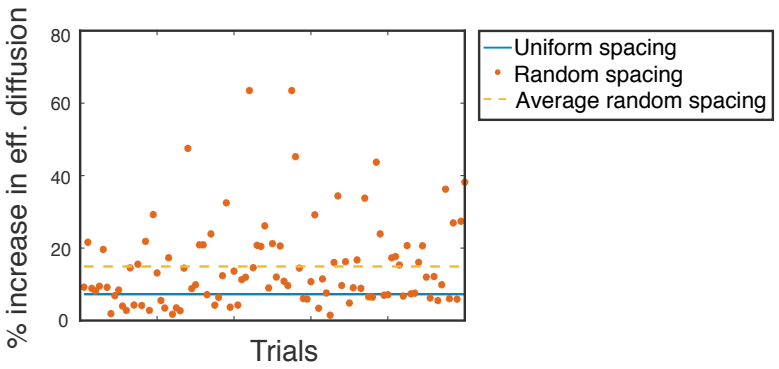

Figure 4. *Increase in effective diffusion of particles when microtubules are arranged uniformly as in Figure 3A (blue line) or randomly as in Figure 3B (red dots for multiple trials and yellow dotted line for average).*

we consider 100 trials, with one sample distribution illustrated in Figure 3B. In this case, the percentage increase varies for each random position trial (red dots), but the average increase reaches roughly 17% (yellow dotted line). While Figure 4 corresponds to a particular set of parameters, we confirmed the larger diffusivity in the random filament arrangement using additional parameters from data in other oocytes as considered in [9].

2.5. Proof of Theorem 2.1.

Proof. Consider the ansatz

$$(u_1, ..., u_n)^T = \bar{v}(x) e^{\lambda t + iky} \tilde{\boldsymbol{u}}_{\mathbf{0}} \,, \tag{14}$$

where $\bar{v}(x)$ is a diagonal matrix with $v_i(x)$ in location (i,i), and $\tilde{\boldsymbol{u}}_{\mathbf{0}}$ is a vector of initial conditions. Plugging this into (3), we obtain:

$$D\bar{v}_{xx}\tilde{\boldsymbol{u}}_{\mathbf{0}} + (A(x) + \nu C + \nu^2 D - \lambda I)\bar{v}(x)\tilde{\boldsymbol{u}}_{\mathbf{0}} = 0 \,.$$

This suggests that we can incorporate vector $\tilde{\boldsymbol{u}}_{\mathbf{0}}$ with matrix $\bar{v}$ into a vector $\boldsymbol{v}(x)$ so that:

$$D\boldsymbol{v}_{xx} + (A(x) + \nu C + \nu^2 D - \lambda I)\boldsymbol{v}(x) = 0 \,. \tag{15}$$

We define the operator

$$L(\lambda, \nu) = D\partial_x^2 + A(x) + \nu C + \nu^2 D - \lambda I \,,$$

defined on $\mathcal{C}^2(\mathbb{R})$. Note this operator is not necessarily self-adjoint: $L(0,0) = D\partial_x^2 + A(x)$, $L^*(0,0) = D\partial_x^2 + A^*(x)$.

We observe that the second derivative with homogeneous boundary conditions is a Fredholm operator with index 0, and the relatively compact perturbation consisting of adding the linear operator $A(x) + \nu C + \nu^2 D - \lambda I$ maintains this property. By assumption, $\dim(ker(L^*(0,0))) = 1$, therefore $\mathrm{codim}(R(L(0,0))) = \dim(N(L(0,0))) = 1$ and we let $N(L^*(0,0)) = \boldsymbol{\psi}_{\mathbf{0}}(x)$ and $N(L(0,0)) = \boldsymbol{u}_{\mathbf{0}}(x)$. A few remarks on the assumption that $\dim(ker(L_0^*)) = 1$ are provided in § 2.3.

Since the nullspace of operator $L(0,0)$ is finite-dimensional, we can apply Lyapunov-Schimdt reduction theory to study the solutions of equation (15). For this construction, we take $\boldsymbol{v}(x) = a\boldsymbol{u_0}(x) + \boldsymbol{w}(x)$, where $w(x)$ satisfies $\langle \boldsymbol{\psi_0}(x), w(x)\rangle = 0$. We can now project the equation (re-written below) on the range and kernel of the operator.

$$D\boldsymbol{v}_{xx} + (A(x) + \nu C + \nu^2 D - \lambda I)\boldsymbol{v}(x) = 0\,.$$

Projection on the range.

$$Lv - \frac{\langle Lv, \boldsymbol{\psi_0}\rangle}{\langle \boldsymbol{\psi_0}, \boldsymbol{u_0}\rangle}\boldsymbol{u_0} = 0\,.$$

This gives:

$$(D\partial_x^2 + A(x))\boldsymbol{w}(x) + (\nu C + \nu^2 D - \lambda I)(a\boldsymbol{u_0} + \boldsymbol{w}) - a\frac{\langle \boldsymbol{\psi_0}, (\nu C + \nu^2 D - \lambda I)\boldsymbol{u_0}\rangle}{\langle \boldsymbol{\psi_0}, \boldsymbol{u_0}\rangle}\boldsymbol{u_0} - \frac{\langle \boldsymbol{\psi_0}, (\nu C + \nu^2 D - \lambda I)\boldsymbol{w}\rangle}{\langle \boldsymbol{\psi_0}, \boldsymbol{u_0}\rangle}\boldsymbol{u_0} = 0\,, \tag{16}$$

where we used that $L_0\boldsymbol{u_0} = 0$ and $L_0^*\boldsymbol{\psi_0} = 0$. Here denote $L_0 = L(0,0)$ and $L_0^* = L^*(0,0)$.

The third term above can be written as

$$a\frac{\langle \boldsymbol{\psi_0}, (\nu C + \nu^2 D - \lambda I)\boldsymbol{u_0}\rangle}{\langle \boldsymbol{\psi_0}, \boldsymbol{u_0}\rangle}\boldsymbol{u_0} = -a\lambda\boldsymbol{u_0} + a\nu(B_\nu\boldsymbol{u_0})\boldsymbol{u_0}\,,$$

with B_ν taking $\boldsymbol{x}$ to $\frac{\langle \boldsymbol{\psi_0}, (C+\nu D)\boldsymbol{x}\rangle}{\langle \boldsymbol{\psi_0}, \boldsymbol{u_0}\rangle}$.

Similarly, the fourth term is

$$\frac{\langle \boldsymbol{\psi_0}, (\nu C + \nu^2 D - \lambda I)\boldsymbol{w}\rangle}{\langle \boldsymbol{\psi_0}, \boldsymbol{u_0}\rangle}\boldsymbol{u_0} = \nu(B_\nu\boldsymbol{w})\boldsymbol{u_0}\,,$$

since $\langle \boldsymbol{\psi_0}, \boldsymbol{\lambda w}\rangle = \lambda\langle \boldsymbol{\psi_0}, \boldsymbol{w}\rangle = 0$.

Combining these, we obtain:

$$(D\partial_x^2 + A(x) + \nu C + \nu^2 D - \lambda I - \nu\boldsymbol{u_0}B_\nu)\boldsymbol{w}(x) + a(\nu C + \nu^2 D)\boldsymbol{u_0} - a\lambda\boldsymbol{u_0} + a\lambda\boldsymbol{u_0} - a\nu(B_\nu\boldsymbol{u_0})\boldsymbol{u_0} = 0\,,$$

therefore

$$(D\partial_x^2 + A(x) + \nu C + \nu^2 D - \lambda I - \nu\boldsymbol{u_0}B_\nu)\boldsymbol{w}(x) + a(\nu C + \nu^2 D - \nu(B_\nu\boldsymbol{u_0}))\boldsymbol{u_0} = 0\,. \tag{17}$$

Projection on the kernel.

$$\langle \boldsymbol{\psi_0}, Lv\rangle = 0\,.$$

This gives:

$$\langle \boldsymbol{\psi_0}, (D\partial_x^2 + A(x) + \nu C + \nu^2 D - \lambda I)(a\boldsymbol{u_0}(x) + \boldsymbol{w}(x))\rangle = 0\,.$$

Using $L_0\boldsymbol{u_0} = 0$, $\langle \boldsymbol{\psi_0}(x), \boldsymbol{w}(x)\rangle = 0$, and $L_0^*\boldsymbol{\psi_0} = 0$:

$$\langle \boldsymbol{\psi_0}, (\nu C + \nu^2 D - \lambda I)a\boldsymbol{u_0}(x) + (\nu C + \nu^2 D)\boldsymbol{w}(x)\rangle = 0\,.$$

Therefore

$$\lambda = \frac{\langle \boldsymbol{\psi_0}, (\nu C + \nu^2 D)(a\boldsymbol{u_0}(x) + \boldsymbol{w}(x))\rangle}{a\langle \boldsymbol{\psi_0}, \boldsymbol{u_0}\rangle}$$

$$= \nu\frac{\langle \boldsymbol{\psi_0}, C\boldsymbol{u_0}\rangle}{\langle \boldsymbol{\psi_0}, \boldsymbol{u_0}\rangle} + \nu^2\frac{\langle \boldsymbol{\psi_0}, D\boldsymbol{u_0}\rangle}{\langle \boldsymbol{\psi_0}, \boldsymbol{u_0}\rangle} + \nu\frac{\langle \boldsymbol{\psi_0}, (C+\nu D)\boldsymbol{w}\rangle}{a\langle \boldsymbol{\psi_0}, \boldsymbol{u_0}\rangle}\,, \tag{18}$$

where $\boldsymbol{w}$ satisfies equation (17).

Note that equation (17) can be expressed as $h(\nu, w(x)) = 0$, where $h(0, \boldsymbol{u_0}) = 0$ and $\lambda(0) = 0$ given (18). Since $\frac{\partial h}{\partial \boldsymbol{w}}|_{(0,\boldsymbol{u_0})} = D\partial_x^2 + A(x)$ with homogeneous Neumann boundary conditions, we conclude that $\boldsymbol{w}(x) = g(\nu, x)$ for each x. Let

$$\boldsymbol{w}(x) = \nu\boldsymbol{w_1}(x) + \nu^2\boldsymbol{w_2}(x) + \mathcal{O}(\nu^3)\,. \tag{19}$$

It follows that equation (18) becomes:

$$\lambda = \nu\frac{\langle \boldsymbol{\psi_0}, C\boldsymbol{u_0}\rangle}{\langle \boldsymbol{\psi_0}, \boldsymbol{u_0}\rangle} + \nu^2\frac{\langle \boldsymbol{\psi_0}, D\boldsymbol{u_0}\rangle}{\langle \boldsymbol{\psi_0}, \boldsymbol{u_0}\rangle} + \nu^2\frac{\langle \boldsymbol{\psi_0}, C\boldsymbol{w_1}(x)\rangle}{a\langle \boldsymbol{\psi_0}, \boldsymbol{u_0}\rangle} + \mathcal{O}(\nu^3)\,, \tag{20}$$

We therefore need to determine $\boldsymbol{w_1}(x)$. Plugging in the expansion of $\boldsymbol{w}$ in the projection onto the range in equation (17) we obtain:

$$(D\partial_x^2 + A(x) + \nu C + \nu^2 D - \nu\frac{\langle \boldsymbol{\psi_0}, C\boldsymbol{u_0}\rangle}{\langle \boldsymbol{\psi_0}, \boldsymbol{u_0}\rangle}I + \mathcal{O}(\nu^2)I - \nu\boldsymbol{u_0}B_\nu)(\nu\boldsymbol{w_1}(x) + \nu^2\boldsymbol{w_2}(x) + \mathcal{O}(\nu^3))$$

$$+ a(\nu C + \nu^2 D - \nu(B_\nu\boldsymbol{u_0}))\boldsymbol{u_0} = 0\,. \tag{21}$$

By collecting powers of ν in (21), we have for $\mathcal{O}(\nu)$:

$$(D\partial_x^2 + A(x))\boldsymbol{w_1}(x) + aC\boldsymbol{u_0}(x) - a\frac{\langle \boldsymbol{\psi_0}, C\boldsymbol{u_0}\rangle}{\langle \boldsymbol{\psi_0}, \boldsymbol{u_0}\rangle}\boldsymbol{u_0}(x) = 0\,. \tag{22}$$

Writing $\lambda = a_1\nu + a_2\nu^2 + \mathcal{O}(\nu^3)$ yields:

$$a_1 = \frac{\langle \boldsymbol{\psi_0}, C\boldsymbol{u_0}\rangle}{\langle \boldsymbol{\psi_0}, \boldsymbol{u_0}\rangle}\,, \tag{23}$$

$$a_2 = \frac{\langle \boldsymbol{\psi_0}, D\boldsymbol{u_0}\rangle}{\langle \boldsymbol{\psi_0}, \boldsymbol{u_0}\rangle} + \frac{\langle \boldsymbol{\psi_0}, C\boldsymbol{w_1}(x)\rangle}{a\langle \boldsymbol{\psi_0}, \boldsymbol{u_0}\rangle}\,, \tag{24}$$

where $\boldsymbol{w_1}$ satisfies equation (22).

We now return with this expansion to the ansatz in (14). We are particularly interested in recovering the concentration of particles in each state for large time given these expansions. Using the inverse Fourier transform gives:

$$\boldsymbol{u}(\boldsymbol{r}, t) \approx \frac{1}{2\pi}\int_{-\delta}^{\delta}(a\boldsymbol{u_0}(x) + \boldsymbol{w}(x))e^{\lambda t + iky}dk$$

$$= \frac{1}{2\pi}\int_{-\delta}^{\delta}(a\boldsymbol{u_0}(x) + \boldsymbol{w}(x))e^{ik(y+a_1t) - a_2k^2t}e^{\sum_{j=3}^{\infty}a_j(ik)^jt}dk\,, \tag{25}$$

with δ small. Making the change of variable $\tilde{k} = kt^{1/2}$ and $\tilde{y} = y + a_1 t$ yields:

$$\begin{aligned} \boldsymbol{u}(\boldsymbol{r},t) &\approx \frac{1}{2\pi\sqrt{t}} \int_{-\delta\sqrt{t}}^{\delta\sqrt{t}} (a\boldsymbol{u_0}(x) + \boldsymbol{w}(x)) e^{i\tilde{k}\frac{\tilde{y}}{t^{1/2}} - \frac{a_2}{2}\tilde{k}^2} e^{\sum_{j=3}^{\infty} a_j \frac{(i\tilde{k})^j}{t^{j/2-1}}} d\tilde{k} \\ &= \frac{1}{2\pi\sqrt{t}} \int_{-\delta\sqrt{t}}^{\delta\sqrt{t}} \left(a\boldsymbol{u_0}(x) + i\frac{\tilde{k}}{t^{1/2}}\boldsymbol{w_1}(x) - \frac{\tilde{k}^2}{t}\boldsymbol{w_2}(x) + \sum_{j=1}^{\infty} \frac{(i\tilde{k})^j}{t^{j/2}}\boldsymbol{w_j}(x) \right) \times \\ &\quad e^{i\tilde{k}\frac{\tilde{y}}{t^{1/2}} - \frac{a_2}{2}\tilde{k}^2} e^{\sum_{j=3}^{\infty} a_j \frac{(i\tilde{k})^j}{t^{j/2-1}}} d\tilde{k} \,. \end{aligned} \tag{26}$$

Since we are interested in long-term asymptotic behavior at $t \to \infty$, we note that the dominant term in the expansion of $\boldsymbol{w}(x)$ is $a\boldsymbol{u_0}(x)$ and that the last exponential term in (27) converges to 1. Therefore:

$$\boldsymbol{u}(\boldsymbol{r},t) \approx \frac{1}{2\pi\sqrt{t}} a\boldsymbol{u_0}(x) \int_{-\infty}^{\infty} e^{i\tilde{k}\frac{\tilde{z}}{t^{1/2}} - \frac{a_2}{2}\tilde{k}^2} d\tilde{k} = \frac{a}{\sqrt{2\pi a_2 t}} e^{\frac{(y+a_1 t)^2}{2a_2 t}} \boldsymbol{u_0}(x) \,. \tag{27}$$

The Gaussian form of the asymptotic solution for large time provides the effective velocity and effective diffusion of the particles, given by a_1 and a_2, respectively, in equations (23) and (24). ∎

2.6. Proof of the 2-state model results.

Set-up for the 2-state system. In the 2-state model, the set-up for equation (15) is as follows:

$$C = \begin{pmatrix} v_0 & 0 \\ 0 & 0 \end{pmatrix}, \; D = \begin{pmatrix} 0 & 0 \\ 0 & D_0 \end{pmatrix}, \; A(x) = \begin{pmatrix} -\beta & \alpha(x) \\ \beta & -\alpha(x) \end{pmatrix} .$$

Solving $L(0,0) = 0$ is equivalent to solving:

$$\begin{aligned} -\beta v_1(x) + \alpha(x) v_2(x) &= 0 \,, \\ D_0 \partial_x^2 (v_2) + \beta v_1(x) - \alpha(x) v_2(x) &= 0 \,, \end{aligned} \tag{28}$$

so that $D_0 (v_2)_{xx} = 0$ and with the homogeneous Neumann boundary conditions, $v_2 = 1$ (constant). Then $v_1 = \alpha(x)/\beta$, yielding:

$$N(L(0,0)) = (\alpha(x)/\beta, 1)^T \,.$$

Similarly for $N(L^*(0,0))$, we solve:

$$\begin{aligned} -\beta(v_1(x) - v_2(x)) &= 0 \,, \\ D\partial_x^2 (v_2) + \alpha(x)(v_2(x) - v_1(x)) &= 0 \,, \end{aligned} \tag{29}$$

which yields $v_1 = v_2 = 1$. Thus

$$N(L^*(0,0)) = (1,1)^T \,,$$

so that both nullspaces are finite and have dimension 1. The assumption in the theorem is therefore satisfied.

Results for the 2-state system. We now write the results in equations (23) and (24) in the context of the 2-state model. In this case we have

$$\boldsymbol{\psi_0} = (1,1)^T$$
$$\boldsymbol{u_0} = (\alpha(x)/\beta, 1)^T\,,$$

and $\langle \boldsymbol{\psi_0}, \boldsymbol{u_0}\rangle = \langle 1, \alpha(x)\rangle/\beta + 1 = \frac{\beta + \langle 1,\alpha(x)\rangle}{\beta}$.

The fact that $\boldsymbol{w} \in N(L_0^*)^\perp$ means that:

$$\int_0^1 w_1(x) + w_2(x)dx = 0\,,$$

for $\boldsymbol{w}(x) = (w_1(x), w_2(x))^T$. This implies that $\int_0^1 w_2(x) = -\int_0^1 w_1(x)$.

Writing $\lambda = a_1\nu + a_2\nu^2 + \mathcal{O}(\nu^3)$ and using (23), we have:

$$a_1 = v_{eff} = \frac{\langle \boldsymbol{\psi_0}, C\boldsymbol{u_0}\rangle}{\langle \boldsymbol{\psi_0}, \boldsymbol{u_0}\rangle} = \frac{v_0\langle 1,\alpha(x)\rangle/\beta}{\frac{\langle 1,\alpha(x)\rangle+\beta}{\beta}} = \frac{\langle 1,\alpha(x)\rangle}{\langle 1,\alpha(x)\rangle + \beta}v_0\,. \tag{30}$$

Similarly, the first term in a_2 is:

$$\frac{\langle \boldsymbol{\psi_0}, D\boldsymbol{u_0}\rangle}{\langle \boldsymbol{\psi_0}, \boldsymbol{u_0}\rangle} = \frac{D_0}{\frac{\langle 1,\alpha(x)\rangle+\beta}{\beta}} = \frac{\beta}{\langle 1,\alpha(x)\rangle + \beta}D_0\,, \tag{31}$$

We now need to evaluate the second term in a_2, namely

$$\frac{\langle \boldsymbol{\psi_0}, C\boldsymbol{w_1}(x)\rangle}{\langle \boldsymbol{\psi_0}, \boldsymbol{u_0}\rangle} = \frac{\beta}{\beta + \langle 1,\alpha(x)\rangle}v_0\langle 1, w_{11}(x)\rangle\,,$$

where $\boldsymbol{w_1}(x) = (w_{11}(x), w_{12}(x))^T$. Recall that $\boldsymbol{w_1}$ satisfies equation (22):

$$(D\partial_x^2 + A(x))\boldsymbol{w_1}(x) + aC\boldsymbol{u_0}(x) - a\frac{\langle \boldsymbol{\psi_0}, C\boldsymbol{u_0}\rangle}{\langle \boldsymbol{\psi_0}, \boldsymbol{u_0}\rangle}\boldsymbol{u_0}(x) = 0\,.$$

Therefore:

$$\begin{pmatrix}0 & 0\\ 0 & D_0\end{pmatrix}\begin{pmatrix}(w_{11})_{xx}\\ (w_{12})_{xx}\end{pmatrix} + \begin{pmatrix}-\beta & \alpha(x)\\ \beta & -\alpha(x)\end{pmatrix}\begin{pmatrix}w_{11}\\ w_{22}\end{pmatrix} + \begin{pmatrix}v_0\alpha(x)/\beta\\ 0\end{pmatrix} - \frac{\langle 1,\alpha(x)\rangle}{\langle 1,\alpha(x)\rangle + \beta}v_0\begin{pmatrix}\alpha(x)/\beta\\ 1\end{pmatrix} = 0\,.$$

This is equivalent to solving the system:

$$-\beta w_{11} + \alpha(x)w_{12} + v_0\frac{\alpha(x)}{\beta + \langle 1,\alpha(x)\rangle} = 0\,,$$
$$D_0(w_{12})_{xx} + \beta w_{11} - \alpha(x)w_{12} - v_0\frac{\langle 1,\alpha(x)\rangle}{\beta + \langle 1,\alpha(x)\rangle} = 0\,,$$

which then yields:

$$D_0(w_{12})_{xx} = \frac{v_0}{\beta + \langle 1,\alpha(x)\rangle}(\langle 1,\alpha(x)\rangle - \alpha(x)) \tag{32}$$
$$w_{11}(x) = \frac{v_0\alpha(x)}{\beta(\beta + \langle 1,\alpha(x)\rangle)} + \frac{\alpha(x)}{\beta}w_{12}(x)\,.$$

Therefore:

$$\frac{\langle \boldsymbol{\psi_0}, C\boldsymbol{w_1}(x)\rangle}{\langle \boldsymbol{\psi_0}, \boldsymbol{u_0}\rangle} = \frac{\beta}{\beta + \langle 1, \alpha(x)\rangle} v_0 \langle 1, w_{11}(x)\rangle$$
$$= \frac{\langle 1, \alpha(x)\rangle}{(\beta + \langle 1, \alpha(x)\rangle)^2} v_0^2 + \frac{1}{(\beta + \langle 1, \alpha(x)\rangle)} v_0 \langle \alpha(x), w_{12}(x)\rangle \,,$$

where w_{12} satisfies (32).

Noting that the right-hand-side (RHS) of equation (32) satisfies $\langle RHS\rangle = \int_0^1 RHS = 0$, we write $w_{12} = d + w_{12}^0$ with arbitrary $d \in \mathbb{R}$ and $\langle w_{12}^0\rangle = 0$. w_{12}^0 then satisfies equation (32) as well. This gives:

$$w_{11} = \frac{v_0 \alpha(x)}{\beta(\beta + \langle 1, \alpha(x)\rangle)} + \frac{\alpha(x)}{\beta} d + \frac{\alpha(x)}{\beta} w_{12}^0(x)$$
$$\langle w_{11}\rangle + \langle w_{12}\rangle = \frac{v_0 \alpha(x)}{\beta(\beta + \langle 1, \alpha(x)\rangle)} + \frac{\alpha(x)}{\beta} d + \frac{\alpha(x)}{\beta} w_{12}^0(x) + d = 0 \,.$$

From this, we find:

$$d = -\frac{1}{\langle \alpha\rangle + \beta} \left(\frac{\langle \alpha\rangle}{\langle \alpha\rangle + \beta} v_0 + \langle \alpha w_{12}^0\rangle \right) ,$$

and the expression for w_{11}:

$$w_{11} = \frac{\langle \alpha\rangle}{(\langle \alpha\rangle + \beta)^2} v_0 - \frac{\langle \alpha\rangle}{\beta(\langle \alpha\rangle + \beta)} \langle \alpha w_{12}^0\rangle + \frac{\alpha}{\beta} w_{12}^0 \,. \tag{33}$$

Then the second term in a_2 becomes:

$$\frac{\langle \boldsymbol{\psi_0}, C\boldsymbol{w_1}(x)\rangle}{\langle \boldsymbol{\psi_0}, \boldsymbol{u_0}\rangle} = \frac{\beta}{\beta + \langle 1, \alpha(x)\rangle} v_0 \langle 1, w_{11}(x)\rangle$$
$$= \frac{\beta \langle \alpha(x)\rangle}{(\beta + \langle 1, \alpha(x)\rangle)^3} v_0^2 + \frac{1}{(\beta + \langle 1, \alpha(x)\rangle)} v_0 \langle \alpha(x), w_{12}^0(x)\rangle \left(-\frac{\langle \alpha\rangle}{(\beta + \langle 1, \alpha(x)\rangle)} + 1 \right) \rangle$$
$$= \frac{\beta \langle \alpha(x)\rangle}{(\beta + \langle 1, \alpha(x)\rangle)^3} v_0^2 + \frac{\beta}{(\beta + \langle 1, \alpha(x)\rangle)^2} v_0 \langle \alpha(x), w_{12}^0(x)\rangle \,. \tag{34}$$

Collecting all the derived terms, we conclude that:

$$a_1 = v_{\text{eff}} = \frac{\langle 1, \alpha(x)\rangle}{\langle 1, \alpha(x)\rangle + \beta} v_0 \,, \tag{35}$$

$$a_2 = \sigma_{\text{eff}} = \frac{\beta}{\langle 1, \alpha(x)\rangle + \beta} D_0 + \frac{\beta \langle 1, \alpha(x)\rangle}{(\beta + \langle 1, \alpha(x)\rangle)^3} v_0^2 + \frac{\beta}{(\beta + \langle 1, \alpha(x)\rangle)^2} v_0 \langle \alpha(x), w_{12}^0(x)\rangle \tag{36}$$

with

$$D_0 (w_{12}^0)_{xx} = \frac{v_0}{\beta + \langle 1, \alpha(x)\rangle} (\langle 1, \alpha(x)\rangle - \alpha(x)) \,. \tag{37}$$

As discussed in § 2.4, this calculation agrees with the results of the quasi-steady-state (QSS) analysis in [7] given their assumption $\alpha(x) \ll \beta$ (which implies $\frac{\beta}{\beta + \alpha(x)} \approx 1$).

3. Random planar microtubule networks and anchoring of mRNA. Our analytical approach applies to determining the large time mobility behavior of biological particles under the assumption of a parallel array of microtubular filaments. However, *Xenopus laevis* oocytes display microtubules that are randomly oriented in the cytoplasm, with a bias towards a radially outward orientation (see [14, Figure S3]). Therefore, we construct microtubule structures $\rho(\boldsymbol{r}, \theta)$ that reflect this outward orientation by adapting the approach proposed in [43] (see Figure 5A). Since the large time analysis is more challenging under the assumption of radially outward microtubules, we use multiple model microtubule structures combined with a more realistic model and a numerical approach similar to [43] to investigate the mRNA spatial distribution at different times during localization.

3.1. Four-state transport model and choice of microtubule networks. In [9], we showed that accounting for bidirectional transport of mRNA using a more complex 4-state model leads to parameter estimation results that agree well with the mRNA localization data in *Xenopus laevis* oocytes [14]. Here we extend the 4-state model in [9] to incorporate the underlying microtubule networks on which active transport of mRNA occurs. In equations (38), u^+ corresponds to a population of particles carried by one type of motor protein down to the vegetal cortex, u^- corresponds to a population transported by other motor proteins up to the nucleus, v is a population freely diffusing in the cytoplasm with diffusion coefficient d, and w corresponds to a population of mRNA paused on the microtubules. As before, these variables refer to the concentrations of particles in each of these states. The switching of the mRNA between these four different dynamical states occurs through binding and unbinding reactions as follows:

$$v_t = d\Delta v - \beta_+ v + \gamma_+ u^+ - \beta_- v + \gamma_- u^- \tag{38a}$$

$$u_t^+ = \nabla(c_+ \boldsymbol{v}_m u^+) + \beta_+ v - \gamma_+ u^+ + \alpha_+ w - \delta_+ u^+ \tag{38b}$$

$$u_t^- = -\nabla(c_- \boldsymbol{v}_m u_y^-) + \beta_- v - \gamma_- u^- + \alpha_- w - \delta_- u^- \tag{38c}$$

$$w_t = \delta_+ u^+ + \delta_- u^- - \alpha_+ w - \alpha_- w\,, \tag{38d}$$

where $\boldsymbol{v_m}$ is a velocity field as in [9] derived from the assumed cytoskeletal network that we describe in § 3.2. The transition rates between the four different states are illustrated in [43, Figure 3B]. We note that these equations extend the 2-state model in [43], but do not account for cytoplasmic flow driven by kinesin motor transport. In *Drosophila* oocytes, the mRNAs are synthesized in the attached nurse cells and transported into the oocyte, so cytoplasmic flows may be important in the mobility of RNA [51]. By contrast in *Xenopus*, oocyte mRNAs are synthesized in the oocyte nucleus, thus we do not consider flows in our simulations of mRNA localization. It is also worth noting that [43] concludes that the cytoplasmic flows do not play a key role in the localization process.

Given the randomness in microtubule orientations in many biological systems, our findings in § 2.4 motivate the study of particle dynamics using realistic geometries of the cytoskeleton informed from experimental data. To better understand mRNA localization mechanisms in *Xenopus* oocytes, we therefore consider accurate filament orientations inspired from microtubule experiments in [14, 15]. In particular, we first generate model microtubule structures by adapting the algorithm in [43] to reflect a 2-dimensional geometry and the assumptions

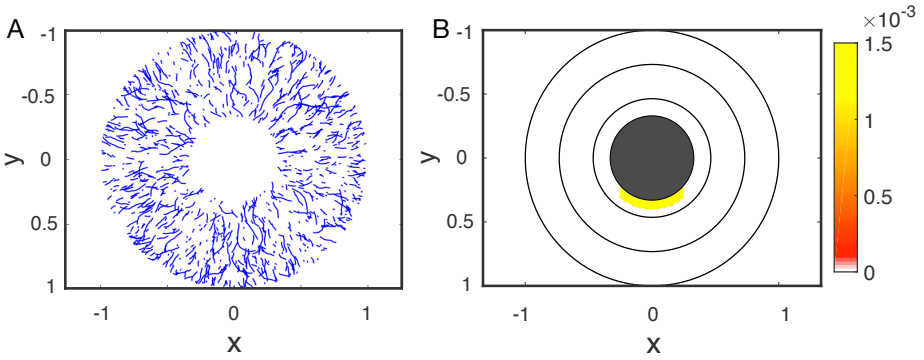

Figure 5. *(A) Sample microtubule structure with 1000 filaments. (B) Initial mRNA particle distribution assuming that the mRNA initially accumulates next to the nucleus. Color bar for the constructed color map is included: yellow corresponds to a high density of mRNA and increasingly red shades denote smaller concentrations of mRNA; white regions have no mRNA traces.*

needed for *Xenopus laevis* oocytes. To create the microtubule network, a random cytoplasmic location (in the circular annulus excluding the nucleus) is chosen as an initiation point for each microtubule. For the microtubule lengths, we consider an exponential distribution of filament lengths and assume that the mean microtubule length is 9 μm, as informed by [16, 17, 35, 41]. Both our results and the findings in [43] are not changed by considering this simpler exponential distribution of microtubule lengths instead of a Gamma distribution that has been proposed to describe the catastrophe lengths of microtubules observed experimentally [17].

As in [43], we model each microtubule as a sequence of straight polymer segments with variable orientations. The direction of the first segment is generated in an outward radial direction or drawn randomly and accepted only if the orientation is pointing inside the allowed geometry [43] (oocyte annulus in our case). For the subsequent segments, we draw directions from the von Mises distribution on a circle with a given likelihood that the next generated segment has a similar orientation to the previous one [43]. For most simulations, the bias for a radially outward orientation of microtubules in *Xenopus* oocytes [15] leads to our modeling assumption that half of the microtubules start with random orientations and half start with radially outward orientations in the first segment.

Simulations of localization discussed in the next sections are run with 50000-60000 filaments for numerical stability, with Figure 5A showing a sample microtubule structure with 1000 filaments for ease of visualization. While it is challenging to quantify the differences between these model structures and images of the microtubule cytoskeleton as in [4, 15], these structures compare well visually with the observed experimental structures. It is worth noting that the microtubule filaments are dynamic and undergo catastrophes on the time scale of localization, with mean lifetimes of roughly 5 minutes on average [17]. As a result, we generate multiple such structures and draw from them at random to set a distinct background microtubule structure at each hour in the simulation of the partial differential equations models (38) considered (more frequent changes do not impact results but increase the computational time).

3.2. Numerical simulations of transport dynamics. In this section we discuss numerical and data analysis methods that will be used in §3.3 below to develop simulations of mRNA localization in *Xenopus* oocytes and to compare results to experimental images.

We consider a two-dimensional domain corresponding to a circular oocyte of radius 150 μm (the average radius for oocytes in stage II of oogenesis [14]) and nucleus of radius 50 μm. In our simulations, we nondimensionalize lengths so that we consider radius $R = 1$, $x \in [-1, 1]$, and $y \in [-1, 1]$. The grid size in our simulations of localization is a square of side 1.5 μm. To ensure that we can simulate transport along microtubules for the advection term in the simulations, we find that we need roughly 9 microtubule segments on average per square grid. Assuming a microtubule diameter of 25 nm, a uniform distribution of microtubules would correspond in our simulations to an average distance of 0.14 μm between microtubules. While there are no references for microtubule spacing in live egg cells, this value is on a similar order of magnitude to distances between microtubule bundles in axons and dendrites ($0.02 - 0.065$ μm) [23].

In addition, we follow the approach in [43] to calculate the velocity field $\boldsymbol{v_m}$ (see equations (38)) where active transport by molecular motor proteins can occur. For this, we calculate the midpoint of each microtubule segment, and sum vectorially the orientations of all segments whose midpoints are located in the same grid area [43]. After normalizing, this yields a local motor-velocity vector field representing the direction along which mRNA molecules can be actively transported by kinesin or dynein motor proteins.

The dynamics of the mRNA is then simulated using the 4-state model in equations (38). The partial differential equations are solved using a finite-volume discretization on staggered grids with no flux boundary conditions [32,43]. Our implementation of the numerical methods extends the algorithm in [43] to account for two active transport states as well as an additional paused state as modeled in equations (38). In addition to considering bidirectional transport in the 4-state model, our simulations use realistic spatially-dependent parameters that we previously estimated from FRAP data in [9]. We note that in that study, we carried out parameter estimation in 3 annular regions where FRAP experiments are performed in the oocyte cytoplasm [9,14]. Here we assume that Region 1 extends 20 μm from the nucleus into the cytoplasm, and Region 3 extends 40 μm from the vegetal cortex into the cytoplasm (see Figure 5B). We use distinct parameters for each region as estimated in [9] (d, c_+, c_-, α_+, α_-, δ_+, δ_-) and set the microtubule binding/unbinding rates (β_+, β_-, γ_+, γ_-) constant as justified in [9]. In our simulations, we set a smooth transition (modeled by a tanh function) over a small spatial radius for parameters that vary in adjacent annular regions. In addition, we set the velocity of the moving population to 0 at the cortex boundary, and allow this speed to decrease from its estimated value in the cytoplasm to 0 in a smooth way as well.

The initial conditions for equations (38) are set to model the early initial accumulation of mRNA in the perinuclear cup region (under the nucleus) in stage II-III *Xenopus* oocytes [14]. We consider a uniform initial condition over a region comparable to experimental observations as illustrated in Figure 5B. This figure also provides the Matlab color map created to visualize the results of our simulations and to compare with [14, Figures 1C, 3D and S2, A-C].

To compare the results of our numerical simulations with experiments, we consider snapshots of the mRNA distribution at different times throughout localization as provided in [14], as well as the time evolution of the mRNA distribution as provided in the Supporting Material

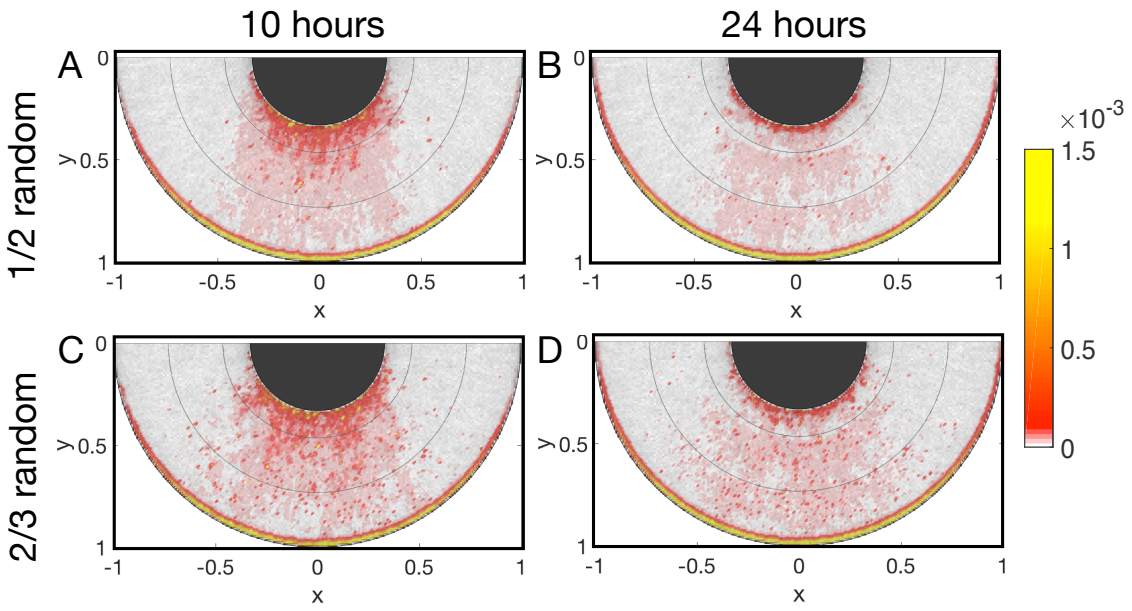

Figure 6. *Predicted mRNA localization distributions 10 (A,C) and 24 (B,D) hours into localization, with transport restricted to microtubule structures (gray background) as in Figure 5A (see also Supporting Material video). The concentric circles drawn in black divide three regions of the vegetal cytoplasm where FRAP experiments have been performed [14]; rate and velocity parameters are constant within each region but differ across regions [9]. (A-B) The label* 1/2 *random corresponds to starting random orientations in half of the model microtubules. (C-D) The label* 2/3 *random corresponds to two thirds of the filaments initialized with random orientations. The color bar from Figure 5 is included.*

video. To extract additional spatial information from the experimental images, cytoplasmic RNA localization in experimental images is also quantified using a custom macro developed for the Fiji distribution of the image processing program ImageJ (version 1.51k; [39, 40]). The macro, which is available at [25], measures the fluorescence intensity in 2D concentric rings (bins) within the oocyte. Based on user-defined input of oocyte and nuclear diameter, the program creates five equally spaced concentric rings (bins) starting at the oocyte periphery and ending at the nuclear periphery. To avoid signal from background and autofluorescence, a threshold is set to consider only pixels within 50% of the maximum observed pixel intensity. The amount of fluorescence is then measured and recorded for each annulus region that forms between consecutive rings.

3.3. Insights into mRNA localization and anchoring at the cell cortex.

The proposed model for mRNA transport on microtubules reproduces observed spatial scales of localization. Figure 6 illustrates the distribution of total mRNA 10 hours (left) and 24 hours (right) into localization. The top panel corresponds to simulations with model microtubule structures where half of the filaments are initialized with random orientations and half with a radial outward direction. The bottom panel corresponds to simulations where 2/3 of the filaments start out with random orientations, leading to a significantly more spread out distribution of mRNA throughout the process. We note that the simulation is run on a full circular

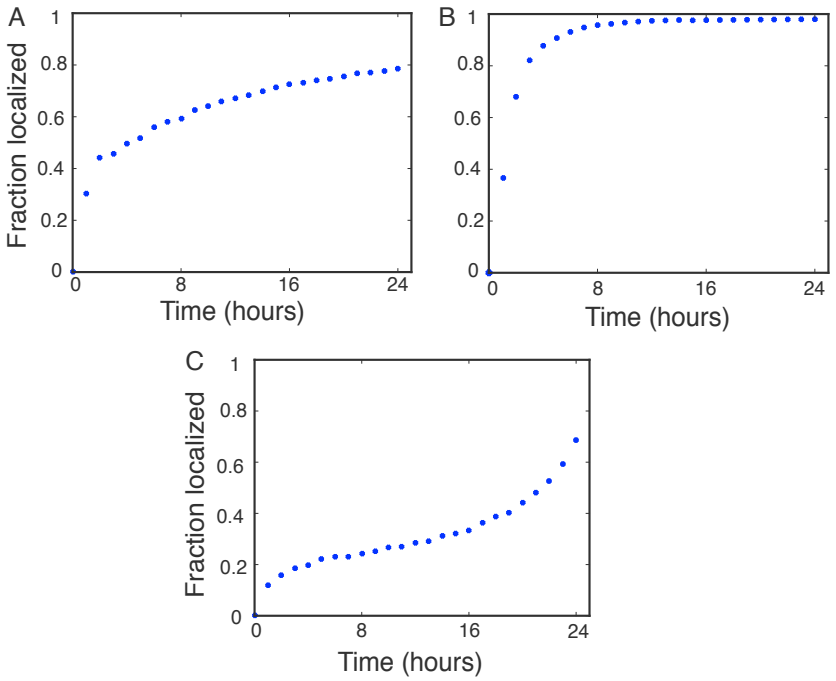

Figure 7. *Predicted fraction of mRNA within* 10% *of the cortex throughout 24 hours of localization for a sample oocyte with no anchoring (A); with anchoring of the transport down state near the vegetal cortex (B); with time-dependent anchoring near the vegetal cortex as described in the text (C). The spatial distribution of the simulated particles at 10 and 24 hours into localization corresponding to (A) is illustrated in Figure 6A-B.*

oocyte, but the dynamics is confined to the vegetal half cytoplasm (as shown) due to the initial accumulation of the particles. In addition, the grey background corresponds to the averaged density of microtubules at each location. This approach allows for comparison to imaging results obtained through injection of fluorescently labeled RNA in *Xenopus* oocytes [14]. The top panel of Figure 6 predicts that the particles are largely confined to a wedge region in the lower cytoplasm, which compares well with the spatial distribution of mRNA in [14, Figures 1C, 3D and S2, A-C]; see also Supporting Material video for an hour-by-hour predicted evolution of the mRNA distribution.

Anchoring a moving population of mRNA particles may be most efficient in achieving faster localization. An alternative way to quantify the amount of mRNA localized at the vegetal cortex is visualized in Figure 7A. There, we plot the time evolution of the fraction of mRNA located within 10% of the cortex as predicted by our simulations. We note that the fraction of localized mRNA reaches roughly 80% in 24 hours of localization, and only slightly increases at the end of 48 hours (results not shown). Since complete localization of mRNA is crucial in this stage of egg cell development and normally occurs within 1-2 days, our results suggest that a potential anchoring mechanism at the cortex may contribute to the observed timescale of healthy localization and development in *Xenopus* oocytes.

While previous studies agree that Vg1 mRNA is anchored at the cell cortex, the mechanisms of this process are not known. Cytoskeleton-dependent RNA anchoring has been sug-

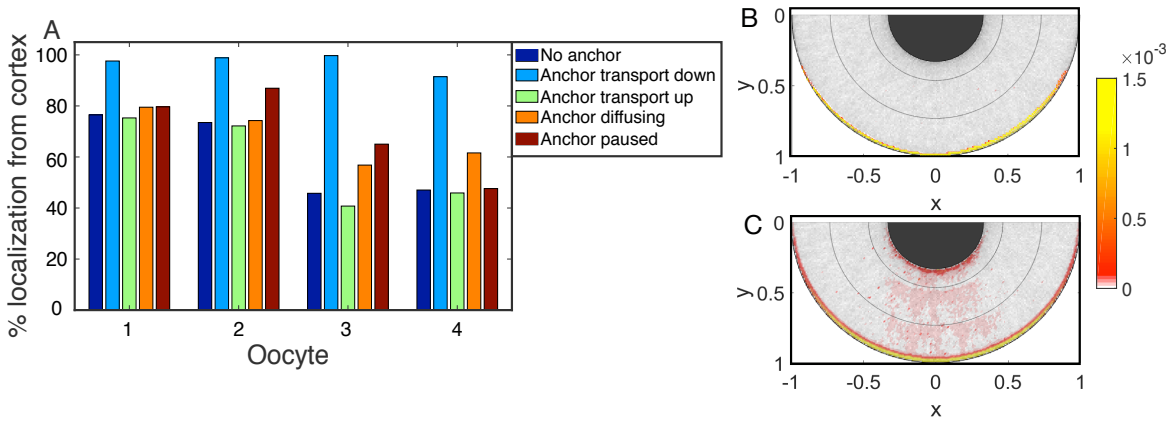

Figure 8. *(A) Predicted fraction of localization at 24 hours of simulation each of the four mRNA states is fully anchored within 5% of the vegetal cortex for parameters from four sample oocytes. The dark blue bar of oocyte 1 corresponds to the RNA distribution illustrated in Figure 6B. (B) Predicted mRNA localization distribution at 24 hours under anchoring of the transport down state (light blue bar for oocyte 1). (C) Predicted mRNA localization distribution at 24 hours under anchoring of the transport up state (green bar for oocyte 1). The color bar from Figure 5 is included.*

gested in other developmental systems. In *Drosophila*, both actin and microtubules have been implicated in anchoring RNA in oocytes and embryos, respectively [2, 11]. Likewise, pharmacological disruption of actin microfilaments [27, 48] in *Xenopus* oocytes causes the release of anchored Vg1 mRNA from the cortex. Evidence for microtubule-mediated anchoring in *Xenopus* oocytes has been inconclusive [1,27], but other cytoskeletal elements, such as cytokeratins, have been implicated [1,29]. Cytoskeleton interacting proteins have also shown a critical role in RNA anchoring in the *Drosophila* oocytes. Such factors include actin-associated proteins [2], endocytic pathway components [42], locally synthesized maternal determinants [47], and even the motor protein dynein [10,11]. Although no anchoring-protein has been identified in *Xenopus*, depletion of other localized RNAs releases anchored Vg1 mRNA, suggesting a potential RNA-dependent RNA anchoring mechanism [20, 26, 28]. Despite the limited experimental insight into the anchoring mechanisms, our model allows to investigate the importance of this process by changing the transition rates between states in an anchoring region (assumed to be 5% from the cortex in our simulations).

In the 4-state model (38) that yields the spatial localization in Figures 6A-B, we can anchor any particular state (transport down, transport up, diffusing, or paused) by setting the reaction rates out of the chosen state to 0 in the anchoring region. For example, setting rates $\gamma_+ = \delta_+ = 0$ (equations (38) and [9, Figure 3B]) next to the vegetal cortex is equivalent to allowing particles to be transported down in this region, but once they reach this state they cannot transition to the diffusion or paused state and are therefore anchored with the attached motor proteins. Figure 8 shows the results of anchoring each state in the 4-state model for simulations of four sample individual oocytes with their corresponding parameter estimates from [9]. While the percentage of localized mRNA increases to some extent when anchoring the paused or diffusing states, Figure 8 clearly suggests that anchoring of the transport down state is most efficient in guaranteeing complete or almost complete localization of mRNA.

These results indicate that anchoring at the cell cortex may depend on stabilization of cargo that is likely actively delivered by molecular motors to the vegetal pole. This hypothesis is supported by experiments in [14, Figure S8], where the motor proteins are found to co-localize with Vg1 RNA at the vegetal cortex 24 hours into localization. While dynein and kinesin motors are hypothesized to be primarily responsible for RNA transport in the upper and lower vegetal cytoplasm in *Xenopus* oocytes [14], our results suggest that an active movement state potentially involving molecular motors may be involved in anchoring of mRNA in this system.

Time-dependent anchoring of mRNA captures the spatial distribution of localization. Figure 8 shows the percentage of mRNA localized 24 hours into localization, yet it does not reveal the dynamics throughout the process. Figure 7B illustrates that allowing complete anchoring of the transport down state (light blue bars in Figure 8) leads to localization of 90% of mRNA particles in less than 8 hours, which is faster than observed in experiments [14]. Therefore, in addition to pointing to a necessary anchoring mechanism in the vegetal cortex, another potential insight from our simulations is that the transition rates in this anchoring region may depend on the amount of mRNA already localized, which may open up more binding sites for anchoring additional mRNA and varies with time [20, 26].

A simple test of this hypothesis is to consider transition rates that vary with time in our simulations. In particular, we allow the rates out of the transport down state (δ_+, γ_+) to decrease smoothly from the estimated values for the lower cytoplasm region in [9] to 0, so that this transport state progresses towards complete anchoring. In addition, we also vary rates β_- and α_- from values an order of magnitude larger than estimated in [9] to their original values, thus allowing for potential recycling of motor proteins so that they can transport additional cargo to the vegetal cortex. We compare our simulations to measures of mRNA content that we extract from experimental images 10 and 24 hours into localization [14, Figure S2] in each spatial annulus around the oocyte nucleus (as described in §3.2). This time-dependent rate scenario provides the best fit of our simulation results to these measurements of mRNA content from experimental images, as illustrated in Figure 9. The progression towards complete anchoring in these transition rates also influences the timescale of localization (see Figure 7C) in our model simulations.

4. Conclusions.

The present work proposes models of intracellular transport that take into account the microtubule networks along which molecular motor proteins transport various proteins and vesicles. We carry out a theoretical analysis of linear PDEs that model concentrations of cargo which can diffuse, pause, or move bidirectionally with space-dependent velocities on a network of parallel microtubules (with space-dependent densities) and determine explicit expressions for effective velocity and diffusion rates for the modeled particles at large times. Numerical simulations building on these theoretical results show that randomly distributed microtubules lead to higher effective diffusion (spread) of cargo, thus indicating that realistic microtubule cytoskeletons should be used in mRNA transport models. Compared with prior theoretical work [7, 19], our theoretical analysis is not restricted to small diffusion and fast reaction rates, as these assumptions may not hold in biological applications as considered here.

We therefore consider a previously-validated model [9] of mRNA transport in *Xenopus*

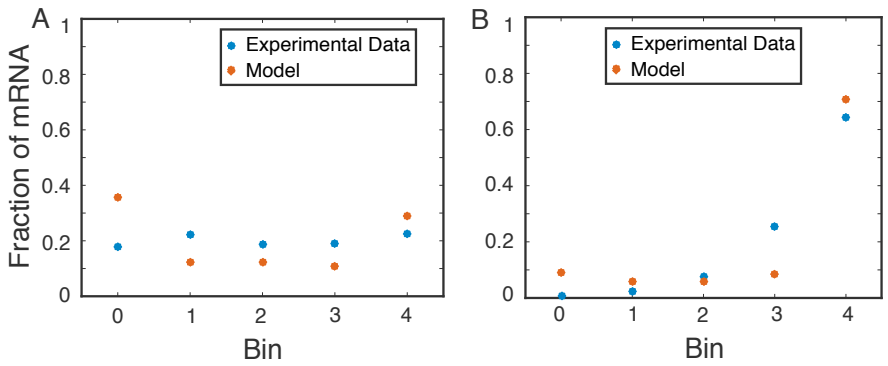

Figure 9. *Comparison of the amount of mRNA localized at 10 (A), respectively 24 (B) hours in each radial spatial bin (Bin 0 is closest to the nucleus and Bin 4 is closest to the vegetal cortex).*

laevis oocytes along microtubules with experimentally-informed geometries. Specifically, we carry out numerical simulations as in [43] of a model that combines diffusion of mRNA in the cell, transport along a discrete microtubule network with orientations and densities as observed in *Xenopus* oocytes, and possible anchoring mechanisms at the cortex (with parameters estimated from FRAP microscopy data in [9]). Our results reproduce experimentally observed localization patterns and indicate that anchoring is needed to reproduce the biological timescales.

Our approach to modeling motor-driven transport of mRNA in *Xenopus* oocytes, as well as previous modeling efforts [7,19,43], assume that molecular motors are available in unlimited supply in the cytoplasm of oocytes at this stage. By including the microtubule cytoskeleton into our models, we are accounting for spatial binding and unbinding of mRNA to the filaments, and are assuming that molecular motors would be available to transport the mRNA once the particles switch to a moving state. While there is no definite experimental evidence, mRNA transport may be rate-limited by the number of kinesin and dynein motors in the cytoplasm. This would explain the need for models that account for bidirectional transport (such as equations (38)). Interactions between cytoplasmic dynein and kinesin have been identified in an array of systems, with mechanisms for interaction of these opposite polarity motors ranging from "tug-of-war" to regulated coordination, as well as roles in motor recycling [3, 5, 8, 12, 18, 21, 22, 24, 30, 31, 45, 46]. Since complete localization of mRNA is key to development of the frog embryo, bidirectional transport may ensure that dynein (and/or kinesin) can fully explore the cytoplasm of the cell while searching for cargo. Including motor availability into these transport models would lead to useful mathematical models that avoid the challenging problem of estimating transition rates for mRNA bound to various numbers (and types) of motors, as these rates are largely unknown.

Acknowledgments. We are grateful to Dr. Raymond Goldstein for providing the polymer microtubule and transport simulation code used in [43] that we subsequently modified for our application.

Part of this research was conducted using computational resources and services at the Center for Computation and Visualization at Brown University and at the Ohio Supercomputer

Center through the Mathematical Biosciences Institute at The Ohio State University.

REFERENCES

[1] V. B. Alarcón and R. P. Elinson, *RNA anchoring in the vegetal cortex of the Xenopus oocyte*, Journal of Cell Science, 114 (2001), pp. 1731–1741.

[2] K. Babu, Y. Cai, S. Bahri, X. Yang, and W. Chia, *Roles of Bifocal, Homer, and F-actin in anchoring Oskar to the posterior cortex of Drosophila oocytes*, Genes & Development, 18 (2004), pp. 138–143.

[3] E. Bananis, S. Nath, K. Gordon, P. Satir, R. J. Stockert, J. W. Murray, and A. W. Wolkoff, *Microtubule-dependent movement of late endocytic vesicles in vitro: requirements for dynein and kinesin*, Molecular Biology of the Cell, 15 (2004), pp. 3688–3697.

[4] B. E. Becker and D. L. Gard, *Visualization of the cytoskeleton in Xenopus oocytes and eggs by confocal immunofluorescence microscopy*, in Xenopus Protocols, Springer, 2006, pp. 69–86.

[5] R. P. Brendza, L. R. Serbus, W. M. Saxton, and J. B. Duffy, *Posterior localization of dynein and dorsal-ventral axis formation depend on kinesin in Drosophila oocytes*, Current Biology, 12 (2002), pp. 1541–1545.

[6] P. C. Bressloff and J. M. Newby, *Quasi-steady-state analysis of two-dimensional random intermittent search processes*, Physical Review E, 83 (2011), p. 061139.

[7] P. C. Bressloff and B. Xu, *Stochastic active-transport model of cell polarization*, SIAM Journal on Applied Mathematics, 75 (2015), pp. 652–678.

[8] A. R. Chaudhary, F. Berger, C. L. Berger, and A. G. Hendricks, *Tau directs intracellular trafficking by regulating the forces exerted by kinesin and dynein teams*, Traffic, 19 (2018), pp. 111–121.

[9] V. Ciocanel, J. A. Kreiling, J. A. Gagnon, K. L. Mowry, and B. Sandstede, *Analysis of active transport by fluorescence recovery after photobleaching*, Biophysical Journal, 112 (2017), pp. 1714–1725.

[10] R. Delanoue and I. Davis, *Dynein anchors its mRNA cargo after apical transport in the Drosophila blastoderm embryo*, Cell, 122 (2005), pp. 97–106.

[11] R. Delanoue, B. Herpers, J. Soetaert, I. Davis, and C. Rabouille, *Drosophila squid/hnRNP helps dynein switch from a gurken mRNA transport motor to an ultrastructural static anchor in sponge bodies*, Developmental Cell, 13 (2007), pp. 523–538.

[12] N. D. Derr, B. S. Goodman, R. Jungmann, A. E. Leschziner, W. M. Shih, and S. L. Reck-Peterson, *Tug-of-war in motor protein ensembles revealed with a programmable DNA origami scaffold*, Science, 338 (2012), pp. 662–665.

[13] C. Eliscovich and R. H. Singer, *RNP transport in cell biology: The long and winding road*, Current opinion in Cell Biology, 45 (2017), pp. 38–46.

[14] J. A. Gagnon, J. A. Kreiling, E. A. Powrie, T. R. Wood, and K. L. Mowry, *Directional transport is mediated by a dynein-dependent step in an RNA localization pathway*, PLOS Biol, 11 (2013), p. e1001551.

[15] D. L. Gard, *Organization, nucleation, and acetylation of microtubules in Xenopus laevis oocytes: a study by confocal immunofluorescence microscopy*, Developmental Biology, 143 (1991), pp. 346–362.

[16] D. L. Gard, B. J. Cha, and E. King, *The organization and animal–vegetal asymmetry of cytokeratin filaments in stage VI Xenopus oocytes is dependent upon F-actin and microtubules*, Developmental Biology, 184 (1997), pp. 95–114.

[17] M. K. Gardner, M. Zanic, C. Gell, V. Bormuth, and J. Howard, *Depolymerizing kinesins Kip3 and MCAK shape cellular microtubule architecture by differential control of catastrophe*, Cell, 147 (2011), pp. 1092–1103.

[18] S. P. Gross, M. A. Welte, S. M. Block, and E. F. Wieschaus, *Coordination of opposite-polarity microtubule motors*, The Journal of Cell Biology, 156 (2002), pp. 715–724.

[19] R. J. Hawkins, O. Benichou, M. Piel, and R. Voituriez, *Rebuilding cytoskeleton roads: Active-transport-induced polarization of cells*, Physical Review E, 80 (2009), p. 040903.

[20] J. Heasman, O. Wessely, R. Langland, E. J. Craig, and D. S. Kessler, *Vegetal localization of maternal mRNAs is disrupted by VegT depletion*, Developmental Biology, 240 (2001), pp. 377–386.

[21] A. G. Hendricks, E. L. Holzbaur, and Y. E. Goldman, *Force measurements on cargoes in living cells*

reveal collective dynamics of microtubule motors, Proceedings of the National Academy of Sciences, 109 (2012), pp. 18447–18452.

[22] A. G. Hendricks, E. Perlson, J. L. Ross, H. W. Schroeder III, M. Tokito, and E. L. Holzbaur, *Motor coordination via a tug-of-war mechanism drives bidirectional vesicle transport*, Current Biology, 20 (2010), pp. 697–702.

[23] N. Hirokawa and R. Takemura, *Molecular motors and mechanisms of directional transport in neurons*, Nature Reviews Neuroscience, 6 (2005), pp. 201–214.

[24] J. Januschke, L. Gervais, S. Dass, J. A. Kaltschmidt, H. Lopez-Schier, D. S. Johnston, A. H. Brand, S. Roth, and A. Guichet, *Polar transport in the Drosophila oocyte requires Dynein and Kinesin I cooperation*, Current Biology, 12 (2002), pp. 1971–1981.

[25] S. Jeschonek, *ImageJ Macro, Available at https://github.com/sjeschonek*.

[26] M. Kloc and L. D. Etkin, *Delocalization of Vg1 mRNA from the vegetal cortex in Xenopus oocytes after destruction of Xlsirt RNA*, Science, 265 (1994), pp. 1101–1103.

[27] M. Kloc and L. D. Etkin, *Two distinct pathways for the localization of RNAs at the vegetal cortex in Xenopus oocytes*, Development, 121 (1995), pp. 287–297.

[28] M. Kloc, K. Wilk, D. Vargas, Y. Shirato, S. Bilinski, and L. D. Etkin, *Potential structural role of non-coding and coding RNAs in the organization of the cytoskeleton at the vegetal cortex of Xenopus oocytes*, Development, 132 (2005), pp. 3445–3457.

[29] M. W. Klymkowsky, L. A. Maynell, and C. Nislow, *Cytokeratin phosphorylation, cytokeratin filament severing and the solubilization of the maternal mRNA Vg1*, The Journal of Cell Biology, 114 (1991), pp. 787–797.

[30] V. Levi, A. S. Serpinskaya, E. Gratton, and V. Gelfand, *Organelle transport along microtubules in Xenopus melanophores: evidence for cooperation between multiple motors*, Biophysical Journal, 90 (2006), pp. 318–327.

[31] L. A. Ligon, M. Tokito, J. M. Finklestein, F. E. Grossman, and E. L. Holzbaur, *A direct interaction between cytoplasmic dynein and kinesin I may coordinate motor activity*, Journal of Biological Chemistry, 279 (2004), pp. 19201–19208.

[32] W. Malalasekera and K. Versteeg, *Computational fluid dynamics, the finite volume method*, 2007.

[33] C. Medioni, K. Mowry, and F. Besse, *Principles and roles of mRNA localization in animal development*, Development, 139 (2012), pp. 3263–3276.

[34] T. J. Messitt, J. A. Gagnon, J. A. Kreiling, C. A. Pratt, Y. J. Yoon, and K. L. Mowry, *Multiple kinesin motors coordinate cytoplasmic RNA transport on a subpopulation of microtubules in Xenopus oocytes*, Developmental Cell, 15 (2008), pp. 426–436.

[35] R. Milo and R. Phillips, *Cell Biology by the Numbers, available at http://book.bionumbers.org/*.

[36] J. Newby and P. C. Bressloff, *Random intermittent search and the tug-of-war model of motor-driven transport*, Journal of Statistical Mechanics: Theory and Experiment, 2010 (2010), p. P04014.

[37] J. M. Newby and P. C. Bressloff, *Quasi-steady state reduction of molecular motor-based models of directed intermittent search*, Bulletin of Mathematical Biology, 72 (2010), pp. 1840–1866.

[38] E. A. Powrie, M.-V. Ciocanel, J. A. Kreiling, J. A. Gagnon, B. Sandstede, and K. L. Mowry, *Using in vivo imaging to measure RNA mobility in Xenopus laevis oocytes*, Methods, 98 (2015), pp. 60–65.

[39] J. Schindelin, I. Arganda-Carreras, E. Frise, V. Kaynig, M. Longair, T. Pietzsch, S. Preibisch, C. Rueden, S. Saalfeld, B. Schmid, et al., *Fiji: an open-source platform for biological-image analysis*, Nature Methods, 9 (2012), pp. 676–682.

[40] C. A. Schneider, W. S. Rasband, and K. W. Eliceiri, *NIH Image to ImageJ: 25 years of image analysis*, Nature Methods, 9 (2012), pp. 671–675.

[41] E. Schulze and M. Kirschner, *Microtubule dynamics in interphase cells.*, The Journal of Cell Biology, 102 (1986), pp. 1020–1031.

[42] T. Tanaka and A. Nakamura, *Oskar-induced endocytic activation and actin remodeling for anchorage of the Drosophila germ plasm*, Bioarchitecture, 1 (2011), pp. 122–126.

[43] P. K. Trong, H. Doerflinger, J. Dunkel, D. St Johnston, and R. E. Goldstein, *Cortical microtubule nucleation can organise the cytoskeleton of Drosophila oocytes to define the anteroposterior axis*, eLife, 4 (2015), p. e06088.

[44] V. Trovisco, K. Belaya, D. Nashchekin, U. Irion, G. Sirinakis, R. Butler, J. J. Lee, E. R.

761 Gavis, and D. St Johnston, *bicoid mRNA localises to the Drosophila oocyte anterior by random*
762 *Dynein-mediated transport and anchoring*, Elife, 5 (2016).
763 [45] A. E. Twelvetrees, S. Pernigo, A. Sanger, P. Guedes-Dias, G. Schiavo, R. A. Steiner, M. P.
764 Dodding, and E. L. Holzbaur, *The dynamic localization of cytoplasmic dynein in neurons is driven*
765 *by kinesin-1*, Neuron, 90 (2016), pp. 1000–1015.
766 [46] R. D. Vale, F. Malik, and D. Brown, *Directional instability of microtubule transport in the presence*
767 *of kinesin and dynein, two opposite polarity motor proteins*, The Journal of Cell Biology, 119 (1992),
768 pp. 1589–1596.
769 [47] N. F. Vanzo and A. Ephrussi, *Oskar anchoring restricts pole plasm formation to the posterior of the*
770 *Drosophila oocyte*, Development, 129 (2002), pp. 3705–3714.
771 [48] J. K. Yisraeli, *VICKZ proteins: a multi-talented family of regulatory RNA-binding proteins*, Biology of
772 the Cell, 97 (2005), pp. 87–96.
773 [49] J. K. Yisraeli, S. Sokol, and D. Melton, *A two-step model for the localization of maternal mRNA in*
774 *Xenopus oocytes: involvement of microtubules and microfilaments in the translocation and anchoring*
775 *of Vg1 mRNA*, Development, 108 (1990), pp. 289–298.
776 [50] W.-m. Zhao, C. Jiang, T. T. Kroll, and P. W. Huber, *A proline-rich protein binds to the localization*
777 *element of Xenopus Vg1 mRNA and to ligands involved in actin polymerization*, The EMBO journal,
778 20 (2001), pp. 2315–2325.
779 [51] V. L. Zimyanin, K. Belaya, J. Pecreaux, M. J. Gilchrist, A. Clark, I. Davis, and D. St John-
780 ston, *In vivo imaging of oskar mRNA transport reveals the mechanism of posterior localization*, Cell,
781 134 (2008), pp. 843–853.